



CENTRO DE INVESTIGACIÓN Y DE ESTUDIOS
AVANZADOS DEL INSTITUTO POLITÉCNICO NACIONAL

UNIDAD ZACATENCO

DEPARTAMENTO DE CONTROL AUTOMÁTICO

**Diseño, modelización y control
de un nuevo tipo de aeronave VTOL**

TESIS

Que presenta

Aurélien Cabarbaye

Para obtener el grado de

DOCTOR EN CIENCIAS

En la especialidad de

Control Automático

Directores de Tesis:

Dr. Rogelio Lozano Leal

Dr. Moisés Bonilla Estrada

Ciudad de México

Octubre 2017

ACKNOWLEDGEMENT

First and foremost, I would like to thank the Consejo Nacional de Ciencia y Tecnología (Conacyt) for its financial support during these four years of Ph.D.

I would like to thank Prof. Rogelio Lozano for inviting me to join the CINVESTAV-IPN / CNRS UMI3175 LAMFIA Cinvestav in Mexico, without whom this thesis would not have been possible. He encouraged me to pursue research on a very innovative concept and assisted me in investigating its feasibility. I appreciate all the time and ideas he contributed. I am very grateful for the scholarship of Mexican government I received thanks to his support.

Moreover, this thesis benefited greatly from the joint supervision between this laboratory and ISAE SUPAERO (Toulouse, France) under the direction of Dr. Patrick Fabiani. I received advice and guidance from top researchers in both of the scientific fields the drone concept relies on: Aeronautics and Control Systems. I am very grateful to my thesis supervisors, Prof. Rogelio Lozano, Prof. Moisés Bonilla Estrada and Dr. Patrick Fabiani for their scientific follow-up and the thoughtful ideas they gave me throughout this research.

My thanks also go to all the staff and colleagues of Cinvestav and ISAE SUPAERO for the help I received throughout the last three years. I particularly appreciated the assistance during the elaboration of the drone demonstrator and the access given to several prototyping machines.

I lastly owe my deepest gratitude to my family for their unfailing support during this rich and long adventure. I would like to thank especially my brother Adrien Cabarbaye for his Electronics, Computer Science and English support.

RESUMEN

Los ingenieros se han esforzado en idear conceptos de convertibles en un intento de conciliar los beneficios de los aviones y de los helicópteros a través de una variedad de términos medios, pero sin lograrlo verdaderamente. Las insuficiencias de las soluciones encontradas han postergado la investigación. Estos últimos han recuperado un cierto entusiasmo con la aparición de aviones no tripulados. Es en este contexto que se ha ideado un concepto innovador de aviones convertibles para aplicaciones de UAVs tácticos. La sustentación en modo helicóptero está asegurada por un rotor situado en la nariz del aparato y propulsado en rotación por hélices montadas sobre sus palas. El rotor se detiene en vuelo para actuar como canard y sus hélices impulsan el avión en modo avión. Un ala fija se añade en la cola del aparato, en el flujo del rotor, para aliviar la carga de este último cuando está detenido. Por lo tanto, el diseño de las hélices no está más sobredimensionado para sostener el avión en modo helicóptero, el tamaño del rotor no está más limitado por el funcionamiento del avión y la mayoría de los sistemas se utilizan en ambos modos, lo que reduce la potencia requerida, el peso y la resistencia aerodinámica. La viabilidad de este concepto se ha demostrado durante esta tesis. Este último incluye el análisis del comportamiento del sistema de rotor, el estudio de las interacciones entre los apéndices aerodinámicos en el vuelo y el control durante la transición entre el vuelo estacionario y el vuelo horizontal. Las ganancias de desempeño de este concepto sobre aviones tácticos existentes, en términos de autonomía y masa de carga útil a bordo, se evaluaron a través de un estudio de tipo diseño conceptual. Además, se ha producido un modelo para demostrar la viabilidad de la realización. Además, el principio de rotor impulsado por hélice ha sido reutilizado y explotado en un nuevo concepto patentado que supera los defectos inherentes de los drones multi-rotor. Estos últimos son inherentemente poco fiables debido a la complementariedad de sus diferentes sistemas de propulsión.

ABSTRACT

Engineers have striven for designing convertible concepts in an attempt to reconcile the benefits of aeroplanes and helicopters through a variety of trade-offs. It seems however that they have not yet managed to satisfactorily reach this goal fully. The inadequacies of the proposed solutions put the research on hold for several decades. Recently however, research has regained a certain enthusiasm with the emergence of UAVs. An innovative concept of convertible aircraft, conceived primarily for tactical UAV applications, is proposed as part of this thesis. The lift in helicopter mode is provided by a rotor located in the nose of the aircraft and driven in rotation by propellers mounted on its blades. The rotor stops in flight to act as a canard and its propellers propel the whole aircraft into airplane mode. A fixed wing is added to the tail, in the rotor flow, to alleviate the latter's load when it is stopped. This removes the previous need for oversized propellers necessary to sustain the aircraft in helicopter mode. The size of the rotor is also no longer limited by airplane operations and almost all the UAV's systems are used in both modes. This has the great advantage of reducing the required power, the weight and the aerodynamic drag. The feasibility of this concept has been demonstrated throughout the thesis work which includes rotor system behaviour analysis, the study of interactions between the different hovering aerodynamic systems and the design of the control during the transition between hover and horizontal flights. The performance gains of this concept over existing tactical drones, in terms of autonomy and on-board payload mass, were evaluated as part of conceptual design study. A model has been produced in order to demonstrate the feasibility of the concept's production. The propeller-driven rotor principle, developed in this thesis, was carried over and implemented in a new patented concept which overcomes the inherent defects of multi-rotor drones.

Contents

RESUMEN	v
ABSTRACT	vii
INTRODUCTION	1
0.1 OPERATIONAL OBJECTIVE	1
0.1.1 TACTICAL UAV (TUAV) DEFINITION	1
0.1.2 TUAV BENEFITS	2
0.1.3 STOL CAPACITY LIMITS	5
0.1.4 VTOL CAPACITY	6
0.1.5 STATEMENT	10
0.2 Concept	11
0.2.1 ROTOR BLADE - FOREWING HYBRID	11
0.2.2 TANDEM WING CONFIGURATION	12
0.2.3 PROPELLER POWERED ROTOR	13
0.2.4 LANDING CONFIGURATION	15
0.2.5 CONCEPT GENERAL OVERVIEW	17
0.3 STATE OF THE ART	17
0.3.1 SIMILAR CONCEPT	18
0.3.2 ROTOR AERODYNAMICS	20
0.3.3 CONTROL ASPECT	21
0.4 PH. D. OBJECTIVES	24
0.4.1 HOVER CHALLENGE	24

0.4.2	TRANSITION CHALLENGE	24
0.4.3	CONCEPTUAL DESIGN	25
0.4.4	PERSPECTIVES	25
1	MODEL AND STUDY OF A PROPELLER POWERED ROTOR ABLE TO COMPLY WITH AEROPLANE MODE CONSTRAINTS.	27
1.1	STUDY OF THE ROTOR PERFORMANCES.....	27
1.1.1	MODEL AND STUDY OF THE HOVERING ROTOR.	28
1.1.2	BENCH TEST OF THE DEMONSTRATOR ROTOR.	32
1.1.3	Complementary tests performed on dedicated bench.	40
1.2	Study of the interactions between the aerodynamic entities.....	43
1.2.1	ROTATING PARTS AND WING INTERACTION	45
1.2.2	PROPELLER AND ROTOR INTERACTION	50
1.3	Partial conclusion	51
2	MODEL OF THE TRANSITION BETWEEN HELICOPTER AND AERO- PLANE MODES	53
2.1	THEORY OF THE ROTOR IN TRANSITION.....	53
2.1.1	ROTOR FORWARD FLIGHT THEORY	54
2.1.2	EXTENDED THEORY	58
2.2	FLIGHT DYNAMICS.....	64
2.2.1	ASSUMPTIONS	64
2.2.2	DYNAMICS RELATIONS	64
2.2.3	FORCES AND MOMENTS	67
2.2.4	AIRCRAFT AERODYNAMICS	70
2.3	PARTIAL CONCLUSION.....	90
3	CONTROL	91
3.1	AIRCRAFT CONTROL TYPE.....	91
3.2	CONTROL STUDY.....	92
3.2.1	LINEAR MODEL	92

3.2.2	CONTROLABILITY	93
3.2.3	OBSERVABILITY	95
3.2.4	CONTROL DESIGN	96
3.3	PARTIAL CONCLUSION.....	102
4	CONCEPTUAL DESIGN	105
4.1	BILL OF SPECIFICATIONS.....	105
4.1.1	COMPETITORS ANALYSIS	105
4.1.2	PAYLOAD	108
4.1.3	ENDURANCE	111
4.1.4	ALTITUDE	111
4.1.5	CLIMB PERFORMANCES	112
4.1.6	SPEEDS	112
4.2	GEOMETRY.....	112
4.2.1	LANDING GEAR DESIGN	113
4.2.2	AIRFOIL	114
4.2.3	FUSELAGE	118
4.2.4	ELECTRIC MOTOR NACELLES	119
4.3	MISSION.....	120
4.4	OPTIMISATION.....	128
4.5	RESULTS.....	131
4.6	PARTIAL CONCLUSION.....	133
5	PERSPECTIVES	135
5.1	AIRCRAFT CONTROL.....	135
5.2	ELECTRIC PROPULSION SYSTEM.....	136
5.3	MINI UAV DERIVATIVE OF THE CONCEPT: “FLYING ROTOR”.....	139
	GENERAL CONCLUSION	143

A	APPENDIX: ROTOR HOVER THEORY	147
A.1	MOMENTUM THEORY.....	147
A.1.1	HOVER	147
A.1.2	IN CLIMB	149
A.1.3	GENERALIZED MOMENTUM THEORY	150
A.1.4	SWIRL IN THE WAKE	152
A.1.5	PROFIL DRAG	154
A.2	BLADE ELEMENT THEORY.....	155
A.3	TIP LOSES.....	157
A.4	ROOT LOSES.....	158
A.5	GENERALISATION (CF: AUTOROTATION)	159
B	APPENDIX: EXTENDED THEORY EQUATIONS	165
B.1	INDUCED VELOCITY.....	165
B.2	AERODYNAMICS FORCES AND MOMENT.....	166
B.2.1	ROTOR LIFT t	168
B.2.2	ROTOR LONGITUDINAL FORCE h	171
B.2.3	ROTOR LATERAL FORCE y	171
B.2.4	ROTOR TORQUE Q	172
B.3	PROPULSION FORCES AND MOMENTS:.....	172
B.3.1	PROPULSION LIFT T_p	175
B.3.2	PROPULSION LONGITUDINAL FORCE H_p	176
B.3.3	PROPULSION LATERAL FORCE Y_p	176
B.3.4	PROPULSION TORQUE Q_p	177
B.4	OVERALL ROTOR FORCES:.....	177
B.5	FLAP MOTION.....	179
B.5.1	LIFT PART	182
B.5.2	PROPULSION PART	184
B.5.3	FINAL FLAP RESULTS	186

C	APPENDIX: DYNAMICS MODEL DERIVATIVE	187
C.1	DYNAMICS RELATIONS DERIVATIVE.....	188
C.1.1	QUATERNION MODEL	188
C.1.2	EULER ANGLES BASED MODEL	192
C.2	STABILITY DERIVATIVES	192
C.2.1	Rotor derivatives	194
C.2.2	STEADY AIRFRAME	202
C.2.3	Modified dynamics	208
D	APPENDIX: CONCEPTUAL DESIGN	209
D.1	AMBIENT CONDITION	209
D.1.1	METEOROLOGY	209
D.1.2	GEOLOGY	210
D.2	WEIGHT AND BALANCE.....	211
D.2.1	FORE PLANE	211
D.2.2	MAIN-ROTOR HUBS AND HINGES	212
D.2.3	MAIN WING WEIGHT	212
D.2.4	VERTICAL TAIL WEIGHT	212
D.2.5	FUSELAGE	213
D.2.6	LANDING GEAR	214
D.2.7	FUEL SYSTEM	215
D.2.8	FLIGHT CONTROLS SYSTEM	216
D.2.9	PROPULSION SYSTEM :	217
D.3	AERODYNAMICS	218
D.3.1	INDUCED DRAG	218
D.3.2	FUSELAGE	219
D.3.3	ELECTRIC MOTOR NACELLES	223
D.3.4	SENSOR TURRET	229
D.3.5	LANDING GEAR	230
D.3.6	ENGINE INSTALLATION DRAG	230

D.4	STABILITY.....	231
D.4.1	LONGITUDINAL STABILITY	231
D.4.2	LATERAL-DIRECTIONAL EQUILIBRIUM AND STABILITY	238
D.5	PERFORMANCES.....	244
D.5.1	HOVER	244
D.5.2	CLIMB PERFORMANCES	245
D.5.3	OGI ALTITUDE	246
D.5.4	STALL SPEED	246
D.5.5	TRANSITION	248
D.5.6	LOITER	249
D.5.7	MAX SPEED	251
E	APPENDIX: MOTOR CONTROL	252
E.1	BDSM modelisation.....	252
E.1.1	Electrical modelisation	252
E.1.2	$\alpha \beta \gamma$ transformation	253
E.2	Control construction.....	254
E.2.1	Modified $d q 0$ transformation	255
E.2.2	Adaptive control design	256
E.3	Simulation results.....	260
F	APPENDIX: “FLYING-ROTOR” CONTROL	264
F.1	Model.....	264
F.1.1	Rotor forces	264
F.1.2	Propellers forces	268
F.1.3	“flying rotor” UAV dynamics	269
F.2	Control.....	271
F.2.1	\dot{X} control	271
F.2.2	\dot{Y} Control	271
F.2.3	\dot{Z} and Ω controls	272
F.3	Simulation.....	273

F.4	Motors acceleration issues:	276
-----	-----------------------------------	-----

List of Figures

1	MALE ground equipment	4
2	Take-off / landing footprint	5
3	Ground vehicle	6
4	Comparison of helicopter and aeroplane flight envelopes	7
5	German project	9
6	Focke-Wulf FW-860 (1957)	11
7	Brennan / Curtiss-Bleecker	14
8	Nagler-Rolz NR 54	14
9	blended landing gear / vertical tailplane (Courtesy of Lockheed Martin)	16
10	Landing configurations	17
11	MALE ground equipment	17
12	Vertical rotor hub aircraft	18
13	StopRotor Technology	19
14	Spinwing	20
15	Tilting rotor hub aircraft	20
16	T-wing	22
17	Tilting-rotor tail-sitter	23
1.1	Un-dimensioned power	29
1.2	Propeller efficiency	30
1.3	Diagram of a brushless motor	31
1.4	Demonstrator	32
1.5	Testbed	33
1.6	First motor	35

1.7	Second motor	35
1.8	Motor observation	36
1.9	Test results	36
1.10	Top view	37
1.11	Propeller efficiency for various blade pitch	39
1.12	Propeller bench	41
1.13	bench test rotational inertia measure	41
1.14	Acceleration pattern of the bench test for propeller rotation speed of 10000RPM	42
1.15	Power and efficiency at 10000RPM	42
1.16	Power and efficiency at 6000RPM	43
1.17	Aircraft meshing	45
1.18	Parameter Q showing the rotor wake blowing the wing	45
1.19	Air velocity showing the propeller wake blowing the wing	46
1.20	Wing axial torque	46
1.21	Wing cross section	47
1.22	TL54 lift coefficient function of the angle of attack and the deflection	48
1.23	TL54 lift coefficient variation function of the deflection	48
1.24	relative wind impacting the main wing	48
1.25	Tufts fixed on the wing	49
1.26	Propeller axial velocity	50
2.1	Horizontal flight incidence air flow	54
2.2	Horizontal flight rotor disk	54
2.3	Horizontal flight blade air flow	55
2.4	Horizontal flight airfoil	55
2.5	Horizontal flight blade forces	56
2.6	U approximation with U_p and U_T varying linearly respectively from 0 to 100 and from 100 to 0	58
2.7	ϕ approximation with U_p and U_T varying linearly respectively from 0 to 100 and from 100 to 0	60
2.8	U optimised estimation	62

2.9	$U\phi$ optimised estimation	63
2.10	Longitudinal dynamics	68
2.11	Lateral dynamics	69
2.12	Directional dynamics	70
2.13	Speed estimation	76
2.14	wing stream tube deflection, where V is the relative wind, v and w are respectively the vertical downwash velocity at the wing location and at the far downstream	77
2.15	Downwash angle of attack	78
2.16	Fuselage normal force Fz_{fus}	82
2.17	Fuselage moment M_{fus}	83
2.18	TL54 lift coefficient function of the angle of attack	83
2.19	TL54 lift coefficient function of the angle of attack	84
2.20	TL54 moment coefficient function of the angle of attack and the deflection	85
2.21	TL54 moment coefficient variation function of the angle of the deflection	85
2.22	TL54 drag coefficient function of the angle of attack for zero deflection	86
2.23	TL54 lift coefficient function of the angle of attack with stall estimation	87
2.24	NACA0012 lift coefficient function of the angle of attack and the deflection	88
2.25	NACA0012 lift coefficient function of the deflection	88
2.26	NACA0012 drag coefficient function of the angle of attack and the deflection	89
2.27	NACA0012 drag coefficient function of the deflection	90
3.1	3D trajectory	99
3.2	θ vs time	100
3.3	U , V and W vs time	100
3.4	ω vs time	101
4.1	Aft landing gear design rule	113
4.2	Landing gear ground stability condition	114
4.3	Landing gear aeroplane condition	114
4.4	Foreplane airfoil comparison	115
4.5	Foreplane airfoil comparison	116

4.6	Foreplane airfoil comparison	117
4.7	3 view plan of the fuselage	119
4.8	Nacelle design	120
4.9	mission	121
4.10	optimisation principle	131
5.1	UAV architecture	139
5.2	UAV payload	140
5.3	Blade articulation	140
5.4	Application 1: Human organs transfer	145
5.5	Application 2: cash-in-transit courier	145
5.6	Application 3: first-aid kit delivery in hazardous environments	146
A.1	Propeller stream tube in hover	148
A.2	Propeller stream tube	149
A.3	swirl in the wake	152
A.4	Pressure drop due to swirl	153
A.5	Profil section	155
A.6	Rotor disk portion	156
A.7	Tip lose in hover	158
A.8	Autorotation tube flow	159
A.9	autorotation profil section	161
B.1	Induced velocity	166
B.2	Self propelled rotor	172
B.3	Propulsion axial and radial forces and torque	173
B.4	teetering-rotor-dynamic	179
D.1	Prandtl biplane interference factor ([?], Figure 5-10)	219
D.2	Friction drag estimation method	220
D.3	Electrical motor characteristics	223
D.4	Nacelle intake zoom	224
D.5	Nacelle exhaust zoom	226

D.6	Nacelle shape	229
D.7	Stability dynamic	232
D.8	Angle of attack deflection	233
D.9	Inter-wing distance	234
D.10	Downwash charts ([?], Figure 5-10)	235
D.11	Main wing airflow	235
D.12	Upwash charts ([?], Fig. 16.11)	236
D.13	Fuselage wing effect and munk-correction	237
D.14	Propeller operation parameters	238
D.15	Stability dynamic (top)	240
D.16	Stability dynamic (back)	240
D.17	Yaw moment derivative ([?], fig. 16.20	242
D.18	Stall condition	247
E.1	Equivalent circuit from electric equation, (courtesy of Pillay [?])	252
E.2	Desired path , T_d in black and T_q in green, A vs s	260
E.3	Obtained path and error evolution, A vs s	261
E.4	Parameter L_d estimation, H vs s	262
E.5	Parameter R_d estimation, ω vs s	262
E.6	Parameter E estimation, E_d real and estimated respectively in black and red, E_q real and estimated respectively in green and yellow, , ω vs s	263
E.7	Parameter E estimation	263
F.1	Rotor references and speeds	264
F.2	Rotor forces	265
F.3	Trajectory K=1	275
F.4	Control K=1	275
F.5	Control K=1	275
F.6	Control K=0.25	276
F.7	Trajectory K=0.25	276

INTRODUCTION

0.1 OPERATIONAL OBJECTIVE

UAVs have long been confined to very specific applications, and hence the family was only composed of very few members. Since the beginning of the 21st century, however, their number has risen extremely quickly and seems to continue increasing in line with the development of new attractive applications. Due to development cost and time required, it does not seem suitable to keep designing an aircraft per application anymore. The UAV market will indeed only be able to truly grow and emerge from its current niche market position if its acquisition cost becomes more affordable, which inevitably requires economies of scale. It, therefore, seems appropriate to conduct a preliminary needs assessment to target all possible uses that a single aircraft would fulfil. Whatever the country, current main UAV customer is the Army and their use for defence purposes: it represents on its own most of the purchases made by Western armies and this trend should continue for the next years and even decades. Nevertheless, the civilian market will also start growing soon when related regulations will allow their use for various applications that are yet to come. Among the different types of UAVs, tactical ones are likely to have a bright future as they will represent a significant part of the market share due to their reasonable cost and their comfortable capacity. Current models in service embody nonetheless some flaws that seem to be rectifiable.

0.1.1 TACTICAL UAV (TUAV) DEFINITION

Armies have developed the most detailed classification for UAVs since they have been the first to find their interest in developing them. UAVs are usually categorised by altitude and range. This categorisation seems relevant as it is used by the industry for their presentations

during events such as ParcAberporth Unmanned Systems forum: “A TUAV has a service ceiling of typically 18,000 ft (5,500 m) with a range of around 160 km” [?]. French state also uses the size to describe their needs [?]: “A TUAV is characterised by a span of few meters, and weight in the range of 100 kg.” In the United States military classification, these drones fall into the following categories: Tier I, which corresponds to a low altitude, long endurance UAV for the U.S. Air Force; Tier II and Tier III for the U.S. Marine Corps; Tier II, which corresponds to the short-range UAV, and Tier III, which refers to the medium range for the U.S. Army. Nevertheless, despite the different categorisations, it is acknowledged that the TUAV is comprised between mini UAV and MALE UAV (medium altitude, long endurance).

For military applications, such aircraft usually serves within the brigades or equivalent and is historically dedicated to Reconnaissance, Surveillance, and Target Acquisition (RSTA) [?].

If the professional use of civil UAVs has been quite low until now due to the lack of appropriate regulations, the recent acceleration of the certification implementation is making the interest rise significantly. French DGAC (the French equivalent of the Federal Aviation Administration) was, for example, the first to deliver a regulation for small civil UAVs a few years ago [?] and Federal Aviation Administration (FAA) is currently conducting its experimental phase [?]. High-end civilian UAVs seem to share similar characteristics to TUAVs, as shown by the civilian Flightech FT-ALTEA [?] or Yamaha R-MAX. Moreover, civilian government institutions re-employ more and more TUAVs coming from military developments.

0.1.2 TUAV BENEFITS

Although TUAVs are historically the oldest operational drones, mini UAVs and MALE UAVs are currently the ones in the limelight. Mini UAVs are indeed predominant in consumer markets while the acquisition of MALE drones has become the priority of many countries [?]. TUAVs are however essential and cannot be replaced by other UAV categories for several reasons.

Comparison with mini UAVs

- TUAVs have a much larger payload capacity than mini UAVs. The TUAV baseline mis-

sion consists of lifting sensors that were historically accommodated onto light aeroplanes or helicopters, such as standard EO/IR (in the sensor turret). SAR/MTI sensors are increasingly adopted though, such as Nano Sar, mounted on AAI RQ-7B Shadow 200 [?]. Communication/Data Relays are the latest most current sensor found on TUAV [?].

- TUAVs have a relatively high service ceiling (5000m). It provides a large scope of vision to its sensors, which is also of particular interest in the context of wireless communication. To the contrary, limitations in facing wind and theoretical service ceiling prevent mini drones from flying too high.
- TUAVs have significant autonomy: over 5 hours compared to the maximum half hour of most mini UAVs. This enables them to cover a team operation over its entire duration (e. g. control of fire, law enforcement operation)
- TUAVs are increasingly expected to accommodate additional payload (optionally, payload deployable in flight). Hereafter are some examples:
 - The use of drones in agriculture for detection and quick treatment promises significant savings in sprayed product compared to traditional methods [?].
 - TUAVs can also be used for dropping incendiary charges during preventive Slash-and-burn,

If MALE UAVs have a larger theoretical capability than TUAVs (sensor, ceiling service, range/flight time, payload, satellite telecommunication ...), TUAVs still present many advantages which should not be put aside: TUAV RQ-7 Shadow entered service in 2004 while MALE UAVs, like MQ-1 Predator, has been in service since 1995.

Comparison with MALE UAVs

- TUAVs are more affordable than MALE drones. For instance, TUAV RQ-7 Shadow unit cost is \$750,000 [?] while MALE MQ-1C Gray Eagle unit cost is \$5.40 million and MALE MQ-9 Reaper unit cost is \$14.42 million [?]. The same applies to the cost in operation which, on a military point of view, has represented one of the main UAV

flight constraints during the past few wars. The civilian market is generally much more sensitive to cost than military's. A small MALE UAV is more than twice as expensive as a light helicopter, which makes their acquisition by civilian agencies unlikely.

- Thanks to their small size, which makes tighter manoeuvres possible, and reduced cost, which allows more risk-taking, TUAVs can fly at very low altitude and therefore overcome any cloud cover [?].
- TUAVs are generally designed to use launch and recovery systems that exempt them from long runways, needed, for instance, by MALE UAVs. Predator RQ-1 / MQ-1 / MQ-9 Reaper UAV require, for example, a take-off and landing length of typically 2,000ft [?]. On the first hand, this is of great concern to the military since airdromes represent the priority targets during conflicts. On the other hand, due to increasing airport congestion, civilian UAVs are more likely to be used from small private airstrips, in the manner of ultralight aircraft, or directly from a portion of closed road [?].
- TUAVs require fewer resources on the ground than MALE UAVs as shown in Figure 1. Thus, they require significantly less logistics.

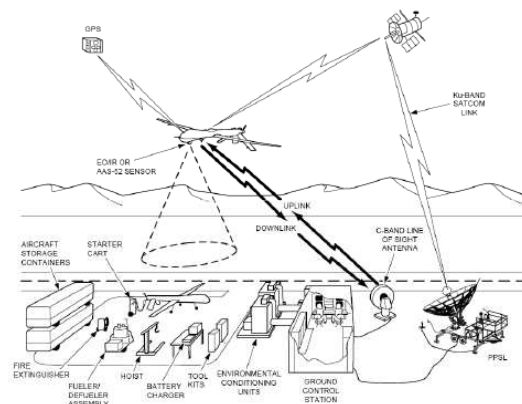


Figure 1: MALE ground equipment

0.1.3 STOL CAPACITY LIMITS

As seen in section 0.1.2, page4, TUAVs generally have a STOL (Short TakeOff and Landing) capacity. This latter does not seem however sufficient enough for several reasons.

NEED FOR EXPOSED AREAS DURING TAKEOFF Aeroplane UAVs require, depending on machine capacities, longer or shorter, more or less prepared airfields. They nevertheless usually need longer fields so as not to create any problems while carrying out specific operations, as illustrated in Figure 2.

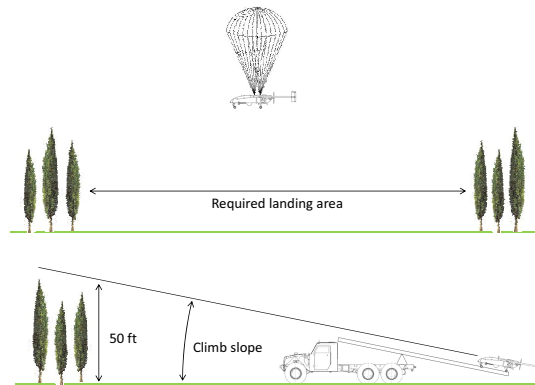


Figure 2: Take-off / landing footprint

For instance, AAI RQ-7 Shadow, a classical aeroplane TUAV, requires a flat surface of about 95m in length for a conventional wheeled landing. Even if this landing distance can be notably reduced, using an air vehicle deployable arresting hook coupled with ground based arresting cables, the drone requires a minimum open space. By analogy with manned aircraft, the landing distance is indeed not only the runway length but also includes the distance travelled in flight since the aeroplane falls below 50 ft [?]. If the necessary landing footprint can be further reduced by using a parachute landing, like for Sagem Sperwer, it cannot be reduced below 50m of diameter. [?].

And the same problem arises for take-offs. Climb slopes are indeed limited for conventional aeroplanes.

NEED FOR LARGE GROUND CREWS If the footprint necessary for operations can be reduced, the required means of this reduction are particularly heavy. For example, in the case of AAI RQ-7 Shadow, a crew of 17 specialised operators is necessary just for the management of the drone. In the case of Sagem Sperwer, a convoy for outdoor operations usually consisting of several specialised vehicles is required, as shown in Figure 3.



Figure 3: Ground vehicle

0.1.4 VTOL CAPACITY

STOL capacity limitations urge to develop Vertical Take-Off and Landing (VTOL) aeroplane. This capability has been tried out successfully on existing machines, such as SR/C Shadow [?]. However, as for manned aviation, it is the helicopter configuration that seems to be the most prolific.

0.1.4.1 HELICOPTER ADVANTAGES

In addition to a simplified implementation, a helicopter provides a long hover flight ability, which is of particular interest for aerial work. It also makes cross developments possible since its geometric constraint on a ship helicopter deck is similar to what can be faced on land. This was, for example, the case of Northrop Grumman MQ-8 Fire Scout which was

co-developed by the U.S. Army and the US Navy. A VTOL capability is lastly of particular interest for civilian use. Not only, it significantly reduces required ground facilities but also, it enables drone usage directly within cities, from heliport-kind platforms.

0.1.4.2 HELICOPTER LIMITS

Even if the first “vertical flight” was performed in 1907 by French inventor Paul Cornu, the first actual viable VTOLs which laid the foundation of helicopters were German Focke-Wulf Fw 61 and American Vought-Sikorsky VS-300. The former did not fly before 1936, and the latter first flew in 1937, when flight theory was sufficiently understood. Then, in order to fulfil the need for hovering aircraft during Second World War, several helicopters came rapidly into production thanks to their promising performances. However, the better helicopters became, the more obvious appeared its main limitation compared to aeroplanes:

- A theoretical maximum speed of 200 kts [?]
- A relatively low service ceiling as shown in Figure 4.

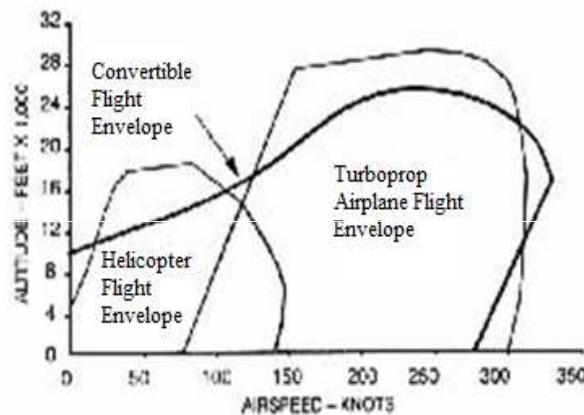


Figure 4: Comparison of helicopter and aeroplane flight envelopes

- A limited range/endurance. For a TUAV, the range being limited by telecommunication span, the decisive quantity is endurance. For instance, for the same payload mass (90kg), AAI RQ-7 Shadow, based on an aeroplane configuration, can fly 9 hours whilst Schiebel Camcopter S-100, its helicopter counterpart, can only fly 5 hours. If the

problems caused by service ceiling and endurance limitations are easy to imagine, it is the speed limitation that is the one of most concern, on a military point of view. By way of illustration, this has been shown during Operation Iraqi Freedom. 33 AH-64 Apache helicopters were engaged against Iraqi Republican Guard's Medina division: 30 AH-64 Apaches were severely damaged, and 1 crashed, whereas only one Fairchild A-10 Thunderbolt II, the AH-64 Apache aeroplane counterpart, was lost during the entire war. As a consequence, the US army aviation chief, Maj Gen Anthony Crutchfield, made the commitment to upgrade the military's entire collection of helicopters to new rotorcraft. It should present a minimum top speed of roughly 200kt (370km/h) by 2030 [?], which is at least 30kt faster than conventional helicopters (i.e. around 170kt (314km/h)[?]).

If an advanced speed is also attractive to classical civilian uses, it will also foster the creation of new applications. For example, following the idea of the payload capacity discussed in section 4.1.2, page 108, a high-speed VTOL UAV would significantly reduce the time taken by organ transport by quickly commuting between hospitals. This concept could be generalised to any transport of valuable goods requiring high speed, such as cash transportation.

0.1.4.3 POWERED-LIFT AIRCRAFT

Germans have been the first to develop designs with such abilities at the end of Second World War. Through many projects, more or less accomplished, they indeed established all major methods to achieve this goal:

- “tilt-thrust” configuration such as Focke Achgelis Fa 269
- A separated sustentation system configuration such as Focke-Wulf Triebflugel.
- “tail-sitter” configuration such as Focke-Wulfe Triebflugel

The three german projects [?], are illustrated in Figure 5. These configurations raised nevertheless new issues, either conceptual or technical, which prevented any complete development until now.

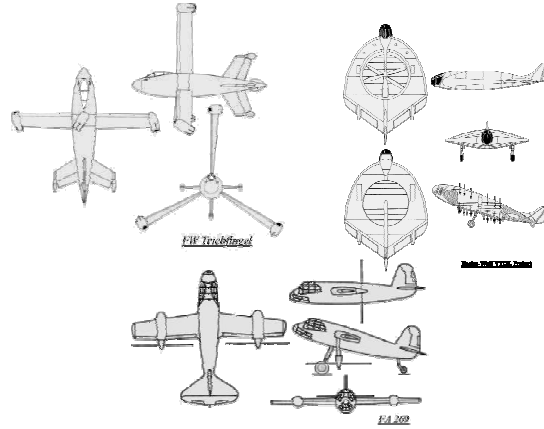


Figure 5: German project

0.1.4.4 “TILT-THRUST” CONFIGURATION

The first operational aircraft of this kind is military Boeing-Bell V-22 Osprey. However, its complexity and its design restrictions prevented him from being either affordable or entirely reliable. “Tilt-thrust” configuration may not respect “KISS Principle” (i.e. acronym of “Keep it simple, stupid”), inherent to aeronautics since one of his founding father, Leonardo Da Vinci, once said “Simplicity is the ultimate sophistication”. The Coast Guards have, for instance, preferred in March 2008 the couple formed by RQ-8A Fire Scout and Predator, to Bell HV-911, a “Tilt-thrust” UAV, for that matter. Although the configuration was attractive for manned aircraft because it kept a conventional pilot and passenger’s position, it had serious drawbacks, making it poorly suited for UAVs applications.

0.1.4.5 SEPARATED SUSTENTATION SYSTEM CONFIGURATION

As for the previous concept, this solution is particularly complex. Moreover, the sustentation system is unused or at least poorly used during high-speed flight, where most of the lift is generated by the wing. It, therefore, constitutes a useless weight and drag generator in these conditions.

0.1.4.6 “TAIL-SITTER” CONFIGURATION

A realistic VTOL formula that seems to be the easiest to implement is “Tail Sitter” configuration. The main advantage of this approach is its simplicity since it is sufficient to land the plane down onto its tail to convert it into a VTOL. It is this apparent simplicity that made this formula the first to be successfully implemented with Convair XFY-1 Pogo. This aircraft achieved a double transition in November the 5th, 1954. Nevertheless, “Tail-sitter” formula also includes significant defects such as:

- Important power required to reach a thrust to weight ratio greater than 1 to take off and land the aircraft smoothly.
- Great sensitivity to the wind due to the attitude of the main wing. This leads to abysmal ability to land out of zero wind conditions.
- Uneasy access to the cockpit, engine and accessories which require the use of ladders and special platforms.
- Issues of pilot safety in an ejection event, whether it is in horizontal or vertical configurations.
- Issues involved when piloting backwards during aircraft landing.

All these defects explain the gradual disinterest in the formula that followed its first successes. Its particularly attractive benefits have nevertheless led engineers to develop solutions more or less utopic to solve its major defects, as Focke-Wulf FW-860 project showed (Figure 6).

However, Pogo proved that VTOL concept in “Tail sitter” configuration is feasible. Furthermore, for the use of this configuration on a TUAV, these defects are reduced or eliminated by the reduced size of the aircraft, the remote control through a small number of cameras and partial automation.

0.1.5 STATEMENT

Therefore, by adding a VTOL capability, all the benefits TUAV class has can fully be exploited. The conceptual design for such configuration should not be made from results



Figure 6: Focke-Wulf FW-860 (1957)

obtained for manned aircraft. The integration of a pilot onboard indeed hugely restrains its design. Thus, “tail sitter” configuration, appraised unsatisfactory for manned aircraft, may represent a promising basis for a TUAV design, providing a guarantee of simplicity. Particular attention to solving its inherent defects should nonetheless be paid.

0.2 Concept

0.2.1 ROTOR BLADE - FOREWING HYBRID

Apart from convertibles using separated distinct helicopter rotors and propellers, all propeller driven VTOL concepts use their rotors for both generating sustentations in hover and horizontal flight propulsion. This coupling is done to limit the number of installed elements to save weight and drag and therefore improve performances. However, this is not obtained without a significant trade-off. Even if aeroplane propellers and helicopter rotors are based on the same principle, they are designed to meet conflicting specifications. A helicopter rotor must be able to generate a lift of at least 1.2 times the weight of the aircraft at almost no airspeed [?]. On the other hand, an aeroplane propeller usually generates $1/5$ of the weight at high speed. This implies that a helicopter rotor may be as big as possible to contain the disk loading while the propeller diameter is limited in diameter by the tip aerofoil Mach limit. For instance, the propeller of EADS Harfang aeroplane has a disk area of $2.62m^2$ whereas

the rotor disk area of Northrop Grumman MQ-8 Fire Scout helicopter is $55.5m^2$. These two aircraft can indeed be compared because their weight is around the same: $1350kg$. If the same propeller is used for both horizontal flight propulsion and hover sustentation, its diameter will inevitably be a trade-off between the two, which highly deteriorates its efficiency. This is, for instance, illustrated by the propellers' efficiency of Bell Boeing V-22 Osprey that does not exceed 60% [?]. As a consequence, the aircraft has to be overpowered, which degrades its overall performances. This latter issue can be easily observed, comparing Northrop Grumman MQ-8 Fire Scout classical helicopter (only powered with $420hp$) to Bell Eagle Eye "tilt-rotor" which requires $641hp$ for an equivalent weight. A small rotor disk implies furthermore a high disk loading, which is particularly unsafe, especially during autorotation. The present concept proposes to couple the two systems of aircraft for the same reasons as exposed before (i.e. gain of both weight and drag): The rotor blades are stopped horizontally in flight in a manoeuvre called "transition" to then work as a fore wing. This latter is referred as "fore plane" in the rest of this thesis. Rotor diameter is thus no longer restrained, which hence solves the problem mentioned previously. The flight can be defined as:

- Helicopter mode: when the fore plane is turning like a helicopter rotor.
- Aeroplane mode: when the fore plane is locked parallel to the lateral axis of the aircraft, acting like an aeroplane wing.

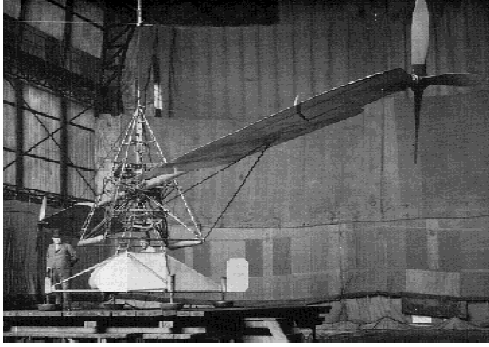
0.2.2 TANDEM WING CONFIGURATION

The rotor is now producing a significant part of the lift in aeroplane mode. However, because of the usually much higher blade loading of the helicopter blade compared to the aeroplane wing one, it is not likely to produce efficiently the lift required in both modes. For instance, Colombian MC100 aeroplane [?] and HELI-SPORT CH-7 KOMPRESS helicopter [?] are both ranging in the same mass category, but there is a ratio of 8.5 between the lifting surface area of the two. Therefore, an additional lifting surface is added to supplement the fore plane. In the rest of the study, this extra lifting surface is called "main wing". For mechanical reasons, the fore plane is placed at the very front of the aircraft. For stability reason, the main wing is positioned at its tail. The configuration obtained is called: "tandem wings". For the current design, this configuration has other significant benefits:

-
- According to Raymer ([?]; ch. 4.5), the greater the distance between two wings, the smaller the wing interaction, and therefore the drag. The present design ensures the most significant separation possible.
 - The fore plane can be designed to stall before the main wing to make the aircraft virtually “unstallable”.
 - This configuration opens the field of view for the sensor mounted under the fuselage. This is the reason of its adoption for the Scaled Composites Proteus, which is designed as a sensor lifter.

0.2.3 PROPELLER POWERED ROTOR

The idea of powering helicopter rotors by reaction has been highly investigated throughout aviation history. The main advantage is that the tail rotor is no longer useful since no more torque is applied to the rotor shaft. Moreover, there is no more need for a sophisticated transmission main gear box. In the present case, another advantage of using a propeller to drive the rotor consists in using the same propeller to propel the aircraft in aeroplane mode, saving thus both weight and drag. If the propulsion by compressed gas is well-known thanks to famous applications as Sud-Ouest S.O.1221 Djinn, Fairey Rotodyne or latest VTOL, Boeing X-50 Dragonfly, the propulsion by propellers mounted on a rotor is much more unusual. First attempts to implement such design happened nonetheless in the early years of helicopter history. Brennan prototypes and Curtiss-Bleeker SX-5-1, constructed respectively in 1924 and 1926, are among them (Figure 7).



(a) Brennan prototypes



(b) Curtiss-Bleeker SX-5-1

Figure 7: Brennan / Curtiss-Bleeker

Although several demonstrators have proved the value of such propulsion system, it did not win a foothold in the market due to its lower efficiency compared to classical mechanical drives. This difference is nonetheless very thin. Conventional helicopter configuration requires a tail rotor, which wastes at least 10% of total power. Moreover, a mechanical drive assembly suffers an efficiency not exceeding 95%. This gives a maximum rotor powering efficiency of 0.85% which is easily matched by modern propellers. The average efficiency of the propeller is however deteriorated by the airspeed variation depending on the azimuth of the angle of the blade on which it is mounted. Nevertheless, if the performances of this configuration are not as good as those of a conventional one, they are very respectable, as demonstrated by Nagler-Rolz NR 54 and 55 [8](#) . These latter were able to lift 140 kg at a speed of 80 km/h and an altitude of 457m with only two engines of 8hp each.

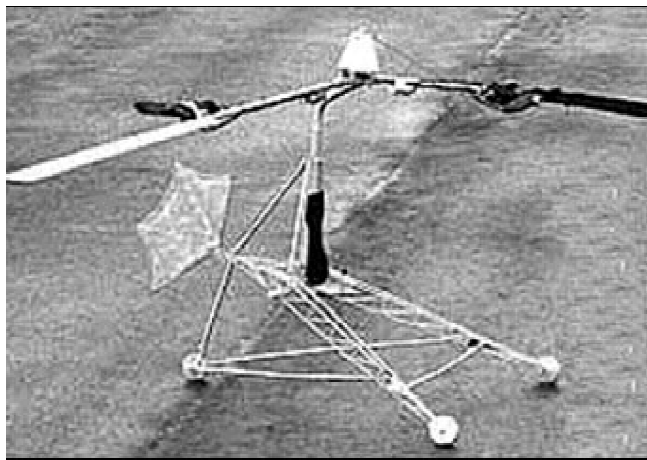


Figure 8: Nagler-Rolz NR 54

The overall efficiency of the lifting system should be significantly improved compared to hybrid rotors/propellers of conventional VTOLs. Another significant obstacle to using such propulsion system is power transmission. New improvements carried out for hybrid series powertrains have however made them suitable for substituting classical arrangements, as demonstrated by DA36 E-star 2 and Pipistrel Panthera. Electric transmission in rotor hub can be performed using a standard high-performance liquid slip ring.

0.2.4 LANDING CONFIGURATION

0.2.4.1 LANDING GEAR DESIGN BASIS

The design of the landing gear is particularly critical for such an unusual aircraft. This latter must respect the two following requirements:

- The aircraft used on boats are usually equipped with wheels landing gears that greatly facilitate operations. This is, for example, the purpose of the wheels which equipped Alouette II SE 313B [?].
- If the conversion of a tail-sitter configuration into an unmanned aircraft solves most of its drawbacks, its ability to land in wind conditions remains a concerning issue. As demonstrated by early tail-sitter configurations such as Convair XFY-1 Pogo and Lockheed XFO-1, shown in Figure 9, the wing offers maximum dragging area in the vertical configuration, which makes landing highly tricky in wind conditions. The design of the landing gear must, therefore, be carried out to compensate the wind disturbed attitude of the aircraft. In order to do so, a retractable landing gear is designed to keep the plan formed by the wheels horizontal, whatever the pitch of the aircraft is.



(a) Convair XFY-1 Pogo



(b) Lockheed XFO-1

Figure 9: blended landing gear / vertical tailplane (Courtesy of Lockheed Martin)

The first consequence of such design is to allow the aircraft to take off and land in aeroplane mode, which improves the redundancy of the system and enhances its flight endurance partially.

0.2.4.2 LANDING GEAR PRELIMINARY DESIGN

To gain both weight and drag, the main landing gear is merged with the vertical rudder which hence becomes a double vertical tail plane.

In flight, the visual field of the sensor turret should be as large as possible. This can be ensured by moving as many external systems to the backside of the aircraft. Applied to the landing gear, the aircraft is likely to take-off and land in aeroplane mode, upside down. This unusual configuration brings another useful advantage: the sensor turret ends up above the fuselage. This configuration enables it to avoid damages by FOD (Foreign Object Damage).

0.2.5 CONCEPT GENERAL OVERVIEW

Views of the resulting concept are shown in Figures 11 and 10. More information about the concept are presented in FR2993245B1 patent[?].

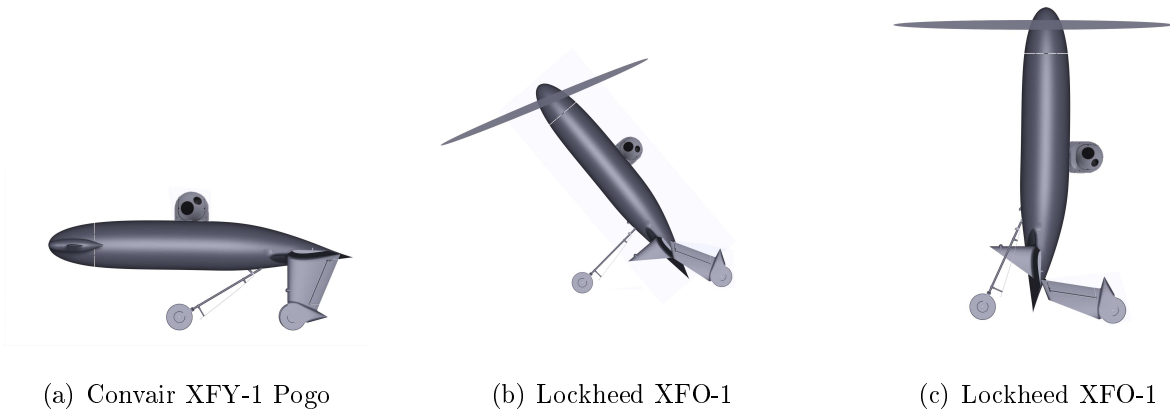


Figure 10: Landing configurations

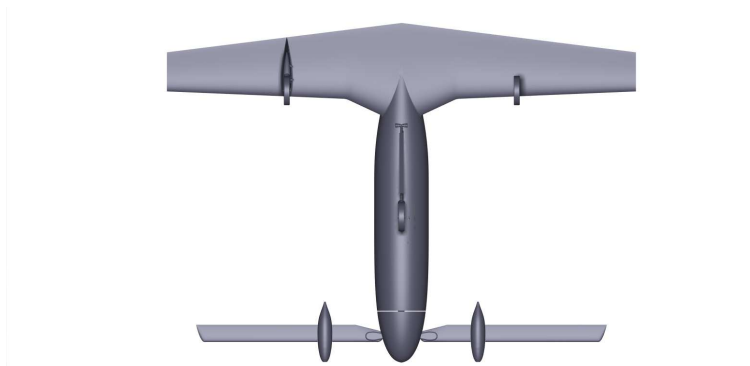


Figure 11: MALE ground equipment

0.3 STATE OF THE ART

Proposed aircraft is a brand new concept which does not have any anteriority in the literature. There are nonetheless few designs that look alike on particular points and which can, therefore, be taken as a starting point for the present study.

0.3.1 SIMILAR CONCEPT

The idea of stopping the lifting rotor of an aircraft in flight to reduce its drag is not new. The first concepts appeared in the 60's, and all existing designs can be classified into two categories:

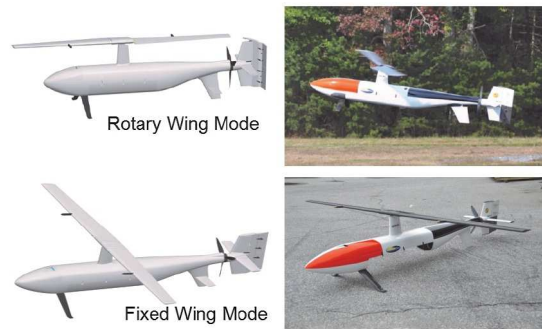
- Concepts with a rotor hub remaining vertical,
- Concepts with a rotor hub passing in flight from vertical to horizontal.

0.3.1.1 VERTICAL ROTOR HUB

The solution with a fix rotor hub is the most common. The idea was born in the sixties with Hughes Y-Wing “Hot Cycle” VTOL, followed by Sikorsky X-Wing in 1983. However, extensive tests only happened in the 20th century with Boeing X-50 Dragonfly. No transition was nevertheless performed due to inherent design flaws [?]. The retreating blade had indeed to generate lift with an inverted airflow. The operating principle of the concept is detailed in US patent 5454530 A [?]. A similar idea has been proposed recently [?] to solve the latter issue: the retreating blade is tilted by half a turn to be aligned with the airflow. The aircraft may, however, lose any lift from its blade during the transition, as suggested by US patent 8070090 B2 [?]. There is no result available regarding its flight test though. Both prototypes are presented in Figure 12.



(a) Boeing X-50 Dragonfly



(b) Stop-Rotor Rotary Wing Aircraft

Figure 12: Vertical rotor hub aircraft

Recently, a concept derived from the first one was proposed by StopRotor Technology

and flied successfully [?]. It consists more in unloading the rotor during the transition than making it generate lift in both modes since fixed wing are added in nose and tail to generate it in aeroplane mode (Figure 13). However, as for the previous concepts, it requires to perform

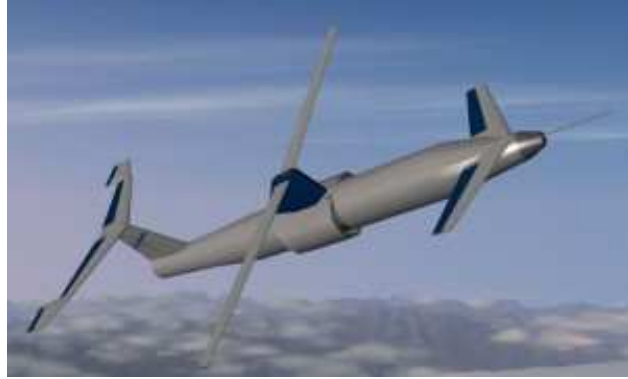


Figure 13: StopRotor Technology

a free fall manoeuvre to stop the rotor (See flight test video [?]).

0.3.1.2 TILTING ROTOR HUB

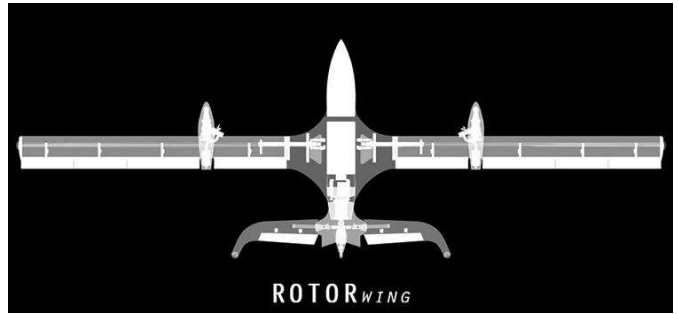
To overcome the main issue inherent to the Vertical rotor hub (i.e. the poor aerodynamic of the inverse flow retreating blade), other concepts have been proposed based on a tail sitter configuration. The main idea is the same as for the concept proposed in the present study: the blades work alternatively with a positive and a negative angle of attack. The first concept that enforced successfully this idea is Spinwing [?], shown in Figure 14. It was a counter-rotating rigid rotor stopped in flight and supplemented by a propeller which generates the thrust in aeroplane mode. Newer applications of this idea can be found in All-Composite ROTORwing [?] and Iridium Dynamics Halo aircraft [?]. These concepts use a propulsion system very similar to the one considered in present work. However, they do not have any additional fixed wing and their rotors do not present any flap degree of liberty. This can be seen in respectively the related patent [?] of the first concept and the presentation video of the second. Both aircraft are shown in Figure 15.



Figure 14: Spinwing



(a) Hola aircraft



(b) All-Composite ROTORwing

Figure 15: Tilting rotor hub aircraft

Main issues with those concepts are that they have to perform a free fall manoeuvre in order to transit from one mode to another. As for both concepts, the aircraft of present work needs, at first glance, untwisted blades fitted with symmetric aerofoil.

0.3.2 ROTOR AERODYNAMICS

0.3.2.1 HOVER

If rotor blades used symmetric aerofoil until very recently, they are unlikely to be untwisted [?]. The twist of the rotor blades is indeed a major parameter of rotor power consumption minimisation in hover. Design theory based on momentum theory and blade element theory

is still valid for the present concept.

There are other, more advanced, aerodynamics methods to assess the performances of the rotor, such as vortex theory or CFD (Computational Fluid Dynamics) studies, but the first method is sufficient enough for an initial design stage since it gives a relatively good assessment of the performances.

0.3.2.2 FORWARD FLIGHT

The power consumption of the rotor in lateral flight is likely to be much less important than in hover [?]. Therefore, there is no need, at this stage of the development, for meticulously assessing the aerodynamics of the rotor. It will be however the starting point of the dynamical model that will be used for the control study of the transition.

0.3.3 CONTROL ASPECT

0.3.3.1 helicopter

Helicopter control is based on the modification of its blades angle of attack by means of a swashplate.

The most usual way to design the control law is done through derivatives of the nonlinear behaviour equations[?]. These derivatives are computed for two flight conditions:

- Near hover, where the lateral airspeed effect on the airframe is neglected and the behaviour of the fixed airframe assessed with vertical airflow
- At relative high lateral speed, where the rotor downwash speed is assumed to be constant, and the fixed airframe works like the one of an aeroplane.

More derivatives can be computed and coupled with a gain scheduling strategy to get a more precise control [?] over the entire flight envelope. Other nonlinear control approaches have been proposed, but they are usually based on a reduced number of state variables, a restricted flight envelope [?] or consider simplified aerodynamics expressions [?].

0.3.3.2 PVTOL

Another way to control a VTOL aircraft is to fit lateral propellers. The simplest implementation of that is the twin motor PVTOL [?]. Axial force and torque are tweaked by controlling its two motors differentially. One of the main advantages of this solution is its high authority on both angle and axial controls. Control of such an assembly can capitalise on the great diversity of control laws initially developed for multi-rotors (i.e. advanced PVTOL) whether they follow linear or nonlinear theories [?] [?] [?] [?].

If this solution provides a precise trajectory tracking ability [?], it implies multiplying the number of thrusters which imposes smaller propellers diameter than a single rotor helicopter, which, unfortunately, tends to reduce the overall efficiency of the aircraft in addition to increasing its complexity.

0.3.3.3 PROPELLER POWERED TAIL SITTER

Historically, the first way to control a tail-sitter consisted in accommodating in the downwash of the propeller the aerodynamics control surfaces used in aeroplane mode. This solution was applied on the first piloted tail sitter aircraft and was reused on successful unmanned T-Wing[?], presented in Figure 16. This design can be greatly simplified by using a wing



Figure 16: T-wing

fitted with two tractor propellers on its leading edge and two flaperons on its trailing edge [?]. The dynamic model used as starting point for the design of the T-wing is based on a

set of various linear estimations of aircraft dynamics computed for the successive conditions encountered by the aircraft. It hence looks like a gain scheduling strategy [?]. The main issue of such control consists in generating sufficient airspeed to provide the flaperons with sufficient authority to control the aircraft. This implies to use small diameter propellers which are not efficient in hover. To overcome this difficulty, other control solutions have been proposed such as merging the tail sitter with a quadrotor, controlling, therefore, the device through the principle developed for PVTOL [?], [?]. However, this, in return, has drawbacks, which are detailed in section 0.3.3.2.

Another issue of this T-wing layout is the inability to dissociate the lift generated by propellers and main wing. They are indeed mechanically offset by a right angle. Thanks to an optimised trajectory [?], the T-wing can fly with a propulsion to weight ratio as low as 1.15. However, since the propeller is quite parallel to the airstream, it represents a huge amount of power. A solution consists in mounting both motors on a hinge [?] to perform the pitch and yaw controls by mean of vectoring the thrust. A hybrid solution entails leaving the low critical control (i.e. the pitch and the yaw) to the aerodynamics flaperons and performing the pitch control by mean of a vectored thrust [?], as shown in Figure 17. .

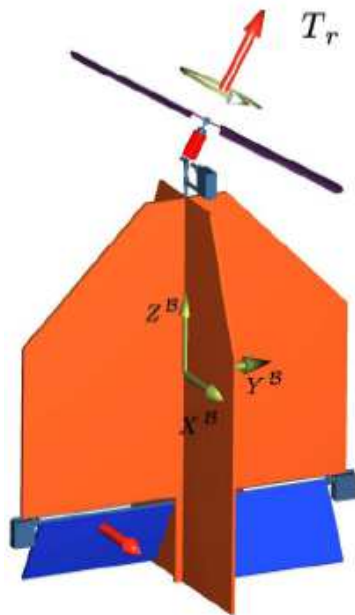


Figure 17: Tilting-rotor tail-sitter

From a control standpoint, this latter solution is the closest to proposed concept. The

propeller has the same role as the teetering rotor of present concept. Yaw and roll control can moreover be performed through aerodynamics control surfaces. However, the teetering rotor of present concept has, in addition, some authority on yaw control.

0.4 PH. D. OBJECTIVES

If it looks very promising and does not present major drawbacks, proposed concept is nonetheless highly challenging.

0.4.1 HOVER CHALLENGE

0.4.1.1 UNUSUAL ROTOR DESIGN

The design of its rotor is more restrictive than for classical helicopters. Its blade aerofoils have to generate lift both upward and downward to work well as a fore wing. They must, therefore, be symmetric. No static twist can, however, be applied to the blades to ensure the lift symmetry in aeroplane mode. Initial study, exposed in section 1.1, page 27, consists in designing a rotor complying with those requirements in order to assess its performances.

0.4.1.2 UNUSUAL GENERAL LAYOUT

If general layout only presents few uncertainties in aeroplane mode, it is quite different in helicopter mode. The several parts of the airframe interact with each other, and the downwash generated by the fore parts is likely to affect the aft ones greatly.

A set of theoretical studies, experimentations and CFD simulations are hence carried out in section 1.2, page 43 in order to assess those impacts.

0.4.2 TRANSITION CHALLENGE

The entire airframe evolves during the transition in a very unusual configuration (e.g. stalled main wing, highly tilted rotor). A dedicated modelling of the aircraft at this stage is therefore performed in section 2, page 53. The flight part between hover and transition is then studied in section 3, page 91.

0.4.3 CONCEPTUAL DESIGN

After having brushed aside main concerns regarding the unusual present concept feasibility, an assessment of its performances over a tactical mission is performed. For that purpose, a conceptual design study is carried out in section [4](#), page [105](#).

0.4.4 PERSPECTIVES

Present work opens up new perspectives which are exposed in section [5](#), page [135](#).

1

MODEL AND STUDY OF A PROPELLER POWERED ROTOR ABLE TO COMPLY WITH AEROPLANE MODE CONSTRAINTS.

The aim of this chapter is to investigate the ability of such a concept to fly in hover without inducing detrimental restrictions.

1.1 STUDY OF THE ROTOR PERFORMANCES.

Even if there have been few examples of propellers powered rotor in history (cf. section [0.2.3](#) page [13](#)), it remains a highly undocumented configuration. Moreover, the rotor is likely to work also as a wing in aeroplane mode, which implies that it must be statically untwisted and be composed of symmetric aerofoils. In the same way, the propulsion system of the rotor is intended to power the entire aircraft in aeroplane mode. In both modes, it should be as efficient as possible to reduce the necessary power in helicopter mode and the fuel consumption in aeroplane mode. Therefore a design of the overall rotor system is proposed, and its performances are estimated.

1.1.1 MODEL AND STUDY OF THE HOVERING ROTOR.

To have a good estimation of the power consumption of the drone in both hover and aeroplane modes, a model of the entire propulsion system is built including rotor, propellers and motors.

1.1.1.1 MODEL OF THE ROTOR.

The model of the rotor is based on the helicopter hover theory presented in section [A.5](#), page [159](#). The blade is sliced along the span in a set of blade elements. For each of them, the system composed of the aerodynamics behaviour of the aerofoil and the momentum theory equations is solved to compute the downwash airspeed. This latter is then used to assess the blade element lift, which is itself used to estimate the swirl in the wake. This latter eventually gives the drag. The resistive torque is thus obtained. The results obtained for each blade element are finally sum from root to tip for the resistive torque and from root to a reduced diameter for the lift (e.g. to take into account the tip vortex losses). The fore plane of the prototype is built by modifying existing helicopter rotor blades. A quick reverse engineering study tends to prove that the NACA0014 was used for the design. However, the finishing of the blade is somewhat sloppy, which may affect the experiments accuracy. The drag of the motor nacelle is added to the rotor drag. This latter is computed as exposed in section [D.3.3](#), page [223](#): it is considered as being a discreet force applied to the blade element positioned at the motor axis, and its intensity is computed for the homogeneous airspeed withstood by this axis.

1.1.1.2 MODEL OF THE PROPELLER.

Wind tunnel test results of plenty of propellers are available [?]. However, those data can't be used as is. The study starts with an estimation of the required propeller rotation speed, which is then used to estimate the required mechanical power. According to the literature, the power of a contra rotating propeller is double in comparison to single propeller layout, while efficiency remains nearly equal [?] [?], [?] and [?].

PROPELLER ROTATION SPEED Equations [\(A.5\)](#) and [\(A.3\)](#) give respectively the propulsion thrust T and the power given to the air P_{air} . The required mechanical power $P_{usefull}$

(in W) is:

$$P_{usefull} = \eta_{propeller} \cdot P_{air} \quad (1.1)$$

Where $\eta_{propeller}$ is the propeller efficiency. Therefore:

$$P_{usefull} = \eta_{propeller} \cdot 2 \cdot \rho \cdot A \cdot v \cdot (V + v)^2$$

Defining the advance ratio $J = \frac{V}{\omega \cdot D}$ and the propeller pitch p is defined as: $V + v = \omega \cdot p$. It leads to:

$$P_{usefull} = \eta_{propeller}(J) \cdot 2 \cdot \rho \cdot A \cdot (p - J \cdot D) \cdot p^2 \cdot \omega^3$$

That is of the form:

$$P_{usefull} = f(J) \cdot \omega^3$$

Making the power dimensionless as respect of the cube rotational speed work pretty well as it can be seen for the 8x7 sport of APC [?]. Propellers shown in Figure 1.1 :

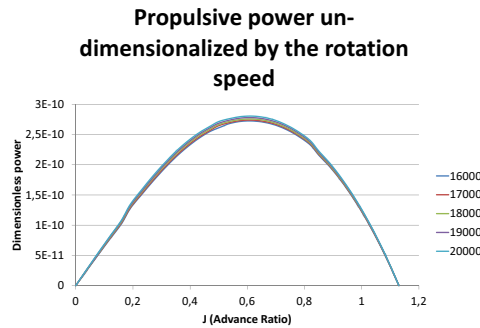


Figure 1.1: Un-dimensioned power

The curve is of the form:

$$f(J) = a \cdot J^2 + b \cdot J$$

It can be notice that the third term of the third degree polynomial is set to zero for $J = 0$. This is due to the zero efficiency at this point.

Then the mechanical required power can be derived from the obtained equation:

$$b \cdot \frac{V}{D} \cdot \omega^2 + a \cdot \left(\frac{V}{D}\right)^2 \cdot \omega - P_{usefull} = 0 \quad (1.2)$$

This rotation speed is then used to compute J , which is necessary for the propeller efficiency assessment.

EFFICIENCY ESTIMATION In order to compute the required mechanical power $P_{mechanical}$, which is equal to P_{air} of equation (1.1), the propeller efficiency $\eta_{propeller}$ remains to be estimated. The efficiency of a fixed pitch propeller is a function of the advance ratio J [?]:

$$\eta_{propeller} = f(J)$$

A test with the aero model propeller 8x7 sport of APC Propellers [?] seems to well confirm this trend as it can be seen in Figure 1.2 :

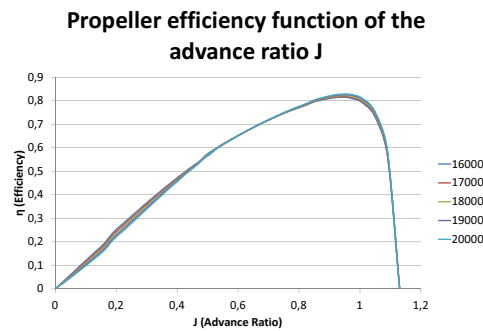


Figure 1.2: Propeller efficiency

It must be noted that the propeller is likely to work for J of the right half of the graph.

PROPELLER REQUIRED TORQUE From equation (1.1), the required torque is computed:

$$Torque = \frac{P_{usefull}}{\eta_{propeller}(J) \cdot \omega} \quad (1.3)$$

1.1.1.3 MODEL OF THE MOTOR.

A brushless engine can be modelled as shown in Figure 1.3 [?]

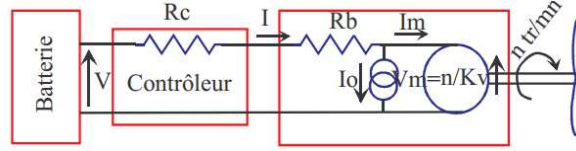


Figure 1.3: Diagram of a brushless motor

It is composed of an ideal perfect motor in parallel with a current generator. There are two main electromechanical motor constants:

$$\omega = Kv \cdot V_m \quad (1.4)$$

And:

$$Torque = Km \cdot I_m \quad (1.5)$$

Where $Kv = \frac{1}{Km}$. Knowing the required torque (1.3) and rotation speed (1.2) of the propeller, the required current and voltage of the motor are computed: Equation (1.5) leads to:

$$I = Torque \cdot Kv + Io \quad (1.6)$$

And equation (1.4) leads to:

$$V = \frac{\omega}{Kv} + (Rc + Rb) \cdot I \quad (1.7)$$

The power consumed by the motor is then simply:

$$P = V \cdot I$$

1.1.1.4 PROPULSION SYSTEM OPTIMISATION.

The propulsion system is optimised to figure out if a propeller, designed to power the aircraft in aeroplane mode, would be suitable to power the rotor in rotation. The optimisation principle is exposed in a conference article of REDUAS'13 [?]. Because of the limited choice of contra-rotating motors off the shelf, the CR28M is chosen. The entire set of APC contra rotating propeller whose wind tunnel test results are available [?], have been considered. The required power of the demonstrator is thus assessed. The result of the design gives a necessary

power of 177.864 W at a loiter speed of $19.896\text{ m}\cdot\text{s}^{-1}$. The motors and propellers are selected to decrease the required electrical power. The chosen propeller is the APC 10x8 sport, which corresponds to an electrical power of 317 W . The optimisation of the rotor rotation speed, blades pitch and propeller position is done to decrease the power consumption in hover (MTOW of 4 Kg) out of ground effect at sea level. The result of the optimisation gives an electric power of 717.826 W .

An estimation of the electrical power required by the propeller to generate the same thrust is performed, to figure out the benefit of such an assembly compared to a classical propeller lift tail sitter. The only method difference is that the static wind tunnel test results of the propeller are used here [?]. The propeller would in those conditions require a mechanical power of 1699 W , which corresponds to 3.457 W of electrical power. It is equivalent to five times the one of the present concept. This last result illustrates very well why the propellers of propeller powered VTOL are de-optimised (their diameter is hugely increased) to decrease a bit the engine size.

1.1.2 BENCH TEST OF THE DEMONSTRATOR ROTOR.

The test are performed on the demonstrator of the concept shown in Figure 1.4. The ro-



Figure 1.4: Demonstrator

tor characterisation tests are based on the variation of two controllable parameters: The speed of the propulsion propellers and the rotor blades pitch. The swashplate servomotors directly control the latter. PIDs implemented independently on each engine control the former. The optimum thrust (4kg : UAV MTOW) is expected for a propeller rotation speed of

812.6 rad.s^{-1} and a rotor blade pitch of 0.26 rad . In this configuration, the rotor is likely to rotate at a speed of 81.7 rad.s^{-1} , which corresponds to a relatively high amount of energy. The flight envelope is therefore only opened step by step.

The tests start with a low propeller rotation speed of 209 rad.s^{-1} . An increase of 52 rad.s^{-1} is added between tests groups. For each engine speed, the measurements are performed for several rotor blades pitch. For each test, the rotor rotation speed, the battery voltage, the consumed current and the generated propulsive force are measured. During the results analysis, the rotor rotation speed data are entered into the model, and the measured forces and torques are compared to the estimated ones.

1.1.2.1 TEST BED

The demonstrator is positioned horizontally, so that ground effect does not alter the air flow. Its landing gear relies on rails providing it full longitudinal liberty. It is held in position by a dynamometer which measures the entire rotor thrust. This latter is hooked at the tail of the aircraft. The batteries are kept on the ground for security reasons. The power goes through the coals of the central hub. Power consumption is measured upstream by means of a voltmeter and an ammeter. The test bed and its instrumentation are presented in Figure 1.5. It can be noticed that the nose landing gear has been modified as regards to Figure 1.4. This



Figure 1.5: Testbed

is due to the fact that it hasn't been possible to construct an affordable multi positioning landing gear.

1.1.2.2 TEST RESULTS

The various performed test, and the corresponding measurements are shown in Table 1.1. The tests were interrupted by the shortage of spare motors following the breakage of two of

test	$\omega_{@motor}$	θ_{blade}	ω_{rotor}	Voltage	Current	Force	Power	Observation
	$rad.s^{-1}$	rad	$rad.s^{-1}$	V	A	N	W	
1	209.43	1.05	6.70	12.8	3.15	1.502	40.32	
2	209.43	0.96	6.28	12.83	2.94	1.502	37.72	
3	209.44	0.78	12.46	12.8	4.16	1.502	53.248	
4	209.44	0.61	12.46	7.8	6.4	1.5	49.92	
5	209.44	0.43	14.66	12	14.42	1.57	173.04	
6	261.8	1.15	N/A	N/A	N/A	N/A	N/A	Alarming noise / motor failure
7	314.15	1.15	5.86	13.27	8.1	2.45	107.49	strong vibration
8	314.16	1.03	10.37	13.19	8.5	2.45	112.12	strong vibration
9	314.16	0.79	9.84	13.58	7.3	0.69	99.13	strong vibration / motor sputtering
10	314.16	0.57	10.687	13.62	8.2	2.94	111.68	strong vibration / motor sputtering
11	366.52	0.78	11.10	13	14.4	4.02	187.2	strong vibration / motor sputtering
12	366.52	1.09	8.37	12.73	12.6	5.98	160.4	strong vibration
13	366.52	0.47	N/A	N/A	N/A	N/A	N/A	strong vibration / motor failure

Table 1.1: Demonstrator test results

them.

1.1.2.3 MOTOR FAILURE

- First motor: The motor that broke first is presented in Figure 1.6 The rotor of the out runner motor broke in half, which spilt up the magnets and the bearings parts. The propeller remained attached to the motor magnet ring by means of its fixations screwed in the external thread. However, the entire block was not anymore connected to the motor shaft and got out of its housing. A growing deep sound preceded the rupture of the engine.
- Second motor: The second failing motor is shown in Figure 1.7 If the rotor was not



Figure 1.6: First motor



Figure 1.7: Second motor

pulled apart, significant cracking appears at the same level as for the first motor. The magnets part and thereby the propeller were only slightly maintained in bending.

- Motor observation: The failure took place in both cases on the weakest part of the rotor. According to its design, the rotating torque applies on the magnets, before spreading through the structure up to the propeller. On the other side, the part located between the bearings and the propeller fixation is likely to withstand the bending and the axial and lateral stresses as shown in Figure 1.8 Axial and lateral forces are quite unlikely the reason for the failure since when the motors broke apart, they were far from being working at their maximum design power. Therefore there is clear evidence that the bending applied by the propellers is responsible for the motors loss.

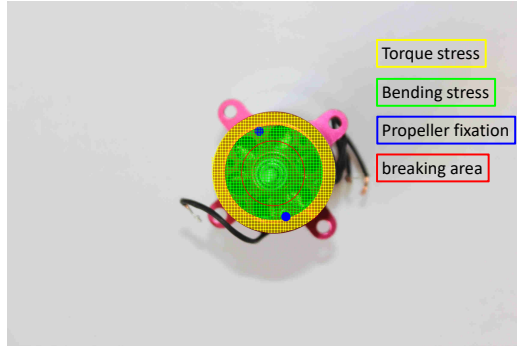
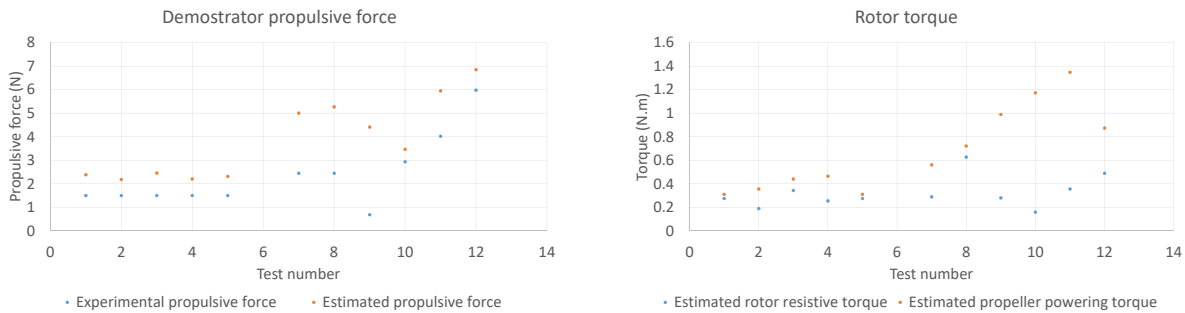


Figure 1.8: Motor observation

1.1.2.4 TEST ANALYSIS

In order to assess the behaviour of the rotor, the measured parameters have been entered in the simulator in order to estimate the longitudinal force generated by the rotor and the torque generated by the propellers to power it, presented in Figure 1.9.



(a) Force

(b) Torque

Figure 1.9: Test results

It can be seen that the experimental values are always lower than the estimated ones. If they are not so far from the first tests, the difference increases for the tests labelled between 7 and 11. The aerodynamics coefficient used in the model is unlikely responsible for such difference since the rotor blade was fully stalled all along the tests. According to Hoerner [?], at those Reynold, the aerodynamics coefficient is indeed almost equal to the one of a flat

plate in a fully detached airflow. On the torque point of view, the friction of the main shaft bearing and the slip ring electrical resistance may explain part of the difference. The high variation of the last tests is mainly due to the strong vibrations encountered, which seem to have resonated. An imperfect static balance may be blamed since the frequency of the vibrations matched the rotor one. It may be noticed that motors operation was not optimal. The noise they generated was not settled, making sometimes fear stall. There is no doubt that this was due to the erratic behaviour of the propellers, combined with the poor resilience of the off the shelves ECS used.

However, most of the difference can be assigned to the abnormal propellers behaviour, which also ended with the breakage of two motors.

Anyway, out of the vibration conditions, the experimental results seem to follow the behaviour predicted by the model. The principle of the propeller powered rotor is therefore not called into question to the extent that a solution is found to remove or at least actively alleviate the motor vibration issue.

1.1.2.5 MOTOR INVESTIGATION

The velocities withstood by the propeller blades depend on their azimuth.

VECTORED PROPELLER THEORY Since the propeller disk is not normal to the airflow, the forward flight theory, developed in chapter 2, is applied. The only distinctive feature is that the incident airspeed is no more constant as shown in Figure 1.10. This speed can be

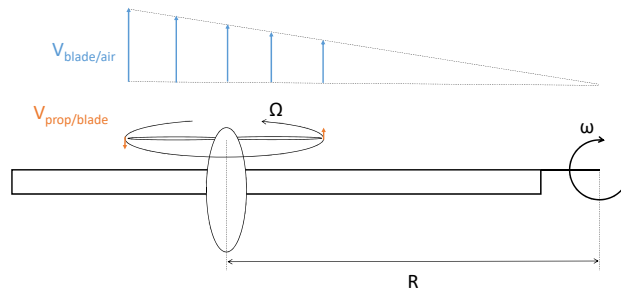


Figure 1.10: Top view

assessed as:

$$V_{blade/air} = \omega (R - r \cdot \cos(\psi))$$

Which, combined with equations (2.1), (2.2), (2.4),(2.5), (2.20) and (2.21), leads to:

$$V = \sqrt{((R - r \cos \psi) \omega \sin \alpha_1 + v)^2 + ((R - r \cos \psi) \sin \psi \omega \cos \alpha_1 + r\Omega)^2}$$

And:

$$\phi = \tan^{-1} \left(\frac{(R - r \cos \psi) \omega \sin \alpha_1 + v}{(R - r \cos \psi) \sin \psi \omega \cos \alpha_1 + r\Omega} \right)$$

Removing the second order speeds:

$$V = \sqrt{((R - r \cos \psi) \omega \sin \alpha_1)^2 + (R\omega \cos \alpha_1 \sin \psi + r\Omega)^2}$$

$$\phi = \tan^{-1} \left(\frac{(R - r \cos \psi) \omega \sin \alpha_1}{R\omega \cos \alpha_1 \sin \psi + r\Omega} \right)$$

And defining the advance ratio as $J = \frac{\omega R}{\Omega r}$, leads to:

$$V = \Omega r \sqrt{\left(\left(J - \frac{\varpi}{\Omega} \cos \psi \right) \sin \alpha_1 \right)^2 + (J \cos \alpha_1 \sin \psi + 1)^2} \quad (1.8)$$

$$\phi = \tan^{-1} \left(\frac{(J - \frac{\varpi}{\Omega} \cos \psi) \sin \alpha_1}{(J \cos \alpha_1 \sin \psi + 1)} \right) \quad (1.9)$$

BREAKAGE EXPLICATION According to equation (1.8) and (1.9), the propeller withstand an airspeed of variable intensity and variable slope angle. These variations directly affect the lift of the blades which is asymmetric between the advancing and the retreating blade. It causes a vibrating torque which the propeller rotation speed dictates frequency. It may correspond to the noise generated. It tends to confirm that the cause of the damage is due to the stresses applied to the rotor by the vibrations due to the non-homogenous axial airspeed withstood by the propeller.

VIBRATION SOLUTION Several solutions have been considered to solve this concept limitation:

- Motor stiffness: The first solution is to consolidate the motor front rotor. It presents indeed a useless weak point that could easily be removed. The rear engine, which is not affected by this fragility has shown no sign of breakage by the way.

- Multi blades: Some improvement can also be made on the propellers. In a two blades propeller case, the two blades being in phase opposition, the frequency doubles while the amplitude decreases by half of those of a single blade. Multiplying the number of blades on the propeller would not only allow a proportional reduction of the vibration amplitude but also would increase its frequency to bring it out of the resonance range. Moreover, an increase in the number of blades would reduce the propeller diameter and thus the lever arm of the lift along the propeller blade.
- Lower pitch propeller: the right-hand side of equation (1.8), which is also the bottom part of equation (1.9) exposes another solution. A decrease of J would lower the weight of the variable portion with respect to the constant one. The easiest way to do so without reducing the propeller efficiency is to lower the pitch of the propeller as it can be seen in Figure 1.10. According to the left-hand side of equation (1.8), which

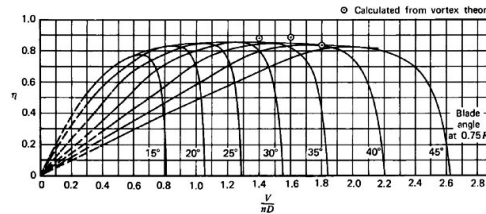


Figure 1.11: Propeller efficiency for various blade pitch

is also the top part of equation (1.9), another way to reduce the vibrations consists in decreasing the ratio $\frac{\omega}{\Omega}$. On the one hand, the former reduction of pitch implies an increase of Ω to produce the same impulse. On the other hand, a modification of the rotor blade geometry (i.e. augmentation of the chord) would lead to a decrease of ω . However, it would hence modify a bit the performances.

- scimitar propeller: In light aviation, a cheaper solution than the variable pitch propeller consists in using a fixed pitch scimitar propeller. This propeller allows an adaptation of the blades pitches depending on the airspeed which would, in the present case, alleviate the vibrations [?], [?]. In the worst case, articulated rotors, similar to those used for helicopter tail rotors could replace the propellers. Indeed, the helicopter tail rotors withstand similar flow, to a lesser extent (the rotating velocity of a chopper rotor

downwash is lower than the one of the blades) [?].

1.1.3 Complementary tests performed on dedicated bench.

Further tests are carried out to verify the previous analysis. The solutions selected for the test are:

- Stiffer motor.
- Reduced pitch propeller (i.e. APC propeller Sport 7X6) combined with motor kv augmentation.

The aim of these complementary tests is to figure out to what extent, the gyration of the propellers affects their efficiency. To this end, a broad range of advance ratio must be investigated since, for such propellers, the withstood Reynold number profoundly affects the performances. Therefore, several rotation speeds are tested. The tests must cover an extensive range of both airspeeds (i.e. bench rotation speed, and propeller rotation speed). One possible path may be to tweak the resistive torque. However, it looks quite difficult to achieve. Another solution consists in taking advantage of the acceleration phases. The propeller rotation speed is fixed by mean of a closed loop control on each motor.

1.1.3.1 Bench test characterisation.

Because there is no other contra rotating motor available of the shelf, a dedicated bench test is built as exposed in Figure 1.12.

The measures are performed by means of:

- An amperemeter and a voltmeter to measure the electrical power consumption.
- An IMU, embedded in the Arduino 101 to measure the rotational velocity and acceleration.
- A camera to film the vibration of one of the propulsion pod.

A more detailed presentation of the bench test is available in the following video: <https://www.youtube.com/watch?v=kONadIisSBI>



Figure 1.12: Propeller bench

In order to extract the propeller performances from the test results, a detailed characterization of the bench test is carried out. The rotational inertia of the moving part is performed following the principle of the rotating pendulum as shown in Figure 1.13.



Figure 1.13: bench test rotational inertia measure

The resistive forces (i.e. aerodynamics and dry frictions) coefficients are estimated measuring the deceleration of the rotating part after turning the motors off. To remove the propeller drag from the result, the analysis has been performed first with all the propellers and then with only half of them. The difference of the results is subtracted to the second one to obtain the resistive force coefficients without propellers.

1.1.3.2 Results.

The test has been carried out for 6000 RPM, 8000 RPM and 10000 RPM. For each rotation speed, the motor slope has been fixed successively to $0 \cdot deg$ (i.e. “no angle”), $2.441 \cdot deg$ (i.e. “2 rings”) $4.884 \cdot deg$ (i.e. “4 rings”) and $7.323 \cdot deg$ (i.e. “6 rings”).

The information received by the IMU is shown in Figure 1.14. One can notice that the

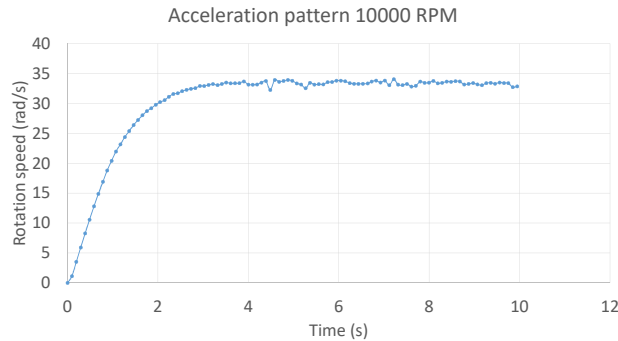
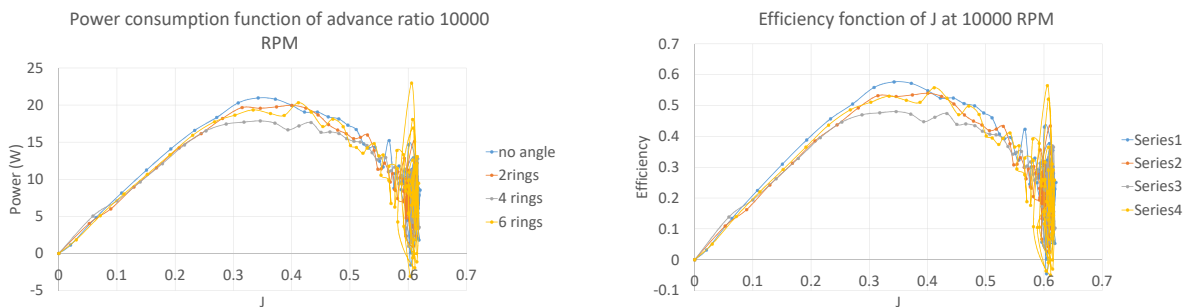


Figure 1.14: Acceleration pattern of the bench test for propeller rotation speed of 10000RPM

signal is a bit noisy though, it is precise enough to do the analysis. The power generated by the propellers is first extracted. The efficiency of the propeller is then estimated with the electrical power consumption and the motor characteristics. The resulting propeller performances at $10000 \cdot RPM$ are exposed in Figure 1.15.



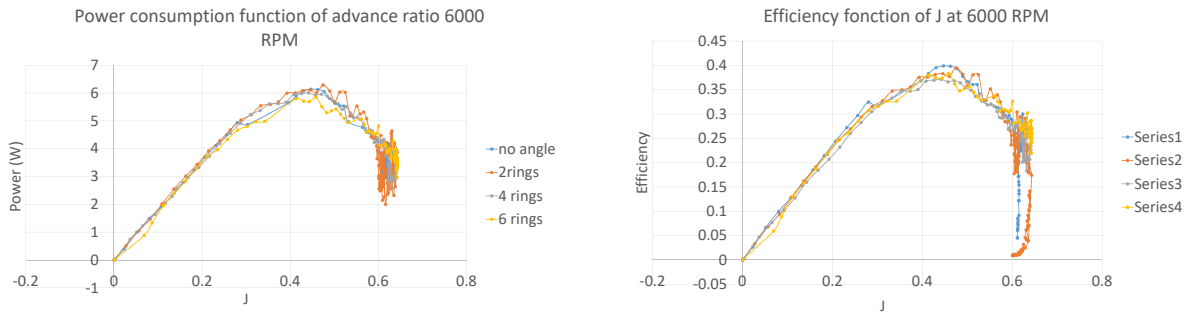
(a) Power

(b) Efficiency

Figure 1.15: Power and efficiency at 10000RPM

The very right of the curve is irrelevant since it is very noisy. It corresponds indeed to the stabilised part of Figure 1.14. It can be seen that the maximum efficiency reach 60%, which corresponds quite well to the one encountered in axial flow wind tunnel tests [?]. A video of the propellers pods can be seen https://www.youtube.com/watch?v=gah4RafPMjE&list=UUPD3gmlC1Hc9B09j-X_4kUQ&index=4. There is no perceptible vibratory phenomenon.

Equivalent experiments performed at propeller rotation speed of 6000 *RPM* are performed to visualize the difference



(a) Power

(b) Efficiency

Figure 1.16: Power and efficiency at 6000RPM

The efficiency is there reduced by 25%. In addition the video of the propeller pod show more severe vibrations.

The modification of the propulsion system to increase its rotation speed seems to be an effective solution to solve the vibration issue.

1.2 Study of the interactions between the aerodynamic entities.

It has been seen that the concept of propellers driven rotor leads to substantial power economy. And the propellers can work correctly as far as their rotation speed is high enough. However, the influence of such assembly on the fixed part of the airframe remains to be evaluated.

The aerodynamic behaviour of the airframe is quite complicated since the arrangement is very unusual. Indeed, the main wing is almost entirely blown by the rotor and the propellers downwashes. This effect is particularly relevant in static flight where the general airflow does not attenuate the local flow. To assess the effect of the interactions, a CFD model is simulated with the software Star-CCM+.

The aim of this simulation is only to visualise the flow behaviour. There is no need for estimating the aerodynamics drag. Therefore a relatively low-resolution meshing is chosen with a number of points ranging between 2 and 3 million.

The simulation is based on a hybrid mesh allowing the rotor motion simulation, which is composed of three main parts:

- The Background mesh which is contained in a 40 meters diameter sphere and includes all the static parts (the fuselage and the main aircraft wing).
- The overset mesh which is constructed from a cylinder of same diameter as the rotor and which includes all the mobile parts (the rotor and the propellers)
- The overlap mesh which manages the interphase between the two latter.

The 3D model of the airframe is exported from the CAD design of the demonstrator, which is simplified a bit to alleviate the calculations:

- The root of the blade, which corresponds to the rotor head fixing mechanism is cut out, and the rotor head is deleted. This modification simplifies a lot the geometry and therefore the calculations. However, it is assumed to have only minimal effect on the results since the blade holders only generate drag and no lift.
- The two contra-rotating propellers doublets are modelled with cylinders whose bases correspond to the rotor disk areas. This simplification not merely alleviates the calculations but also overcomes the doubt about the propellers shape.
- The fins are not modelled since they are mounted tangentially with respect to the stream tube. The interaction may then have only little effect on the behaviour.

-
- The landing gear is not modelled since it is much less bulky than the other components. Therefore, its impact on the global behaviour does not justify the substantial increase in complexity it would bring to the calculation.

The final surface meshing of the airframe used for the calculation is shown in Figure 1.17. The boundary layer is not well detailed since it will have only little effects on the overall

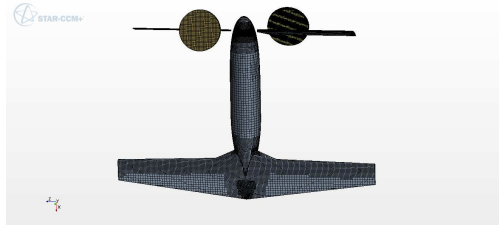


Figure 1.17: Aircraft meshing

airflow. Nonetheless, the air is modelled as viscous to assess the flow mixing closely. The simulation is carried out in standard atmosphere at sea level out of ground effect.

1.2.1 ROTATING PARTS AND WING INTERACTION

If there is little doubt about the feasibility of a rotor powered by propellers mounted on its blade, since working prototypes have already demonstrated it, there are much more uncertainties about the behaviour of a wing placed in the wake of such an arrangement.

1.2.1.1 ROTOR AND WING INTERACTION

The parameter Q is shown in Figure 1.18 in order to visualize the impact of the rotor wake. One can notice that the rotor downwash blows almost the entire wing. The drag of the

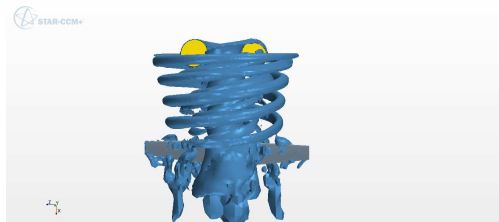


Figure 1.18: Parameter Q showing the rotor wake blowing the wing

rotor blades generates a rotary motion to the wake, which impacts the main wing creating an anticlockwise moment about the X axis.

1.2.1.2 PROPELLER AND WING INTERACTION

The streamlines passing through the propellers are shown in Figure 1.19, with their respective velocity in order to assess the impact of the propellers on the wing. It can be seen that

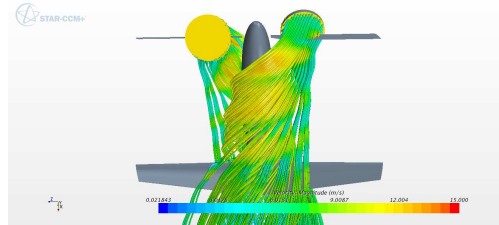


Figure 1.19: Air velocity showing the propeller wake blowing the wing

contrary to the rotor blades, the rotary motion generated by the propellers creates a clockwise moment about the X axis when it impacts the main wing.

1.2.1.3 WING REACTION

The axial torque generated by the rotating airflow around the wing is shown in Figure 1.20. The torque is roughly periodic, with a frequency around $26s^{-1}$. IT corresponds to twice the

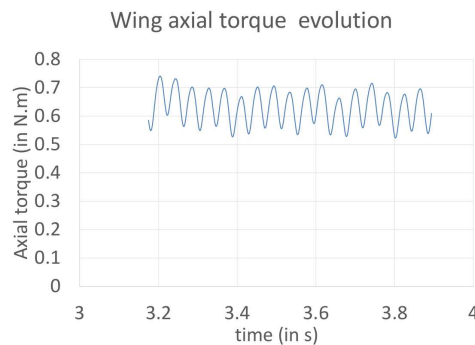


Figure 1.20: Wing axial torque

frequency of rotation of the rotor, which was simulated at $74rad.s^{-1}$. The periodic behaviour is due to the turbulent flow generated by the rotor and in particular the blades tips vortexes

which impact the wings twice a gyration. These variations are far too fast to affect the control, and the structural flexibility may mostly absorb them. Therefore, only the average torque, which is of $0.630N.m$, is considered. One can notice that the torque is positive. It involves that the torque generated by the propellers wakes is higher than the one of the rotor blades, despite the fact that the action of the rotor blades on the wing has a longer lever arm. This can be explained analysing two cross-sections of the wing at $0.2m$ and $0.4m$ from the symmetric plane of the aircraft as presented respectively in Figure 1.21.

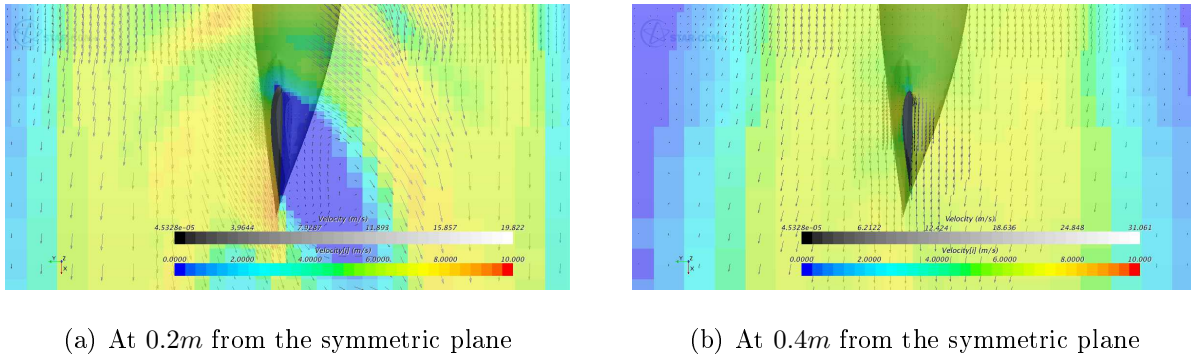


Figure 1.21: Wing cross section

It can be noticed that in the wake of the propeller, at $0.2m$ from the symmetric plane, the aerofoil angle of attack is around 45° , which greatly exceeds the stalling conditions and, according to Hoerner [?], corresponds to almost its maximum lift ($c_l = 1.4$). In addition, the relative wind is relatively fast with an average of $9m.s^{-1}$.

Contrariwise, in the wake of the propeller, at $0.4m$, the aerofoil angle of attack is minimal as well as the relative wind with an average of $6m.s^{-1}$.

It is necessary to check if the ailerons are sufficient enough to balance this torque. The following of the study is done assuming the same deflexion for each aileron. With this in mind, an analysis is done with Xfoil to assess the effectiveness of the ailerons covering 25% of the chord of the TL54 aerofoil. The analysis is done at a Reynold of $65 \cdot 10^3$. The lift coefficient variation with the angle of attack and the aileron deflection is shown in Figure 1.22. The effect of the ailerons deflection is approximated linearly as shown in Figure 1.23. Finally the following calculation is carried out:

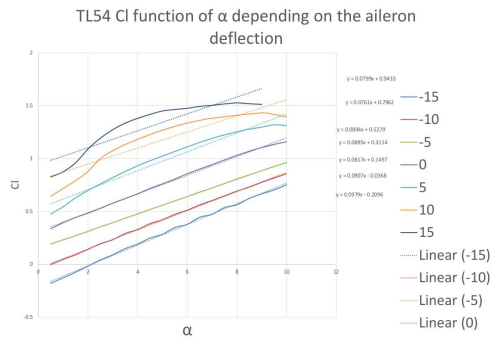


Figure 1.22: TL54 lift coefficient function of the angle of attack and the deflection

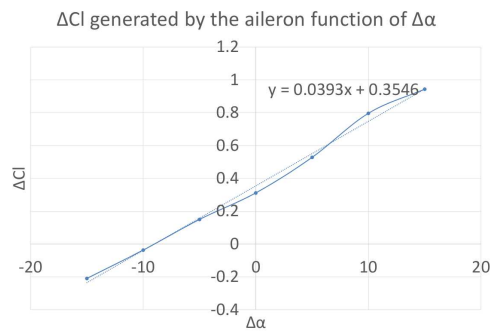


Figure 1.23: TL54 lift coefficient variation function of the deflection

$$\Delta C_l = \frac{Torque}{\frac{1}{2}\rho \int_{tip}^{tip} x \cdot c \cdot V^2 dx}$$

Where *Torque* is the torque that must be balanced, ρ is the air density, x is the distance between the aerofoil and the symmetric plan, c is the chord of the aerofoil and V is its relative velocity which is extracted from Figure 1.24 (in order to be conservative, when the aerofoil is stalled, the velocity V is set to zero) Applying the inverse function defined in Figure 1.23

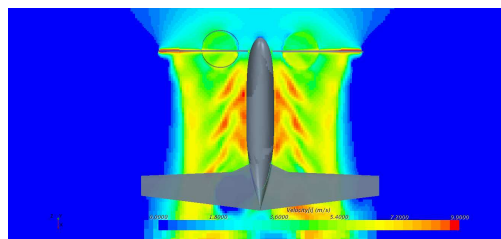


Figure 1.24: relative wind impacting the main wing

to ΔC_l , it gives the required aileron deflection $\Delta e = 10.083^\circ$, which is quite small compared to the maximum deflection of 45° . That is to say only a fourth of the aileron authority is required to counteract the torque generated by the downwashes.

Moreover, according to Hoerner [?], the stalled aerofoil perpendicular force can be assessed as:

$$cn = 2 \cdot \sin \alpha$$

While for the flow-attached aerofoil, it is:

$$cn \approx cl = 2 \cdot \pi \cdot \sin \alpha$$

That is to say, when the aircraft accelerates, a horizontal airspeed is likely to increase the wing angle of attack, which increases the flow-attached aerofoil lift much faster than the stalled wing one. Therefore the ailerons authority increases with horizontal speed and the required deflection decreases.

1.2.1.4 BENCH TEST VISUALISATION

In order to ensure the results given by the CFD analysis, a visualisation of the turbulent flow is carried out thanks to tufts fixed on the stalling part of the wing as shown in figure 1.25. The dynamics behaviour can be seen on the online video: <https://www.youtube.com/watch?v=nriwmH2o7pg>

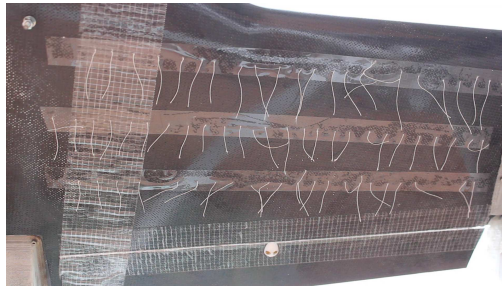


Figure 1.25: Tufts fixed on the wing

[watch?v=nriwmH2o7pg](https://www.youtube.com/watch?v=nriwmH2o7pg). One can notice that the bench test gives quite the same results as the CFD analysis since the propellers downwash stalls the wing each time it pass in front of it.

1.2.2 PROPELLER AND ROTOR INTERACTION

The last interaction that must be investigated is the one between the propellers doublets and the rotor blades. The main uncertainty about this interaction is the airflow withstood by the propellers when the rotor is turning. Indeed, the efficiency of the propellers is very sensitive to the relative wind and, until now, the propeller velocity has been assumed to be equal to the rotation speed of the rotor at their location. But a variation can be expected because of the rotor blades drag. To assess the velocity withstood by the propellers, the cross section of the propeller cylinder is shown in Figure 1.26 (the view is, therefore, rotating with the rotor) It can be seen that contrary to expectations, the airflow is not positive on one blade

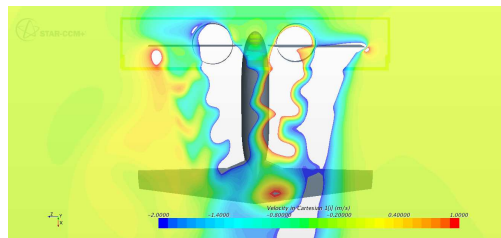


Figure 1.26: Propeller axial velocity

and negative on the other, which would have been consistent with a vortex flow, although it looks more or less symmetric around the central plan with an intensity which increases from the root to the tip. It reminds a bit the downwash velocity pattern. Considering the blade slope of $0.228rad$ and an estimated downwash velocity of $2.166m.s^{-1}$ at the propeller location ($0.267m$ from the symmetric plan) the component of the downwash velocity axial to the propeller cylinder is of $0.49m.s^{-1}$. This latter speed corresponds pretty well to the tendency exposed in Figure 1.26. Therefore, the rotor model exposed in section 1.1.1n page 28, is modified to take this difference into account. It was until now based on the assumption that the propeller velocity is equal to its rotation speed at its location. This approximation is widely used in the rotor theory and begins to show its limits.

1.3 Partial conclusion

In this chapter, the rotor performances are first assessed in section 1.1 page 27. It is found that such a propulsion assembly would lead to tremendous power saves compared to a traditional propeller generating the lift in helicopter mode. However, the tests of the prototype rotor realised on bench reveal a design limitation of the propellers used in a rotating airspeed. Further investigation and additional tests realised on a specific bench show that design constraint on the propeller pitch can remove this limitation with minimal performance penalties.

In order to complete the study of the rotor taken separately, an overall aircraft dynamic CFD study is carried out in section 1.2 page 43. It shows that the downwash of the rotor assembly generates a torque when it impacts the main wing. A study on the flaperons authority reveals that they manage to balance this torque to keep the aircraft controllable in roll.

Therefore the concept seems to be practical in hover and to provide benefits compared to the competing ideas. However, the aim of this unusual layout is to transform in flight into a pure aeroplane, which implies a transition where the rotor stops. This transition is far from being straight forward. It is thus the aim of next chapter.

2

MODEL OF THE TRANSITION BETWEEN HELICOPTER AND AEROPLANE MODES

Uncertainties about the ability of the present concept to hover have been removed in chapter 1, 27. Its flight quality in aeroplane mode is moreover ensured by the design methodology exposed in chapter 4, page 105. However, the transition between both modes remains highly unpredictable at this stage of the study. In other words, is the present concept able to fly in helicopter mode at a sufficient airspeed not to stall while stopping its rotor to turn to aeroplane mode? The answer to this question is made by simulating the aircraft during this phase of the flight. The simulation is based on an accurate flight dynamics model of the aircraft whose construction is detailed in this chapter.

The behaviour of the rotor in translation is analysed in section 2.1. The complete dynamics model is then constructed accordingly in section 2.2 page 64.

2.1 THEORY OF THE ROTOR IN TRANSITION

The rotor model construction starts with the theory proposed by Johnson [?].

2.1.1 ROTOR FORWARD FLIGHT THEORY

2.1.1.1 THEORY BASIS

The incident airspeed can be decomposed into axial V_λ and radial V_μ components as shown in Figure 2.1. Therefore, the components become:

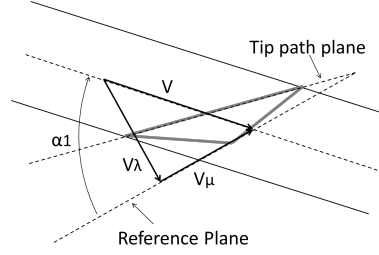


Figure 2.1: Horizontal flight incidence air flow

$$V_\lambda = V \sin \alpha_1 + v \quad (2.1)$$

$$V_\mu = V \cos \alpha_1 \quad (2.2)$$

Obtained airspeeds can be decomposed further into circumferential U_T and radial U_r components over the whole rotor disk, as shown in Figure 2.2.

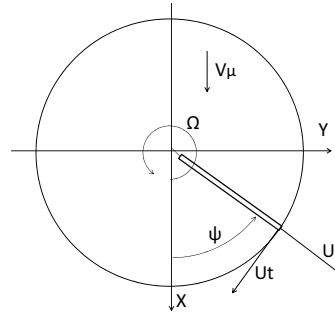


Figure 2.2: Horizontal flight rotor disk

$$U_r = V_\mu \cos \psi \quad (2.3)$$

$$U_T = V_\mu \sin \psi + r\Omega \quad (2.4)$$

Airspeed component U_P , presented in Figure 2.3, can now be computed, as follows:

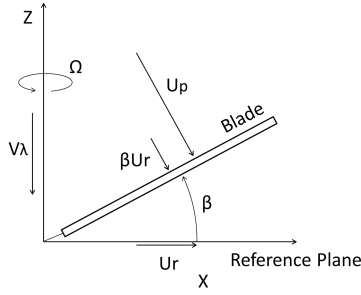


Figure 2.3: Horizontal flight blade air flow

$$U_P = \cos \beta V_\lambda + \sin \beta U_r + r\dot{\beta} = \cos \beta V_\lambda + \sin \beta V_\mu \cos \psi + r\dot{\beta} \quad (2.5)$$

For better understanding, airspeed components U_P and U_T are presented in aerofoil plan (Figure 2.4). Aerodynamics calculation can thus be performed:

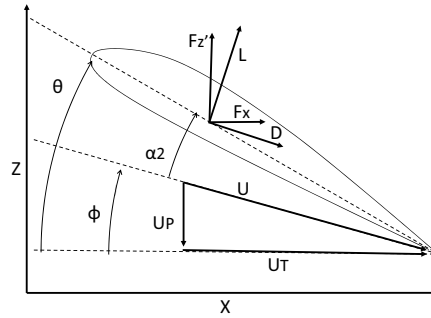


Figure 2.4: Horizontal flight airfoil

$$U = \sqrt{U_T^2 + U_P^2} \quad (2.6)$$

$$\phi = \tan^{-1} \left(\frac{U_P}{U_T} \right) \quad (2.7)$$

$$L = \frac{1}{2} \rho U^2 c c_l \quad (2.8)$$

where: $a(\theta - \phi - \alpha_0)$

$$D = \frac{1}{2} \rho U^2 c c_d \quad (2.9)$$

$$F_x = L \sin \phi + D \cos \phi \quad (2.10)$$

$$F_{z'} = L \cos \phi - D \sin \phi \quad (2.11)$$

Equations (2.8), (2.9) and (2.10) can be combined with following trigonometric properties:

$$\sin \phi = \sin \left(\tan^{-1} \left(\frac{U_P}{U_T} \right) \right) = \frac{U_P}{U}$$

$$\cos \phi = \cos \left(\tan^{-1} \left(\frac{U_P}{U_T} \right) \right) = \frac{U_T}{U}$$

$$F_x = \frac{1}{2} \rho c U (U_P a (\theta - \phi - \alpha_0) + c_d U_T) \quad (2.12)$$

In the same way, equations (2.8), (2.9) and (2.11) become when combined:

$$F_{z'} = \frac{1}{2} \rho c U (U_T a (\theta - \phi - \alpha_0) - c_d U_P) \quad (2.13)$$

Lifting force is then projected into axial and radial axes (respectively F_z and F_r)

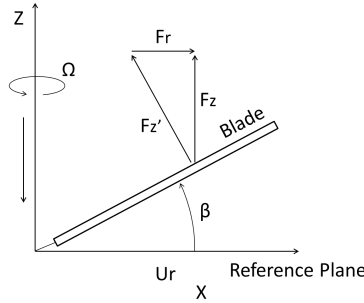


Figure 2.5: Horizontal flight blade forces

$$F_z = F_{z'} \cos \beta \quad (2.14)$$

$$F_r = -\sin \beta F_{z'} \quad (2.15)$$

Average forces over a turn are then computed:

$$t = \frac{1}{2\pi} \int_0^{2\pi} F_z d\psi \quad (2.16)$$

$$h = \frac{1}{2\pi} \int_0^{2\pi} (F_x \sin \psi + F_r \cos \psi) d\psi \quad (2.17)$$

$$y = \frac{1}{2\pi} \int_0^{2\pi} (-F_x \cos \psi + F_r \sin \psi) d\psi \quad (2.18)$$

$$Q = \frac{1}{2\pi} \int_0^{2\pi} r F_x d\psi \quad (2.19)$$

These expressions cannot be analytically resolved because of the non-linearity of both U and ψ . The rotor forward flight theory method to solve this problem consists in making the assumption that $U_T \gg U_P$, which makes possible the linearisation of U and ϕ . This then enables the calculations of t , h , y and Q .

2.1.1.2 ROTOR FORWARD FLIGHT THEORY LIMITATION

A specificity of the concept presented in section 0.2 page 11, is that $U_T \gg U_P$ does not apply since the rotor ends the transition fully stopped. A new extended theory must then be developed. The idea consists in finding new linear approximations of U and ϕ so that following properties are verified:

- When $U_T \gg U_P$:

$$U = \sqrt{U_P^2 + U_T^2} \approx U_T$$

$$\phi = \tan^{-1} \left(\frac{U_P}{U_T} \right) \approx \frac{U_P}{U_T}$$

- When $U_T \ll U_P$:

$$U = \sqrt{U_P^2 + U_T^2} \approx U_P$$

$$\phi = \cot^{-1} \left(\frac{U_T}{U_P} \right) \approx \frac{\pi}{2} - \frac{U_T}{U_P}$$

Another requirement for these approximations would be low calculation complexity of equations (2.16), (D.4.1), (2.18) and (2.19).

2.1.2 EXTENDED THEORY

2.1.2.1 U APPROXIMATION

U can quite naturally be estimated as:

$$U = k_1 U_P + k_2 U_T \quad (2.20)$$

where k_1 and k_2 are two adjusting parameters that depends on the flight phase. It can be seen that, setting $k_1 = \left(1 - \frac{\sqrt{2}}{2}\right) \frac{U_T - U_P}{U_T + U_P} + \frac{\sqrt{2}}{2}$ and $k_2 = \left(1 - \frac{\sqrt{2}}{2}\right) \frac{U_P - U_T}{U_T + U_P} + \frac{\sqrt{2}}{2}$, the approximation meets expectations, as shown in Figure 2.6. However, U_T and U_P are not constant throughout

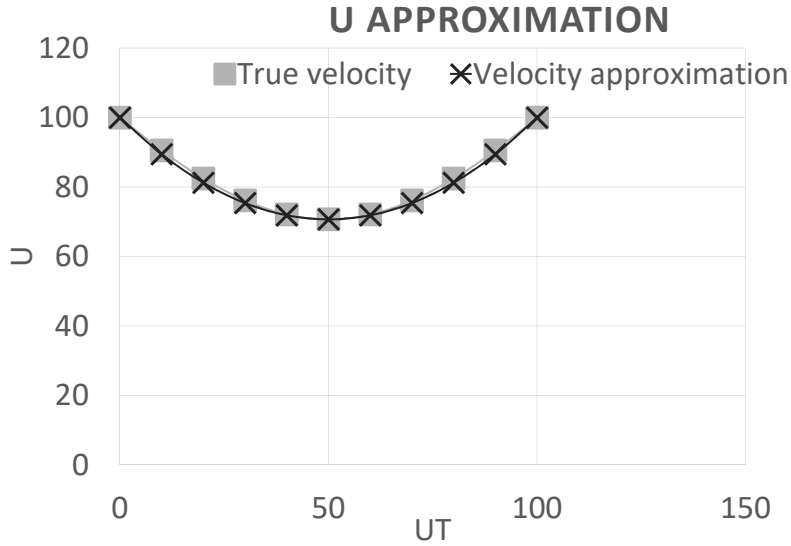


Figure 2.6: U approximation with U_P and U_T varying linearly respectively from 0 to 100 and from 100 to 0

the whole rotor disk. k_1 and k_2 must therefore be independent from blade position, in order to enable the integration computation. They can nevertheless depend on the flight conditions of the overall rotor, which are constant. It has been decided to make k_1 and k_2 dependent on V_λ and $r_{ref} \cdot \Omega$ which give an indication on the respective weights of U_P and U_T . Parameter $x_{ref} = \frac{\Omega r_{ref} - V_\lambda}{\Omega r_{ref} + V_\lambda}$ is then defined, where r_{ref} is a reference radius parameter that will be optimised in section 2.1.2.3. At first sight, k_1 and k_2 verify the following properties:

- When $\Omega r_{ref} \gg V_\lambda$: $k_1 \approx 0$, $k_2 \approx 1$

-
- When $\Omega r_{ref} \approx V_\lambda$: In this situation, we have: $U \approx \sqrt{U_P^2 + U_T^2} \approx \sqrt{2U_T^2} \approx \sqrt{2}U_T \approx \sqrt{2}U_P \approx \frac{\sqrt{2}}{2}(U_P + U_T)$. Therefore: $k_1 \approx k_2 \approx \frac{\sqrt{2}}{2}$
 - When $U_T \ll U_P$: $k_1 \approx 1$ and $k_2 \approx 0$

Since three conditions must be verified, a quadratic expression can be used to define k_i ($i = \{1, 2\}$):

$$k_i = \alpha_i x_{ref}^2 + \beta_i x_{ref} + \gamma_i$$

where α_i , β_i and γ_i are constant parameters that will be optimised to reduce as much as possible the U approximation error, as presented in section 2.1.2.3.

2.1.2.2 ϕ APPROXIMATION

Following the same approach as in section 2.1.2.1, ϕ is approximated using the following expression:

$$\phi = \frac{k_3 U_P - k_5 U_T}{U} + k_5 \quad (2.21)$$

where k_3 , k_4 and k_5 are three adjusting parameters. Setting $k_3 = k_4 = k_5 = \frac{\pi}{2}$, the approximation works pretty well, as shown in Figure 2.7.

As for U approximation, parameters k_3 , k_4 and k_5 are set as functions of the flight conditions parameters defined as: $x'_{ref} = \frac{\Omega r'_{ref} - V_\lambda}{\Omega r'_{ref} + V_\lambda}$ where r'_{ref} is the reference radius for the ϕ approximation. k_i ($i = \{3, 4, 5\}$) is defined as:

$$k_i = \alpha_i x_{ref}'^2 + \beta_i x_{ref}' + \gamma_i$$

where α_i , β_i and γ_i are constant parameters that will be optimised to reduce as much as possible the ψ approximation error, as presented in section 2.1.2.3.

2.1.2.3 APPROXIMATION METHODOLOGY

The aim of the approximation is to simplify the equations to enable their integration. Its results must though remain acceptable whatever the flight conditions of the rotor. In other words, for every possible combination of Ω , V_λ and V_μ , obtained t , h , y and Q must be close enough to real life behaviour. For present aircraft:

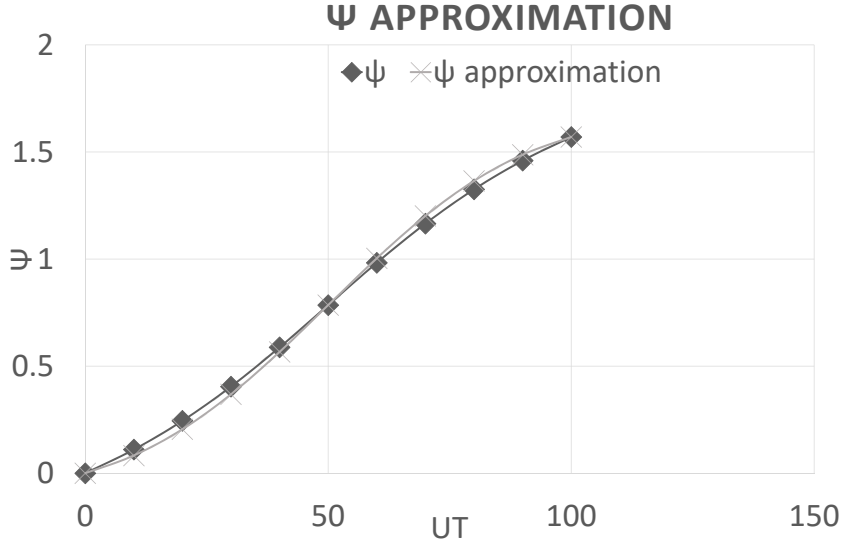


Figure 2.7: ϕ approximation with U_p and U_T varying linearly respectively from 0 to 100 and from 100 to 0

- $0 \text{ rad} \cdot \text{s}^{-1} \leq \Omega \leq 74 \text{ rad} \cdot \text{s}^{-1}$ where $74 \text{ rad} \cdot \text{s}^{-1}$ is the optimal rotation speed in hover and $0 \text{ rad} \cdot \text{s}^{-1}$ corresponds to the stopped rotor.
- $0 \text{ m} \cdot \text{s}^{-1} \leq V_\mu \leq 17 \text{ m} \cdot \text{s}^{-1}$ where $0 \text{ m} \cdot \text{s}^{-1}$ corresponds to the flight in hover and $17 \text{ m} \cdot \text{s}^{-1}$ to the maximum speed in helicopter mode.
- $1 \text{ m} \cdot \text{s}^{-1} \leq V_\lambda \leq 17 \text{ m} \cdot \text{s}^{-1}$ where $1 \text{ m} \cdot \text{s}^{-1}$ corresponds to the minimum rotor downwash in hover and $17 \text{ m} \cdot \text{s}^{-1}$ to the maximum speed in helicopter mode.

It can be noticed that the flight envelope is quite large and covers some cases that are unlikely to happen. It may be possible to reduce it in a second phase, when the flight path of the aircraft will be better known. Optimal parameters search was carried out using a hybrid optimisation tool (Gencab by CAB INNOVATION [?]) based on Genetic Algorithms and nonlinear Simplex (Nelder Mead algorithm). Hybridisation of both global and local approaches makes the search of global optima much more efficient. Potential solution evaluation throughout the flight envelope was performed by Monte Carlo simulation (Simcab by CAB INNOVATION) using an original coupling technique [?] [?] which enables the overall

processing time to be divided by 30 approximately. The principle of this coupling consists of performing a rough estimation of each solution (from 50 simulations for example) before estimating them again with a higher precision depending on initial results (between 50 to 2000 simulations for example). This coupling ensures the same probability of inappropriate rejection for each solution. The aim of combining optimisation and simulation is to generate a potential solution for the parameters and to assess its suitability at the same time to ensure that the resulting parameters are the best ones which work whatever the flight condition.

2.1.2.4 OPTIMISATION METHODOLOGY

Rearranging equation (2.12) gives:

$$F_x = \frac{1}{2}\rho c(U_p a(\theta - \alpha_0) + c_d U_T)U - \frac{1}{2}\rho c U_p a U \phi$$

and equation (2.13):

$$F_{z'} = \frac{1}{2}\rho c(U_T a(\theta - \alpha_0) - c_d U_P)U - \frac{1}{2}\rho c U_T a U \phi$$

This latter gives required equations (2.14) and (2.15). All force projections can be written as:

$$F = AU + BU\phi$$

where A and B are known all over the rotor disk whatever the flight conditions. It seems therefore logical to approximate first U and then $U\phi$. To this end, both real and approached expressions are numerically integrated over the entire rotor disk, and the relative difference between the two is then minimised tweaking parameters α , β and γ . Only the parameters numbered 1 and 2 are modified during the optimisation of U , whereas only the parameters numbered from 3 to 5 are adjusted for the optimisation of $U\phi$.

2.1.2.5 OPTIMISATION RESULTS

U OPTIMISATION RESULTS The optimisation result of airspeed U is shown in Figure 2.8 together with the result obtained with the simulation that considers the basic theory simplification. The error rate obtained with basic theory simplification has an average of

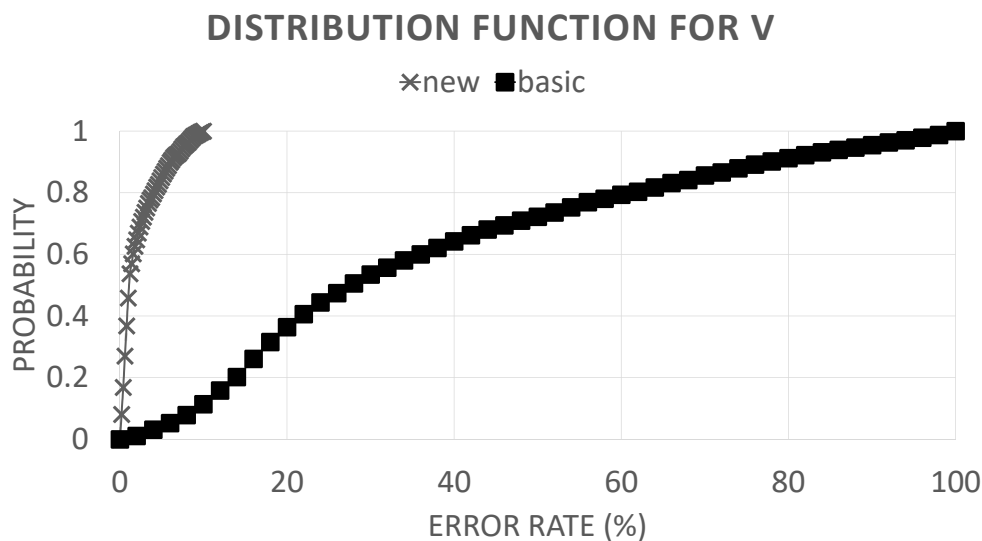


Figure 2.8: U optimised estimation

36.1 and a standard deviation of 25.9. When using the new theory, these fall down to an average of 2.21 and a standard deviation of 2.37. The optimised parameters are exposed in Table 2.1 An optimisation is carried out in order to find the flight situation where the error

r_{ref}	α_1	β_1	γ_1	α_2	β_2	γ_2
0.414242929	-0.189763849	0.380971657	0.835585466	-0.150955968	-0.528866662	0.703105628

Table 2.1: U optimised parameters

rate is the highest. This is reached for $\omega = 10.394$, $V_\lambda = 15.328$ and $V_\mu = 0$. In this case, error rate is equal to 9.88779683, which means that the error rate of the velocity approximation has been divided by a factor greater than 10.

$U\phi$ OPTIMISATION RESULTS The result of the optimisation of $U\phi$ is shown in Figure 2.9 together with the result obtained with the simulation based on the basic theory simplification.

The error rate obtained with basic theory simplification has an average of 16.8 and a standard deviation of 11.2 which fall down to an average of 3.64 and a standard deviation of 2.51 for the new theory. The optimised parameters are exposed in Table 2.2.

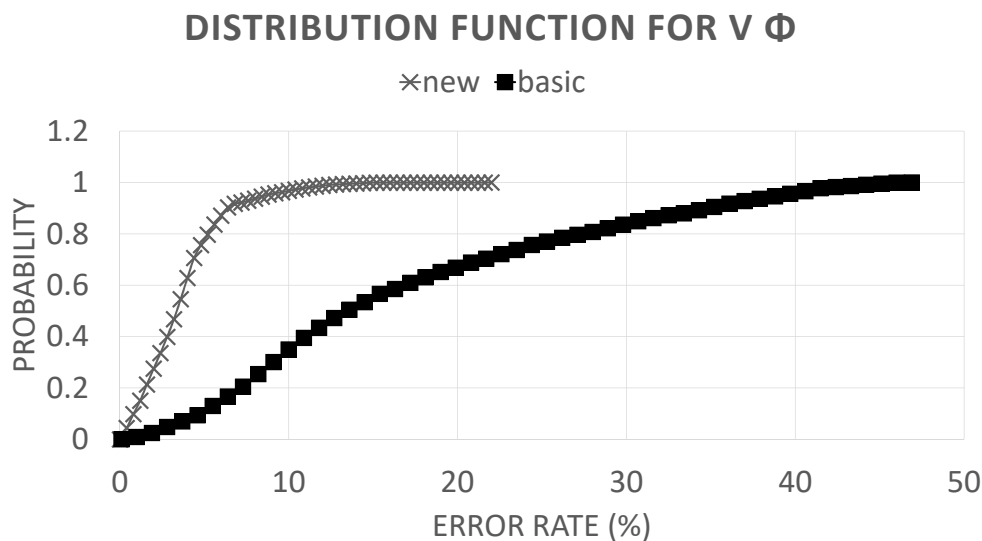


Figure 2.9: $U\phi$ optimised estimation

r'_{ref}	α_3	β_3	γ_3	α_4
0.280322824	0.184001964	0.958091404	0.195733731	0.085332217
β_4	γ_4	α_5	β_5	γ_5
1.01708203	-0.142208603	0.193078488	0.850224706	-0.085003449

Table 2.2: $U\phi$ optimised parameters

The highest error rate is reached for $\omega = 0$, $V_\lambda = 17$ and $V_\mu = 16$, and is equal to 15.31177453. The error rate is thus divided by a factor greater than 3. One can notice in Figure 2.9 that the distribution function almost reaches 1 for error rates lower than 10. Moreover, for $\omega = 0$, the integrations ((2.16)), ((D.4.1)), ((2.18)) and ((2.19)) do not have so much sense anymore (a new dynamic should be used at the very end of the rotor stop). So, as explained in section 2.1.2.3 page 59, the flight envelope could be reduced further to lower the error rate. Nonetheless, the results are already highly satisfactory and will be used in their current form.

The analytical expressions procurement of the forces and moments applying to the rotor are detailed in the appendix B, page 165. The construction of the flight dynamics can then begin.

2.2 FLIGHT DYNAMICS

2.2.1 ASSUMPTIONS

The demonstrator is equipped with an electrical propulsion system feed by a battery, so the aircraft is of constant mass and has a constant inertial matrix.

To simplify the dynamics of flight, some assumptions are made.

- The aircraft is supposed to be rigid. Thanks to the construction and average aspect ratio of the main wing, this assumption is not compromising at all.
- The earth is assumed to be flat and is considered as a Galilean referential frame. Thanks to the low speed of the aircraft, this assumption is acceptable.
- The wind is considered as linear and constant velocity
- The sideslip angle is controlled to be as low as possible

2.2.2 DYNAMICS RELATIONS

Following the method of [?] but working in the aircraft reference frame, the dynamics relations of the aircraft can be written as follows:

$$\begin{aligned}
X - mg \sin \theta &= m (\dot{u}^E + qw^E - rv^E) \\
Y + mg \cos \theta \sin \phi &= m (\dot{v}^E + ru^E - pw^E) \\
Z + mg \cos \theta \cos \phi &= m (\dot{w}^E + pv^E - qu^E) \\
L &= I_x \dot{p} - I_{zx} \dot{r} + qr (I_z - I_y) - I_{zx} pq \\
M &= I_y \dot{q} + rp (I_x - I_z) + I_{zx} (p^2 - r^2) \\
N &= I_z \dot{r} - I_{zx} \dot{p} + pq (I_y - I_x) + I_{zx} qr \\
p &= \dot{\phi} - \dot{\psi} \sin \theta \\
q &= \dot{\theta} \cos \phi + \dot{\psi} \cos \theta \sin \phi \\
r &= \dot{\psi} \cos \theta \cos \phi - \dot{\theta} \sin \phi \\
\dot{\phi} &= p + (q \sin \phi + r \cos \phi) \tan \theta \\
\dot{\theta} &= q \cos \phi - r \sin \phi \\
\dot{\psi} &= (q \sin \phi + r \cos \phi) \sec \theta \\
\dot{x}^E &= u^E \cos \theta \cos \psi + v^E (\sin \phi \sin \theta \cos \psi - \cos \phi \sin \psi) + w^E (\cos \phi \sin \theta \cos \psi + \sin \phi \sin \psi) \\
\dot{y}^E &= u^E \cos \theta \sin \psi + v^E (\sin \phi \sin \theta \sin \psi + \cos \phi \cos \psi) + w^E (\cos \phi \sin \theta \sin \psi - \sin \phi \cos \psi) \\
\dot{z}^E &= -u^E \sin \theta + v^E \sin \phi \cos \theta + w^E \cos \phi \cos \theta \\
u^E &= u + W_x \\
v^E &= v + W_y \\
w^E &= w + W_z
\end{aligned} \tag{2.22}$$

One can notice that the expressions of $\dot{\phi}$ and $\dot{\psi}$ depend respectively on $\tan \theta$ and $\sec \theta$ both undefined for $\theta = \frac{\pi}{2}$. If it does not pose any problem for classical aeroplanes whose flight envelope does not cover this situation, the present concept is likely to take off and land vertically, therefore when $\theta = \frac{\pi}{2}$. A good solution to overcome this issue consists in substituting the Euler angle representation of the aircraft attitude by the Quaternions one [?]. The rotation quaternion between the earth and the aircraft reference frames is defined as:

$$q = \begin{pmatrix} q_1 \\ q_2 \\ q_3 \\ q_4 \end{pmatrix}$$

Its dynamics equations are [?]:

$$\begin{pmatrix} \dot{q}_1 \\ \dot{q}_2 \\ \dot{q}_3 \\ \dot{q}_4 \end{pmatrix} = \frac{1}{2} \begin{pmatrix} 0 & -p & -q & -r \\ p & 0 & r & -q \\ q & -r & 0 & p \\ r & q & -p & 0 \end{pmatrix} \begin{pmatrix} q_1 \\ q_2 \\ q_3 \\ q_4 \end{pmatrix}$$

One solution to deal with the remaining Euler angles in the expressions of equation (2.22) is to estimate them from the quaternion q as proposed in reference [?]. However, this would not fully enjoy the benefits of the quaternions (i.e. continuity, stability), therefore, it is decided to only work with quaternions and therefore remove all the Euler angle expressions. One can notice that those expressions have been obtained thanks to the application of the rotation matrix R between the two reference frame (i.e. earth and aeroplane):

$$R = \begin{pmatrix} \cos \theta \cos \psi & -\cos \phi \sin \psi + \sin \phi \sin \theta \cos \psi & \sin \phi \sin \psi + \cos \phi \sin \theta \cos \psi \\ \cos \theta \sin \psi & \cos \phi \cos \psi + \sin \phi \sin \theta \sin \psi & -\sin \phi \cos \psi + \cos \phi \sin \theta \sin \psi \\ -\sin \theta & \sin \phi \cos \theta & \cos \phi \cos \theta \end{pmatrix}$$

Nevertheless, this rotation matrix can be expressed in quaternion form:

$$R = \begin{pmatrix} 1 - 2(q_3^2 + q_4^2) & 2(q_2q_3 - q_1q_4) & 2(q_1q_3 + q_2q_4) \\ 2(q_2q_3 + q_1q_4) & 1 - 2(q_2^2 + q_4^2) & 2(q_3q_4 - q_1q_2) \\ 2(q_2q_4 - q_1q_3) & 2(q_1q_2 + q_3q_4) & 1 - 2(q_2^2 + q_3^2) \end{pmatrix}$$

Equation (2.22) thus becomes:

$$\begin{aligned}
X + 2mg(q_2q_4 - q_1q_3) &= m(\dot{u}^E + qw^E - rv^E) \\
Y + 2mg(q_1q_2 + q_3q_4) &= m(\dot{v}^E + ru^E - pw^E) \\
Z + mg(1 - 2(q_2^2 + q_3^2)) &= m(\dot{w}^E + pv^E - qu^E) \\
L &= I_x\dot{p} - I_{zx}\dot{r} + qr(I_z - I_y) - I_{zx}pq \\
M &= I_y\dot{q} + rp(I_x - I_z) + I_{zx}(p^2 - r^2) \\
N &= I_z\dot{r} - I_{zx}\dot{p} + pq(I_y - I_x) + I_{zx}qr \\
\dot{q}_1 &= -\frac{1}{2}(pq_2 + qq_3 + rq_4) \\
\dot{q}_2 &= \frac{1}{2}(pq_1 + rq_3 - qq_4) \\
\dot{q}_3 &= \frac{1}{2}(qq_1 - rq_2 + pq_4) \\
\dot{q}_4 &= \frac{1}{2}(rq_1 + qq_2 - pq_3) \\
\dot{x}^E &= u^E(1 - 2(q_3^2 + q_4^2)) + 2v^E(q_2q_3 - q_1q_4) + 2w^E(q_1q_3 + q_2q_4) \\
\dot{y}^E &= 2u^E(q_2q_3 + q_1q_4) + v^E(1 - 2(q_2^2 + q_4^2)) + 2w^E(q_3q_4 - q_1q_2) \\
\dot{z}^E &= 2u^E(q_2q_4 - q_1q_3) + 2v^E(q_1q_2 + q_3q_4) + w^E(1 - 2(q_2^2 + q_3^2)) \\
u^E &= u + W_x \\
v^E &= v + W_y \\
w^E &= w + W_z
\end{aligned} \tag{2.23}$$

An additional dynamics must be added to the aeroplane or helicopter traditional ones. The rotor is indeed intended to be stopped in flight, so its dynamics is modelled:

$$J_{rotor}\dot{\Omega} = -Q_r$$

Where J_{rotor} is the moment of inertia of the rotor around its rotation axis.

2.2.3 FORCES AND MOMENTS

In equation (2.23), the resultant forces and moments are still unknown.

2.2.3.1 LONGITUDINAL DYNAMICS

The forces and moments of the longitudinal dynamics are represented in Figure 2.10. One can notice that the centre of application of the fuselage force is not defined. This is due to the fact that it applies all along the fuselage axis and therefore the resulting force and moment are computed at the x origin. Defining:

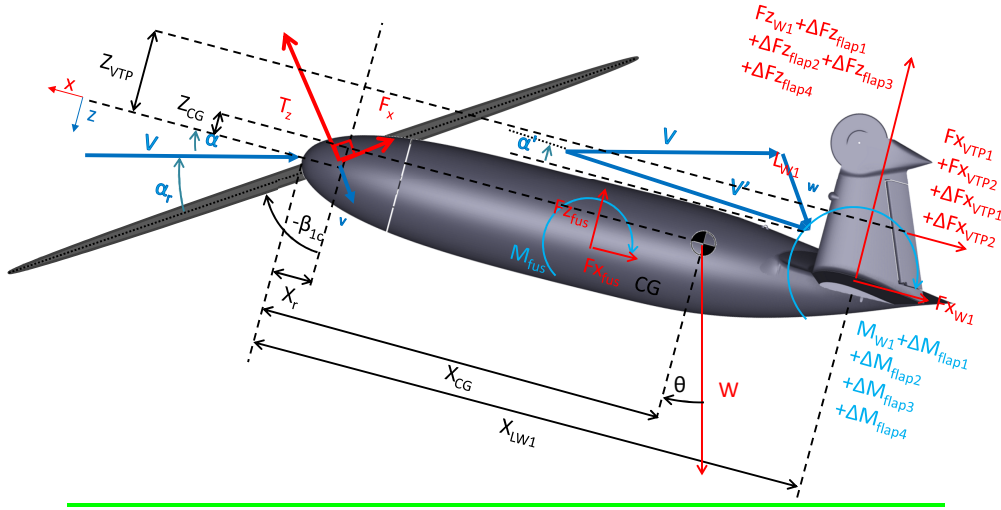


Figure 2.10: Longitudinal dynamics

$$R_z = T_z \sin \beta_{1c} - F_x \cos \beta_{1c} \quad (2.24)$$

$$R_x = T_z \cos \beta_{1c} + F_x \sin \beta_{1c} \quad (2.25)$$

It leads to:

$$Z = -R_z - Fz_{fus} - Fz_{w1} - \Delta Fz_{flap1} - \Delta Fz_{flap2} - \Delta Fz_{flap3} - \Delta Fz_{flap4} \quad (2.26)$$

$$X = R_x - Fx_{fus} - Fx_{w1} - Fx_{VTP1} - Fx_{VTP2} - \Delta Fz_{VTP1} - \Delta Fz_{VTP2} \quad (2.27)$$

$$\begin{aligned}
M &= R_z (X_r - X_{CG}) + R_x Z_{CG} \\
&+ Fz_{fus} X_{CG} - M_{fus} \\
&+ (Fz_{w1} + \Delta Fz_{flap1} + \Delta Fz_{flap2} + \Delta Fz_{flap3} + \Delta Fz_{flap4}) (X_{CG} - X_{LW1}) \\
&+ (M_{w1} + \Delta M_{flap1} + \Delta M_{flap2} + \Delta M_{flap3} + \Delta M_{flap4}) \\
&+ (Fx_{VTP1} + Fx_{VTP2} + \Delta Fx_{VTP1} + \Delta Fx_{VTP2}) (Z_{VTP} - Z_{CG})
\end{aligned} \tag{2.28}$$

2.2.3.2 LATERAL DYNAMICS

The forces and moments of the lateral dynamics are exposed in Figure 2.11 Defining:

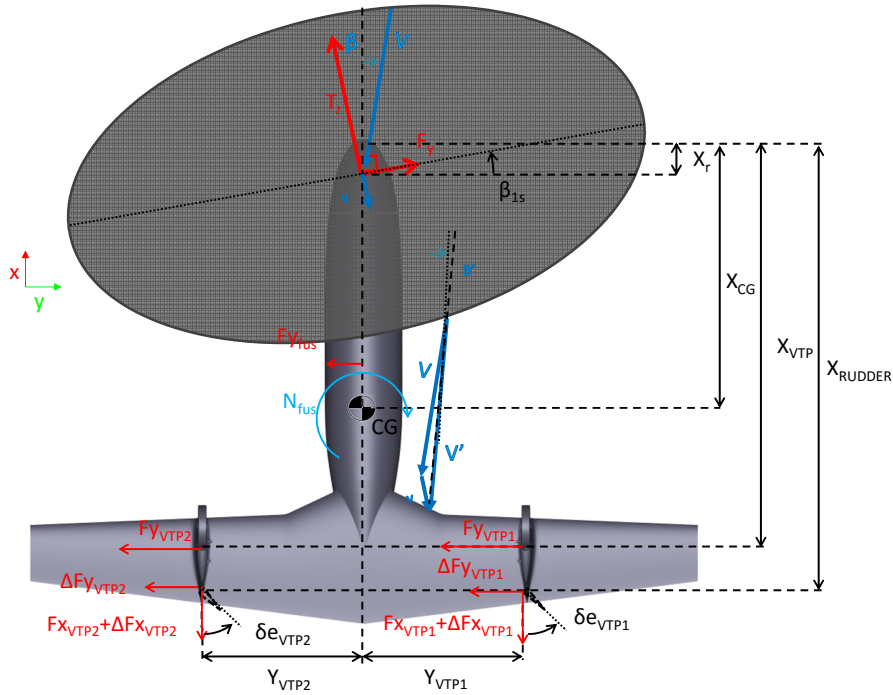


Figure 2.11: Lateral dynamics

$$\begin{aligned}
R_y &= -R_x \sin \beta_{1s} + F_y \cos \beta_{1s} \\
&= -T_z \cos \beta_{1c} \sin \beta_{1s} - F_x \sin \beta_{1c} \sin \beta_{1s} + F_y \cos \beta_{1s}
\end{aligned} \tag{2.29}$$

It leads to:

$$Y = R_y - Fy_{fus} - Fy_{VTP1} - Fy_{VTP2} - \Delta Fy_{VTP1} - \Delta Fy_{VTP2} \tag{2.30}$$

$$\begin{aligned}
N &= R_y (X_{CG} - X_r) - Fy_{fus}X_{CG} + N_{fus} \\
&+ (Fy_{VTP1} + Fy_{VTP2} + \Delta Fy_{VTP1} + \Delta Fy_{VTP2}) (X_{VTP} - X_{CG}) \\
&+ (Fx_{VTP1} + \Delta Fx_{VTP1}) Y_{VTP1} + (Fx_{VTP2} + \Delta Fx_{VTP2}) Y_{VTP2}
\end{aligned} \tag{2.31}$$

2.2.3.3 DIRECTIONAL DYNAMICS

The forces and moments of the directional dynamics are shown in Figure 2.12

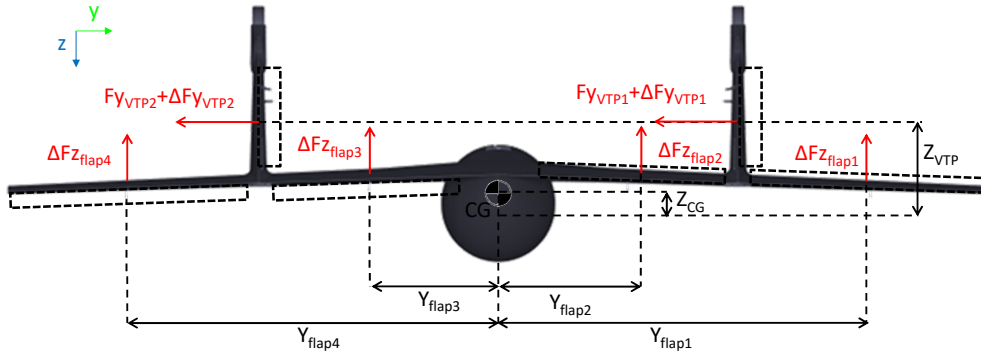


Figure 2.12: Directional dynamics

$$\begin{aligned}
L &= L_{w1} + (Fy_{VTP1} + Fy_{VTP2} + \Delta Fy_{VTP1} + \Delta Fy_{VTP2}) (Z_{CG} - Z_{VTP}) \\
&- \Delta Fz_{flap1} Y_{flap1} - \Delta Fz_{flap2} Y_{flap2} - \Delta Fz_{flap3} Y_{flap3} - \Delta Fz_{flap4} Y_{flap4}
\end{aligned} \tag{2.32}$$

2.2.4 AIRCRAFT AERODYNAMICS

2.2.4.1 ROTOR

SPEED The airspeed V withstood by the rotor is defined as:

$$V = \sqrt{(u)^2 + (w_r)^2} \tag{2.33}$$

One can notice that the side component of the airspeed is neglected following assumptions exposed in section 2.2.1, page 64. w_r is computed as:

$$w_r = w + q(X_r - X_{CG}) \quad (2.34)$$

where X_r and X_{CG} are respectively the longitudinal locations of the rotor and the CG.

The angle of attack α withstood by the aircraft is defined as:

$$\alpha = \tan^{-1} \left(\frac{w_r}{u} \right) \quad (2.35)$$

FLAP MOTION The computation of the flap angles starts with the definition of the reference angles and speeds: According to what was shown in the appendix B.5 page 179, the computation is done in a reference plane close to the rotor's actual one. Then defining α'_r , the temporary rotor angle of attack:

$$\alpha'_r + \alpha - \beta'_{1c} = \frac{\pi}{2} \quad (2.36)$$

Where β'_{1c} is a virtual rotor longitudinal flap angle chosen close to actual one (for example by mean of a first order filter applied on the latter).

The downwash velocity v varies slowly with V and T , and these latter change themselves slowly thanks to the inertia, the former can be considered as constant in the control and computed separately by means of a first order filter applied on equation (B.1).

Then the axial and radial velocity sustained by the rotor becomes:

$$V'_\lambda = V \sin \alpha'_r + v \quad (2.37)$$

$$V'_\mu = V \cos \alpha'_r \quad (2.38)$$

The estimations of the flap angles increments $\Delta\beta_{1s}$ and $\Delta\beta_{1c}$ are performed from equations (B.6) (B.7)

The equations are simplified a bit considering the following approximations:

- $K_\beta = 0$ since no spring has been integrated in the rotor head.
- $\beta_0 = 0$ because of the teetering design of the rotor.
- The second order terms $c_d\beta_{1c}^2$, $c_d\beta_{1s}^2$ or $c_d\beta_{1c}\beta_{1s}$ are neglected. Since β_{1c} and β_{1s} are very small and that the drag (i.e. c_d) is very small compared to the lift they are indeed supposed to have almost no effect on the behaviour.

The following parameters are substituted in the resulting equations:

- $A_\beta = \frac{k_1\rho}{2} \int_{root}^{tip} rca(\theta_t - \alpha_0) dr - \frac{(k_1k_5+k_3)\rho}{2} \int_{root}^{tip} rcadr - \frac{k_2\rho}{2} \int_{root}^{tip} rcc_d dr$
- $B_\beta = \frac{k_1\rho}{2} \int_{root}^{tip} rcadr$
- $C_\beta = \frac{k_1\rho}{2} \int_{root}^{tip} r^3ca(\theta_t - \alpha_0) dr - \frac{(k_1k_5+k_3)\rho}{2} \int_{root}^{tip} r^3cadr - \frac{k_2\rho}{2} \int_{root}^{tip} r^3cc_d dr$
- $D_\beta = \frac{k_1\rho}{2} \int_{root}^{tip} r^3cadr$
- $E_\beta = \frac{k_1\rho}{2} \int_{root}^{tip} r^2cadr$
- $F_\beta = k_2\rho \int_{root}^{tip} r^2ca(\theta_t - \alpha_0) dr + (k_4 - k_2k_5)\rho \int_{root}^{tip} r^2cadr$
- $G_\beta = k_2\rho \int_{root}^{tip} r^2cadr$
- $H_\beta = \frac{k_2\rho}{2} \int_{root}^{tip} rcadr$
- $I_\beta = \frac{k_2\rho}{2} \int_{root}^{tip} r^3cadr$
- $J_\beta = \frac{k_1\rho}{2} \int_{root}^{tip} c_d r^2 c dr$

The flap equations become:

$$\begin{aligned}
0 = & \Delta\beta_{1c} \left(\frac{1}{4} V_\mu'^2 (A_\beta + B_\beta\theta_0) - \Omega^2 (C_\beta + \theta_0 D_\beta) - \frac{1}{2} V_\mu' \Omega \theta_{1s} E_\beta + 2\Omega V_\lambda' J_\beta \right) \\
& + \Delta\beta_{1s} \frac{1}{2} V_\mu' \Omega \theta_{1c} E_\beta + V_\lambda' V_\mu' (A_\beta + B_\beta\theta_0) + V_\lambda' \Omega \theta_{1s} E_\beta + (F_\beta + \theta_0 G_\beta) \Omega V_\mu' \\
& + \frac{3}{4} V_\mu'^2 \theta_{1s} H_\beta + \theta_{1s} \Omega^2 I_\beta + r_p F_{p_s} \sin(\theta_0 + \theta_p) + r_p F_{p_0} \theta_{1s} \cos(\theta_0 + \theta_p)
\end{aligned} \tag{2.39}$$

$$\begin{aligned}
0 = & \Delta\beta_{1s} \left(\frac{1}{4}V_\mu'^2 (A_\beta + \theta_0 B_\beta) + \Omega^2 (C_\beta + \theta_0 D_\beta) + \frac{1}{2}\theta_{1s}V_\mu'\Omega E_\beta - 2\Omega V_\lambda'J_\beta \right) \\
& + \Delta\beta_{1c} \frac{1}{2}\Omega V_\mu'\theta_{1c}E_\beta + \Omega V_\lambda'\theta_{1c}E_\beta + \frac{1}{4}V_\mu'^2\theta_{1c}H_\beta + \Omega^2\theta_{1c}I_\beta \\
& + r_p F_{p_c} \sin(\theta_0 + \theta_p) + r_p F_{p_0}\theta_{1c} \cos(\theta_0 + \theta_p)
\end{aligned} \tag{2.40}$$

which is of the form:

$$\begin{cases} A\Delta\beta_{1s} + B\Delta\beta_{1c} + C = 0 \\ A'\Delta\beta_{1s} + B'\Delta\beta_{1c} + C' = 0 \end{cases}
\Rightarrow \begin{cases} \Delta\beta_{1c} = \frac{AC' - A'C}{A'B - AB'} \\ \Delta\beta_{1s} = \frac{-B'\Delta\beta_{1c} - C'}{A'} \end{cases}$$

The actual flap angles are thus obtained:

$$\beta_{1c} = \beta'_{1c} + \Delta\beta_{1c} \tag{2.41}$$

$$\beta_{1s} = \beta'_{1s} + \Delta\beta_{1s} \tag{2.42}$$

The actual angle withstood by the rotor disk can be computed:

$$\alpha_r + \alpha - \beta_{1c} = \frac{\pi}{2} \tag{2.43}$$

as well as the airspeeds:

$$V_\lambda = V \sin \alpha_r + v \tag{2.44}$$

$$V_\mu = V \cos \alpha_r \tag{2.45}$$

ROTOR LIFT T_z Applying the same simplification as for the flap motion to equation (B.2), and defining:

- $A_T = \frac{k_1\rho}{2}p \int_{r_0}^r rca(\theta_t - \alpha_0) dr - \frac{(k_1k_5+k_3)\rho}{2}p \int_{r_0}^r rcadr - \frac{k_2\rho}{2}p \int_{r_0}^r rcc_d dr$
- $B_T = \frac{k_1\rho}{2}p \int_{r_0}^r rcadr$
- $C_T = \frac{k_1\rho}{4}p \int_{r_0}^r cadr$
- $D_T = \frac{k_2\rho}{4}p \int_{r_0}^r ca(\theta_T - \alpha_0) dr + \frac{(k_4-k_5k_2)\rho}{4}p \int_{r_0}^r cadr$

-
- $E_T = \frac{k_2\rho}{4}p \int_{r_0}^r c adr$
 - $F_T = \frac{k_2\rho}{2}p \int_{r_0}^r r^2 ca (\theta_T - \alpha_0) dr + \frac{(k_4-k_5k_2)\rho}{2}p \int_{r_0}^r r^2 c adr$
 - $G_T = \frac{k_2\rho}{2}p \int_{r_0}^r r^2 c adr$
 - $H_T = \frac{k_2\rho}{2}p \int_{r_0}^r r c adr$
 - $I_T = \frac{k_1\rho}{2}p \int_{r_0}^r c c_d dr$

It leads to:

$$\begin{aligned}
T_z = & V_\lambda \Omega (A_T + \theta_0 B_T) + \theta_{1s} V_\lambda V_\mu C_T + V_\mu^2 (D_T + \theta_0 E_T) + \Omega^2 (F_T + \theta_0 G_T) \\
& + \theta_{1s} V_\mu \Omega H_T - V_\lambda^2 I_T + 2F_{p0} \sin(\theta_p + \theta_0) + \cos(\theta_p + \theta_0) (\theta_{1c} F_{pc} + \theta_{1s} F_{ps})
\end{aligned} \tag{2.46}$$

ROTOR LATERAL FORCE F_y Applying the same simplification as previously and defining:

- $A_y = \frac{\rho k_1}{4}p \int_{r_0}^r c adr$
- $B_y = \frac{k_2\rho}{4}p \int_{r_0}^r r c adr$

Equation (F.8) leads to:

$$F_y = -\theta_{1c} V_\lambda^2 A_y - \theta_{1c} V_\lambda \Omega B_y + F_{pc} \cos(\theta_p + \theta_0) - F_{p0} \theta_{1c} \sin(\theta_p + \theta_0) \tag{2.47}$$

ROTOR DRAG F_x Equation (F.9) is simplified and undergoes the following substitutions:

- $A_x = \frac{k_1\rho}{4}p \int_{r_0}^r c adr$
- $B_x = \frac{k_2\rho}{4}p \int_{r_0}^r ca (\theta_t - \alpha_0) dr + \frac{(k_4-k_5k_2)\rho}{4}p \int_{r_0}^r c adr + \frac{k_1\rho}{4}p \int_{r_0}^r c c_d dr$
- $C_x = \frac{k_2\rho}{4}p \int_{r_0}^r c adr$
- $D_x = \frac{k_2\rho}{4}p \int_{r_0}^r r c adr$

- $E_x = \frac{k_2\rho}{2}p \int_{r_0}^r rcc_d dr$

It becomes:

$$F_x = \theta_{1s}V_\lambda^2 A_x + V_\lambda V_\mu (B_x + \theta_0 C_x) + \theta_{1s}V_\lambda \Omega D_x + V_\mu \Omega E_x - F_{ps} \cos(\theta_p + \theta_0) + F_{p0}\theta_{1s} \sin(\theta_p + \theta_0) \quad (2.48)$$

ROTOR TORQUE Q_r Lastly equation (B.5) is simplified and combined with the following equations

- $A_Q = \frac{k_1\rho}{2}p \int_{r_0}^r rca(\theta_t - \alpha_0)dr - \frac{(k_5k_1+k_3)\rho}{2}p \int_{r_0}^r rca dr$
- $B_Q = \frac{k_1\rho}{2}p \int_{r_0}^r rca dr$
- $C_Q = \frac{k_2\rho}{2}p \int_{r_0}^r r^2ca(\theta_t - \alpha_0)dr + \frac{(k_4-k_5k_2)\rho}{2}p \int_{r_0}^r r^2ca dr + \frac{k_1\rho}{2}p \int_{r_0}^r r^2cc_d dr$
- $D_Q = \frac{k_2\rho}{2}p \int_{r_0}^r r^2ca dr$
- $E_Q = \frac{k_2\rho}{4}p \int_{r_0}^r rca dr$
- $F_Q = \frac{k_2\rho}{4}p \int_{r_0}^r rcc_d dr$
- $G_Q = \frac{k_2\rho}{2}p \int_{r_0}^r r^3cc_d dr$

Which gives:

$$Q_r = V_\lambda^2 (A_Q + \theta_0 B_Q) + V_\lambda \Omega (C_Q + \theta_0 D_Q) + \theta_{1s}V_\mu V_\lambda E_Q + V_\mu^2 F_Q + \Omega^2 G_Q - r_p (2F_{p0} \cos(\theta_p + \theta_0) - \sin(\theta_p + \theta_0) (F_{pc}\theta_{1c} + F_{ps}\theta_{1s})) \quad (2.49)$$

2.2.4.2 STEADY AIRFRAME

RELATIVE WIND DEFINITION Contrary to a traditional aircraft, the downwash of the rotor highly affects the behaviour of the fixed airframe. Therefore, it must not be neglected.

- At speed close to zero, the standard assumption considering a constant relative wind withstood by the entire airframe can't be used. Indeed, at those speeds, the prevailing airflow is the one generated by the downwash of the main rotor. Therefore, the air-speed withstood by the body parts located in the downwash is entirely different from the general aircraft one. The downwash velocity generated by the rotor is shown in Figure 2.13 The first assessment is that the flow in the wake of the rotor is particularly

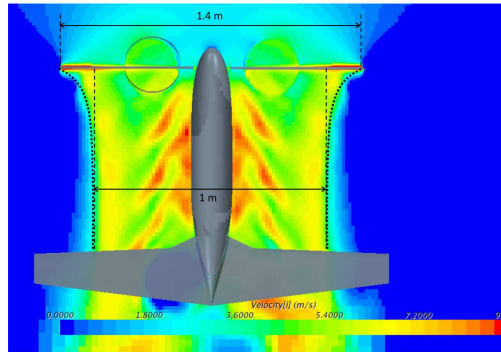


Figure 2.13: Speed estimation

turbulent because of the mix of the different flow sources. However, because of the frequency of this variation, it can be assumed that the body will react in the same way as in a uniform flow of average velocity. It can be seen that the stream tube reduces in diameter after crossing the rotor disk. The ratio of diameter at the rotor location and where the flow is stabilised is of around 1.4 which implies a ratio of cross section area around two just as the one expected by the momentum theory (cf. section A.1.1, page 147). In addition to that, the stream tube evolves very quickly, and only a small part of the fuselage works in a unstabilized flow. Therefore, to simplify the calculation, the entire fixed body in the downwash tube is assumed to withstand the same velocity, which corresponds to the theoretical stabilised downwash.

- The faster the rotor works, the more similar it is to a circular wing of same span [?]. According to Hoerner ([?], ch. VII-1), for an elliptical wing and all the more so for a circular wing, "the equivalent stream of air deflected is that within a cylinder having a diameter equal to the wing span" b as shown in Figure 2.15 Applying the energy

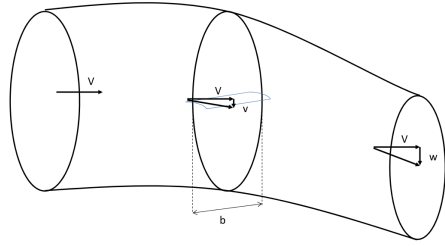


Figure 2.14: wing stream tube deflection, where V is the relative wind, v and w are respectively the vertical downwash velocity at the wing location and at the far downstream

conservation to the stream:

$$\begin{aligned} \frac{1}{2}\dot{m} (V^2 + v'^2) - \frac{1}{2}\dot{m}V^2 &= F \cdot v \\ \Leftrightarrow \frac{1}{2}\dot{m}v'^2 &= F \cdot v \end{aligned}$$

Which combined with the expression of the resulting force:

$$F = \dot{m} (v' - 0)$$

leads to:

$$\frac{1}{2}\dot{m}v'^2 = \dot{m}v' \cdot v$$

So just as for the rotor theory, the velocity impacting the fixed body is:

$$v' = 2v$$

Therefore, it is twice the airspeed at the rotor disk given by equation (B.1). As for hover flight, the span of the wing blown by the rotor downwash is slightly smaller than the rotor diameter. Applying the mass conservation:

$$\dot{m} = cste$$

In other words:

$$\rho S_1 \sqrt{(V^2 + v'^2)} = \rho A \sqrt{(V^2 + v^2)}$$

That is to say:

$$S_1 = A \sqrt{\frac{1}{1 + 3 \frac{v^2}{V^2 + v^2}}}$$

One can notice that there is continuity with the rotor hover theory since when V is zero, $S_1 = \frac{1}{2}A$ where A is equal to the rotor disk area.

Therefore, the induced airspeed is first computed thanks to equation (B.1) where the force T , used as input, is the total force generated by the rotor:

$$T = \sqrt{T_z^2 + F_x^2}$$

It can be noticed that F_y is neglected since it is likely to be much smaller than the two other rotor forces. The obtained downwash velocity is collinear with the resultant force. The angle between the induced airspeed and the X axis is therefore computed following Figure 2.15:

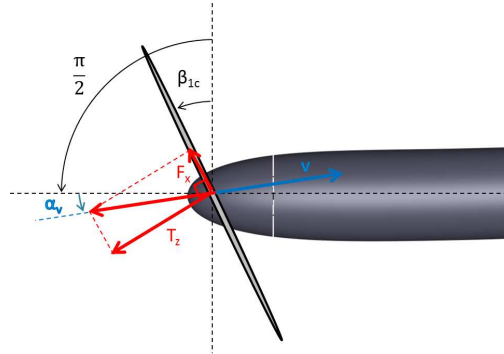


Figure 2.15: Downwash angle of attack

$$\alpha_v = \tan^{-1} \left(\frac{T_z}{F_x} \right) + \beta_{1c} - \frac{\pi}{2} \quad (2.50)$$

Then, the downwash velocity components are computed as:

$$u_{downwash} = v' \cos(\alpha_v) \quad (2.51)$$

$$w_{downwash} = v' \sin(\alpha_v) \quad (2.52)$$

Out of the downwash surface S_1 , those latter speeds are assumed to be zero.

The airspeed V_i withstood by the aerodynamic element i is defined as:

$$V_i = \sqrt{(u + u_{downwash})^2 + (w_i + w_{downwash})^2} \quad (2.53)$$

One can notice that the side component of the airspeed is neglected, and w_i is computed as:

$$w_i = w + p \cdot Y_i + q(X_i - X_{CG}) \quad (2.54)$$

where X_i and Y_i are respectively the longitudinal and lateral locations of the element i . The angle of attack α_i withstood by the aerodynamic element i is thus defined as:

$$\alpha_i = \tan^{-1} \left(\frac{w_i + w_{downwash}}{u + u_{downwash}} \right) \quad (2.55)$$

Following the same method for the sideslip downwash, it leads to:

$$v_{downwash} = -u_{downwash} \sin \beta_{1s} \quad (2.56)$$

The sideslip airspeed v_i withstood by element i is:

$$v_i = v - r(X_i - X_{CG}) \quad (2.57)$$

It leads to:

$$\beta_i = \tan^{-1} \left(\frac{v_i + v_{downwash}}{u + u_{downwash}} \right)$$

v is supposed to be very small. It leads to:

$$\beta_i = \frac{v_i + v_{downwash}}{u + u_{downwash}} \quad (2.58)$$

At low airspeed, when the load is mostly sustained by the rotor, the main wing is likely to be fully stalled in lateral translation. For instance, when the aircraft accelerate after take-off to reach the transition conditions, the main wing is stalled until the lateral airspeed is sufficient enough to push it up, which reduces the angle of attack up to the reattachment of the flow.

The dynamics of this flight when the rotor is spinning can't be done as it is usually for classical aircraft. A method to estimate it is proposed in this section based on the aerodynamics developed by Sighard F.Hoerner [?]

FUSELAGE The fuselage of the drone is nearly cylindrical and has a circular cross section from the very beginning to the wing leading edge. The aerodynamics forces applying on the fuselage are of three types. The circulation of the air around the body generated the first part while the cross flow force is responsible for the second and the friction and the form drag of the fuselage are responsible for the last one.

According to Munk ([?],eq. 23), the circulation of the air around the body generates a lift force computed as:

$$\frac{dF}{dx} = q \left(\frac{dS_x}{dx} \right) \sin(2\alpha)$$

which gives in the aircraft frame:

$$\frac{dFz_{fus}}{dx} = q \left(\frac{dS_x}{dx} \right) \sin(2\alpha) \cos(\alpha)$$

The longitudinal component of this force is usually insignificant in comparison with the friction drag. The moment generated by the fuselage computed at the x-origin becomes:

$$\frac{dM_{fus}}{dx} = x \frac{dF}{dx} = xq \left(\frac{dS_x}{dx} \right) \sin(2\alpha) \cos(\alpha)$$

Where, q is the dynamic pressure and S_x is the cross section area at the position x . According to the equation, the total lift generated by the fuselage may be zero, but according to Hoerner ([?], section 19), the flow turning around a streamlined body does not keep attached all along it and therefore produce a lift on the growing part of its section. The presence of the stalled wing over all the slimming part of the body may accentuate this effect. Therefore the lift due to circulation can be estimated as:

$$\begin{aligned} Fz_{fus} &= q \sin(2\alpha) \cos(\alpha) \int_{nose}^{\max \text{ cross section}} \frac{dS_x}{dx} \cdot dx \\ &= q \sin(2\alpha) \cos(\alpha) S_{\max \text{ cross section}} \end{aligned}$$

And the moment becomes:

$$M_{fus} = q \sin(2\alpha) \cos(\alpha) \int_{nose}^{\max \text{ cross section}} x \cdot \frac{dS_x}{dx} \cdot dx$$

The cross flow force acting on the fuselage is due to the cross flow passing around the fuselage and produces a force corresponding to the drag generated on a cylinder by a radial airspeed ([?], section 3). The force is normal to the fuselage and is computed as ([?], section 19):

$$Fz_{fus} = qS_{lateralsection} \sin^2 \alpha C_c$$

The moment generated by this force is:

$$M_{fus} = q \sin^2 \alpha C_c \int_{nose}^{tail} x \frac{dS_{lateralsection}}{dx} \cdot dx$$

Where $S_{lateralsection}$ is the fuselage lateral section area, and C_c is the cylinder drag coefficient which is for the Reynolds number encountered by the aircraft of $C_c = 1.2$.

The friction and form drags, Mx_{fus} are estimated following the method exposed in section D.3.2, page 219. They are supposed to create only negligible moment because of their magnitude and the small level arm they form in respect of the centre of gravity. To simplify their estimation to alleviate the future control, and thanks to the small range of Reynold numbers encountered by the aircraft, its aerodynamic coefficient, $\frac{Fx_{fus}}{q}$, is assumed to be constant, and is computed for an average Reynold. And following the same approach as for the cross flow, the force becomes:

$$Fx_{fus} = q \frac{Fx_{fus}}{q} \cos^2 \alpha$$

Because of the weakness and the small lever arm of the force, the resulting moment is neglected.

Lastly, the different forces and moments components become:

Fz_{fus} , the normal force acting on the fuselage can be of two kinds: Both are plotted in Figure 2.16. One can notice that the forces are equivalent at around $0.251rad$ which

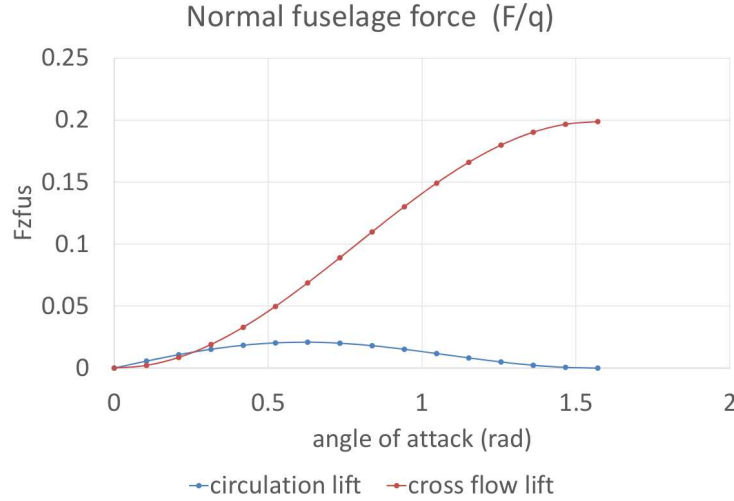


Figure 2.16: Fuselage normal force Fz_{fus}

is very close to the Hoerner expectations ([?], section 19). Thus this may be the angle of attack where the transition occurs from one phenomenon to another. However, the circulation force is much lower than the cross flow one. Therefore, the only acting force is assumed to be the cross flow one, throughout the angle of attack range, to avoid a tricky transition between two control laws. Thus:

$$Fz_{fus} = qS_{lateralsection} \sin^2 \alpha C_c \quad (2.59)$$

M_{fus} As for Fz_{fus} , the two kinds of moments generated at the x origin by the normal force acting on the fuselage are plotted in Figure 2.17. The same statement apply for M_{fus} as for Fz_{fus} . Thus:

$$M_{fus} = q \sin^2 \alpha C_c \int_{nose}^{tail} x \frac{dS_{lateralsection}}{dx} \cdot dx \quad (2.60)$$

Fx_{fus} the fuselage drag remains:

$$Fx_{fus} = q \frac{Fx_{fus}}{q} \cos^2 \alpha \quad (2.61)$$

WING As it has been seen in section 2.2.4.2, page 75, the wing does not sustain the same relative wind all its span long. This effect is furthermore enhanced by the roll velocity.

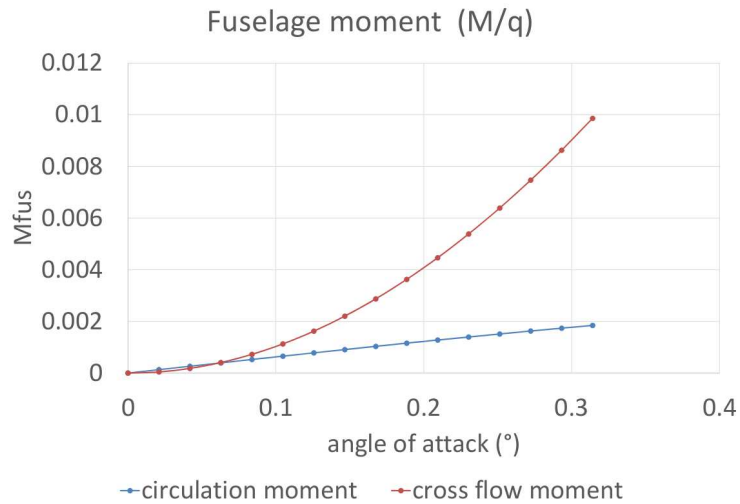


Figure 2.17: Fuselage moment M_{fus}

Therefore the panel method is used for the wing surface: it is split into six panels along the span: the two outboard parts of the wing out of the downwash, the two remaining parts of the wing corresponding to the outboard flaperons and the two parts of the wing corresponding to the inboard flaperons. The panels are presenting in Figure 2.18. Each part is assumed to

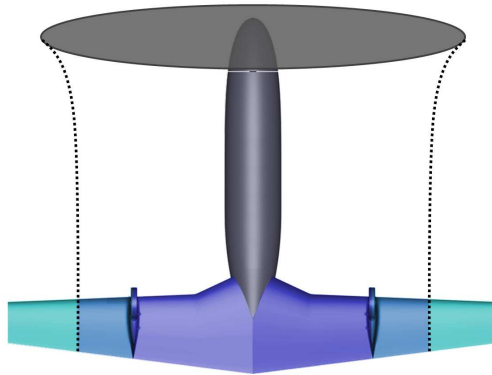


Figure 2.18: TL54 lift coefficient function of the angle of attack

withstand the airspeed of the point at half of its span and at 25% of its chord and to generate the resultant force on the same point. Because of the nature of the aircraft, the wing works either stalled or in attached airflow.

- Stalled wing: Hoerner proposes a method to estimate the forces acting on a stalled wing ([?], section 19). For a wing in an air flow forming an angle of attack α and

without any sideslip angle, the force generated is normal to the wing plane and can be estimated as:

$$Fz = qS_{wing_i} (1.8 \text{ to } 2.0) \sin \alpha \quad (2.62)$$

where S_{wing_i} is the fixed wing panel area. In fact, this corresponds to the drag generated by a flat plate in a flow ([?], section 3), of an area equal to the projection of the wing on the flow's perpendicular plan. The moving surfaces attached to the wing do not have the same authority when the wing is stalled as when the flow is fully attached. However, they have still an effect that may be useful to steer the aircraft. Indeed the deflection of the moving surfaces affects the projected area of the wing and thus alters the generated force. The force generated by each surface (fixed wing surfaces, wing moving surfaces) is computed independently. The normal force generated by each surface becomes:

$$\Delta Fz_{flapi} = qS_{surface_i} (1.8 \text{ to } 2.0) \sin (\alpha + \delta e_i) \quad (2.63)$$

Where δe is the surface deflection, $S_{surface_i}$ and Fz_i are respectively the surface area and the resulting force of the wing part i.

- Attached airflow wing: When the flow catches up with the aerofoil, the force acting on the wing is estimated by simulation just as in section 1.2.1.3, page 46. The model is based on the equation proposed by Etkin ([?], eq. 2.4,2 a) The lift of the aerofoil is shown in Figure 2.19.

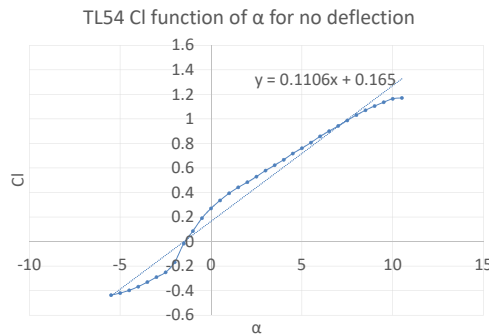


Figure 2.19: TL54 lift coefficient function of the angle of attack

$$Cl = 0.1106\alpha + 0.165 \quad (2.64)$$

The effect of the ailerons has already been computed in section 1.2.1.3 page 46:

$$\Delta Cl = 0.0393\delta e \quad (2.65)$$

The moment is estimated in the same way. The evolution of the moment coefficient generated by the aerofoil is shown in Figure 2.20. The aileron deflections curves are

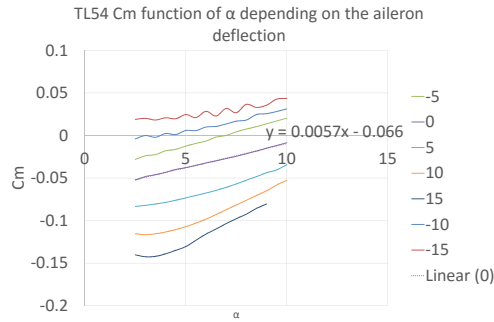


Figure 2.20: TL54 moment coefficient function of the angle of attack and the deflection

quite parallel which enables to apply the model proposed by Etkin ([?], eq. 2.4,2 b):

$$Cm = 0.0057\alpha + 0.066 \quad (2.66)$$

Then the variation of the moment coefficient due to the aileron deflection can be estimated as shown in Figure 2.21.

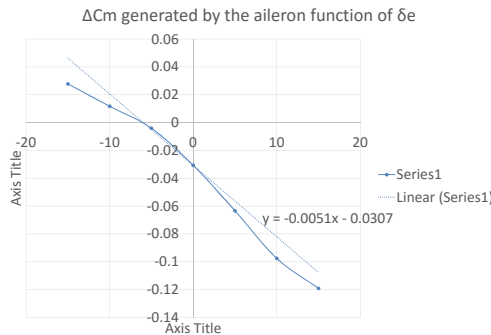


Figure 2.21: TL54 moment coefficient variation function of the angle of the deflection

$$\Delta Cm = -0.0051\delta e \quad (2.67)$$

Lastly the drag coefficient is approached by the following equation.

$$Cd = a\alpha^2 + b\alpha + c$$

According to Figure 2.22. it becomes:

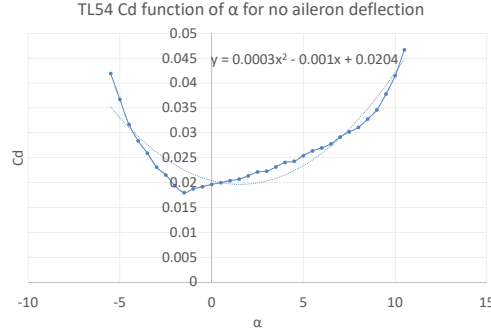


Figure 2.22: TL54 drag coefficient function of the angle of attack for zero deflection

$$Cd = 0.0003\alpha^2 - 0.001\alpha + 0.0204 \quad (2.68)$$

The effect of the flaperons is not considered since they are not intended to work as airbrakes. Lastly in the aircraft reference frame, the aerodynamic forces and moments generated by the fixed wing are:

$$Fz_{w1} = qS_{wing_i}Cl \cos \alpha + qS_{wing_i}cds \sin \alpha \quad (2.69)$$

$$Fx_{w1} = -qS_{wing_i}Cl \sin \alpha + qS_{wing}Cd \cos \alpha \quad (2.70)$$

$$M_{w1} = qS_{wing_i}Cm \quad (2.71)$$

In the same way the forces and moments increments due to the wing flap i :

$$\Delta Fz_{flapi} = qS_{wing_i}\Delta Cl_i \cos \alpha \quad (2.72)$$

$$\Delta M_{flapi} = qS_{wing_i}\Delta Cm_i \quad (2.73)$$

- Stalling transition: The stalling angle prediction is somewhat difficult since it depends

on a lot of parameters. The main wing has aspect and taper ratios of respectively 8 and 0.5 which falls well in the type of planar wing studied by Hoerner ([?], ch. 4-26 8.) It thus seems to be relevant to consider the result of the 2D aerofoil. The extended simulation of Cl is shown in Figure 2.23. For positive angles of attack, the

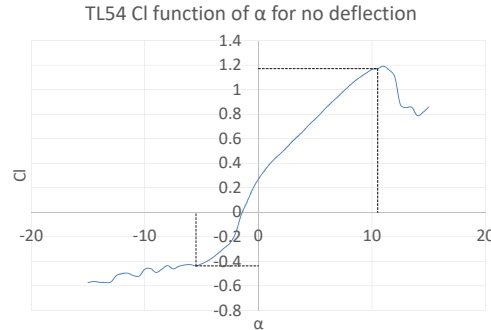


Figure 2.23: TL54 lift coefficient function of the angle of attack with stall estimation

stall is expected to happen at $\alpha = 10.5$, when the wing generates a lift coefficient of $Cl = 1.1713$. For negative angles of attack, the stall happens at a much lower angle. So there is no clear split between attached and stalled modes. However, the stall may occur for $\alpha = -5.5$, when the wing generates a lift coefficient of $Cl = -0.4366$. It is assumed that for $alpha > 15$ and $alpha < -10$ the wing is working in full stalled mode.

FIN The fin is designed around the NACA0012 aerofoil that is widely used for such application. The fin is intended to generate both lateral forces as a classical rudder and drag as an airbrake. The analysis is only carried out at a low angle of attack since the control law is design to fly as symmetric as possible. Then the analysis is very close to the one of the wing section 2.2.4.2 page 84.

The Cl of the NACA 0012 variation is shown in Figure 2.24. Which gives the side force coefficient Cl :

$$Cl = 0.1174\beta \quad (2.74)$$

where β is the sideslip angle. The influence of the rudder deflection is shown in Figure 2.25. Which gives the variation of the lift coefficient ΔCl

$$\Delta Cl = 0.033\delta e \quad (2.75)$$

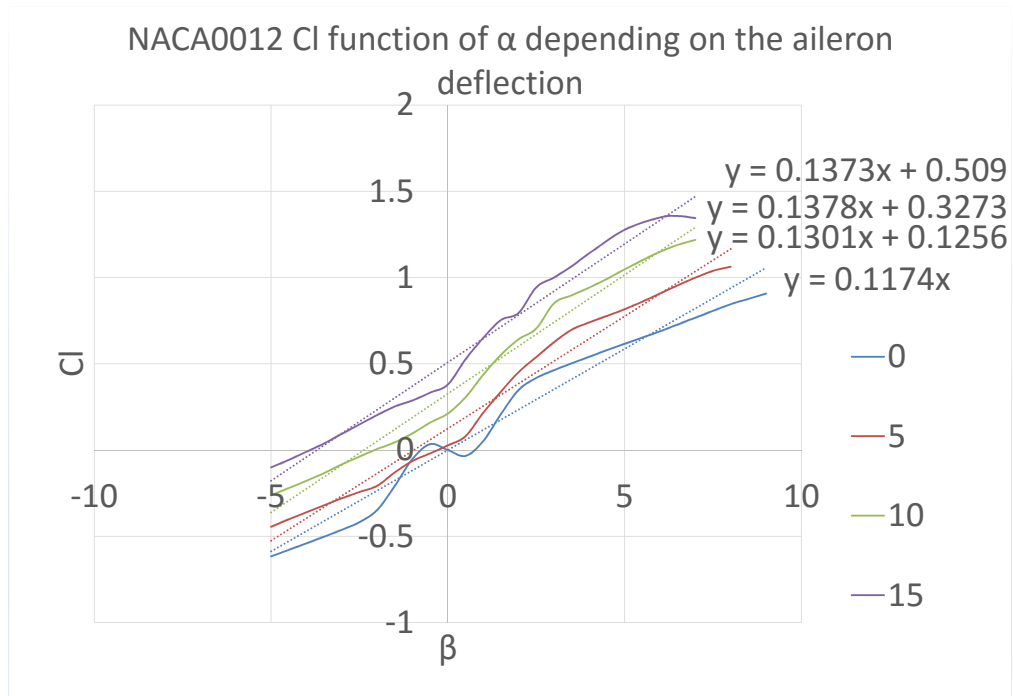


Figure 2.24: NACA0012 lift coefficient function of the angle of attack and the deflection

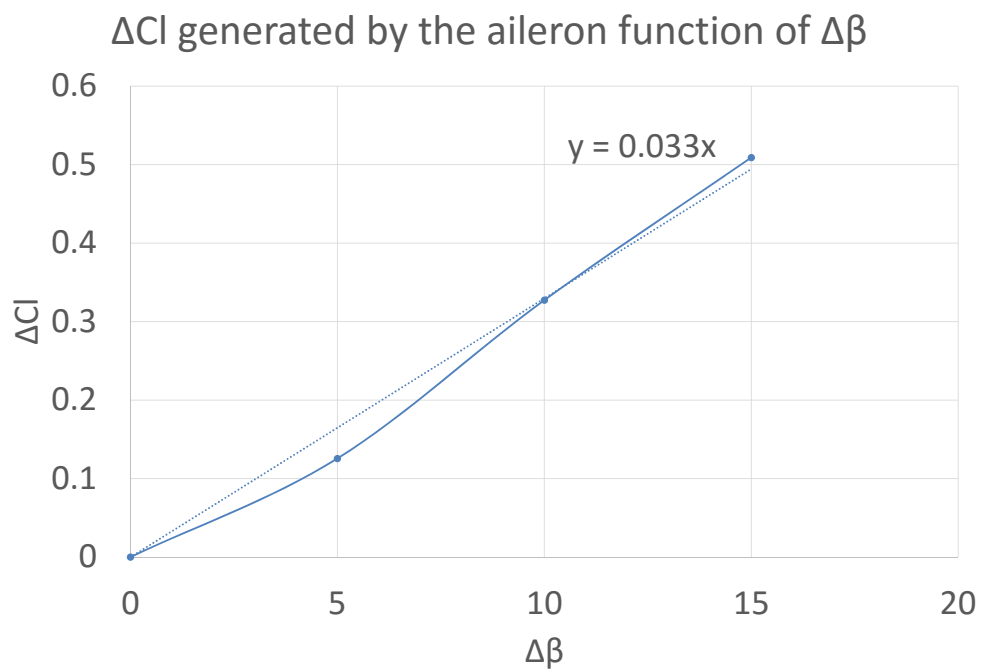


Figure 2.25: NACA0012 lift coefficient function of the deflection

where δe is the rudder deflection.

The drag of the rudder is then studied. Since the sideslip of the aircraft remains low, the drag of the fin can be considered as constant. However, the drag increases due to the rudder deflection as shown in Figure 2.26 which enables to use it as airbrake.

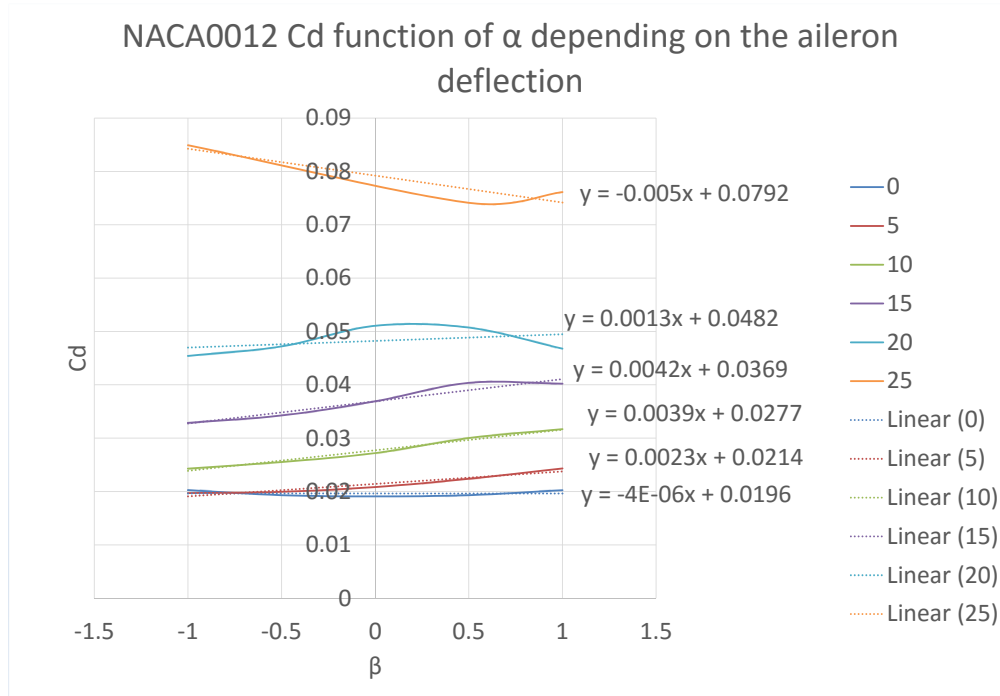


Figure 2.26: NACA0012 drag coefficient function of the angle of attack and the deflection

The drag coefficient is:

$$Cd = 0.0196 \quad (2.76)$$

Then the influence of the rudder deflection is shown in Figure 2.27. which gives the variation of the drag coefficient ΔCd

$$\Delta Cd = 9 \cdot 10^{-5} \delta e^2 \quad (2.77)$$

Lastly in the aircraft reference frame, the sideslip angle is assumed to be very low. Therefore the aerodynamic forces and moments generated by the fin i are:

$$F_{y_{VTPi}} = qS_{VTP}Cl \quad (2.78)$$

$$F_{x_{VTPi}} = qS_{VTP}Cd \quad (2.79)$$

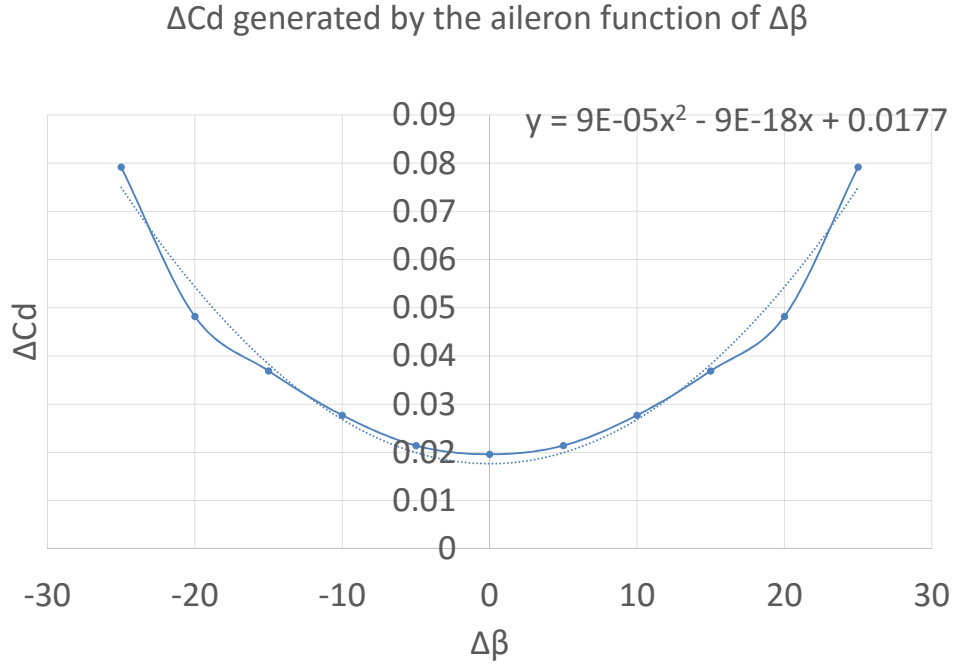


Figure 2.27: NACA0012 drag coefficient function of the deflection

In the same way forces and moments increments due to the rudder i are:

$$\Delta F_{y_{VTPi}} = qS_{section}\Delta C_{l_i} \quad (2.80)$$

$$\Delta F_{x_{VTPi}} = qS_{section}\Delta C_{d_i} \quad (2.81)$$

2.3 PARTIAL CONCLUSION

In this chapter, a dedicated theory of the rotor has been developed in section 2.1, page 53 to assess its behaviour in the very specific flight envelope it is likely to performs. In particular, it takes into account the aerodynamics specificities implied by the slowing down of the rotor rotation speed. The dynamics model of the whole aircraft has been then constructed, based on this new rotor forward flight theory, in section 2.2 page 64. If this construction relies on the methods developed for a classical aeroplane, it differs in the sense that the interactions between the different aerodynamics elements have been thoroughly taken into account. The dynamics model is now complete, the control analysis of such an aircraft can start.

3

CONTROL

The work presented so far is only provides the dynamics of the proposed aircraft. The control study remains to be done.

3.1 AIRCRAFT CONTROL TYPE

The dynamics of the aircraft during the transition has been precisely investigated in section 2.2, page 64. To assess the behaviour of the aircraft, a control of the aircraft in this flight phase is investigated. The design of the control law is based on what have been exposed in the literature for classical aircraft.

MANNED AIRCRAFT CONTROL An overwhelming majority of the control laws designed for manned aircraft are based on linear control theory. The required linear models are obtained by derivation of the aircraft dynamics equations as explained by Etkin [?] or Roskam [?]. Contrary to helicopter (cf. section 0.3.3.1, page 21), most of aeroplane control laws are designed for a single flight phase, and a gain scheduling strategies is only considered for highly valuable aircraft [?].

Latest researches in the field endeavour to apply nonlinear control laws to aircraft [?].

UAV CONTROL Similarly to manned aircraft, UAVs control laws have been first developed based on linear control theory [?]. In order to fulfil the need for increasing performances and reliability, nonlinear flight control techniques are currently developed [?]. Those techniques are mainly based on the nonlinear model which in the present case is far from being simple as it can be noticed in section 2.2, page 64. Furthermore, most of the proposed techniques are designed to make the aircraft control more robust to noise and aircraft model uncertainties.

On the contrary, the model of the present aircraft has been very well detailed in order to demonstrate its capacities for flight. The aim of the control is not to deal with any variation that could be encountered during a real experiment but more to demonstrate that a transition is possible.

In addition to that, the nonlinear model is already based on adjustment parameters in order to be as representative as possible (cf. section 2.1.2, page 58), and the wing is likely to stall or reattach during the transition which gives no choice but considering at least two distinct dynamics models (cf. section 2.2.4.2, page 75),. Therefore, the “gain scheduling” technique seems to be the most suitable one.

GAIN SCHEDULING Gain scheduling main idea consists in linearizing the flight dynamics equations for several flight phases. A specific control is designed for each linear model thus obtained. This methodology is not proper to aircraft control, and numerous variants exist [?]. Linear parameter-varying (LPV) control is naturally well adapted for aircraft control thanks to the linearization method employed. However, a LPV control is subjected to robustness issues. The widest used controls follow therefore the H_∞ technic [?].

3.2 CONTROL STUDY

The control design starts with the procurement of the linear model.

3.2.1 LINEAR MODEL

The linearization of the model equations presented in section 2, page 53, is presented in appendix C, page 187. These latter equations are numerically combined to provide a dynamics

equation of the form:

$$\dot{X}' = A'X' + B'U$$

where the state vector is defined as:

$$X' = \left(u \ v \ w \ p \ q \ r \ q_1 \ q_2 \ q_3 \ q_4 \ x \ y \ z \ \omega \right)^T$$

and the control vector as:

$$U = \left(\theta_0 \ \theta_{1c} \ \theta_{1s} \ F_0 \ F_{1c} \ F_{1s} \ a_1 \ a_2 \ a_3 \ a_4 \ r_1 \ r_2 \right)^T$$

Moreover, the output equation is defined as:

$$Y = C'X'$$

Before any control design, the controllability and observability of the system are studied.

3.2.2 CONTROLABILITY

The magnitude of matrix A and B parameters has first been reduced because of the critical size of the state vector (i.e. 14) which makes the results reach the computing precision limit.

The controllability matrix R is computed online:

$$Co = \left[B' \ A'B' \ \dots \ A'^{12}B' \ A'^{13}B' \right]$$

Equation (3.1) gives the number of states that are not controllable.

$$R = \text{lenght}(A') - \text{rank}(Co) \tag{3.1}$$

The result of the simulation gives: $R = 1$. In order to figure out why the system is not fully controllable, the same process is applied to modified model based on Euler angles *phi*, *theta* and *psi*. This model is constructed with equation (2.22) and its linear derivatives are computed with equation (C.4). The result is: $R = 0$ which proves the controllability of the Euler angles based model, however, this latter cannot be used for non-continuity issues as

itemized in section 2.2.2, page 64. The non-controllability of the quaternion based system is actually due to the fact that a quaternion is made of four states when there are only three degrees of freedom (i.e. pitch, yaw and roll). In order to solve this problem, the system is modified substituting the four states quaternion by its relative axis-angle vector. The angle vector is defined as [?]:

$$\vec{\theta} = 2 \cdot \ln(\vec{q})$$

Where, taking into account that the orientation quaternion of the model is normalized in line:

$$\ln(\vec{q}) = \begin{cases} \frac{\vec{Q}}{|\vec{Q}|} \arccos(q_0), & \text{if } |\vec{Q}| \neq 0 \\ 0, & \text{if } |\vec{Q}| = 0 \end{cases}$$

where q_0 is the scalar part of the quaternion and \vec{Q} is the vector part, following: $q = \begin{pmatrix} q_0 \\ \vec{Q} \end{pmatrix}$

The dynamics of the angle vector $\vec{\theta}$ is:

$$\begin{pmatrix} \dot{\theta}_1 \\ \dot{\theta}_2 \\ \dot{\theta}_3 \end{pmatrix} = \begin{pmatrix} p \\ q \\ r \end{pmatrix}$$

An improved model state is thus adopted based on the following state vector:

$$X = \left(u \ v \ w \ p \ q \ r \ \theta_1 \ \theta_2 \ \theta_3 \ x \ y \ z \ \xi \right)^T \quad (3.2)$$

Using the additional derivatives detailed in section C.2.3, page 208, a new linear model is obtained, of the form:

$$\dot{X} = AX + BU \quad (3.3)$$

with

$$Y = CX \quad (3.4)$$

Computing the new controllability matrix Co

$$Co = \left[B \ AB \ \dots \ A^{11}B \ A^{12}B \right]$$

Equation (3.1) gives: $R = 0$. All the state of X are controllable which proves the controllability of the system.

3.2.3 OBSERVABILITY

The concept is likely to be used only outdoor and is sufficiently bulky to accommodate any required sensor. The basic sensor set would be made up of:

- A 9 DoF IMU (gyroscope accelerometer magnetometer)
- A GPS
- 3 angular sensors on the rotor head: ψ , β_1c and β_1s
- 2 sets of pitot-tube/weathercocks: one fixed outside of the downwash and the other inside

On the first hand, this sensor set gives all the information required to compute matrices A and B of equation(3.3). On the other hand, it provides the following information:

- Linear speeds: u , v and w
- Angular speeds: p , q and r
- Attitude orientation: θ_1 , θ_2 and θ_3
- Position: x , y and z

Therefore matrix C of equation (3.4) is:

$$C = I_n$$

The observability matrix Ob being:

$$Ob = \begin{pmatrix} C \\ CA \\ \dots \\ CA^{12} \\ CA^{13} \end{pmatrix}$$

it leads to:

$$\text{rank}(Ob) \geq \text{rank}(C) = 13$$

The following equation gives the number of states that are not observable:

$$R = \text{lenght}(A) - \text{rank}(Co) \tag{3.5}$$

It appears that $R = 0$ which proves that the system is fully observable.

3.2.4 CONTROL DESIGN

The control law design can start. The aim of the proposed LPV system is to linearize in real time the simulated nonlinear dynamics in order to compute the control gains that must stabilise the latter throughout the transition which starts in hover and ends when the rotor is almost stopped.

However it has not been possible to do so because of Simulink compilation issues. Despite numerous attempts, it has indeed not been possible to inject successfully the computed matrix A and B in the gain computation process.

Therefore, it has been decided to study the behaviour of the aircraft in the different flight phases, separately.

3.2.4.1 HOVERING CONTROL

The linearization of the aircraft dynamics in hover is first performed providing the matrices A and B of equation(3.3), page 94:

$$A = \begin{pmatrix} -4.8395 & 0.0000 & 3.2193 & 0 & 1.3668 & -0.0000 & 3.9783 & -2.2587 & 3.9783 & 0 & 0 & 0 & 1.9993 \\ 0.0000 & -4.0876 & 0.0000 & -0.0013 & -0.0000 & 0.3849 & 6.2370 & 0.0000 & 6.2499 & 0 & 0 & 0 & 0.0000 \\ -0.4666 & 0 & -13.7844 & 0.0000 & -3.0174 & 0 & 1.7102 & -10.7897 & 1.7102 & 0 & 0 & 0 & 0.0107 \\ 0.0000 & -2.0636 & 0.0000 & -16.7217 & -0.0000 & 0.5675 & 0 & 0 & 0 & 0 & 0 & 0 & -0.0000 \\ -3.0582 & -0.0000 & -14.3214 & 0.0000 & -13.6041 & 0.0000 & 0 & 0 & 0 & 0 & 0 & 0 & 1.0001 \\ -0.0000 & 11.4506 & 0.0000 & -1.4415 & -0.0000 & -3.1489 & 0 & 0 & 0 & 0 & 0 & 0 & -0.0000 \\ 0 & 0 & 0 & 1.0000 & 0 & 0 & 0 & 0 & 0 & 0 & 0 & 0 & 0 \\ 0 & 0 & 0 & 0 & 1.0000 & 0 & 0 & 0 & 0 & 0 & 0 & 0 & 0 \\ 0 & 0 & 0 & 0 & 0 & 1.0000 & 0 & 0 & 0 & 0 & 0 & 0 & 0 \\ -0.0021 & -0.0000 & 1.0000 & 0 & 0 & 0 & 0.1294 & -0.8133 & 0.1294 & 0 & 0 & 0 & 0 \\ -0.0000 & 1.0000 & 0.0000 & 0 & 0 & 0 & 0.4718 & -0.0000 & 0.4691 & 0 & 0 & 0 & 0 \\ -1.0000 & -0.0000 & -0.0021 & 0 & 0 & 0 & 0.2995 & -0.1687 & 0.2995 & 0 & 0 & 0 & 0 \\ -46.0211 & 0 & -0.4999 & 0 & 0.3099 & 0 & 0 & 0 & 0 & 0 & 0 & 0 & -0.4506 \end{pmatrix} \quad (3.6)$$

$$B = \begin{pmatrix} 10.3723 & -0.0000 & -0.8948 & 0.1714 & -0.0000 & -0.0127 & 0.0854 & 0.2841 & 0.2841 & 0.0854 & -0.0895 & -0.0895 \\ -0.0000 & -3.0913 & 0.0000 & 0 & 0.2947 & 0.0000 & 0 & 0 & 0 & 0 & -0.5728 & -0.5728 \\ 0.0572 & 0 & -0.9180 & 0.0009 & 0 & 0.3219 & -0.5691 & -1.8945 & -1.8945 & -0.5691 & 0 & 0 \\ -0.0000 & -2.7884 & -0.0000 & 0 & 0.2353 & -0.0000 & -4.0320 & -5.6305 & 5.6305 & 4.0320 & -0.2892 & -0.2892 \\ 3.5255 & 0.0000 & 22.9518 & 0.0829 & 0.0000 & -1.1493 & -1.1847 & -4.0222 & -4.0222 & -1.1847 & 0.0354 & 0.0354 \\ 0.0000 & -28.6425 & -0.0000 & 0 & 1.8034 & -0.0000 & -0.3476 & -0.4854 & 0.4854 & 0.3476 & 1.6047 & 1.6047 \\ 0 & 0 & 0 & 0 & 0 & 0 & 0 & 0 & 0 & 0 & 0 & 0 \\ 0 & 0 & 0 & 0 & 0 & 0 & 0 & 0 & 0 & 0 & 0 & 0 \\ 0 & 0 & 0 & 0 & 0 & 0 & 0 & 0 & 0 & 0 & 0 & 0 \\ 0 & 0 & 0 & 0 & 0 & 0 & 0 & 0 & 0 & 0 & 0 & 0 \\ 0 & 0 & 0 & 0 & 0 & 0 & 0 & 0 & 0 & 0 & 0 & 0 \\ -23.5471 & 0 & -0.4460 & 8.2277 & 0 & -0.0056 & 0 & 0 & 0 & 0 & 0 & 0 \end{pmatrix} \quad (3.7)$$

The chosen control law is of the form:

$$U = -KX$$

The control gain matrix K is computed thanks to the pole placement method.

Though matrix A and B are of high amplitude, Simulink does not manage to compute the gain matrix. A problem analysis reveals that software reach its computation limits. The

pole placement technique takes advantage of the controllability matrix to compute the gain through the formula of Ackermann. The gain expression is [?]:

$$K = \begin{bmatrix} 0 & 0 & \dots & 0 & 1 \end{bmatrix} \begin{bmatrix} B & AB & \dots & A^{n-2}B & A^{n-1}B \end{bmatrix}^{-1} \phi(A)$$

where $\phi(A)$ is obtained from:

$$\phi(A) = A^n + \alpha_1 A^{n-1} + \dots + \alpha_{n-1} A + \alpha_n I$$

Since $\|A\| = 46.4$, the results of the equations are too high (i.e. $46.4^{13} = 4.62 \cdot 10^{21}$).

In order to solve this problem it has been decided to reduce the matrix A size removing the control of x and y of the state vector, by means of equation:

$$B' = R_{Simplification} B$$

and:

$$A' = R_{Simplification} A R_{Simplification}^T$$

where:

$$R_{Simplification} = \begin{pmatrix} 1 & 0 & 0 & 0 & 0 & 0 & 0 & 0 & 0 & 0 & 0 & 0 & 0 & 0 \\ 0 & 1 & 0 & 0 & 0 & 0 & 0 & 0 & 0 & 0 & 0 & 0 & 0 & 0 \\ 0 & 0 & 1 & 0 & 0 & 0 & 0 & 0 & 0 & 0 & 0 & 0 & 0 & 0 \\ 0 & 0 & 0 & 1 & 0 & 0 & 0 & 0 & 0 & 0 & 0 & 0 & 0 & 0 \\ 0 & 0 & 0 & 0 & 1 & 0 & 0 & 0 & 0 & 0 & 0 & 0 & 0 & 0 \\ 0 & 0 & 0 & 0 & 0 & 1 & 0 & 0 & 0 & 0 & 0 & 0 & 0 & 0 \\ 0 & 0 & 0 & 0 & 0 & 0 & 1 & 0 & 0 & 0 & 0 & 0 & 0 & 0 \\ 0 & 0 & 0 & 0 & 0 & 0 & 0 & 1 & 0 & 0 & 0 & 0 & 0 & 0 \\ 0 & 0 & 0 & 0 & 0 & 0 & 0 & 0 & 1 & 0 & 0 & 0 & 0 & 0 \\ 0 & 0 & 0 & 0 & 0 & 0 & 0 & 0 & 0 & 0 & 1 & 0 & 0 & 0 \\ 0 & 0 & 0 & 0 & 0 & 0 & 0 & 0 & 0 & 0 & 0 & 0 & 1 & 0 \\ 0 & 0 & 0 & 0 & 0 & 0 & 0 & 0 & 0 & 0 & 0 & 0 & 0 & 1 \end{pmatrix}$$

The control is designed to keep the flight height to zero. Therefore, the expected state vector

is fixed to:

$$X_{ref} = \begin{pmatrix} 0 \\ 0 \\ 0 \\ 0 \\ 0 \\ 0 \\ 0 \\ \frac{\pi}{2} \\ 0 \\ 0 \\ 82 \end{pmatrix}$$

The resulting trajectory is shown in Figure 5.6. It can be seen that if the X and Y positions

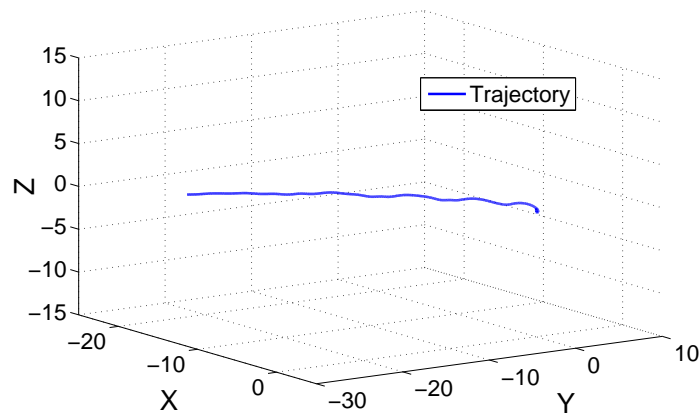


Figure 3.1: 3D trajectory

are not controlled, the Z position is well maintained to zero. The attitude angles are shown in Figure 3.2. It can be seen that if the control is slow to stabilise the attitude angles. However those latter converge eventually to their expected values.

Because of the varying angles, the control struggles to stabilise the velocities to zero as shown in Figure 3.3. Lastly, the control of the rotor rotation speed seems difficult as shown in Figure 3.4. This can be explained by the magnitude of parameter $B_{13,12} = -23.5$, of equation (3.7), page 97. Indeed θ_0 is the main control of velocity U since it is by far the

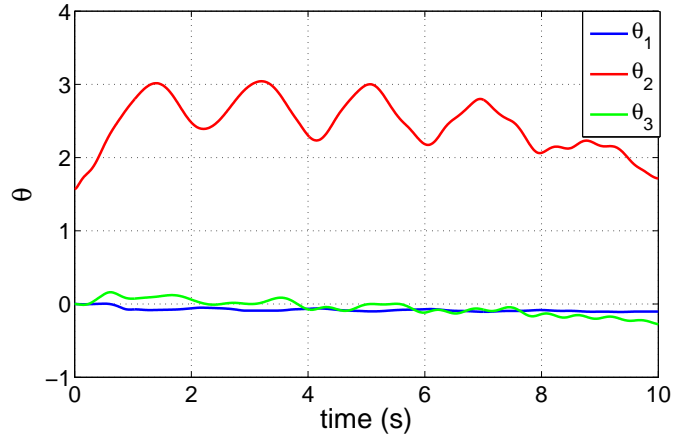


Figure 3.2: θ vs time

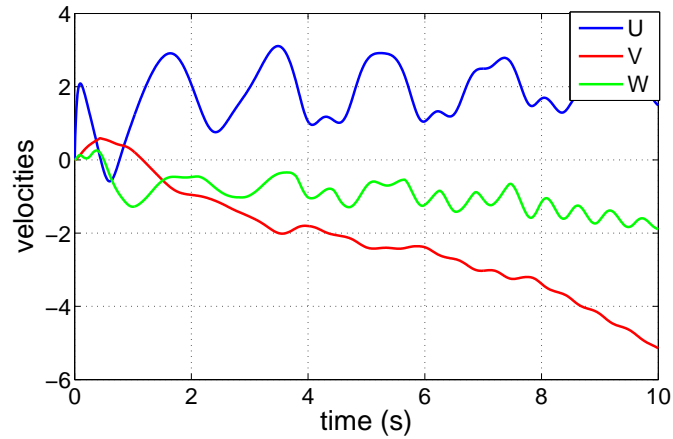


Figure 3.3: U , V and W vs time

highest parameter of equation (3.7) first line (cf. $B_{1,1} = 10.3723$), however, θ_0 has also a bigger impact on the rotor rotation speed ω than F_0 (cf. $B_{13,4} = 8.2$).

If the control manages to stabilise the aircraft altitude, it is not satisfactory as is, mainly because of high digital instability. Therefore, no control will be proposed for the following flight case.

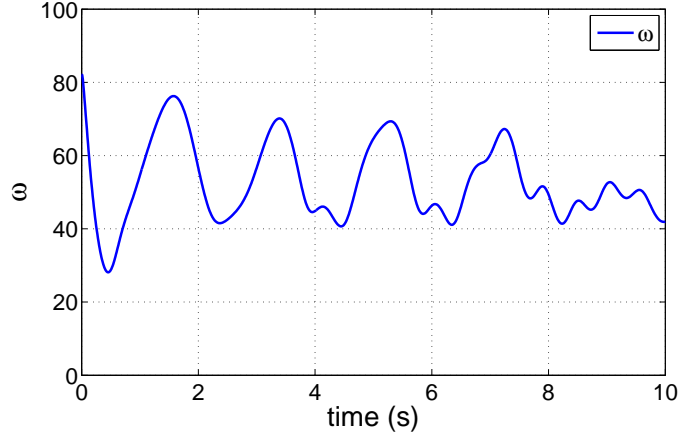


Figure 3.4: ω vs time

3.2.4.2 TRANSITION SPEED CONTROL

The dynamics is now linearized at transition longitudinal speed and hover rotor rotation speed velocity. The new matrices A and B are:

$$A = \begin{pmatrix} -4.9065 & 0.0000 & 3.7987 & 0.0000 & 1.2214 & -0.0000 & -0.0009 & -9.8109 & -0.0009 & 0 & 0 & 0 & 1.0486 \\ 0.0000 & -47.7229 & -0.0000 & 0.0378 & 0.0000 & -3.9030 & 9.8100 & 0.0000 & -0.0013 & 0 & 0 & 0 & 0.0000 \\ -0.3861 & 0 & -197.6208 & 0.0000 & -48.4727 & 0 & 0.0000 & 0.0026 & 0.0000 & 0 & 0 & 0 & -0.0014 \\ -0.0000 & -24.0923 & 0.0000 & -491.8016 & -0.0000 & 6.6254 & 0 & 0 & 0 & 0 & 0 & 0 & -0.0000 \\ -2.9197 & -0.0000 & -358.0479 & 0.0000 & -123.0467 & 0.0000 & 0 & 0 & 0 & 0 & 0 & 0 & 0.5341 \\ -0.0000 & 133.6865 & 0.0000 & -42.3967 & -0.0000 & -36.7638 & 0 & 0 & 0 & 0 & 0 & 0 & -0.0000 \\ 0 & 0 & 0 & 1.0000 & 0 & 0 & 0 & 0 & 0 & 0 & 0 & 0 & 0 \\ 0 & 0 & 0 & 0 & 1.0000 & 0 & 0 & 0 & 0 & 0 & 0 & 0 & 0 \\ 0 & 0 & 0 & 0 & 0 & 1.0000 & 0 & 0 & 0 & 0 & 0 & 0 & 0 \\ 1.0000 & 0.0000 & -0.0003 & 0 & 0 & 0 & 0.0000 & 0.0424 & 0.0000 & 0 & 0 & 0 & 0 \\ -0.0000 & 1.0000 & 0.0000 & 0 & 0 & 0 & -0.0401 & -0.0000 & 17.0268 & 0 & 0 & 0 & 0 \\ 0.0003 & -0.0000 & 1.0000 & 0 & 0 & 0 & -0.0015 & -17.0283 & -0.0015 & 0 & 0 & 0 & 0 \\ 47.4603 & 0 & -0.0821 & 0 & 0.0509 & 0 & 0 & 0 & 0 & 0 & 0 & 0 & -10.3549 \end{pmatrix} \quad (3.8)$$

and

$$B = \begin{pmatrix} 49.5584 & -0.0000 & -5.0954 & 0.1714 & -0.0000 & -0.0103 & 0.0201 & 0.0302 & 0.0302 & 0.0201 & -1.0452 & -1.0452 \\ -0.0000 & 52.5109 & -0.0000 & 0 & 0.4555 & -0.0000 & 0 & 0 & 0 & 0 & -6.6879 & -6.6879 \\ 0.9087 & 0 & 257.4579 & -0.0001 & 0 & 0.8770 & -14.8493 & -22.3556 & -22.3556 & -14.8493 & 0 & 0 \\ -0.0000 & 22.4719 & -0.0000 & 0 & 0.3278 & -0.0000 & -128.1539 & -66.4414 & 66.4414 & 128.1539 & -3.3763 & -3.3763 \\ 27.1167 & 0.0000 & 567.5225 & 0.0875 & 0.0000 & -0.3286 & -30.6543 & -47.4102 & -47.4102 & -30.6543 & 0.4137 & 0.4137 \\ 0.0000 & -269.7610 & 0.0000 & 0 & 1.6979 & 0.0000 & -11.0477 & -5.7277 & 5.7277 & 11.0477 & 18.7349 & 18.7349 \\ 0 & 0 & 0 & 0 & 0 & 0 & 0 & 0 & 0 & 0 & 0 & 0 \\ 0 & 0 & 0 & 0 & 0 & 0 & 0 & 0 & 0 & 0 & 0 & 0 \\ 0 & 0 & 0 & 0 & 0 & 0 & 0 & 0 & 0 & 0 & 0 & 0 \\ 0 & 0 & 0 & 0 & 0 & 0 & 0 & 0 & 0 & 0 & 0 & 0 \\ 0 & 0 & 0 & 0 & 0 & 0 & 0 & 0 & 0 & 0 & 0 & 0 \\ 0 & 0 & 0 & 0 & 0 & 0 & 0 & 0 & 0 & 0 & 0 & 0 \\ -458.5657 & 0 & -0.9453 & 8.2277 & 0 & -0.0019 & 0 & 0 & 0 & 0 & 0 & 0 \end{pmatrix} \quad (3.9)$$

All the parameters of the matrix A diagonal are negatives which ensure some stability.

It may be noticed that for state variable q , W has more influence than q (cf. $\|A_{5,3}\| > \|A_{5,5}\|$). This is because of the relative rear position of the main wing compared with the CG location. Nonetheless the influence of the control θ_{1s} is there very high which may ensure the control of the aircraft pitch angle.

In addition, for state variable r , V has much more influence than r (cf. $\|A_{6,2}\| > \|A_{6,6}\|$). This ensures symmetrical flight, which proves the satisfactory design of the rudders.

Lastly, for state variable ω , U has more influence than ω (cf. $\|A_{13,1}\| > \|A_{13,13}\|$). In addition, it seems that the most influent control of the rotor rotation speed is the blade pitch angle θ_0 which is also the main control of the state variable U . If it appears to be a major problem, one can notice that the amplitude of F_0 can be much higher than θ_0 one. The main control may thus be respectively F_0 for ω and θ_0 for U .

3.3 PARTIAL CONCLUSION

In this chapter, the dynamics model built in section 2, page 53, is modified to make the system controllable. To do so, the classical four variables quaternion representation is substituted by the reduced three angles quaternion representation. The controllability and the observability of the system is checked throughout the entire flight envelope (i.e. from hover flight to transition). A control is first proposed for hover flight. Because of the system size, this latter

is reduced removing the control of state variables x and y . This reduction brings some more instability to the behaviour that already suffers from digital instability. Lastly, the dynamics of the concept at transition speed is studied to assess its ability to fly. The concept appears to be flyable as long as a suitable solution is found for the digital instability issue due to the excessive state size.

4

CONCEPTUAL DESIGN

The study carried out until now focused on the fly ability of the concept. However, the doubt whether the drone would be competitive in its operational form remains. To clear it up, the performances of the drone are estimated in this chapter through a conceptual design approach. The idea consists in sizing a conventional aircraft by means of an optimisation process to maximise its performances, assessing its probable characteristics. The study is based mainly on the approach proposed by Raymer [?]. Nevertheless, the method suggested by other authors are also used to take into account the specificities of the concept.

4.1 BILL OF SPECIFICATIONS

The first step of a conceptual design is to fix the main specifications of the aircraft. In the present study, an analysis of the already operational competitors is used as a basis.

4.1.1 COMPETITORS ANALYSIS

The main specifications of the principal competitors on TUAV market are summarised in Table 4.9 (Some of the information comes from unreliable sources and are provided as guidelines only).

It can be seen that the specifications usually tend to increase over time:

-
- The payload mass seems to stabilise around 100 kg.
 - The required endurance has exceeded 9 hours.
 - The range distance depends much more on the transmission technology than on the UAV capability. Modern technologies allow a range of 200 km.
 - The operational ceiling seems to have stabilised at 6000 m.

These latter values are taken as rules for the design of the UAV. The maximum cruise speed is fixed to match or exceed the one defined as the objective for the Bell Eagle Eye VTOL UAV, that is to say around 150 kt [?].

Class		Aeroplane										Helicopter VTOL	
Specs		RQ-2 Pioneer	RQ-5 Hunter	RQ-7B Shadow 200	RQ-7 Shadow M2	Sperwer A	Sperwer B	Hermes 450	Falco	Falco	Falco EVO	Camcopter S-100	Camcopter Eye
Manufacturer		AAI	AAI	AAI	AAI	SAGEM	SAGEM	Elbit Systems	Selex ES	Selex ES	Selex ES	Schiebel	Bell Helicopter
Introduction	1986	1995	2002	2014	2005	2007	1998	2009	2011	2005	2005	2005	Canceled
Take-off	Classic / JATO	Classic / JATO	Classic / Catabult	Classic / Catabult	Classic / Catabult	Catapult	Classic	Classic / Catabult	Classic / Catabult	Classic / Catabult	Classic / Catabult	vtol	Classic / Vtol
Landing	Classic / Tail-hook	Classic	Classic / Tail-hook	Classic / Tail-hook	Classic / Tail-hook	Parachute + Airbag	Classic / Tail-hook	Classic	Classic	Classic	Classic	vtol	Classic / Vtol
Length	4 m	7 m	3.7 m	3.7 m	3.7 m	3.5 m	6.1 m	5.25 m	6.2 m	6.2 m	3.1 m	3.1 m	5.46 m
Wingspan	5.2 m	8.9 m	6.2 m	7.6 m	4.2 m	6.8 m	10.5 m	7.2 m	12.5 m	12.5 m	N/A	N/A	4.63 m
Rotor ϕ	N/A	N/A	N/A	N/A	N/A	N/A	N/A	N/A	N/A	N/A	N/A	3.4 m	2.9 m
Height	1 m	1.7 m	1 m	1 m	1.3 m	1.3 m	?	1.8 m	2.5 m	2.5 m	1.1 m	1.1 m	1.73 m
Empty W	?	?	84 kg	?	275 kg	275 kg	?	?	?	?	97 kg	97 kg	590 kg
Gross W	205 kg	727 kg	212 kg	266 kg	330 kg	350 kg	550 kg	420 kg	650 kg	650 kg	200 kg	200 kg	1200 kg
Payload	?	90 kg	27kg	36 kg	50 kg	100 kg	180 kg	70 kg	100 kg	100 kg	50 kg	50 kg	95 kg
Power	28.3 kW	2x45 kW	28 kW	47 kW	48 kW	48 kW	39 kW	49 kW	49 kW	49 kW	40 kW	40 kW	478 kW
Max speed	200 km/h	204 km/h	250 km/h	220 km/h	240 km/h	240 km/h	176 km/h	216 km/h	216 km/h	216 km/h	222 km/h	222 km/h	370 km/h
Stall speed	?	?	111 km/h	?	130 km/h	?	?	130 km/h	130 km/h	130 km/h	0 km/h	0 km/h	0 km/h
Cruise speed	?	?	148 km/h	?	166 km/h	?	130 km/h	?	?	?	101 km/h	101 km/h	?
Range	185 km	260 km	109 km	125 km	180 km	200 km	300 km	200 km	200 km	200 km	180 km	180 km	?
Endurance	5 h	11.6 h	9 h	16 h	6h	12h	17 h	8-14 h	18 h	18 h	6h (25kg)	6h (25kg)	6 h
S. ceiling	4575 m	4600 m	4572 m	?	4572 m	6096 m	5486 m	5000 m	6000 m	6000 m	5486 m	5486 m	6096 m
Source	?	?	[?]	[?], [?]	[?]	?	[?]	[?]	[?]	[?]	[?]	[?]	[?]

Table 4.1: Competitors specification

4.1.2 PAYLOAD

The payload mass is then estimated. The payload of a TUAV includes in general, the embedded set of sensors, the external features and aircraft avionics ([?]; ch. 2.2).

Sensor turret: The sensor turret is a gyro-stabilized platform adjustable to orientate the devices it contains in the desired direction. The main specifications of the first sensors turrets mounted on TUAVs are summarised in Table 4.2.

Name	CoMPASS	Star SAFIRE HD	MX-10	MX-15	EUROFLIR 410
Maker	Elbit Systems	Flir	WESCAM	WESCAM	SAGEM
Picture					
Diameter	38.1 cm	38 cm	26 cm	39.4 cm	?
Power	?	200W (650W max)	112W (280W max)	280W (900W max)	?
Weight	38 Kg	45kg	17 Kg	45.4 kg	45 kg
Sensors	Day Channel (HD) Thermal Imager Rangefinder Designator	COLOR CAMERA (HD) Thermal Imager LOW-LIGHT CAMERA (HD) Rangefinder Illuminator Pointer	COLOR CAMERA (Zoom) Thermal Imager LOW-LIGHT CAMERA (Zoom) Rangefinder 2 x Illuminator	COLOR CAMERA (HD) (Zoom) COLOR Spotter (HD) Thermal Imager LOW-LIGHT CAMERA Rangefinder Illuminator	Day Channel (HD) / LLTV Thermal Imager Spotter Pointer Designator
Source	[?]	[?]	[?]	[?]	[?]

Table 4.2: Sensor turrets specifications

It can be seen that a provision of 45 kg is sufficient for the sensor turret weight, and 900 W for its power consumption. Furthermore, the diameter of the sensor turret is assumed to be $0.4m$ for the drag estimation.

Radar: The main specifications of the principal radars mounted on TUAVs are summarized in Table 4.3. A provision of 10 kg is adopted for the sensor turret weight with 300 W



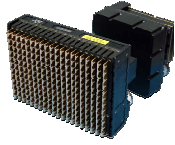
Name	ELM-2054	NanoSAR B	PicoSAR
Maker	IAI ELTA	IMSAR	Selex ES
Picture			
Consumption	250 W	30 W	300W
Weight	12 Kg	1.6 Kg	10 Kg
Type	SAR/GMTI	SAR	SAR/GMTI
Source	[?]	[?]	[?]

Table 4.3: Radar specifications

for its power consumption.

Pods: All TUAVs present in Table 4.9 which were introduced after 2005, are capable of embarking an additional modular payload. Usually, this payload is installed in the fuselage or under wing pods. The most adopted configuration consists of 2 pods with one under each wing. This pod capacity allows the embarking of several additional devices:

- Additional systems
- Weapons
- Dropable payload
- Fuel tank

It seems that 30kg of additional payloads is a good average of what is done by the competitors. A provision of 15 kg under each pod is therefore added (this payload would also be accommodated in the fuselage if required)

Avionic: It is quite difficult to estimate the mass of the avionic. There is indeed no such value in the scientific literature. However the avionic of a UAV is mainly composed of

an inboard computer and transmission system. The main specifications of the principal transmission systems mounted on TUAVs are summarized in Table 4.4. A provision




Name	AN/ARC-210	LMAR	MMAR
Maker	Rockwell Collins	Thales Communications	Thales Communications
Picture			
Consumption	200 W (TX)	50 W	?
Weight	5.53 Kg	1.45 kg	3.35 kg
Modes	AM/FM SINCGARS SATCOM Have Quick I & II	AM/FM ave Quick I & II	AM/FM SINCGARS SATCOM Have Quick I & II ANDVT
Application	MQ-1 Predator RQ-4 Global Hawk MQ-9 Reaper IAI RQ-5 Hunter	Watchkeeper WK450	TUAV
Source	[?]	[?]	[?]

Table 4.4: Radio specifications

of 200 W and 5 kg is sufficient. The inboard computer is very probably built with off the shelves civil components such as PC/104 family of embedded computer standards. Therefore, a power consumption of 500 W and a mass of 5 kg seem credible (upper bound values for commercial computers). The conservativeness of these latter assumptions can be checked thanks to a particular example: the Boeing Insitu ScanEagle [?]. Its payload weighs 3.4 kg which implies that its inboard computer weight is well under 5 kg. In addition to that, the electrical power provision for the payload is of 60 W, which is well beyond the 500 W assumed [?].

Requirements regarding weight and consumption can be therefore established to 95kg and 1.9kW. However, a provision of 5% is added in anticipation for future weight growth as

advised by Raymer ([?]; ch. 15.4). In addition to that some required payload power values of equivalent UAVs are available:

- The Hermes 450 TUAV has a electrical power provision of 1.6 kW for its payload [?].
- The AAI RQ-7 Shadow 200 TUAV has a electrical power provision of 2 kW [?].

Thereby, the payload requirement is fixed to:

$$W_{payload} = 100kg$$

$$P_{payload} = 2kW$$

Furthermore, the drag induced by the payload is assumed to be only due to the sensor turret: a sphere of 40cm of diameter.

4.1.3 ENDURANCE

The endurance is going to be maximised as much as possible. As seen in Table 4.9, page132, the endurance should be higher than 9 hours to match the competitors. Nevertheless, the VTOL capacity of the present TUAV should allow it to be operated much closer to the area of interest than the others, and therefore economise the transit duration.

4.1.4 ALTITUDE

As seen in Table 4.9, page132, a service ceiling of 6000 m seems to be reasonable in aeroplane mode. In helicopter mode, two new ceilings must be defined:

- In Ground Effect (IGE) Hover Ceiling is the maximum altitude reachable when the downwash of air from the main rotor reacts with a hard surface generating a useful reaction to the helicopter which decreases the required power. This limitation is evaluated at full power. It defines the maximum altitude where the TUAV can take-off in helicopter mode. For safety reasons, the UAV is likely to hover at a height from the ground of at least half its length.

-
- Out of Ground Effect (OGE), Hover Ceiling is the maximum altitude reachable in clean air in opposition to the above definition. This limitation will be evaluated at full power. According to the performances of similar size helicopters, such as the Heli-Sport CH-7, the OGE is fixed at 2500 m [?].

An ultimate altitude may be defined: the loiter altitude. It is not strictly speaking a performance as the latter tree but will be needed during the optimisation process. According to the CONOPS ([?], ch. 3.2.1) the nominal operating/survivable height ranges between 8,000 and 10,000 feet Above Ground Level (AGL), that is to say around 3000m. This latter value is added to the average terrestrial altitude of 840m [?] to fix the loiter height of the present study.

4.1.5 CLIMB PERFORMANCES

In helicopter mode, another performance criterion is the climb speed achievable in helicopter mode. A typical value for small helicopters is $180ft.min^{-1}$. That is to say $1m.s^{-1}$. Without further specification, this value will be considered for the present aircraft.

4.1.6 SPEEDS

As seen in Table 4.9, page132, the minimum required maximum cruising speed is fixed at 150 kt (i.e. $75m.s^{-1}$). The loiter (observation) speed should be around $160km/h$ (i.e. $45m.s^{-1}$), to match the competitors. Nevertheless, this speed will be optimised to maximise the endurance of the drone and should be at least 1.1 times the stalling speed for security concerns. The same security constraint applies for the transition speed between helicopter and aeroplane flights, being, however, a much more aerobatic manoeuvre, the margin of safety is increased to 1.3 times the stalling speed for the transition.

4.2 GEOMETRY

The proposed concept has been generally exposed in section 0.2, page 11. However, some precisions of the geometry are required to estimate its characteristics.

4.2.1 LANDING GEAR DESIGN

To ensure the stability of the aircraft on the ground, the wheelbase of its landing gear must respect some rules. Roskam exposed the design rules for aeroplanes ([?];PART II Chapter 9). It seems that the same standards can be applied on helicopters as shown in a thesis of the US NAVAL SCHOOL [?].As seen in section 4.2.1, page 113, the aircraft must be able to land whatever its slope angle from vertical to horizontal. Those two extreme positions are therefore analysed to ensure safety in all possible situation.

vertical position The angle formed between the ground plane and the CG around a rotation axis of the aircraft should never be smaller than 55° as shown in Figure 4.1.

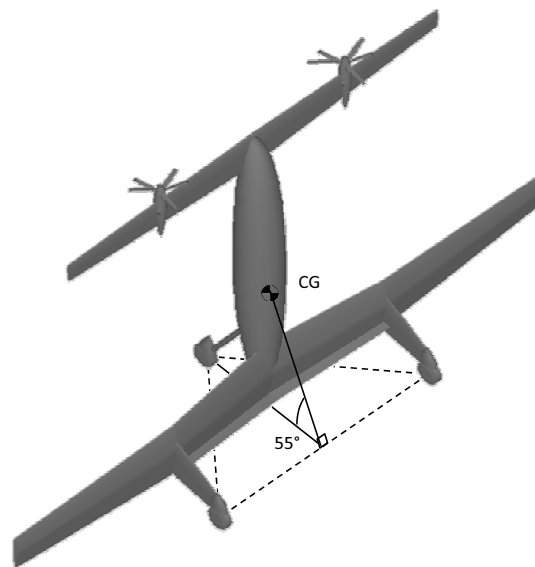


Figure 4.1: Aft landing gear design rule

However, Raymer [?] fixes this same angle limits at 63° and 54° for respectively classical and carrier-based aircrafts ([?]; ch. 11.2). It seems that 54° is quite conservative since the UAV is not likely to suffer ground loop. This angle is therefore adjusted between 54° and 63° depending on other design criteria. In order to fully respect the ground stability conditions, the landing gears are designed so that the wheels on the ground form an equilateral triangle centred around the CG location as presented in Figure 4.2.

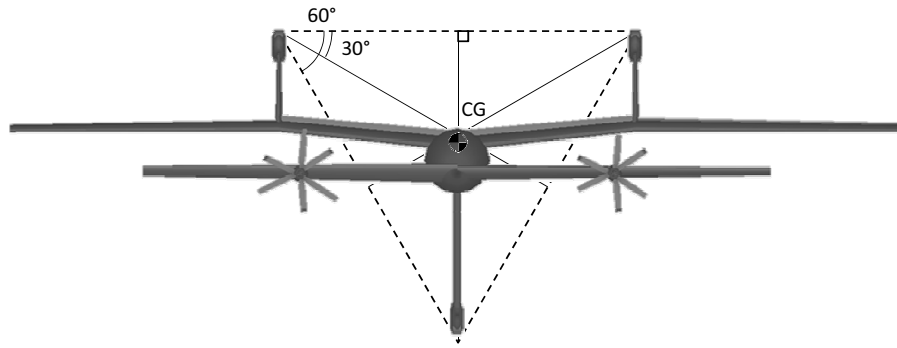


Figure 4.2: Landing gear ground stability condition

Horizontal position The front landing gear is now positioned. According to Raymer ([?]; ch. 11.2), the distance between the front wheel and the CG should be at least as great as the one between the CG and the rear landing gear. Because of the extreme rear position of the main landing gear, it is decided to place the front one at its rearmost acceptable position. That is to say to have the CG right halfway between main and rear landing gears. The aircraft being symmetric, only the left angle requirement is shown in Figure 4.3:

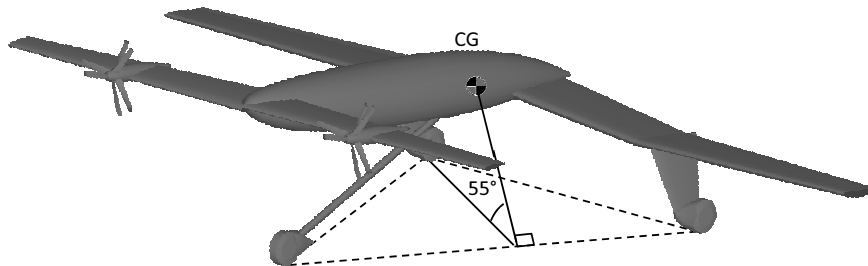


Figure 4.3: Landing gear aeroplane condition

4.2.2 AIRFOIL

4.2.2.1 FORE PLANE AIRFOIL

Helicopter rotor blades have a much higher aspect ratio than aeroplane wings which decrease their torsional stiffness. Therefore, aerofoil with very low pitching moment coefficient has to be used. With this in mind, in the early days of helicopters, the rotor blades were initially

designed using non-cambered aerofoils. The first attempt to use cambered aerofoil takes place on Juan de la Cierva autogyro. But it resulted in a crash in 1939. Progress didn't happen before the 60's, 70's with the new development of reflex aerofoils, which are now widely used . However, for the present design, the retreating blade works upside down in aeroplane mode. Therefore, a symmetric aerofoil is adopted to preserve the whole aircraft symmetry. Two aerofoils have been considered.

- NACA 0012: This aerofoil has been almost systematically used for the blades mounted on helicopters designed before the apparition of reflex airfoils.
- NASA SC(2)-0012: This aerofoil is the latest attempt to improve the NACA 0012 aerofoil characteristics maximising its the laminar flow.

The aerofoil of the fore plane of the actual design is likely to work at low Reynolds number in aeroplane mode. The laminar aerofoils, like the latest NASA SC(2)-0012, are designed to overpass performances of traditional aerofoils, such as the NACA 0012, at high Reynolds number but usually reveals worse at low Reynolds number. In aircraft mode, the fore plane is likely to encounter Reynolds numbers varying between 2×10^5 and 8.5×10^5 and a Mach number of 0.24. Therefore a XFOil simulation of the two aerofoils performed and the results are shown in Figure 4.4.

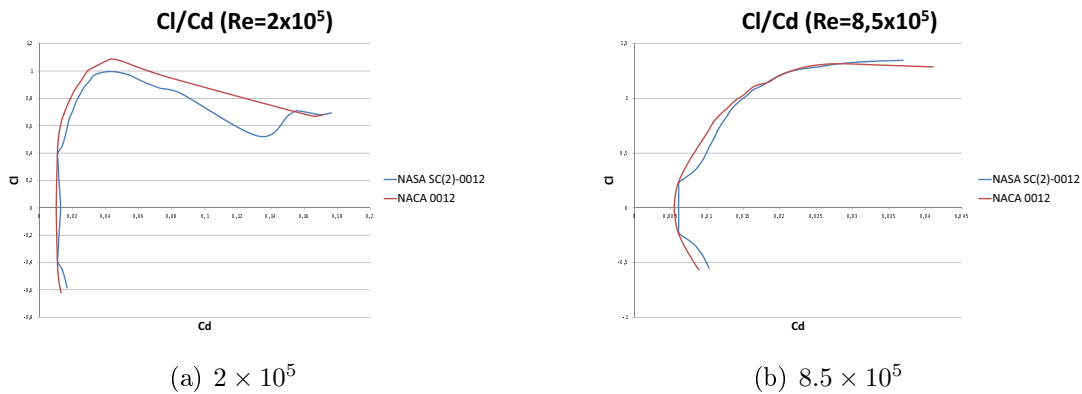


Figure 4.4: Foreplane airfoil comparison

It can be seen that because of the relative small Reynolds number, the classical turbulent NACA 0012 is better than the laminar NASA SC(2)-0012 on the entire range of expected Reynolds number.

Another Xfoil simulation, shown in Figure 4.5, is done to compare the two aerofoils in helicopter mode where they are likely to fly at a classical tip Mach number of 0.7 [?] which corresponds to a Reynolds number of 3×10^6 .

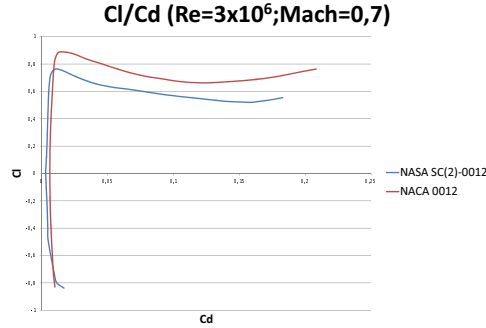


Figure 4.5: Foreplane airfoil comparison

The laminar NASA SC(2)-0012 generates a bit less drag than the NACA 0012. However, this drag diminution is too tiny and would only be present at the tip of the blade in helicopter mode. The NACA 0012 is therefore adopted as foreplane aerofoil. With the optimisation process in mind, the aerofoil characteristics are modelled for 3 Reynolds: $2 \cdot 10^5$, $8.5 \cdot 10^5$ and $8.5 \cdot 10^6$ using Xfoil, to cover the entire flight envelope. The results are presented in Table 4.5.

NACA 0012				
Blade airfoil thickness	t	12%		
Reynolds		$2 \cdot 10^5$	$8.5 \cdot 10^5$	$8.5 \cdot 10^6$
Max lift coeficient	Cl_{max}	1,088	1,317	1,466
Zero moment coeficient	Cm_0	-0,0205	0,00586	0,00544
Lift curve slope	a	6,480	6,36	6,366
zero angle lift	Cl_0	0	0	0
Zero angle drag	Cd_0	0,01	0,0053	0,0053
Angle drag component	K_{Cd}	0,657	0,364	0,271

Table 4.5: NACA 0012 characteristics

The characteristics of the aerofoil at a given Reynolds are estimated by linear interpolation.

4.2.2.2 MAIN WING AIRFOIL

The aircraft is likely to spend most of its flight loitering, trying to maximise its flying time on the spot, and therefore flying at relatively low speed. The Reynolds numbers in those conditions are quite the same as the ones encountered on sailplanes. A particularity of tandem wing configuration consists in that the fore plane is the most loaded lifting surface for stability reasons. A low pitching moment aerofoil is therefore required. New gigantic very high performances sailplanes present extremely high aspect ratios wings that make them suffering the same issues as rotorcraft blades, as discussed in section 4.2.2.1, page 115. Very little pitch moment, very high-performance reflex aerofoils have thus been developed, such as the first-rate Althaus family:

- AH 81-131
- AH-93-131

The expected Reynolds number is expected to range between 5×10^5 and 2.25×10^6 . Comparisons of the two aerofoils, simulated with Xfoil for both Reynolds in incompressible conditions, are shown in Figure 4.6.

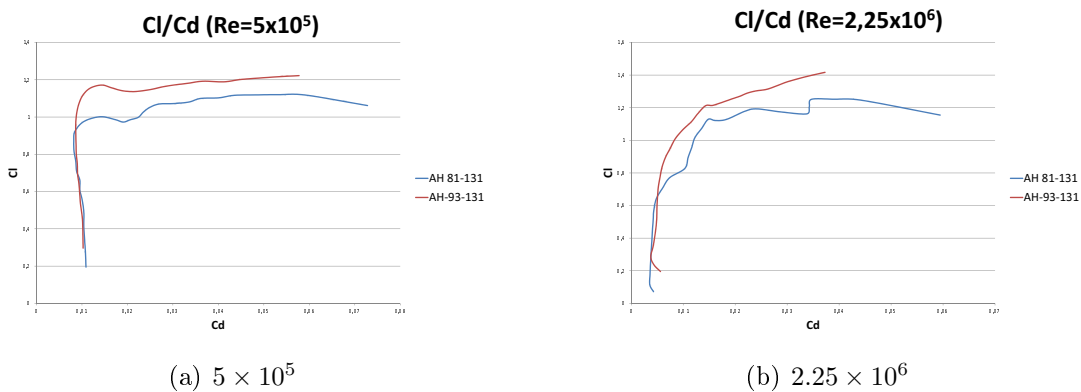


Figure 4.6: Foreplane airfoil comparison

For a given lift coefficient, the AH-93-131 aerofoil drags less than the AH 81-131. The pitching moment coefficient at 25% of the chord of the AH-93-131 aerofoil is $Cm_{0(AH-93-131)} = -0.0077$ while it is $Cm_{0(AH-81-131)} = 0.02325$ for the AH 81-131. The AH-93-131 is adopted as main wing aerofoil.

As for the fore plane aerofoil, the main wing aerofoil characteristics are modelled at three Reynolds numbers, based on Xfoil simulations: $5 \cdot 10^5$, $2 \cdot 10^6$ and $4 \cdot 10^6$, as summarised in Table 4.6.

AH-93-131				
Blade airfoil thickness	t	13.1%		
Reynolds		$5 \cdot 10^5$	$2 \cdot 10^6$	$4 \cdot 10^6$
Max lift coefficient	Cl_{max}	1,184	1,225	1,341
Zero moment coefficient	Cm_0	-0,0613	-0,00442	-0,00772
Lift curve slope	a	6,033	7,2	6,67
zero angle lift	Cl_0	0,38	0,191	0,204
Zero angle drag	Cd_0	0,00922	0,00502	0,004
Angle drag component	K_{Cd}	0	0,443	0,391

Table 4.6: AH-93-131 characteristics

The characteristics of the aerofoil at a given Reynolds are once again estimated by linear interpolation.

4.2.2.3 FIN AIRFOIL

The fin aerofoil must be symmetric and generate as low drag as possible. Because of its relatively short span and the low relative speed it withstands, it is likely to encounter low Reynolds numbers. Therefore, according to the comparison performed in section 4.2.2.1, page 114, the NACA 0012 is adopted.

4.2.3 FUSELAGE

To reduce as much as possible the drag due to fuselage the laminar flow part is maximised. A body of revolution based on an extended laminar flow aerofoil offers good characteristics[?]. NACA 7-series aerofoils family was the ultimate NACA advancement in maximising laminar flow achieved by separately identifying the low-pressure zones on upper and lower surfaces of the aerofoil. Based on competitor TUAVs, the fuselage dimensions are fixed to 0.5m in diameter and 3.5m in length, which gives a thickness to length ratio of 14%.

The NACA 07-014 is chosen as a basis for the fuselage. Its maximum thickness is at 50% of its chord. Therefore, according to Hoerner, the laminar flow is likely to take place over a bit more than the first half of the fuselage ([?]; ch. II 7.). This aerofoil being symmetric,

it corresponds, as is, to fuselage top view. To shift the two lifting surfaces and therefore reduce their induced drag, the aerofoil defining fuselage side view is curved. Nevertheless, this curvature should be limited, on the first hand, to conserve the laminar flow and on the other hand to accommodate the rotor head systems within the fuselage nose. Therefore, the first half of the fuselage is defined by the aerofoil NACA 07-514, and an inverted NACA 07-514 defines the second one. A three-views plan is presented in Figure 4.7.

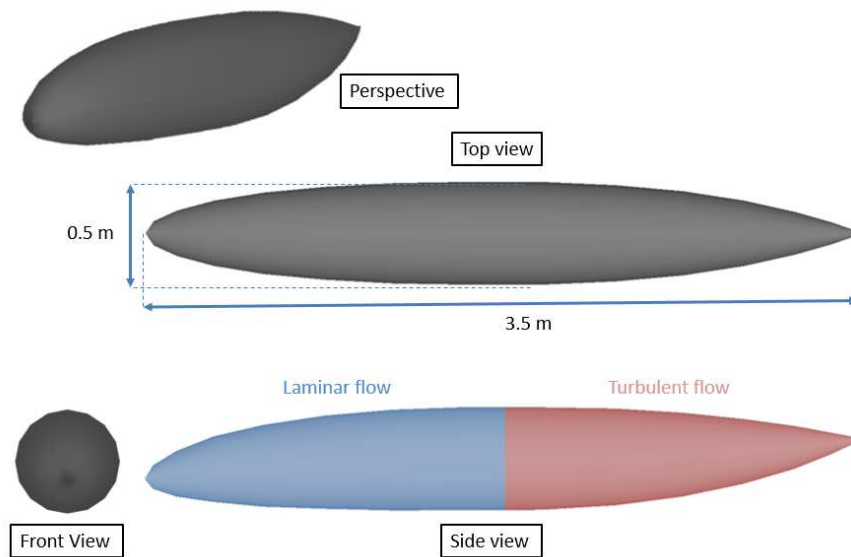


Figure 4.7: 3 view plan of the fuselage

4.2.4 ELECTRIC MOTOR NACELLES

The nacelle has two purposes. On the first hand, it streamlines the outer shape to decrease the drag. On the other hand, it provides fresh air to cool the engines. Contrary to a traditional aircraft, the cooling nacelles are not likely to work at slow airspeed since they turn continuously at a relatively high airspeed whether it is in helicopter or aeroplane modes. A so called "low drag cowling" can thus be used. The design of the outer shape of the nacelle follows the philosophy of the NACA E-type cowling as presented by John V. Becker [?]: it consists in a common aerofoil shape sectioned at the nose and rear location to let the air pass through. A sketch of the nacelle is presented in Figure 4.8.

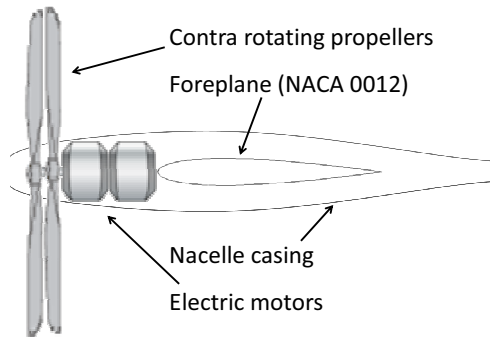


Figure 4.8: Nacelle design

The forward propellers are likely to alter the air flow to turbulent over the nacelle surface. However, it seems to be advantageous to use an extended laminar shape to limit the expansion of the turbulent sickness and then to limit the drag. A laminar body is obtainable by revolting a symmetric NLF aerofoil [?], and the cylindrical like obtained shape would accommodate perfectly an electric motor. That is why an investigation of several NLF aerofoils of the NACA 6-series is carried out. It seems that the NACA 65 has the lowest drag coefficient for a thickness of around 15%. This aerofoil is the starting-point of the nacelle design. Depending on the motor length and width, the external shape of the nacelles is adjusted as close as possible to reduce their length, and consequently their moment of inertia to ensure a proper pitch control.

4.3 MISSION

A typical mission must be designed before optimising the specifications of the UAV. It consists of twelve steps exposed in Figure 4.9.

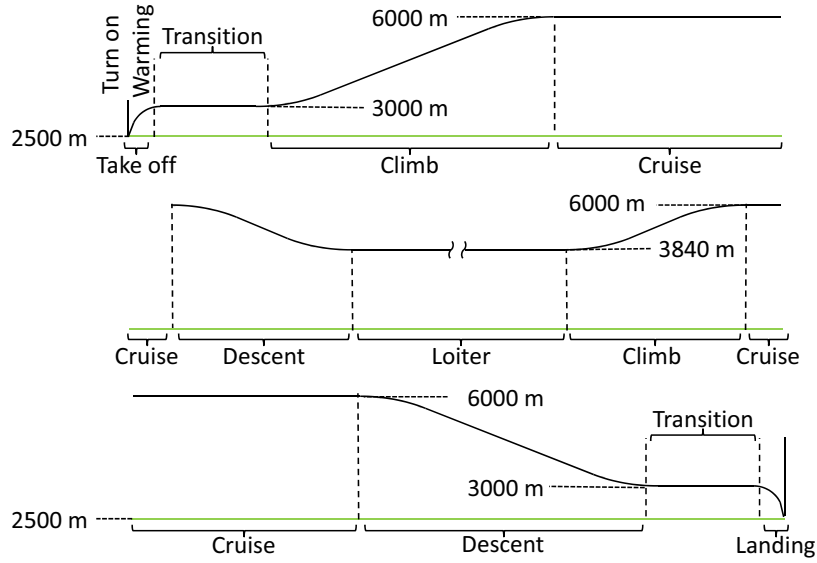


Figure 4.9: mission

The model of each step, followed by an integration of the entire mission, gives a good assessment of aircraft performances during classical operation.

Turn on / warming: It consists of letting the engine warm up after being turned on.

- Main engine fuel flow: $FC_{Main\ engine\ Turn\ on\ Warming} \approx 500\ g.h^{-1}$ (Arbitrary value, the true value depending too much on the engine model).
- Boost engine fuel flow: $FC_{Boost\ engine\ Turn\ on\ Warming} = 0\ g.h^{-1}$ (Assumed to be warmed by the main engine).
- Duration: $T_{Turn\ on\ Warming} \approx 2\ minutes$ (Conventional value in light aviation).
- Fuel consumed:

$$F_{Turn\ on\ Warming} = T_{Turn\ on\ Warming} \left(FC_{Main\ engine\ Turn\ on\ Warming} + FC_{Boost\ engine\ Turn\ on\ Warming} \right)$$

Take-off: • Altitude: Take off is done at OGE (The power is the largest when the aircraft is not moving, that is to say almost on the ground, then in translation, the power decreases).

-
- Required power: $P_{Take-off} = P_{hover}$ (cf. section D.5.1, page244).
 - Main engine power: $P_{Main\ engine\ Take-off} = P_{Main\ engine\ Max}$
 - Main engine fuel flow: $FC_{Main\ engine\ Take-off} = SFC_{Main\ engine} \cdot P_{Main\ engine\ Take-off}$
 - Boost engine power: $P_{Boost\ engine\ Take-off} = P_{Take-off} - P_{Main\ engine\ Take-off}$
 - Boost engine fuel flow: $FC_{Boost\ engine\ Take-off} = SFC_{Boost\ engine} \cdot P_{Boost\ engine\ Take-off}$
 - Duration: $T_{Take-off} \approx 2.5\ minutes$ (Conventional value in light aviation).
 - Fuel consumed:

$$F_{Take-off} = T_{Take-off} \left(FC_{Main\ engine\ Take-off} + FC_{Boost\ engine\ Take-off} \right)$$

Transition: • Altitude: The transition is done in level flight at OGI altitude.

- Required power: $P_{Transition}$ (cf. section D.5.5, page248)
- Main engine power: $P_{Main\ engine\ Transition} = P_{Main\ engine\ Max}$
- Main engine fuel flow: $FC_{Main\ engine\ Transition} = SFC_{Main\ engine} \cdot P_{Main\ engine\ Transition}$
- Boost engine power: $P_{Boost\ engine\ Transition} = P_{Transition} - P_{Main\ engine\ Transition}$
- Boost engine fuel flow: $FC_{Boost\ engine\ Transition} = SFC_{Boost\ engine} \cdot P_{Boost\ engine\ Transition}$
- Duration: $T_{Transition} \approx 2.5\ minutes$ (Value taken arbitrarily).
- Fuel consumed:

$$F_{Transition} = T_{Transition} \left(FC_{Main\ engine\ Transition} + FC_{Boost\ engine\ Transition} \right)$$

- Horizontal speed: $V_{Transition}$ (section D.5.5, page248)
- Travelled distance: $R_{transition} = V_{transition} \times T_{transition}$

Climb: • Altitude: During the first climb, $h_{Climb} = \frac{h_{Transition} + h_{Service\ ceiling}}{2}$ During the second climb: $h_{Climb} = \frac{h_{Loiter} + h_{Service\ ceiling}}{2}$

- Required power: $P_{Climb} = P_{hover}$ (cf. section D.5.2, page245)
- Main engine power: $P_{Main\ engine\ Climb} = P_{Main\ engine\ Max}$
- Main engine fuel flow: $FC_{Main\ engine\ Climb} = SFC_{Main\ engine} \cdot P_{Main\ engine\ Climb}$
- Boost engine power: $P_{Boost\ engine\ Climb} = P_{Take-off} - P_{Main\ engine\ Climb}$
- Boost engine fuel flow: $FC_{Boost\ engine\ Climb} = SFC_{Boost\ engine} \cdot P_{Boost\ engine\ Climb}$
- Horizontal speed: $V_{Climb} = V_{Loiter}$ (section D.5.6, page249, according to Raymer ([?], ch. 17.3), the maximum rate climb is achieved at the minimum power speed).
- Vertical speed: $V_{vertical\ Climb} = \frac{(P_{Climb} - P_{electrical}) \cdot \eta_{propulsion}}{M \cdot g} - \frac{D \cdot V_{climb}}{M \cdot g}$ ([?], eq.17.42)
Where $\eta_{propulsion}$ is the propulsion efficiency ($\eta_{propulsion} = \eta_{propeller} \cdot \eta_{electric\ motor}$), M is the aircraft mass (in kg), g is the gravitational constant (in $m \cdot s^{-2}$), D is the aircraft drag (in N) and V is the aircraft speed. $\eta_{propeller} = 0.8$
- Duration: $T_{climb} = \frac{h_{final} - h_{initial}}{V_{vertical}}$ where h_{final} and $h_{initial}$ are respectively the final and initial altitude (in m)
- Fuel consumed:

$$F_{Climb} = T_{Climb} \cdot (FC_{Main\ engine\ Climb} + FC_{Boost\ engine\ Climb})$$

- Travelled distance: $R_{climb} = V_{climb} \times T_{climb}$

Cruise: This step takes place when the aircraft is at 11 000 ft. The SFC at this regime is of about 194 g/kWhr. The distance travelled during the cruise is computed considering:

- Altitude: $h_{Service\ ceiling}$
- Horizontal speed: $V_{Cruise} = V_{Max\ speed}$ (section D.5.7, page251)

-
- Required power: $P_{Cruise} = \frac{V_{Cruise} \cdot D_{Cruise}}{\eta_{propulsion}} + P_{electrical}$, where D_{Cruise} is the drag in cruise. This latter is estimated as:

$$D_{Cruise} = \frac{1}{2} \rho \cdot V_{Cruise}^2 \cdot S (Cd_0 + Cd_i)$$

- Cd_0 is estimated as in section D.5.7, page251
- $Cd_i = K \cdot Cl^2$ ([?]; eq. 12.4). It is assumed that, the flight condition being close to the one of section D.5.7, page251, the factor K remains unchanged.

$$\text{And } Cl = \sqrt{\frac{2 \cdot M \cdot g}{\rho \cdot V_{Cruise}^2 \cdot S}}$$

- Main engine power: $P_{Main\ engine\ Cruise} = P_{Main\ engine\ Max}$
- Main engine fuel flow: $FC_{Main\ engine\ Cruise} = SFC_{Main\ engine} \cdot P_{Main\ engine\ Cruise}$
- Boost engine power: $P_{Boost\ engine\ Cruise} = P_{Take-off} - P_{Main\ engine\ Cruise}$
- Boost engine fuel flow: $FC_{Boost\ engine\ Cruise} = SFC_{Boost\ engine} \cdot P_{Boost\ engine\ Cruise}$
- Travelled distance: $R_{Cruise} = Range - (R_{Transition} + R_{Climb} + R_{Descent})$
- Duration: $T_{Cruise} = \frac{R_{Cruise}}{V_{Cruise}}$
- Fuel consumed:

$$F_{Cruise} = T_{Cruise} \cdot (FC_{Main\ engine\ Cruise} + FC_{Boost\ engine\ Cruise})$$

Descent: This step happens twice during the mission: First, it starts at the end of the first cruise and ends when the aircraft reaches the loiter altitude. The second time, it starts at the end of the second cruise and ends at the second transition.

- Altitude: During the first climb, $h_{Descent} = \frac{h_{Service\ ceiling} + h_{Loiter}}{2}$ During the second climb: $h_{Climb} = \frac{h_{Service\ ceiling} + h_{Transition}}{2}$
- Required power: $P_{Descent} = 0$ (section D.5.1, page244)
- Main engine fuel flow: $FC_{Main\ engine\ Descent} = FC_{Main\ engine\ Turn\ on\ Warming}$

-
- Boost engine fuel flow: $FC_{Boost\ engine\ Descent} = FC_{Boost\ engine\ Turn\ on\ Warming}$ (Assumed turned off).
 - Horizontal speed: according to Raymer ([?]; ch. 17.3), the maximum range in gliding flight is achieved at the best lift over drag ratio. That is to say: $V_{Descent} = \sqrt{\frac{2 \cdot M \cdot g}{\rho \cdot S}} \sqrt{\frac{K}{Cd_0}}$ Where:
 - Cd_0 is estimated as in section D.5.6, page 249
 - K remains the one of section D.5.6
 - Vertical speed: $v_{Descent} = \sqrt{\frac{2 \cdot M \cdot g}{\rho \cdot S \left(\frac{Cl^3}{Cd^2}\right)}}$ (from [?]; eq. 17.35; eq. 17.37; eq. 17.38)

With

 - $Cl = \sqrt{\frac{2 \cdot M \cdot g}{\rho \cdot V_{Cruise}^2 \cdot S}}$
 - $Cd = Cd_0 + Cd_i$

With $Cd_i = K \cdot Cl^2$
 - Duration: $T_{Descent} = \frac{h_{initial} - h_{final}}{V_{vertical}}$ Where h_{final} and $h_{initial}$ are respectively the final and initial altitude (in m)
 - Fuel consumed:

$$F_{Descent} = T_{Descent} \left(FC_{Main\ engine\ Descent} + FC_{Boost\ engine\ Descent} \right)$$

- Travelled distance: $R_{climb} = V_{Descent} \times T_{Descent}$

Loiter: This constitutes the main part of the flight. It starts at the end of the first descent and ends at the beginning of the second climb. Due to the relative longer duration of the loiter step, a more detailed computation is done. It is assumed that the aircraft will fly at constant speed. Therefore, the Breguet equation is adopted as a start [?]. But this latter is refined to take into account some specifics of the current aircraft as its relatively high electrical power consumption or the efficiency of its electric motors.

- Altitude: h_{Loiter}

-
- Horizontal speed: V_{Loiter} (section [D.5.6](#), page249)
 - Required power: $P_{Loiter} = \frac{V_{Loiter} \cdot D_{Loiter}}{\eta_{propulsion}} + P_{electrical}$, where D_{Loiter} is the drag in cruise.
 - Main engine power: $P_{Main\ engine\ Loiter} = P_{Loiter}$
 - Boost engine power: $P_{Boost\ engine\ Loiter} = 0$
 - Fuel flow: $FC_{Loiter} = SFC_{Main\ engine} \cdot P_{Main\ engine\ Loiter}$

$$FC_{Loiter} = SFC_{Main\ Engine} \cdot P_{Loiter} = SFC_{Main\ Engine} \left(\frac{V_{Loiter} \cdot D_{Loiter}}{\eta_{Propulsion}} + P_{electrical} \right) \quad (4.1)$$

The aerodynamic equations give:

$$L_{Loiter} = \frac{1}{2} \rho \cdot V_{Loiter}^2 \cdot S \cdot Cl = M \cdot g$$

$$D_{Loiter} = \frac{1}{2} \rho \cdot V_{Loiter}^2 \cdot Cd$$

Which recombined, lead to:

$$D_{Loiter} = \frac{Cd}{Cl} M \cdot g$$

Where $\frac{Cd}{Cl}$ is assumed to be constant over the entire loiter. $Cl = \frac{2 \cdot M \cdot g}{\rho \cdot V_{Loiter}^2 \cdot S}$ and $Cd = Cd_0 + Cd_i$

- Cd_0 is estimated as in section [D.5.7](#), page251
- $Cd_i = K \cdot Cl^2$ where K is assumed to be unchanged regarding section [D.5.6](#), page249.

Then equation (4.1) becomes:

$$FC_{Loiter} = SFC_{Main\ Engine} \left(\frac{V_{Loiter} \cdot \frac{Cd}{Cl} M \cdot g}{\eta_{Propulsion}} + P_{electrical} \right) \quad (4.2)$$

- Travelled distance: The mass evolution is:

$$\frac{dM}{dt} = -FC_{Loiter}$$

It leads to:

$$\begin{aligned} \frac{dM}{dR_{Loiter}} &= \frac{\frac{dM}{dt}}{\frac{dR_{Loiter}}{dt}} = -\frac{FC_{Loiter}}{V_{Loiter}} \\ \Leftrightarrow \frac{dR_{Loiter}}{dt} &= -\frac{V_{Loiter}}{FC_{Loiter}} \frac{dM}{dt} \end{aligned}$$

which combined with equation (4.2) becomes:

$$\begin{aligned} \frac{dR_{Loiter}}{dt} &= -\frac{V_{Loiter}}{SFC_{Main\ Engine} \cdot \left(\frac{V_{Loiter} \cdot \frac{C_d}{C_l} M \cdot g}{\eta_{Propulsion}} + P_{electrical} \right)} \frac{dM}{dt} \\ R_{Loiter} &= \int_{M_{initial}}^{M_{final}} -\frac{V_{Loiter}}{SFC_{Main\ Engine} \cdot \left(\frac{V_{Loiter} \cdot \frac{C_d}{C_l} M \cdot g}{\eta_{Propulsion}} + P_{electrical} \right)} dM \\ \Leftrightarrow R_{Loiter} &= \frac{\eta_{Propulsion} \frac{C_l}{C_d}}{SFC_{Main\ Engine} \cdot g} \int_{t_{final}}^{t_{initial}} \frac{dM}{M + \frac{\eta_{Propulsion} \frac{C_l}{C_d} \cdot P_{electrical}}{g \cdot V_{Loiter}}} \\ \Leftrightarrow R_{Loiter} &= \frac{\eta_{Propulsion} \frac{C_l}{C_d}}{SFC_{Main\ Engine} \cdot g} \ln \left(\frac{M_{initial} + \frac{\eta_{Propulsion} \frac{C_l}{C_d} \cdot P_{electrical}}{g \cdot V_{Loiter}}}{M_{final} + \frac{\eta_{Propulsion} \frac{C_l}{C_d} \cdot P_{electrical}}{g \cdot V_{Loiter}}} \right) \end{aligned}$$

- Duration: $T_{Loiter} = \frac{D_{Loiter}}{V_{Loiter}}$

$$\begin{aligned} F_{Cruise} &= T_{Cruise} \\ &= (FC_{Main\ engine\ Cruise} + FC_{Boost\ engine\ Cruise}) \end{aligned}$$

Landing: This step starts when the aircraft reaches IGE altitude at the end of the last descent and ends when the wheels touch the ground at OGE altitude.

- Altitude: OGE.
- Required power: $P_{Landing} = P_{hover}$ (cf. section D.5.1, page 244).

-
- Main engine power: $P_{Main\ engine\ Landing} = P_{Main\ engine\ Max}$
 - Main engine fuel flow: $FC_{Main\ engine\ Landing} = SFC_{Main\ engine} \cdot P_{Main\ engine\ Landing}$
 - Boost engine power: $P_{Boost\ engine\ Landing} = P_{Landing} - P_{Main\ engine\ Landing}$
 - Boost engine fuel flow: $FC_{Boost\ engine\ Landing} = SFC_{Boost\ engine} \cdot P_{Boost\ engine\ Landing}$
 - Duration: $T_{Take-off} \approx 2.5\ minutes$ (Conventional value in light aviation).
 - Fuel consumed:

$$F_{Landing} = T_{Landing} \left(FC_{Main\ engine\ Landing} + FC_{Boost\ engine\ Landing} \right)$$

Taxing / Turn off: This last step is considered as being very short and is therefore neglected.

A mass integration is lastly performed on the entire mission to obtain, at the end of the loop, the range of the aircraft.

4.4 OPTIMISATION

The optimisation of the aircraft characteristics is performed to maximise its performances on the typical mission. It may look strange and even inappropriate not to propose a method of evaluating the cost. This parameter is indeed chosen as the optimisation criterion for the overwhelming majority of conceptual design studies as it is highly recommended in All the reference literature ([?]; ch. 18), ([?]; ch. 11.8), ([?]; Part. VIII). However, it can be noticed that all these references have been written to guide manned aircraft design. The unmanned aircraft context is indeed somewhat different. The product is there not only an “aircraft”, but a “system of drone” which includes airframe, ground station, transmission system, sensors and so on. It explains the high price of such aircraft compared to simple airframes of similar dimensions. For instance the acquisition by the French army of 30 SAGEM Sperwer UAVs have cost 77 million Euros [?], that is to say, 2.5 million per unit. That is more or less 35

times the usual price of an ULM of the same mass. Therefore the cost of the airframe has only little influence on the overall system price, and its evaluation is unnecessary. It seems now much more relevant to try to improve the endurance of the aircraft which seems to be the showpiece of actual UAV marketing as it appears in Table 4.9, page 132. However, this latter should be increased while containing the dimensions of the airframe, keeping in mind the essential tactical aspect of the current design. This would avoid falling into the same category, denominated “light MALE” [?], as the SAGEM Patroller which does not own any SATCOM.

The aim of the optimisation is therefore to size the different systems of the aircraft to maximise its endurance while keeping its bulk acceptable. To implement the optimisation process, some assumptions have been made:

The fuel quantity: Either fuel quantity or endurance must be fixed. Traditionally for transport aircraft, the expected range is defined, and the fuel capacity is optimised to reach it. However, for TUAV, it seems that the custom comes from light aviation industry where fuel quantity is fixed. After having tried several possibilities, the fuel mass is set to 45 kg which provides a suitable endurance.

Aircraft parameters: The parameters that can be optimised during the design of an aircraft are very numerous. However, some of them cannot be defined during the conceptual design process since they depend on structural details that are studied in subsequent phases or have only little impact on the result. Therefore these parameters are arbitrarily set to realistic values to decrease the computing power:

- Fore plane taper ratio: 0.5 (typical)
- Rotor height (in aeroplane mode): at a third of the fuselage diameter (bulk of the rotor mechanical)
- Main wing taper ratio 0.5 (typical)
- Main wing height (in aeroplane mode): at the top of the fuselage diameter (typical)
- Vertical tail plane taper ratio: 0.5 (typical)
- Main engine type: gasoline Otto engine

-
- Boost engine type: gas turbine engine

The optimisation problem can be constructed, considering these assumptions:

The optimisation settings: 6 remaining parameters are defined as optimisation settings:

- The fore plane span
- The fore plane mean chord
- The main wing span
- The main wing mean chord
- The main engine power
- The boost engine power

The optimisation constraints: The only truly penalising constraint is to have a loiter speed at least 1.1 times superior to stalling speed. Another constraint is defined to ensure that during the transition, the angle between the rotor disk and the fuselage is lower than the one admissible by the mechanics.

the optimisation criterion: As discussed before the optimisation criterion is the aircraft endurance.

Because of the nonlinear aspect of the proposed model, only global methods such as stochastic method can be used to find a good solution. Stochastic methods like heuristic or Meta heuristics have indeed proved, to a great extent, their effectiveness in finding global optima although the optimality of obtained solutions cannot be guaranteed or theoretically proven. The software used for this study is based on genetic algorithms, differential evolution and nonlinear simplex (Nelder Mead algorithm). This hybridization of global and local techniques makes the convergence of the overall algorithm be speeded up and also increases the robustness of the tool over a variety of problems [?]. Developed by Cab Innovation on Microsoft Excel, Gencab tool is illustrated in Figure 4.10. The chromosomes, composed of various parameters (i.e. genes) of floating point, integer or binary types, are subjected to random mutations, cross-overs and differential evolutions (i.e. summation of a gene of a chromosome

to the difference between the same genes present on two other chromosomes). After selection, the best elements of the population can be improved at a local level by computing several steps of Simplex.

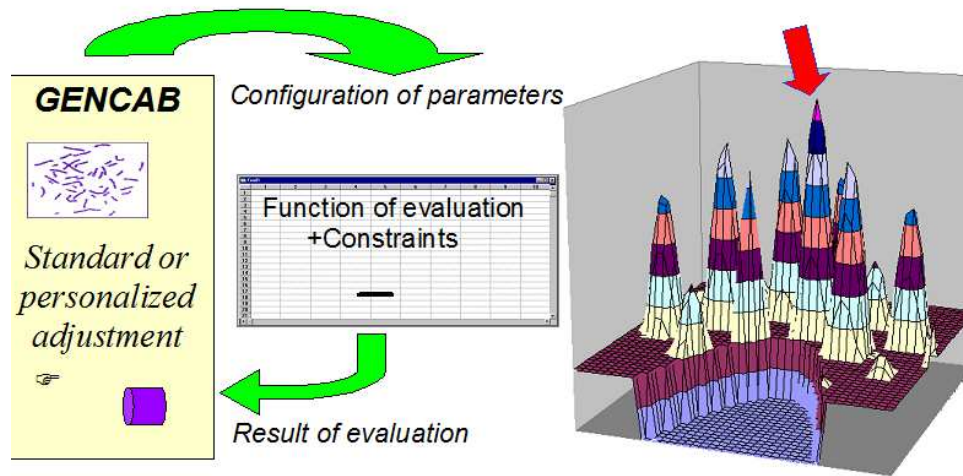


Figure 4.10: optimisation principle

4.5 RESULTS

The main dimensions of the aircraft are represented on the tree views plan exposed hereafter.

The main Characteristics of the aircraft are summarised in Table 4.7.

Empty weight	Fuel	Payload	MTOW	MLW	Powertrain
156.8 kg	45 kg	100 kg	301.8 kg	301.8 kg	1 x Gasoline Otto engine, 15.9 kW 1 x Gas turbine, 33.6 kW

Table 4.7: Main characteristics

The main performances of the aircraft are summarised in Table 4.8.

Stall speed	Cruising speed	Loiter speed	Range	Endurance	OGE	OGI	Service ceiling
33.9 m/s	95.2 m/s	36.5 m/s	200 km	12.15	2500 m	3027 m	6000 m

Table 4.8: Main performances

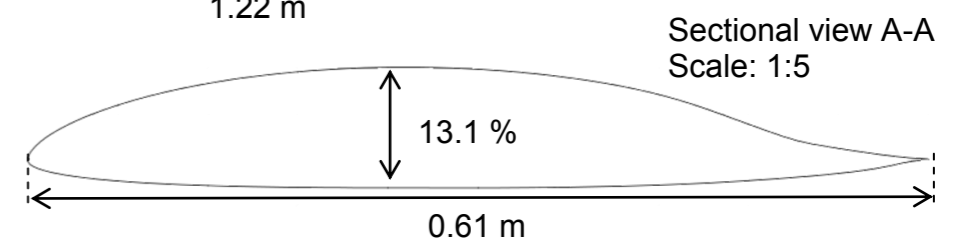
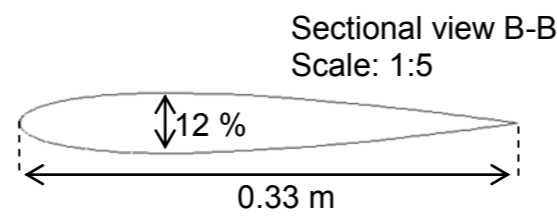
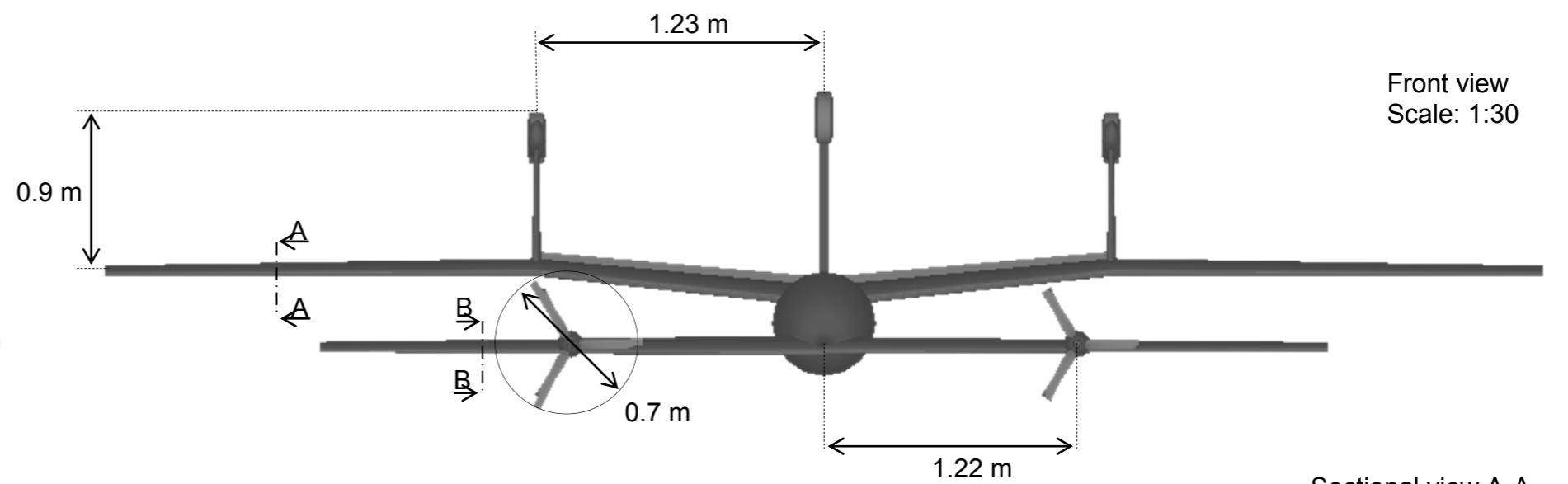
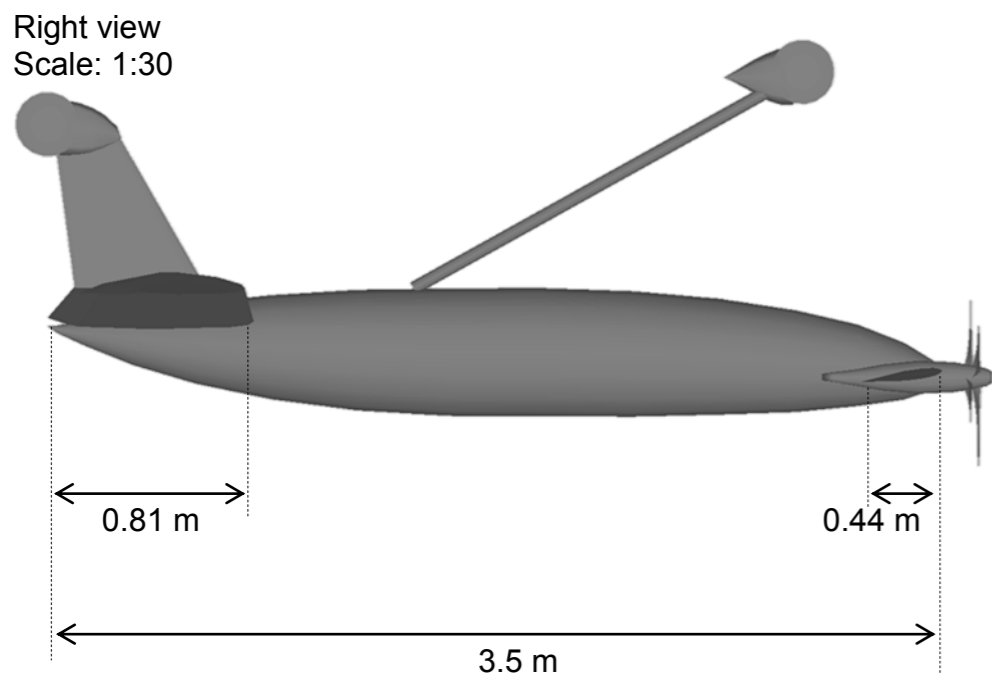
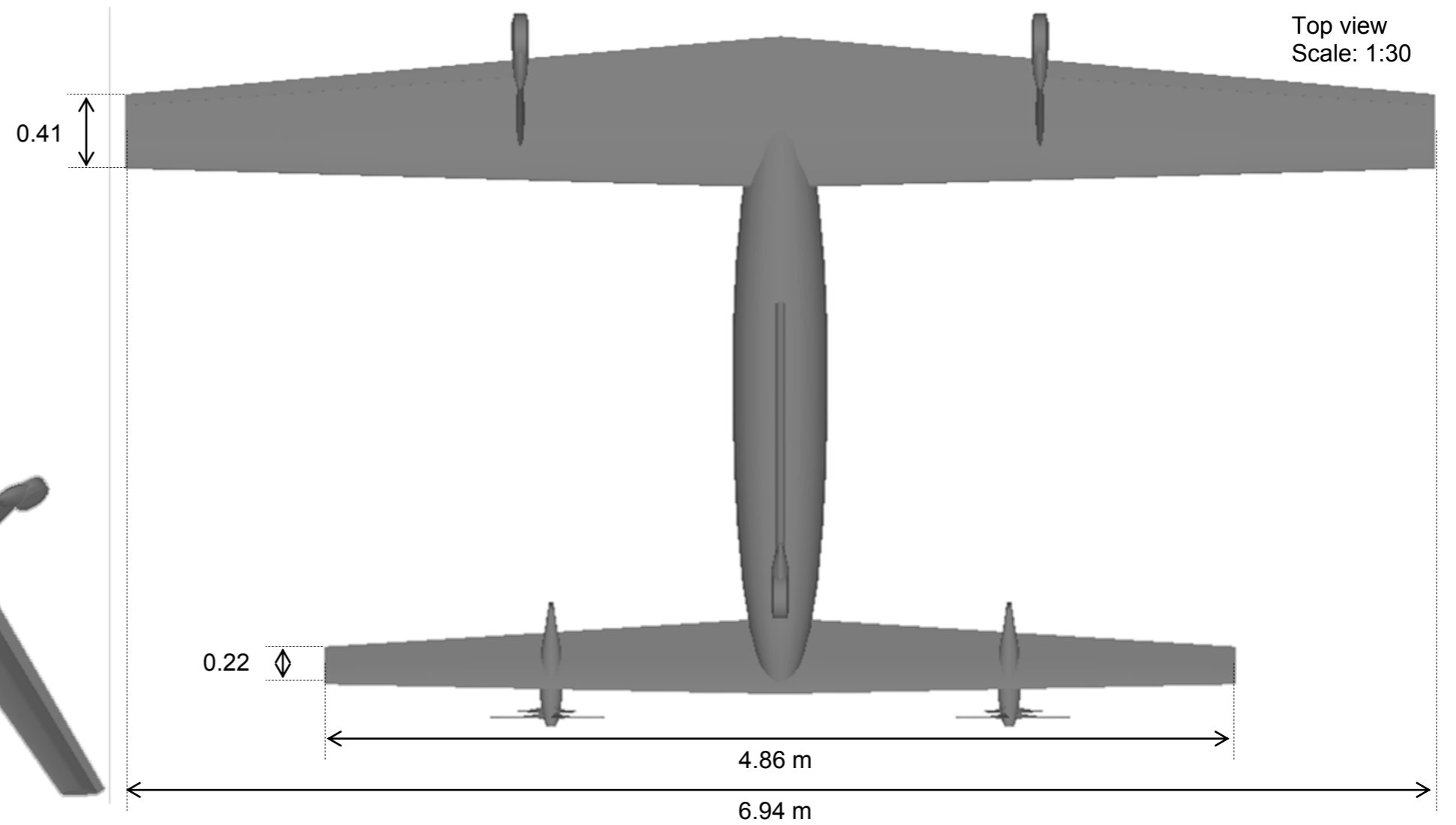
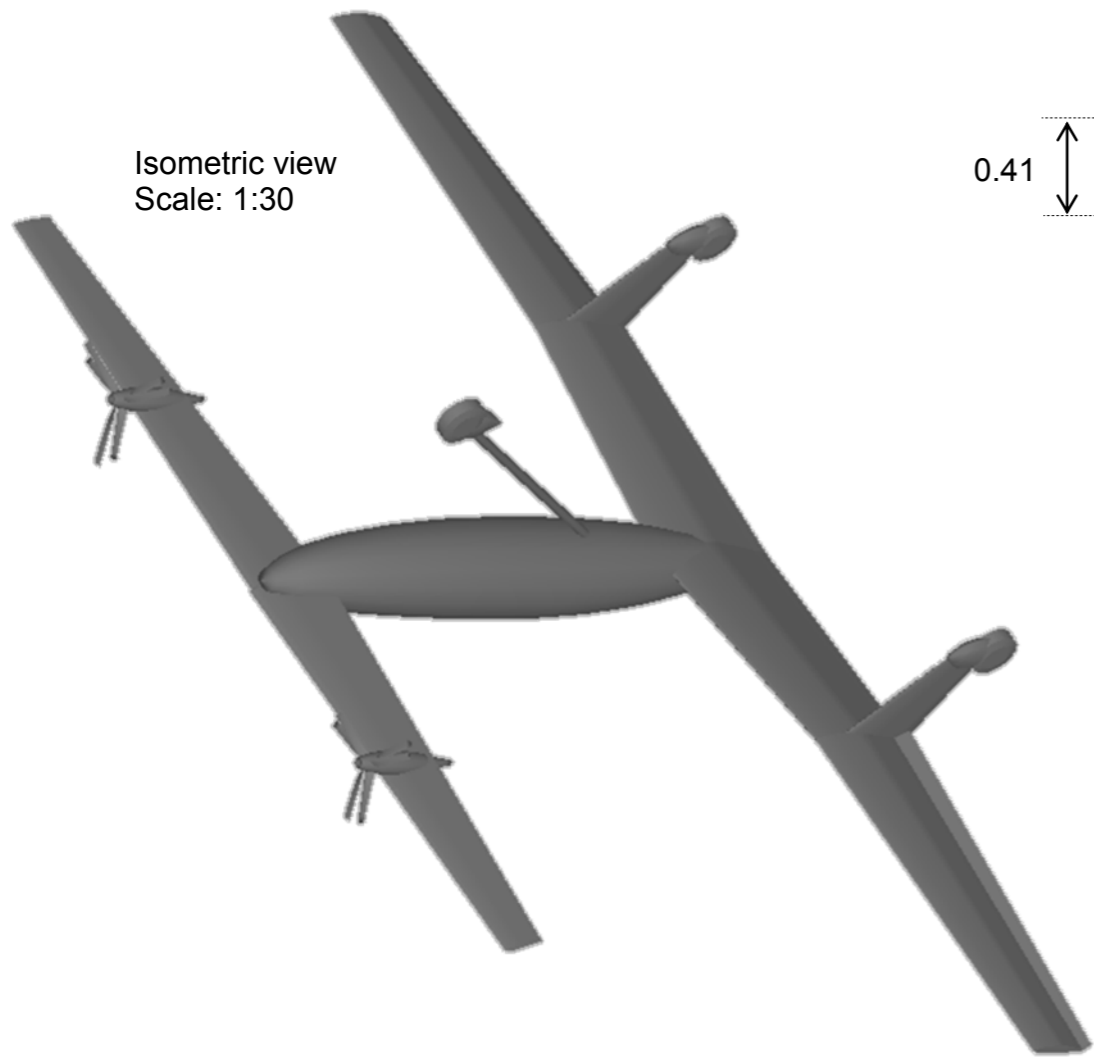
Specs	Aeroplane				Helicopter	VTOL
	Class	Sperwer B	Hermes 450	Falco EVO		
Name	RQ-7 Shadow M2				Camcopter S-100	Cab UAV
Manufacturer	AAI	SAGEM	Elbit Systems	Selex ES	Schiebel	Bell Helicopter ?
Introduction	2014	2007	1998	2011	2005	2017
Take-off	Classic / Catapult	Catapult	Classic	Classic / Catapult	vtol	Classic / Vtol
Landing	Classic / Tailhook	Parachute + Airbag	Classic / Tailhook	Classic	vtol	Classic / Vtol
Length	3.7 m	3.5 m	6.1 m	6.2 m	3.1 m	3.65 m
Wingspan	7.6 m	6.8 m	10.5 m	12.5 m	N/A	6.9 m
Rotor ϕ	N/A	N/A	N/A	N/A	3.4 m	4.86 m
Height	1 m	1.3 m	?	2.5 m	1.1 m	1.4 m
Empty W	?	275 kg	?	?	97 kg	156.8
Gross W	266 kg	350 kg	550 kg	650 kg	200 kg	301.8
Payload	36 kg	100 kg	180 kg	100 kg	50 kg	100 kg
Power	47 kW	48 kW	39 kW	49 kW	40 kW	15.9 + 33.6 = 49.5 kW
Max speed	220 km/h	240 km/h	176 km/h	216 km/h	222 km/h	342 km/h
Stall speed	?	?	?	130 km/h	0 km/h	0 km/h
Cruise speed	?	?	130 km/h	?	101 km/h	?
Range	125 km	200 km	300 km	200 km	180 km	200 km
Endurance	16 h	12h	17 h	18 h	6h (25kg)	12.15 h
Serv ceiling	?	6096 m	5486 m	6000 m	5486 m	6000 m
Source	[?], [?]	[?]	[?]	[?]	[?]	[?]

Table 4.9: Competitors specification comparison

4.6 PARTIAL CONCLUSION

A conceptual design has been carried out to fulfil a typical TUAV mission. To evaluate the performances of the present aircraft, it is compared with its youngest competitors described in Table 4.9, page 132. One can notice that both dimensions and weight of the present TUAV are very well contained, which will ensure easy operations. It is indeed very close to being the smallest in span, while its length feats in the average. More of all, it has a MTOW ranging with the two lightest competitors. However, its payload of 100 kg is the second greater, that makes it able to carry at least two payloads at a time which begins to be very sought-after [?]. This classifies it as a polyvalent tool suitable for demanding tactical missions. Contrary to what is expectable, its maximal power is well contained too. This can be explained by the quite large rotor disk area that is not limited neither by helicopter maximum speed nor by "tilt-rotor" mechanical limitations. Nevertheless, this relatively small amount of power allows it an astonishing top speed 50% greater than the average one. In addition to that, its endurance is more than 100% higher than the other TUAVs having a VTOL capability and matches the classical aeroplanes one.

Nevertheless, the results of the Conceptual design must be treated with great caution even if the chosen assumptions were always the most pessimistic available ones. Indeed it is based on semi empirical equations that have not been designed for it. It is currently accepted that the results of such a study have an accuracy level of about 80%. Notwithstanding, according to Chris Van Buiten, vice president of Sikorsky Innovations, there is a general aviation rule of thumb which says that "you don't want a new aeroplane unless you can get a 25% improvement in 2 or 3 measures" [?]. The present concept fulfils this requirement entirely while merging the capabilities of two different kinds of aircraft. At least, its operating cost should be in the range of a classical helicopter since its mechanical design is very close. This last analysis tends to forecast an unusually promising future and is, therefore, the subject of a conference article in ICUAS2016 [?].



5

PERSPECTIVES

The presented work consists of a preliminary study of the new TUAV VTOL concept. If many analyses have been carried out, primary results arise many other ones.

5.1 AIRCRAFT CONTROL

The control of the aircraft is studied in section 3, page 91. It appears that it represents a sensitive work that has to deal with the complexity of the model and digital limitations due to its size.

A control in hover is proposed in section 3.2.4.1, page 96. However, this control does not stabilise the aircraft state variables x and y which makes it unsuitable for practical uses.

Even if the states and controls are mutually highly dependent, it appears that a decomposition may be possible: allocating each control to a single state variable as glimpsed through the dynamics matrices analysis performed in section 3.2.4.2, page 101. Such a decomposition of the dynamics in a set of smaller ones may solve the digital limitation issue. However, the idea of designing a single control law, computed from the flight parameters and working from hover to almost rotor stop, is not any more feasible. Indeed, as explained in section 3.2.4.2, at transition speed, before slowing down the rotor, the blade average pitch angle θ_0 may be used to control the longitudinal velocity u while the propellers mean thrust F_0 may be the rotor rotation speed ω primary control. However, when the rotor is almost stopped, the blade

being almost parallel to the general airflow, the controls may be swapped around (i.e. θ_0 and F_0 control respectively ω and u). One solution would consist in splitting this flight into two phases: acceleration of the aircraft at constant rotor rotation speed and deceleration of the latter at constant aircraft airspeed. The motor thrust and the blade pitch would respectively control the rotor behaviour and the aircraft speed in the first phase. It would substitute one another in the second phase.

Moreover, one can notice that, after decomposition, some of the state variables are assigned more than one flight control (e.g. rudder and rotor *theta_{1c}* for lateral force). Therefore an optimal control may be used for better control.

Lastly, some flight controls affect equally to state variables (cf. flaperons and rudders/airbrakes). The control may be computed as the sum of two sub controls to keep both functionalities. For instance, the flaperon deflection may be calculated as the sum of the flap and the aileron deflection.

However, the design of a smooth control is out of the scope of the present thesis.

Nevertheless such a control would pave the way to a more autonomous navigation system that would greatly extend the capability of the aircraft [?] [?][?].

5.2 ELECTRIC PROPULSION SYSTEM

The use of electric motor driven propellers as rotor propulsion system has been alluded in section 0.2.3, page 13. However, no more information was provided at this stage of the study. The main issue the motors have to deal with is the high rate evolution of the required torque and rotation speed. This rate is due to two factors:

- According to the rotor theory exposed in section 2.1.1, page 54, the propellers endure a variable axial velocity of a frequency corresponding to the main rotor rotation speed. Nevertheless, according to the propeller model exposed in section 1.1.1.2, page 28, this variable velocity implies to fluctuate the propeller rotation speed to keep the thrust at a required intensity.
- The propellers forces have been assumed to depend on the blade azimuth, as presented in section B.3, page 172, which implies a variable motor rotation speed for the same

reason as previously.

Brushless motors advantages over brushed DC motors and induction motors are high efficiency, superior torque-speed characteristics, compactness and high torque-to-inertia ratio which make them ideal for the present application [?]. However, the main drawback of these motors is the need for an accurate knowledge of the rotor position. The operating principle of any electric motor is indeed to generate a variable magnetic field in both the rotor and stator knocked out of alignment by an angle of around $\frac{\pi}{2}rad$ to maximise generated torque. The aim of the brushes is to maintain this angle while rotating, selecting the coils sequentially. Their removal imposes thus to transfer this duty to another mean, which is electronics for the brushless motor technology. There have been several control methods developed over the years, as listed in [?] [?]. Most motor controllers are based upon trapezoidal sensorless control, which consists of powering two motor phases at a time while measuring the back EMF on the third one to detect the voltage zero-crossing [?] [?]. If this solution is quite simple to implement and is relatively inexpensive, it is not providing the best performance. Indeed, this control does not maintain the angle between the magnetic fields of the stator and the rotor at $\frac{\pi}{2}rad$. Thus, for a given power consumption, the torque is not optimal, which reduces both performance and responsiveness. Therefore, this is not the most optimal way of control. FOC generates the best results indeed up to now. This technique consists of generating a sinusoidal magnetic field vector normal to the stator one to maximise the efficiency, which makes it best suited for any three-phases machines, including Permanent Magnet DC brushless Motor [?]. An additional sensor (Encoders, Resolvers or Hall Effect sensors) is usually added to measure the rotor position. However, this solution increases size and cost, requires extra wiring, complicates the driver electronics, has a limited operational temperature, range and speed and is subject to failures [?], [?]. In the present design, the motors are accommodated in dedicated nacelles, shaped to generate as less drag as possible as exposed in section 4.2.4, page 119. A size augmentation of the motor would result in an increase in drag, in particular in helicopter mode which would deteriorate the overall performances. Advanced control laws have been recently intensively investigated to take away this sensor and only base the control on current and voltage measurements. According to [?], there are two main types of closed loop sensorless control methods for Permanent Magnet

d.c. Brushless Motor:

- Intrusive sensorless control: based on the machine saliency, it superimposes a high-frequency signal to the primary phase voltages and currents. This method presents drawbacks: first, it requires a good saliency ratio and then, the inverter switches age prematurely due to their intensive use.
- Sensorless control based on Back-EMF measurement: this method suffers from bad reliability at standstill or very low-speed. However, it seems to be the cheapest way of control and looks ideal for all applications with relatively high operating minimum speed.

Various sensorless control techniques have been developed based on Back-EMF measurement. However, they are all based on the knowledge of the motor parameters. However, those parameters are subject to variations due, for instance, to the ageing or the temperature elevation while running. In the present case, as shown in section 2.1.1, page 54, the nacelles are subject to fast variation of airspeed. So, if the nacelles design ensures the limitation of their internal temperature average, the motors are likely to withstand fast temperature changes.

The control must, therefore, be tweaked to adapt itself to the variations. Some adaptive controls, such as the one presented in [?], have been even proposed, but they still need the motor parameters as the adaptive techniques are only used to estimate the rotor position. Another significant advantage of the precise tracking of the motor parameters is that they may be highly valuable when considering its maintenance in a health monitoring approach, as introduced in [?]. This last point is of particular interest in aviation.

A direct adaptive control without relying on motor characteristics has therefore been designed and is exposed in appendix E, page 252. The design proves its ability to withstand rapid rotation speed variations (at higher frequencies than the one estimated for the rotor designed for the present concept), without stalling as it would have been the case with a trapezoidal sensorless control (cf. section 1.1.2.4, page 36).

If the feasibility to control the propulsion system has been demonstrated, this latter should be designed in detail to check if an electric motor would be able to offset the inertia at such high frequencies. However, this design is out of the scope of the present study.

5.3 MINI UAV DERIVATIVE OF THE CONCEPT: “FLYING ROTOR”

It has been seen in section 1.1.3, page 40 that well designed, a propeller mounted on a blade could be an efficient way to propel a rotor. Moreover, it has been shown in section 5.2, page 136, that a proper motor control enables to follow high frequency periodic trajectories such as the one proposed in section B.3, page 172.

These two observations are the starting point of a new configuration development, shown in figure 5.1. This concept has been patented [?] in cooperation with the CNES (Centre National d’Etudes Spatiales), so that it could be used in complex applications such as Martian drones and means to control stratospheric balloon payload descent. The new UAV consists of a flying rotor composed of three or more blades and powered by a propeller mounted on each blade as shown in Figure 5.1. This concept is called “flying rotor” UAV in the rest of this article as it does not have any proper fuselage. The idea is based on two main principles.

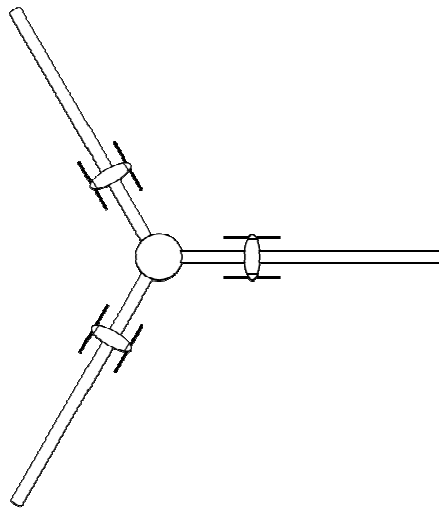


Figure 5.1: UAV architecture

On the one hand, any device likely to generate drag in the downwash of the rotor is removed. On the other hand, most of the subsystems are positioned in the blades, to remove the blade ballast, flatten even more the rotor cone and alleviate the stress concentration in the rotor hub. It can be noticed in Figure 5.1 that each propulsive unit is also composed of a contra-

rotating doublet of propellers. This would either improve somewhat the propulsive efficiency or reduce the diameter of a single propeller arrangement. The latter is still acceptable. “Flying rotor” UAV can be also of great advantage for some devices that usually require its own motorisation (e.g. RADAR, LIDAR...). However for static payload, a stabilisation by gimbal can be added underneath the rotor head as shown in Figure 5.2. The blades of “flying

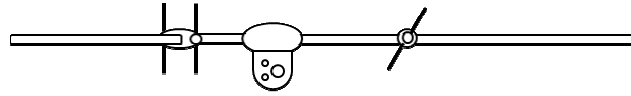


Figure 5.2: UAV payload

rotor” are articulated with a flap hinge as shown in Figure 5.3, well known on full scale helicopter rotors [?]. This articulation adds to the concept a natural stability on both lateral

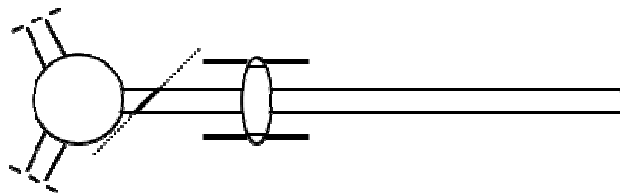


Figure 5.3: Blade articulation

displacement and pitch angle. On lateral displacement point of view, the advancing blade withstands a higher airspeed and therefore generates a higher lift than the retreating one. The lift hence does not balance anymore the centrifugal force component perpendicular to the blade. The advancing blade climbs, and the retreating one descends accordingly and so on until the lateral airspeed does not have any effect (e.g. when the blade is parallel to the airspeed). The rotor disk is, in consequence, tilted and generates a lift normal to the rotor disk that opposes the displacement. On pitch angle point of view, rotor generated lift has a lateral component which makes a lateral movement which consequently creates an opposed tilt of the rotor employing the lateral displacement stability previously exposed. One can notice that in Figure 5.3 the flap articulation is not perpendicular to the blade. This is done to alleviate the previous stability effects that are very effective, and that would otherwise prohibit “flying rotor” UAV from any movement. Indeed with an angle, the flap motion produces a pitch motion that decreases the effect of the airspeed [?]. Moreover, in the case of

a propulsion failure, the rotation speed of the rotor decreases, which increases the flap angle and therefore decreases the pitch angle of the blades enabling them to work in autorotation mode. This fact ensures a safe landing of the aircraft in such circumstances. All these facts imply a substantial reliability improvement compared to multi-rotors [?]. A control for such aircraft is proposed in appendix F, page 264. The design is currently under development, and the primary flight is planned to check its feasibility.

GENERAL CONCLUSION

After having detailed the importance of developing a VTOL tactical drone, a new concept was proposed, and its main characteristics were exposed (section , page 1). As part of a state of the art presentation, a review of the different concepts aiming at similar goals was carried out. For each of them, a summary of related research and work in aerodynamics and control fields was achieved.

Further study regarding the newly introduced concept was then performed. First, hover flight was investigated (section 1, page 1). Parts of the design are indeed quite revolutionary in the fact that their feasibility had not been proven before. A propeller powered rotor is, for instance, one of these new features and hence, a series of design studies and real-world tests had to be carried out to demonstrate its feasibility. For this particular example, it appeared that the implementation of such idea presented great performances as long as some precautions were taken with regard to powertrain strength and rotation speed. A CFD study was also necessary to visualise the interaction between the different aerodynamic entities and prove that no detrimental phenomena were happening, their layout being also quite novel.

The transition between helicopter and aeroplane configurations was then studied in section 2, page 2. It was first observed that rotor forward flight theory could not be applied as is since the flight envelope of present concept is far larger than the one of a helicopter. Therefore, an extended theory had to be established and proposed. The behaviour of the aircraft was thus assessed from hover flight to almost stopped rotor flight. Then, all forces and attitudes estimated were incorporated into flight dynamics model. Aerodynamics fixed part, taking into account the downwash incidence of the rotor and the stall of the main wing, was also included in the model.

Obtained model was then considered as a basis for the control study (section 3, page 3).

The controllability and observability of the system were first checked. A control law was then proposed to stabilise the aircraft in hover. The linear dynamics model was lastly studied at transition speed.

After having proven concept feasibility, a conceptual design of an operational version of the concept was carried out (section 4, page 4). This study proved its flight ability in aeroplane mode. It also led to the estimation of its potential future performances as a real aircraft. It then appeared that the penalties entailed by VTOL capacity could be of the same order of magnitude as the ones created by STOL capacity in competitors' versions.

The perspectives offered by present work were exposed in section 5, page 5. Ways to improve current concept were also described so that it could have an even bigger impact in aviation near future. For instance, the need for developing a more advanced control was emphasised, and some potential solutions were proposed such as the use of a FOC control for rotor electric motor. The rotor head mechanism could also be improved to remove its current play.

Nevertheless, although a lot of work remains to be done to obtain an operational version that flies, no blocking limitations have been found during this work, and hence, the goal of building such aircraft seems more achievable than ever. According to its expected performances and abilities, such a concept could have substantial benefits compared to current competitors, outperforming them in a lot of scenarios, and could open new markets, not yet targeted by the UAV business.

It would indeed be extremely well suited to high-value goods and first-aid kits transportation [?]. As illustrated in Figure 5.4, human organs could be sent and received straight from hospitals' heliports thanks to drone's VTOL capability. Moreover, its high speed and long range would enable direct journeys without any time-consuming airport halts in between. These aptitudes could also be tremendously beneficial to cash-in-transit, illustrated in Figure 5.5, since over-the-air transportation and absence of crew would make such operations much safer than they currently are. This autonomy and the fact that, as a result, it does not have any human on board mean it could be lastly used for critical and highly dangerous missions such as providing first assistance in a shipwreck, as presented in Figure 5.6.

Therefore, considering the significant impacts such aircraft could bring to our societies by helping solving some of their new challenges (e.g. lack of space, ever increasing need for fast



Figure 5.4: Application 1: Human organs transfer



Figure 5.5: Application 2: cash-in-transit courier

and reliable transportation and interconnection in a global world, need for quick deployment of aerial vision to assess catastrophic events such as floods, fire, nuclear explosion and for which, manned aircraft are no more of an option), the author hopes the proposed concept will soon become reality and play fully the role our modern world needs so urgently.



Figure 5.6: Application 3: first-aid kit delivery in hazardous environments

A

APPENDIX: ROTOR HOVER THEORY

Most of the rotor hover theory is based on the work of Johnson [?]. However, this theory is revised to be valid through the entire flight vertical flight envelope in section [A.5](#), page [159](#) .

A.1 MOMENTUM THEORY

A.1.1 HOVER

The tube flow is modelled at infinite upstream, infinite downstream, and at the propeller level as can be seen in Figure [A.1](#). The energy conservation gives:

$$\frac{1}{2}\dot{m}w^2 = Tv$$

where \dot{m} is the mass flow, w is the infinite downstream velocity, T is the propeller thrust and v is the velocity at the propeller level. The fluid mechanics gives:

$$T = \dot{m}(w - 0)$$

which leads to:

$$w = 2v$$

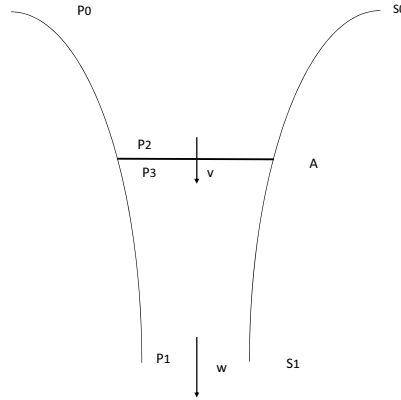


Figure A.1: Propeller stream tube in hover

The mass conservation gives:

$$\dot{m} = cste = \rho Av = \rho Sw$$

Assuming that ρ is constant, it becomes:

$$Av = Sw$$

which gives with the previous calculation:

$$A = 2S$$

Assuming that $P_0 = P_1$, and applying Bernoulli's principle upstream and downstream of the propeller:

$$P_0 = P_2 + \frac{1}{2}\rho v^2; P_0 + \frac{1}{2}\rho w^2 = P_3 + \frac{1}{2}\rho v^2$$

Nevertheless, $T = (P_3 - P_2)A$ which gives:

$$\frac{1}{2}\rho w^2 = \frac{T}{A}$$

which can be rewritten as:

$$w = \sqrt{\frac{2T}{\rho A}}$$

And which combined with the previous result leads to:

$$v = \sqrt{\frac{T}{2\rho A}} \quad (\text{A.1})$$

The expression of the thrust power can be now expressed:

$$P = Tv = T\sqrt{\frac{T}{2\rho A}} = \sqrt{\frac{T^3}{2\rho A}} \quad (\text{A.2})$$

A.1.2 IN CLIMB

The tube flow is modelled as shown in Figure A.2. As computed in section A.1.1, page 147,

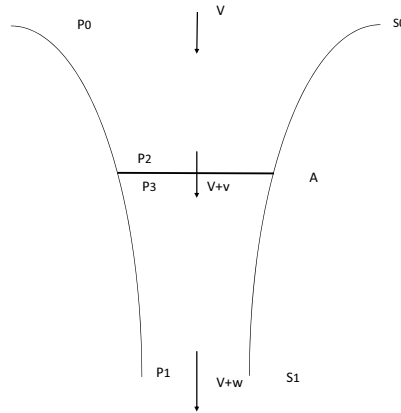


Figure A.2: Propeller stream tube

the thrust is:

$$T = \dot{m}((V + w) - (V)) = \dot{m}w$$

So the power P becomes:

$$P = T(V + v) = \dot{m}w(V + v) \quad (\text{A.3})$$

Using the difference of energy, it can also be expressed as:

$$P = \frac{1}{2}\dot{m}(V + w)^2 - \frac{1}{2}\dot{m}V^2 = \frac{1}{2}\dot{m}w(w + 2V)$$

It therefore leads to:

$$P = \frac{1}{2}\dot{m}w(w + 2V) = \dot{m}w(V + v)$$

$$\Leftrightarrow 2V + 2v = 2V + w$$

Which ultimately gives:

$$2v = w \tag{A.4}$$

Assuming that $P_0 = P_1$, and applying Bernoulli's principle upstream and downstream of the propeller give:

$$P_0 + \frac{1}{2}\rho V^2 = P_2 + \frac{1}{2}\rho(V + v)^2; P_0 + \frac{1}{2}\rho(V + w)^2 = P_3 + \frac{1}{2}\rho(V + v)^2$$

However, $T = (P_3 - P_2)A$, which gives:

$$T = \frac{1}{2}\rho w(w + 2V)A$$

Which combined with the previous result:

$$T = \frac{1}{2}\rho 2v(2v + 2V)A = 2\rho Av(v + V) \tag{A.5}$$

Defining v_h (the hover induced velocity) as:

$$v_h = \sqrt{\frac{T}{2\rho A}}$$

Finally the power is:

$$P = T(V + v) \tag{A.6}$$

A.1.3 GENERALIZED MOMENTUM THEORY

Until now it has been considered that the flow was uniform throughout the rotor disk. The momentum theory is now extended to a non-uniform distribution. The mass conservation gives:

$$\dot{m} = \rho V S_0 = \rho \int (V + v)dA = \rho \int (V + w)dS_1$$

As computed in section [A.1.2](#), page 149:

$$T = \int \Delta p dA = \int \frac{d\dot{m}}{dS_1} ((V + w) - (V)) dS_1 = \rho \int (V + w) w dS_1 = \rho \int (V + v) w dA$$

So the power P can be computed as:

$$P = \int \Delta p (V + v) dA \quad (\text{A.7})$$

Using the difference of energy, it can also be expressed as:

$$\begin{aligned} P &= \int \frac{1}{2} \frac{d\dot{m}}{dS_1} (V + w)^2 dS_1 - \frac{1}{2} \dot{m} V^2 \\ &= \int \frac{1}{2} \rho (V + w) (V + w)^2 dS_1 - \frac{1}{2} \rho \int (V + w) V^2 dS_1 \\ &= \int \frac{1}{2} \rho (V + w) (w^2 + 2Vw) dS_1 \end{aligned}$$

Assuming that $P_0 = P_1$, and applying Bernoulli's principle upstream and downstream of the propeller:

$$P_0 + \frac{1}{2} \rho V^2 = P_2 + \frac{1}{2} \rho (V + v)^2; P_0 + \frac{1}{2} \rho (V + w)^2 = P_3 + \frac{1}{2} \rho (V + v)^2$$

The differential equivalents are:

- Mass conservation: $(V + v) dA = (V + w) dS_1$
- Thrust: $dT = \Delta p dA = \rho (V + w) w dS_1 = \rho (V + v) w dA$
- Power: $dP = \Delta p (V + v) dA = \frac{1}{2} \rho (V + w) (w^2 + 2Vw) dS_1$

Assuming that the equation [\(A.4\)](#), $v = \frac{1}{2}w$, is always true:

$$dT = 2\rho (V + v) v dA \quad (\text{A.8})$$

$$dP = dT (V + v) dA$$

A.1.4 SWIRL IN THE WAKE

The drag of the blades makes, by reaction, the downwash rotate as shown in Figure A.3. As

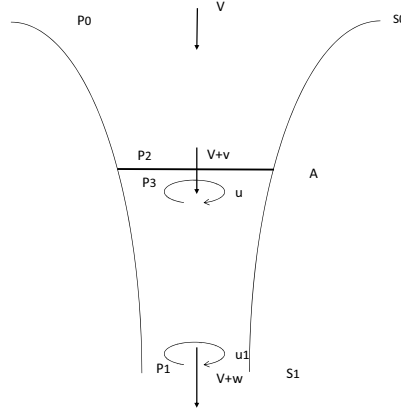


Figure A.3: swirl in the wake

in section A.1.3, page 150, mass conservation gives:

$$\dot{m} = \rho V S_0 = \rho \int (V + v) dA = \rho \int (V + w) dS_1$$

Assuming that the density ρ is constant:

$$V S_0 = \int (V + v) dA = \int (V + w) dS_1$$

The thrust becomes:

$$T = \int \Delta p dA = \int \frac{d\dot{m}}{dS_1} ((V + w) - (V)) dS_1 + \int (P_1 - P_0) dS_1 = \rho \int (V + w) w dS_1 + \int (P_1 - P_0) dS_1$$

The torque Q is:

$$Q = \int \frac{d\dot{m}}{dA} u r dA = \rho \int (V + v) u r dA = \rho \int (V + w) u_1 r_1 dS_1$$

The energy taken by the swirl movement is $P_u = \frac{dE_u}{dt}$, which gives:

$$P_u = \frac{1}{2} \frac{dm}{dt} u^2$$

So, taking the results obtained in section A.1.3, page 150, the power P can be computed as:

$$P = \int \Delta p (V + v) dA + \int \frac{1}{2} \rho (V + v) u^2 dA \quad (\text{A.9})$$

which is also:

$$\begin{aligned} P &= \int (P_1 - P_0) (V + w) dS_1 + \int \frac{1}{2} \rho (V + w) u_1^2 dS_1 + \int \frac{1}{2} \rho (V + w) (w^2 + 2Vw) dS_1 \\ &= \int (P_1 - P_0) (V + w) dS_1 + \int \frac{1}{2} \rho (V + w) (w^2 + 2Vw + u_1^2) dS_1 \end{aligned}$$

The swirl of the air generates a pressure drop by centrifugal force as illustrated in Figure A.4.

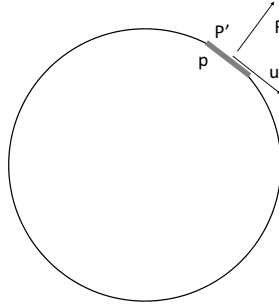


Figure A.4: Pressure drop due to swirl

$$\frac{dp}{dr} = \frac{dF}{S dr} = \frac{d m a}{S dr} = \frac{d m \frac{u^2}{r}}{S dr} = \frac{d m}{S dr} \frac{u^2}{r} = \rho \frac{u^2}{r}$$

Therefore, it leads to:

$$P_0 - P_1 = \int \rho \frac{u_1^2}{r_1} dr_1$$

Knowing that $P = \Omega Q$, the mechanical power P is:

$$P = \Omega \rho \int (V + v) u r dA$$

Then equalizing the two expressions of P , it leads to:

$$\int \Delta p(V + v)dA = \int \rho(V + v)u(\Omega r - \frac{1}{2}u)dA$$

Knowing that $\Delta p dA = dT$:

$$\int (V + v)dT = \int \rho(V + v)u(\Omega r - \frac{1}{2}u)dA$$

Using the thrust differential form (A.8) $dT = 2\rho(V + v)v dA$, it leads to:

$$\begin{aligned} \int 2\rho(V + v)(V + v)v dA &= \int \rho(V + v)u(\Omega r - \frac{1}{2}u)dA \\ \rightarrow 2(V + v)v - u(\Omega r - \frac{1}{2}u) &= 0 \end{aligned}$$

Finally the goal of the rotor design is to minimize the mechanical power P :

$$P = \Omega \rho \int (V + v)ur dA$$

with the constraint of the required thrust T defined as:

$$T = \rho \int (V + w)wdS_1 + \int (P_1 - P_0)dS_1 = \rho \int (V + v)2vdA + \int (P_1 - P_0)dS_1$$

The term depending on the pressures is neglected (2%), which leads to:

$$T = \rho \int (V + v)2vdA$$

and:

$$2(V + v)v - u(\Omega r - \frac{1}{2}u) = 0$$

A.1.5 PROFIL DRAG

Here, additional power is provided to the air to compensate the losses due to profile drag:

$$P_{profil\ drag} = \int \Omega r dD = \int \Omega r \frac{Cd}{Ct} dT = \int \rho \Omega r \frac{Cd}{Ct} (V + v)2vdA$$

So, adding this component to power P equation (A.9), it becomes:

$$P = \int \Delta p(V + v)dA + \int \frac{1}{2}\rho(V + v)u^2dA + \int \rho\Omega r \frac{Cd}{Ct}(V + v)2vdA$$

Then equalizing the two expressions of P , it leads to:

$$\begin{aligned} P &= \Omega\rho \int (V + v)urdA = \int \Delta p(V + v)dA + \int \frac{1}{2}\rho(V + v)u^2dA + \int \rho\Omega r \frac{Cd}{Ct}(V + v)2vdA \\ &\rightarrow \int \Delta p(V + v)dA + \int \rho\Omega r \frac{Cd}{Ct}(V + v)2vdA = \int \rho(V + v)u(\Omega r - \frac{1}{2}u)dA \end{aligned}$$

Knowing that $\Delta pdA = dT$, it becomes:

$$\int (V + v)dT + \int \rho\Omega r \frac{Cd}{Ct}(V + v)2vdA = \int \rho(V + v)u(\Omega r - \frac{1}{2}u)dA$$

Using the thrust differential form (A.8), $dT = 2\rho(V + v)vdA$:

$$\begin{aligned} \int 2\rho(V + v)(V + v)vdA + \int \rho\Omega r \frac{Cd}{Ct}(V + v)2vdA &= \int \rho(V + v)u(\Omega r - \frac{1}{2}u)dA \\ \rightarrow 2(V + v)v + \Omega r \frac{Cd}{Ct}2v - u(\Omega r - \frac{1}{2}u) &= 0 \end{aligned}$$

A.2 BLADE ELEMENT THEORY

Blade element theory consists in studying the behaviour of the aerofoil of a small portion of the span. It depends on the parameters illustrated in Figure A.5.

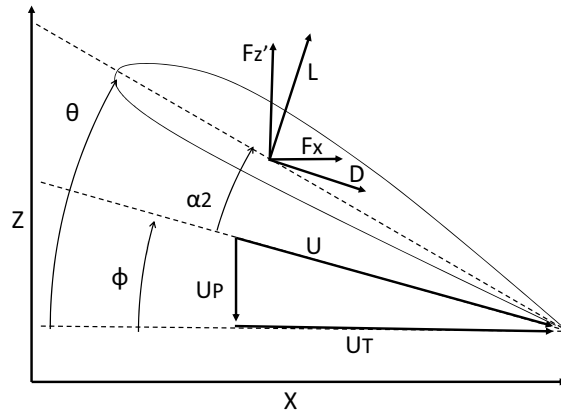


Figure A.5: Profil section

$$U = \sqrt{U_T^2 + U_P^2}$$

$$\phi = \tan^{-1} \left(\frac{U_P}{U_T} \right)$$

$$L = \frac{1}{2} \rho U^2 c c_l$$

$$D = \frac{1}{2} \rho U^2 c c_d$$

$$F_z = L \cos \phi - D \sin \phi$$

$$F_x = L \sin \phi + D \cos \phi$$

Then the physic over the small span portion is studied as shown in Figure A.6. So the thrust,

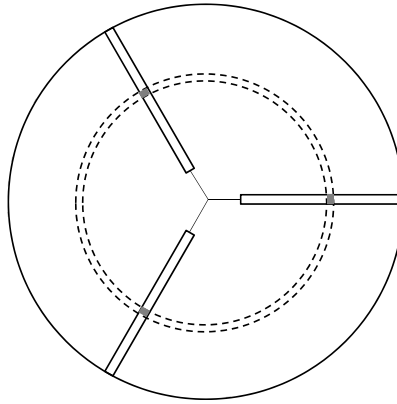


Figure A.6: Rotor disk portion

torque and power can be expressed as:

$$dT = N F_z dr$$

$$dQ = N F_x r dr$$

$$dP = \Omega dQ = N F_x \Omega r dr$$

with N the number of blades. Substituting $U_P = V + v$ and $U_T = \Omega r$, it leads to:

$$\frac{U_P}{U_T} = \frac{V + v}{\Omega r} \lll 0$$

So $\sin \phi \approx \phi$; $\cos \phi \approx 1$ and $\frac{U_P}{U_T} \approx \phi$.

$$U = \sqrt{U_T^2 + U_P^2} \approx U_T \sqrt{1 + \left(\frac{U_P}{U_T}\right)^2} \approx U_T$$

$$L \approx \frac{1}{2} \rho U_T^2 c a \left(\theta - \frac{U_P}{U_T} - \alpha_0 \right)$$

$$D = \frac{1}{2} \rho U_T^2 c c_d$$

where a is the lift curve slope. Then, it leads:

$$F_z \approx L - D\phi$$

$$F_x \approx L\phi + D$$

But with $D \lll L$:

$$F_z \approx L$$

$$F_x \approx L\phi + D$$

And:

$$dT \approx NLdr$$

$$dQ \approx N(L\phi + D)rdr$$

$$dP \approx N(L\phi + D)\Omega rdr$$

A.3 TIP LOSES

As it happens for aircraft, helicopter rotors lose some power by vortex emergence at the tips of the blades as shown in Figure A.7. To take into account this phenomenon, it is considered that the effective power is produced on a rotor disk of radius r , shorter than the actual on R .

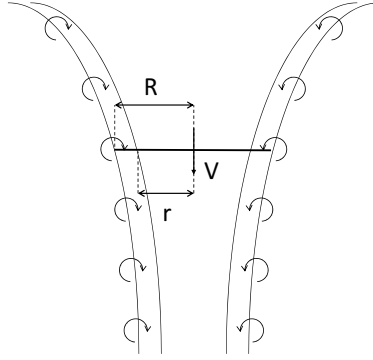


Figure A.7: Tip lose in hover

The parameter B is defined as:

$$B = \frac{r}{R} \quad (\text{A.10})$$

B can be computed using several semi-empirical formulas. The tree most populars are:

Brandlt (1941): $B = 1 - \frac{\sqrt{2C_T}}{N}$ Weathly (1934): $B = 1 - \frac{1}{2} \frac{\text{Chord}_{Tip}}{R}$ Sissingh (1939): $B = 1 - \frac{1}{3} \frac{\text{Chord}_{0.7\text{oftheradius}}}{R}$ So now, the total Thrust is:

$$T = N \int_0^r L dr$$

A.4 ROOT LOSES

There is usually no lift produced at the centre of the rotor since the rotor mechanism moves aside the beginning of the blade aerofoil shape. Therefore, the total thrust becomes:

$$T = N \int_{r_0}^r L dr$$

where r_0 is the radius where the aerofoil shape starts.

A.5 GENERALISATION (CF: AUTOROTATION)

A personal work has been carried out to generalise the theory to all possible conditions such as the autorotation. The previous analysis is generalised to all vertical and induced velocities, upward and downward.

The sign convention is positive for upward forces, positive for downward speed and positive for power given by the rotor to the fluid.

As previously seen in section A.1.5, page 154, the autorotation can be modelled as shown in Figure A.8. Mass conservation gives:

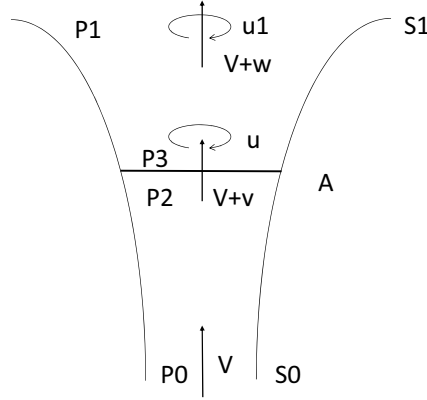


Figure A.8: Autorotation tube flow

$$\dot{m} = \rho V S_0 = \rho \int (V + v) dA$$

Torque Q is:

$$Q = \int \left| \frac{d\dot{m}}{dS_1} \right| u r dA = \rho \int |V + v| u r dA$$

Knowing that $P_{rotor} = \Omega Q$, the mechanical power P is:

$$P = \Omega \rho \int |V + v| u r dA$$

Using the thrust differential generalised form (A.8) $dT = 2\rho|V + v|vdA$:

$$T = \int dT = \int 2\rho|V + v|vdA$$

Knowing that $dP_{lift} = (V + v)dT$, the mechanical power P is:

$$P_{lift} = \int dP_{lift} = \int (V + v)dT = \int 2\rho(V + v)|V + v|vdA$$

The power P_{swirl} does not change from (A.9), except the expression of the mass flow:

$$P_{swirl} = \int \frac{1}{2}\rho|V + v|u^2dA$$

The aerofoil drag power becomes:

$$P_{profil\ drag} = \int \Omega r dD = \int \Omega r \frac{Cd}{Ct} dT = \int \rho \Omega r \frac{Cd}{Ct} |V + v| 2vdA$$

So, adding these components together, it becomes:

$$P = P_{lift} + P_{swirl} + P_{profil\ drag} = \int 2\rho(V + v)|V + v|vdA + \int \frac{1}{2}\rho|V + v|u^2dA + \int \rho \Omega r \frac{Cd}{Ct} |V + v| 2vdA$$

Then equalizing the two expressions of P :

$$\begin{aligned} P &= \Omega \rho \int |V + v| urdA = \int 2\rho(V + v)|V + v|vdA + \int \frac{1}{2}\rho|V + v|u^2dA + \int \rho \Omega r \frac{Cd}{Ct} |V + v| 2vdA \\ &\rightarrow \int 2\rho(V + v)|V + v|vdA + \int \rho \Omega r \frac{Cd}{Ct} |V + v| 2vdA = \int \rho|V + v|u(\Omega r - \frac{1}{2}u)dA \end{aligned}$$

Eventually:

$$\begin{aligned} \int 2\rho(V + v)|V + v|vdA + \int \rho \Omega r \frac{Cd}{Ct} |V + v| 2vdA &= \int \rho|V + v|u(\Omega r - \frac{1}{2}u)dA \\ \rightarrow 2(V + v)v + \Omega r \frac{Cd}{Ct} 2v - u(\Omega r - \frac{1}{2}u) &= 0 \end{aligned}$$

Finally the goal of the rotor design is to minimize the mechanical power:

$$P = \Omega \rho \int |V + v| urdA$$

with the constraint of the required thrust:

$$T = \rho \int |V + v| 2vdA + \int (P_1 - P_0)dS_1$$

The term depending on the pressures is neglected (2%):

$$T = \rho \int |V + v| 2vdA$$

It leads to:

$$2(V + v)v + \Omega r \frac{Cd}{Ct} 2v - u(\Omega r - \frac{1}{2}u) = 0$$

The blade element theory is done as in section A.2, page 155, the autorotation blade element theory can be modelled as shown in Figure A.9.

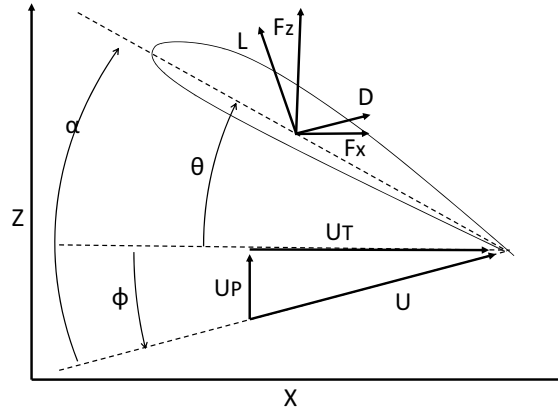


Figure A.9: autorotation profil section

$$U = \sqrt{U_T^2 + U_P^2}$$

$$\phi = \tan^{-1} \left(\frac{U_P}{U_T} \right)$$

$$L = \frac{1}{2} \rho U^2 c c_l$$

$$D = \frac{1}{2} \rho U^2 c c_d$$

$$F_z = L \cos \phi - D \sin \phi$$

$$F_x = L \sin \phi + D \cos \phi$$

The thrust, torque and power can be expressed:

$$dT = NF_z dr$$

$$dQ = NF_x r dr$$

$$dP = \Omega dQ = NF_x \Omega r dr$$

with N the number of blades. Substituting $U_P = V + v$ and $U_T = \Omega r$ it becomes:

$$\left| \frac{U_P}{U_T} \right| = \left| \frac{V + v}{\Omega r} \right| \ll 1$$

So $\sin \phi \approx \phi$; $\sin \cos \approx 1$ and $\frac{U_P}{U_T} \approx \phi$.

$$U = \sqrt{U_T^2 + U_P^2} \approx U_T \sqrt{1 + \left(\frac{U_P}{U_T} \right)^2} \approx U_T$$

$$L \approx \frac{1}{2} \rho U_T^2 c a \left(\theta - \frac{U_P}{U_T} - \alpha_0 \right)$$

$$D = \frac{1}{2} \rho U_T^2 c c_d$$

With a the lift curve slope, becomes:

$$F_z \approx L - D\phi$$

$$F_x \approx L\phi + D$$

With $D \ll L$, it leads to:

$$F_z \approx L$$

$$F_x \approx L\phi + D$$

And:

$$dT \approx NLdr$$

$$dQ \approx N(L\phi + D)rdr$$

$$dP \approx N(L\phi + D)\Omega r dr$$

The blade element theory gives the lift to drag ratio required in the swirl computation:

$$\frac{Cd}{Ct} = \frac{F_x}{F_z} = \frac{L\phi + D}{L} = \frac{c_l\phi + c_d}{c_l} = \phi + \frac{c_d}{c_l}$$

B

APPENDIX: EXTENDED THEORY EQUATIONS

An extended theory has been proposed in section 2.1.2, page 58, to get free from the classical theory flight envelope limitations. The aim of this appendix is to expose the main results of this new theory.

B.1 INDUCED VELOCITY

The induced velocity v is assumed to follow the equation [?]:

$$T = 2\rho Av\sqrt{V^2 + 2Vv \sin \alpha + v^2}$$

where α is the rotor disk angle of attack as shown in Figure B.1. or otherwise:

$$v^4 + v^3 2V \sin \alpha + v^2 V^2 = \left(\frac{T}{2\rho A} \right)^2$$

It can be checked that in hover ($V = 0$), the expression verifies equation (A.1), and at high speed ($V \gg 0$) it becomes:

$$v = \frac{T}{2\rho AV}$$

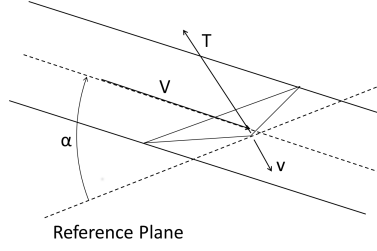


Figure B.1: Induced velocity

which corresponds to the induced velocity of an elliptical wing which is consistent with the fact that a rotor disk can be assimilated to a circular wing.

As in hover, the disk rotor encounter tip loses. So in order to take them into account, the expression retained is:

$$v^4 + v^3 2V \sin \alpha + v^2 V^2 = \left(\frac{T}{2\rho A'} \right)^2 \quad (\text{B.1})$$

where A' is the effective rotor area and follow the expression:

$$A' = B^2 A$$

where B is defined in equation (A.10)

B.2 AERODYNAMICS FORCES AND MOMENT

Combining equation (2.12) with $\phi = \frac{k_3 U_p - k_4 U_T}{U} + k_5$ leads to:

$$\begin{aligned} F_x &= \frac{1}{2} \rho c U \left(U_p a \left(\theta - \left(\frac{k_3 U_p - k_4 U_T}{U} + k_5 \right) - \alpha_0 \right) + c_d U_T \right) \\ &= \frac{1}{2} \rho c U \left(U_p a (\theta - k_5 - \alpha_0) - U_p a \frac{k_3 U_p - k_4 U_T}{U} + c_d U_T \right) \\ &= \frac{1}{2} \rho c (U U_p a (\theta - k_5 - \alpha_0) - U_p a (k_3 U_p - k_4 U_T) + c_d U_T U) \end{aligned}$$

Substituting $U = k_1 U_p + k_2 U_T$, it becomes:

$$\begin{aligned} F_x &= \frac{1}{2} \rho c ((k_1 U_p + k_2 U_T) U_p a (\theta - k_5 - \alpha_0) - U_p a (k_3 U_p - k_4 U_T) + c_d U_T (k_1 U_p + k_2 U_T)) \\ &= \frac{1}{2} \rho c (a (\theta - k_5 - \alpha_0) k_1 U_p^2 + a (\theta - k_5 - \alpha_0) k_2 U_T U_p - a k_3 U_p^2 + a k_4 U_T U_p + k_1 c_d U_T U_p + k_2 c_d U_T^2) \\ &= \frac{1}{2} \rho c (a ((\theta - k_5 - \alpha_0) k_1 - k_3) U_p^2 + (a ((\theta - k_5 - \alpha_0) k_2 + k_4) + k_1 c_d) U_T U_p + k_2 c_d U_T^2) \end{aligned}$$

In the same way, combining equation (2.13) with $\phi = \frac{k_3 U_p - k_4 U_T}{U} + k_5$ gives:

$$\begin{aligned}
F_{z'} &= \frac{1}{2} \rho c U \left(U_T a \left(\theta - \left(\frac{k_3 U_p - k_4 U_T}{U} + k_5 \right) - \alpha_0 \right) - c_d U_P \right) \\
&= \frac{1}{2} \rho c U \left(U_T a (\theta - k_5 - \alpha_0) - U_T a \frac{k_3 U_p - k_4 U_T}{U} - c_d U_P \right) \\
&= \frac{1}{2} \rho c (U U_T a (\theta - k_5 - \alpha_0) - U_T a (k_3 U_p - k_4 U_T) - c_d U_P U)
\end{aligned}$$

And inserting $U = k_1 U_p + k_2 U_T$ leads to:

$$\begin{aligned}
F_{z'} &= \frac{1}{2} \rho c ((k_1 U_p + k_2 U_T) U_T a (\theta - k_5 - \alpha_0) - U_T a (k_3 U_p - k_4 U_T) - c_d U_P (k_1 U_p + k_2 U_T)) \\
&= \frac{1}{2} \rho c (k_1 U_p U_T a (\theta - k_5 - \alpha_0) + k_2 U_T^2 a (\theta - k_5 - \alpha_0) - U_p U_T a k_3 + U_T^2 a k_4 - c_d k_1 U_p^2 - c_d k_2 U_T U_P) \\
&= \frac{1}{2} \rho c (U_p U_T (a (k_1 (\theta - k_5 - \alpha_0) - k_3) - c_d k_2) + U_T^2 a (k_2 (\theta - k_5 - \alpha_0) + k_4) - c_d k_1 U_p^2)
\end{aligned}$$

which gives:

$$F_z = F_{z'} \cos \beta = F_{z'} \cos \beta_0$$

And:

$$F_r = -F_{z'} \sin \beta = -F_{z'} \sin \beta_0$$

The last parameters that must be defined before doing the integrations are $\beta(\psi)$ and $\theta(\psi)$. According to Johnson [?], only the first harmonic is really relevant on a flight dynamics point of view. Parameters are first defined:

$$\beta(\psi) = \beta_0 + \beta_{1c} \cos \psi + \beta_{1s} \sin \psi$$

where β_0 , β_{1c} and β_{1s} are computed in section (B.5) page 179. and:

$$\theta(\psi) = \theta_0 + \theta_{1c} \cos \psi + \theta_{1s} \sin \psi$$

where θ_0 , θ_{1c} and θ_{1s} depend on the swashplate control. It seems that the integrations of F_z and F_r are uneasy ($\int \cos(A \cos \psi + B \sin \psi + C) d\psi$). To make them easier, the overall computation is done in the rotor disk reference plane. Thus, the parameters become:

$$\beta_{1c} = 0$$

$$\beta_1 s = 0$$

$$\beta(\psi) = \beta_0$$

B.2.1 ROTOR LIFT t

The integration is fully detailed only for t to show how it is performed.

$$\begin{aligned}
 t &= \frac{1}{2\pi} \int_0^{2\pi} F_z d\psi = \frac{1}{2\pi} \int_0^{2\pi} F_{z'} \cos \beta_0 d\psi \\
 &= \frac{1}{2\pi} \int_0^{2\pi} \left(\frac{1}{2} \rho c \left(\begin{array}{l} U_p U_T (a(k_1(\theta - k_5 - \alpha_0) - k_3) - c_d k_2) \\ + U_T^2 a(k_2(\theta - k_5 - \alpha_0) + k_4) - c_d k_1 U_p^2 \end{array} \right) \right) \cos \beta_0 d\psi \\
 &= \frac{\rho c \cos \beta_0}{4\pi} \left(\begin{array}{l} \int_0^{2\pi} U_p U_T (a(k_1(\theta - k_5 - \alpha_0) - k_3) - c_d k_2) d\psi \\ + a \int_0^{2\pi} U_T^2 (k_2(\theta - k_5 - \alpha_0) + k_4) d\psi \\ - c_d k_1 \int_0^{2\pi} U_p^2 d\psi \end{array} \right)
 \end{aligned}$$

$$\begin{aligned}
& \int_0^{2\pi} U_p U_T (a(k_1(\theta - k_5 - \alpha_0) - k_3) - c_d k_2) d\psi \\
&= \int_0^{2\pi} ((a(k_1(\theta_0 - k_5 - \alpha_0) - k_3) - c_d k_2) + ak_1\theta_{1c} \cos \psi + ak_1\theta_{1s} \sin \psi) \\
& (\cos \beta_0 V_\lambda + \sin \beta_0 V_\mu \cos \psi) (V_\mu \sin \psi + r\Omega) d\psi \\
&= \int_0^{2\pi} (a(k_1(\theta_0 - k_5 - \alpha_0) - k_3) - c_d k_2) \cos \beta_0 V_\lambda V_\mu \sin \psi \\
& + (a(k_1(\theta_0 - k_5 - \alpha_0) - k_3) - c_d k_2) \cos \beta_0 V_\lambda r\Omega \\
& + (a(k_1(\theta_0 - k_5 - \alpha_0) - k_3) - c_d k_2) \sin \beta_0 V_\mu V_\mu \sin \psi \cos \psi \\
& + (a(k_1(\theta_0 - k_5 - \alpha_0) - k_3) - c_d k_2) \sin \beta_0 V_\mu r\Omega \cos \psi \\
& + ak_1\theta_{1c} \cos \beta_0 V_\lambda V_\mu \cos \psi \sin \psi + ak_1\theta_{1c} \cos \beta_0 V_\lambda r\Omega \cos \psi + ak_1\theta_{1c} \sin \beta_0 V_\mu V_\mu \sin \psi \cos^2 \psi \\
& + ak_1\theta_{1c} \sin \beta_0 V_\mu r\Omega \cos^2 \psi \\
& + ak_1\theta_{1s} \cos \beta_0 V_\lambda V_\mu \sin^2 \psi + ak_1\theta_{1s} \cos \beta_0 V_\lambda r\Omega \sin \psi + ak_1\theta_{1s} \sin \beta_0 V_\mu V_\mu \sin^2 \psi \cos \psi \\
& + ak_1\theta_{1s} \sin \beta_0 V_\mu r\Omega \cos \psi \sin \psi d\psi \\
&= 2\pi (a(k_1(\theta_0 - k_5 - \alpha_0) - k_3) - c_d k_2) \cos \beta_0 V_\lambda r\Omega + ak_1\pi\theta_{1c} \sin \beta_0 V_\mu r\Omega + ak_1\pi\theta_{1s} \cos \beta_0 V_\lambda V_\mu
\end{aligned}$$

$$\begin{aligned}
& \int_0^{2\pi} (k_2 (\theta - k_5 - \alpha_0) + k_4) U_T^2 d\psi \\
&= \int_0^{2\pi} ((k_2 (\theta_0 - k_5 - \alpha_0) + k_4) + k_2 \theta_{1c} \cos \psi + k_2 \theta_{1s} \sin \psi) (V_\mu \sin \psi + r\Omega)^2 d\psi \\
&= \int_0^{2\pi} ((k_2 (\theta_0 - k_5 - \alpha_0) + k_4) V_\mu^2 \sin^2 \psi \\
&+ (k_2 (\theta_0 - k_5 - \alpha_0) + k_4) r^2 \Omega^2 \\
&+ 2 (k_2 (\theta_0 - k_5 - \alpha_0) + k_4) V_\mu r \Omega \sin \psi \\
&+ k_2 \theta_{1c} V_\mu^2 \cos \psi \sin^2 \psi + k_2 \theta_{1c} r^2 \Omega^2 \cos \psi + 2k_2 \theta_{1c} V_\mu r \Omega \cos \psi \sin \psi \\
&+ k_2 \theta_{1s} V_\mu^2 \sin^3 \psi + k_2 \theta_{1s} r^2 \Omega^2 \sin \psi + 2k_2 \theta_{1s} V_\mu r \Omega \sin^2 \psi) d\psi \\
&= \pi (k_2 (\theta_0 - k_5 - \alpha_0) + k_4) V_\mu^2 + 2\pi (k_2 (\theta_0 - k_5 - \alpha_0) + k_4) r^2 \Omega^2 + 2\pi k_2 \theta_{1s} V_\mu r \Omega
\end{aligned}$$

$$\begin{aligned}
\int_0^{2\pi} U_P^2 d\psi &= \int_0^{2\pi} (\cos \beta_0 V_\lambda + \sin \beta_0 V_\mu \cos \psi)^2 d\psi \\
&= \int_0^{2\pi} (\cos^2 \beta_0 V_\lambda^2 + \sin^2 \beta_0 V_\mu^2 \cos^2 \psi + 2 \cos \beta_0 \sin \beta_0 V_\lambda V_\mu \cos \psi) d\psi \\
&= 2\pi \cos^2 \beta_0 V_\lambda^2 + \pi \sin^2 \beta_0 V_\mu^2
\end{aligned}$$

$$t = \frac{\rho c \cos \beta_0}{4\pi} \left(\begin{array}{l} 2\pi (a (k_1 (\theta_0 - k_5 - \alpha_0) - k_3) - c_d k_2) \cos \beta_0 V_\lambda r \Omega \\ + a k_1 \pi \theta_{1c} \sin \beta_0 V_\mu r \Omega + a k_1 \pi \theta_{1s} \cos \beta_0 V_\lambda V_\mu \\ + \pi a (k_2 (\theta_0 - k_5 - \alpha_0) + k_4) V_\mu^2 \\ + 2\pi a (k_2 (\theta_0 - k_5 - \alpha_0) + k_4) r^2 \Omega^2 + 2\pi a k_2 \theta_{1s} V_\mu r \Omega \\ - 2\pi c_d k_1 \cos^2 \beta_0 V_\lambda^2 - \pi c_d k_1 \sin^2 \beta_0 V_\mu^2 \end{array} \right)$$

B.2.2 ROTOR LONGITUDINAL FORCE h

$$\begin{aligned}
h &= \frac{1}{2\pi} \int_0^{2\pi} (F_x \sin \psi + F_r \cos \psi) d\psi \\
&= \frac{\rho c}{4\pi} \left(\begin{aligned} &\pi a k_1 \theta_{1s} \cos^2 \beta_0 V_\lambda^2 + \frac{\pi}{4} a k_1 \theta_{1s} \sin^2 \beta_0 V_\mu^2 \\ &+ \pi (a ((\theta_0 - k_5 - \alpha_0) k_2 + k_4) + k_1 c_d) \cos \beta_0 V_\lambda V_\mu \\ &+ \frac{\pi}{4} a k_2 \theta_{1c} \sin \beta_0 V_\mu V_\mu + \pi a k_2 \theta_{1s} \cos \beta_0 V_\lambda r \Omega \\ &+ k_2 c_d 2\pi V_\mu r \Omega \end{aligned} \right) \\
&\quad - \frac{\rho c \sin \beta_0}{4\pi} \left(\begin{aligned} &[a (k_1 (\theta_0 - k_5 - \alpha_0) - k_3) - c_d k_2] [\pi \sin \beta_0 r \Omega V_\mu] \\ &+ \pi \cos \beta_0 r \Omega V_\lambda a k_1 \theta_{1c} + \frac{\pi}{4} \sin \beta_0 V_\mu V_\mu a k_1 \theta_{1s} \\ &+ \frac{\pi}{4} a k_2 \theta_{1c} V_\mu^2 + \pi a k_2 \theta_{1c} r^2 \Omega^2 \\ &- k_1 c_d 2\pi \cos \beta_0 \sin \beta_0 V_\lambda V_\mu \end{aligned} \right)
\end{aligned}$$

B.2.3 ROTOR LATERAL FORCE y

$$\begin{aligned}
y &= \frac{1}{2\pi} \int_0^{2\pi} (-F_x \cos \psi + F_r \sin \psi) d\psi \\
&= -\frac{\rho c}{4\pi} \left(\begin{aligned} &2\pi a ((\theta_0 - k_5 - \alpha_0) k_1 - k_3) \cos \beta_0 \sin \beta_0 V_\lambda V_\mu \\ &+ \pi a k_1 \theta_{1c} \cos^2 \beta_0 V_\lambda^2 + \frac{3\pi}{4} a k_1 \theta_{1c} \sin^2 \beta_0 V_\mu^2 \\ &+ \pi (a ((\theta_0 - k_5 - \alpha_0) k_2 + k_4) + k_1 c_d) \sin \beta_0 V_\mu r \Omega \\ &+ \pi a k_2 \theta_{1c} \cos \beta_0 V_\lambda r \Omega + \frac{\pi}{4} a k_2 \theta_{1s} \sin \beta_0 V_\mu V_\mu \end{aligned} \right) \\
&\quad - \frac{\rho c \sin \beta_0}{4\pi} \left(\begin{aligned} &(a (k_1 (\theta_0 - k_5 - \alpha_0) - k_3) - c_d k_2) \pi \cos \beta_0 V_\lambda V_\mu \\ &+ \frac{\pi}{4} \sin \beta_0 V_\mu^2 a k_1 \theta_{1c} + \pi \cos \beta_0 r \Omega V_\lambda a k_1 \theta_{1s} \\ &+ 2\pi a (k_2 (\theta_0 - k_5 - \alpha_0) + k_4) V_\mu r \Omega + \frac{3\pi}{4} a k_2 \theta_{1s} V_\mu^2 + \pi a k_2 \theta_{1s} r^2 \Omega^2 \end{aligned} \right)
\end{aligned}$$

B.2.4 ROTOR TORQUE Q

$$Q = \frac{1}{2\pi} \int_0^{2\pi} r F_x d\psi$$

$$= \frac{r\rho c}{4\pi} \left(\begin{array}{l} 2\pi a ((\theta_0 - k_5 - \alpha_0) k_1 - k_3) \cos^2 \beta_0 V_\lambda^2 \\ + \pi a ((\theta_0 - k_5 - \alpha_0) k_1 - k_3) \sin^2 \beta_0 V_\mu^2 + 2\pi a k_1 \theta_{1c} \cos \beta_0 \sin \beta_0 V_\lambda V_\mu \\ + 2\pi (a ((\theta_0 - k_5 - \alpha_0) k_2 + k_4) + k_1 c_d) \cos \beta_0 V_\lambda r \Omega \\ + \pi a k_2 \theta_{1c} \sin \beta_0 V_\mu r \Omega + \pi a k_2 \theta_{1s} \cos \beta_0 V_\lambda V_\mu \\ + k_2 c_d \pi V_\mu^2 + 2k_2 c_d \pi r^2 \Omega^2 \end{array} \right)$$

B.3 PROPULSION FORCES AND MOMENTS:

The propulsion system is installed on the concept rotor blades, as shown in Figure B.2.

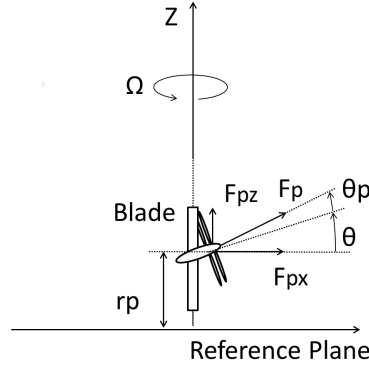


Figure B.2: Self propelled rotor

$$F_{px} = F_p \cos(\theta + \theta_p)$$

$$F_{pz'} = F_p \sin(\theta + \theta_p)$$

As for the aerodynamic lift, the propulsion lifting force has to be projected between the axial force F_{pz} and the radial force F_{pr} :

$$F_{pz} = F_{pz'} \cos \beta$$

$$F_{pr} = -\sin \beta F_{pz'}$$

The average over a revolution is obtained by integration of the force generated by both propulsion systems as shown in Figure B.3

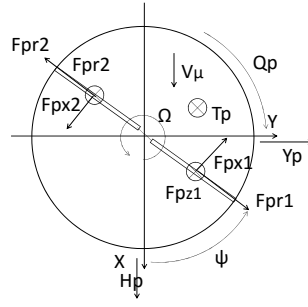


Figure B.3: Propulsion axial and radial forces and torque

$$T_p = \frac{1}{2\pi} \int_0^{2\pi} F_{pz1} + F_{pz2} d\psi$$

$$H_p = \frac{1}{2\pi} \int_0^{2\pi} (-F_{px1} \sin \psi + F_{pr1} \cos \psi + F_{px2} \sin \psi - F_{pr2} \cos \psi) d\psi$$

$$Y_p = \frac{1}{2\pi} \int_0^{2\pi} (F_{px1} \cos \psi + F_{pr1} \sin \psi - F_{px2} \cos \psi - F_{pr2} \sin \psi) d\psi$$

$$Q_p = \frac{1}{2\pi} \int_0^{2\pi} -r_p F_{px1} - r_p F_{px2} d\psi$$

As for the aerodynamics analysis, the study is done in the rotor blade tip reference frame:

$$F_{px} = F_p \cos(\theta + \theta_p)$$

$$F_{pz'} = F_p \sin(\theta + \theta_p)$$

$$F_{pz} = F_{pz'} \cos \beta_0$$

$$F_{pr} = -F_{pz'} \sin \beta_0$$

Considering the Fourier decomposition of θ :

$$\theta = \theta_0 + \theta_{1c} \cos \psi + \theta_{1s} \sin \psi$$

It comes:

$$\begin{aligned} F_{pz'} &= F_p \sin(\theta + \theta_p) = F_p \sin(\theta_p + \theta_0 + \theta_{1c} \cos \psi + \theta_{1s} \sin \psi) \\ &= F_p \sin(\theta_p + \theta_0) \cos(\theta_{1c} \cos \psi + \theta_{1s} \sin \psi) + F_p \cos(\theta_p + \theta_0) \sin(\theta_{1c} \cos \psi + \theta_{1s} \sin \psi) \end{aligned}$$

Considering that θ_0 can be high but θ_{1c} and θ_{1s} remain low, the following approximation is made:

$$F_{pz'} \approx F_p \sin(\theta_p + \theta_0) + F_p \cos(\theta_p + \theta_0) (\theta_{1c} \cos \psi + \theta_{1s} \sin \psi)$$

In the same way, F_{px} becomes:

$$\begin{aligned} F_{px} &= F_p \cos(\theta + \theta_p) = F_p \cos(\theta_p + \theta_0 + \theta_{1c} \cos \psi + \theta_{1s} \sin \psi) \\ &= F_p \cos(\theta_p + \theta_0) \cos(\theta_{1c} \cos \psi + \theta_{1s} \sin \psi) - F_p \sin(\theta_p + \theta_0) \sin(\theta_{1c} \cos \psi + \theta_{1s} \sin \psi) \\ &\approx F_p \cos(\theta_p + \theta_0) - F_p \sin(\theta_p + \theta_0) (\theta_{1c} \cos \psi + \theta_{1s} \sin \psi) \end{aligned}$$

The propulsion force is assumed to be of the form: $F_p = F_{p0} + F_{pc} \cos \psi + F_{ps} \sin \psi$ Since the two engines are offset by an angle of π , it comes:

$$F_{p1} = F_{p0} + F_{pc} \cos \psi + F_{ps} \sin \psi$$

$$F_{p2} = F_{p0} + F_{pc} \cos(\psi + \pi) + F_{ps} \sin(\psi + \pi) = F_{p0} - F_{pc} \cos \psi - F_{ps} \sin \psi$$

The integration over the rotor disk can be performed.

B.3.1 PROPULSION LIFT T_p

As for the aerodynamics lift of the blade in section B.2.1 page 168, the detail of the calculation is exposed only for the propulsion lift:

$$\begin{aligned}
T_p &= \frac{1}{2\pi} \int_0^{2\pi} F_{pz1} + F_{pz2} d\psi \\
&= \frac{\cos \beta_0}{2\pi} \left(\int_0^{2\pi} F_{pz'1} d\psi + \int_0^{2\pi} F_{pz'2} d\psi \right) \\
&= \frac{\cos \beta_0}{2\pi} \left(\int_0^{2\pi} \begin{pmatrix} (F_{p0} + F_{pc} \cos \psi + F_{ps} \sin \psi) \\ (\sin(\theta_p + \theta_0) + \cos(\theta_p + \theta_0) (\theta_{1c} \cos \psi + \theta_{1s} \sin \psi)) \end{pmatrix} d\psi \right. \\
&\quad \left. + \int_0^{2\pi} \begin{pmatrix} (F_{p0} + F_{pc} \cos(\psi + \pi) + F_{ps} \sin(\psi + \pi)) \\ (\sin(\theta_p + \theta_0) + \cos(\theta_p + \theta_0) (\theta_{1c} \cos(\psi + \pi) + \theta_{1s} \sin(\psi + \pi))) \end{pmatrix} d\psi \right)
\end{aligned}$$

Applying the variable substitution $\psi' = \psi + \pi$ to the second term of the integration:

$$T_p = \frac{\cos \beta_0}{2\pi} \left(\int_0^{2\pi} \begin{pmatrix} (F_{p0} + F_{pc} \cos \psi + F_{ps} \sin \psi) \\ (\sin(\theta_p + \theta_0) + \cos(\theta_p + \theta_0) (\theta_{1c} \cos \psi + \theta_{1s} \sin \psi)) \end{pmatrix} d\psi \right. \\
\left. + \int_{\pi}^{3\pi} \begin{pmatrix} (F_{p0} + F_{pc} \cos \psi + F_{ps} \sin \psi) \\ (\sin(\theta_p + \theta_0) + \cos(\theta_p + \theta_0) (\theta_{1c} \cos \psi + \theta_{1s} \sin \psi)) \end{pmatrix} d\psi \right)$$

Noting that the second term is periodic of period 2π , it gives:

$$\begin{aligned}
T_p &= \frac{\cos \beta_0}{\pi} \int_0^{2\pi} (F_{p0} + F_{pc} \cos \psi + F_{ps} \sin \psi) (\sin(\theta_p + \theta_0) + \cos(\theta_p + \theta_0) (\theta_{1c} \cos \psi + \theta_{1s} \sin \psi)) d\psi \\
&= \frac{\cos \beta_0}{\pi} \int_0^{2\pi} F_{p0} \sin(\theta_p + \theta_0) + F_{p0} \cos(\theta_p + \theta_0) (\theta_{1c} \cos \psi + \theta_{1s} \sin \psi) \\
&\quad + F_{pc} \cos \psi \sin(\theta_p + \theta_0) + \cos(\theta_p + \theta_0) (\theta_{1c} F_{pc} \cos^2 \psi + \theta_{1s} F_{pc} \cos \psi \sin \psi) \\
&\quad + F_{ps} \sin \psi \sin(\theta_p + \theta_0) + \cos(\theta_p + \theta_0) (\theta_{1c} F_{ps} \sin \psi \cos \psi + \theta_{1s} F_{ps} \sin^2 \psi) d\psi \\
&= \cos \beta_0 (2F_{p0} \sin(\theta_p + \theta_0) + \cos(\theta_p + \theta_0) (\theta_{1c} F_{pc} + \theta_{1s} F_{ps}))
\end{aligned}$$

which corresponds to twice the force generated by the first propeller.

B.3.2 PROPULSION LONGITUDINAL FORCE H_p

In the same way:

$$\begin{aligned}
H_P &= \frac{1}{2\pi} \int_0^{2\pi} -F_{px1} \sin \psi + F_{pr1} \cos \psi + F_{px2} \sin \psi - F_{pr2} \cos \psi d\psi \\
&= -(F_{ps} \cos(\theta_p + \theta_0) - \sin(\theta_p + \theta_0) F_{p0} \theta_{1s} + F_{pc} \sin(\theta_p + \theta_0) \sin \beta_0 + \cos(\theta_p + \theta_0) F_{p0} \theta_{1c} \sin \beta_0)
\end{aligned}$$

B.3.3 PROPULSION LATERAL FORCE Y_p

$$\begin{aligned}
Y_P &= \frac{1}{2\pi} \int_0^{2\pi} F_{px1} \cos \psi + F_{pr1} \sin \psi - F_{px2} \cos \psi - F_{pr2} \sin \psi d\psi \\
&= F_{pc} \cos(\theta_p + \theta_0) - \sin(\theta_p + \theta_0) F_{p0} \theta_{1c} - F_{ps} \sin(\theta_p + \theta_0) \sin \beta_0 - \cos(\theta_p + \theta_0) F_{p0} \theta_{1s} \sin \beta_0
\end{aligned}$$

B.3.4 PROPULSION TORQUE Q_p

$$\begin{aligned}
Q_P &= \frac{1}{2\pi} \int_0^{2\pi} -r_p F_{px1} - r_p F_{px2} d\psi \\
&= -r_p (2F_{p0} \cos(\theta_p + \theta_0) - \sin(\theta_p + \theta_0) (F_{pc} \theta_{1c} + F_{ps} \theta_{1s}))
\end{aligned}$$

B.4 OVERALL ROTOR FORCES:

The forces must be integrated along the span in addition to the already performed integration over rotation. This new integration takes place from the starting radius of the rotor to the tip of the rotor for drags and power entities, and to a smaller radius for the lift to take into account the vortex tip loss. Therefore the overall thrust becomes:

$$\begin{aligned}
T_z &= p \int_{r_0}^r t dr + T_p \\
&= \frac{\rho p \cos \beta_0}{4} \int_{r_0}^r c \left(\begin{array}{l} 2(a(k_1(\theta_0 - k_5 - \alpha_0) - k_3) - c_d k_2) \cos \beta_0 V_\lambda r \Omega \\ + a k_1 \theta_{1c} \sin \beta_0 V_\mu r \Omega + a k_1 \theta_{1s} \cos \beta_0 V_\lambda V_\mu \\ + a(k_2(\theta_0 - k_5 - \alpha_0) + k_4) V_\mu^2 \\ + 2a(k_2(\theta_0 - k_5 - \alpha_0) + k_4) r^2 \Omega^2 + 2a k_2 \theta_{1s} V_\mu r \Omega \\ - 2c_d k_1 \cos^2 \beta_0 V_\lambda^2 - c_d k_1 \sin^2 \beta_0 V_\mu^2 \end{array} \right) dr \quad (\text{B.2}) \\
&+ \cos \beta_0 (2F_{p0} \sin(\theta_p + \theta_0) + \cos(\theta_p + \theta_0) (\theta_{1c} F_{pc} + \theta_{1s} F_{ps}))
\end{aligned}$$

where: $r = B \times R$ The lateral force F_y is:

$$\begin{aligned}
F_y &= p \int_{r_0}^R y dr + Y_p \\
&= -p \frac{\rho}{4} \int_{r_0}^R c \left(\begin{array}{l} \left(\begin{array}{l} 2a((\theta_0 - k_5 - \alpha_0)k_1 - k_3) \cos \beta_0 \sin \beta_0 V_\lambda V_\mu \\ + ak_1 \theta_{1c} \cos^2 \beta_0 V_\lambda^2 + \frac{3}{4} ak_1 \theta_{1c} \sin^2 \beta_0 V_\mu^2 \\ + (a((\theta_0 - k_5 - \alpha_0)k_2 + k_4) + k_1 c_d) \sin \beta_0 V_\mu r \Omega \\ + ak_2 \theta_{1c} \cos \beta_0 V_\lambda r \Omega + \frac{1}{4} ak_2 \theta_{1s} \sin \beta_0 V_\mu V_\mu \end{array} \right) \\ + c \sin \beta_0 \left(\begin{array}{l} (a(k_1(\theta_0 - k_5 - \alpha_0) - k_3) - c_d k_2) \cos \beta_0 V_\lambda V_\mu \\ + \frac{1}{4} \sin \beta_0 V_\mu^2 ak_1 \theta_{1c} + \cos \beta_0 r \Omega V_\lambda ak_1 \theta_{1s} \\ + 2a(k_2(\theta_0 - k_5 - \alpha_0) + k_4) V_\mu r \Omega \\ + \frac{3}{4} ak_2 \theta_{1s} V_\mu^2 + ak_2 \theta_{1s} r^2 \Omega^2 \end{array} \right) \end{array} \right) dr \\
&+ F_{p_c} \cos(\theta_p + \theta_0) - \sin(\theta_p + \theta_0) F_{p_0} \theta_{1c} - F_{p_s} \sin(\theta_p + \theta_0) \sin \beta_0 - \cos(\theta_p + \theta_0) F_{p_0} \theta_{1s} \sin \beta_0
\end{aligned} \tag{B.3}$$

The overall drag F_x becomes:

$$\begin{aligned}
F_x &= p \int_{r_0}^R h dr + H_p \\
&= \frac{\rho p}{4} \int_{r_0}^R c \left(\begin{array}{l} \left(\begin{array}{l} ak_1 \theta_{1s} \cos^2 \beta_0 V_\lambda^2 + \frac{1}{4} ak_1 \theta_{1s} \sin^2 \beta_0 V_\mu^2 \\ + (a((\theta_0 - k_5 - \alpha_0)k_2 + k_4) + k_1 c_d) \cos \beta_0 V_\lambda V_\mu \\ + \frac{1}{4} ak_2 \theta_{1c} \sin \beta_0 V_\mu V_\mu + ak_2 \theta_{1s} \cos \beta_0 V_\lambda r \Omega \\ + k_2 c_d 2 V_\mu r \Omega \end{array} \right) \\ - c \sin \beta_0 \left(\begin{array}{l} [a(k_1(\theta_0 - k_5 - \alpha_0) - k_3) - c_d k_2] [\sin \beta_0 r \Omega V_\mu] \\ + \cos \beta_0 r \Omega V_\lambda ak_1 \theta_{1c} + \frac{1}{4} \sin \beta_0 V_\mu V_\mu ak_1 \theta_{1s} \\ + \frac{1}{4} ak_2 \theta_{1c} V_\mu^2 + ak_2 \theta_{1c} r^2 \Omega^2 - k_1 c_d 2 \cos \beta_0 \sin \beta_0 V_\lambda V_\mu \end{array} \right) \end{array} \right) dr \\
&- (F_{p_s} \cos(\theta_p + \theta_0) - \sin(\theta_p + \theta_0) F_{p_0} \theta_{1s} + F_{p_c} \sin(\theta_p + \theta_0) \sin \beta_0 + \cos(\theta_p + \theta_0) F_{p_0} \theta_{1c} \sin \beta_0)
\end{aligned} \tag{B.4}$$

The torque Q_r becomes:

$$\begin{aligned}
 Q_r &= p \int_{r_0}^R Q dr + Q_p \\
 &= \frac{p\rho}{4} \int_{r_0}^R r c \left(\begin{aligned}
 &2a((\theta_0 - k_5 - \alpha_0)k_1 - k_3) \cos^2 \beta_0 V_\lambda^2 \\
 &+ a((\theta_0 - k_5 - \alpha_0)k_1 - k_3) \sin^2 \beta_0 V_\mu^2 + 2ak_1\theta_{1c} \cos \beta_0 \sin \beta_0 V_\lambda V_\mu \\
 &+ 2(a((\theta_0 - k_5 - \alpha_0)k_2 + k_4) + k_1 c_d) \cos \beta_0 V_\lambda r \Omega \\
 &+ ak_2\theta_{1c} \sin \beta_0 V_\mu r \Omega + ak_2\theta_{1s} \cos \beta_0 V_\lambda V_\mu \\
 &+ k_2 c_d V_\mu^2 + 2k_2 c_d r^2 \Omega^2
 \end{aligned} \right) dr \quad (\text{B.5}) \\
 &\quad -r_p (2F_{p_0} \cos(\theta_p + \theta_0) - \sin(\theta_p + \theta_0) (F_{p_c}\theta_{1c} + F_{p_s}\theta_{1s}))
 \end{aligned}$$

The flap motion is lastly studied to complete the study of horizontal flight.

B.5 FLAP MOTION

The proposed rotor is a self-propelled teetering rotor constituted with two blades attached together without any flap or lag hinge as shown in Figure B.4, with a propulsion system installed over its blade. The fundamental principle of the dynamics is applied considering

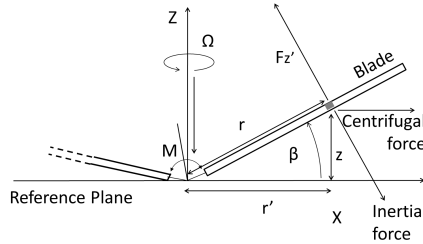


Figure B.4: teetering-rotor-dynamic

the following forces:

- The centrifugal force: $F_{centrifugal} = m\Omega^2 r'$
- The aerodynamic force F'_z
- The propulsive force F_P

The equation of moments over the blade is:

$$\begin{aligned}
& J_{2\Delta blade} \ddot{\beta}_1 \\
&= \int_{root}^{tip} r F_{z'1} dr - \int_{root}^{tip} r \sin \beta_1 m \Omega^2 r' dr + r_p F_{p1} \sin(\theta_1 + \theta_p) \\
&- \left(\int_{root}^{tip} r F_{z'2} dr - \int_{root}^{tip} r \sin \beta_2 m \Omega^2 r' dr + r_p F_{p2} \sin(\theta_2 + \theta_p) \right) - K_\beta (\beta_1 - \beta_K) \\
&\Leftrightarrow J_{2\Delta blade} (\ddot{\beta}_1) + J_{\Delta blade} \Omega^2 (\sin \beta_1 \cos \beta_1 - \sin \beta_2 \cos \beta_2) + K_\beta (\beta_1 - \beta_K) \\
&= \int_{root}^{tip} r F_{z'1} dr - \int_{root}^{tip} r F_{z'2} dr + r_p F_{p1} \sin(\theta_1 + \theta_p) - r_p F_{p2} \sin(\theta_2 + \theta_p)
\end{aligned}$$

In the classical theory, the integration is done in the horizontal plane, where β remains small. This is not true anymore in the present case, therefore, the calculation is performed in a slowly moving reference plane close to the one of the rotor disk for simplified calculations. The first consequence is that $\beta \ll \pi$, which implies:

$$\begin{aligned}
& J_{2\Delta blade} (\ddot{\beta}_1) + J_{\Delta blade} \Omega^2 (\beta_1 - \beta_2) + K_\beta (\beta_1 - \beta_K) \\
&= \int_{root}^{tip} r F_{z'1} dr - \int_{root}^{tip} r F_{z'2} dr + r_p F_{p1} \sin(\theta_1 + \theta_p) - r_p F_{p2} \sin(\theta_2 + \theta_p)
\end{aligned}$$

Using the development in Fourier series, it leads to:

$$\beta_1 = \beta_0 + \beta_{1c} \cos \psi + \beta_{1s} \sin \psi$$

It becomes:

$$\ddot{\beta}_1 = -\Omega^2 ((\beta_{1c} \cos \psi + \beta_{1s} \sin \psi))$$

For the second blade the equation is:

$$\beta_2 = \beta_0 + \beta_{1c} \cos(\psi + \pi) + \beta_{1s} \sin(\psi + \pi) = \beta_0 - \beta_{1c} \cos \psi - \beta_{1s} \sin \psi$$

It becomes:

$$\begin{aligned} & - J_{2\Delta blade} (\Omega^2 ((\beta_{1c} \cos \psi + \beta_{1s} \sin \psi))) \\ & + J_{\Delta blade} \Omega^2 (\beta_0 + \beta_{1c} \cos \psi + \beta_{1s} \sin \psi - \beta_0 + \beta_{1c} \cos \psi + \beta_{1s} \sin \psi) + K_\beta (\beta_1 - \beta_K) \\ & = \int_{root}^{tip} r F_{z'1} dr - \int_{root}^{tip} r F_{z'2} dr + r_p F_{p1} \sin(\theta_1 + \theta_p) - r_p F_{p2} \sin(\theta_2 + \theta_p) \\ & \Leftrightarrow K_\beta (\beta_0 + \beta_{1c} \cos \psi + \beta_{1s} \sin \psi - \beta_K) \\ & = \int_{root}^{tip} r F_{z'1} dr - \int_{root}^{tip} r F_{z'2} dr + r_p F_{p1} \sin(\theta_1 + \theta_p) - r_p F_{p2} \sin(\theta_2 + \theta_p) \end{aligned}$$

Considering that by construction $\beta_0 = \beta_K$, it becomes:

$$\begin{aligned} K_\beta (\beta_{1c} \cos \psi + \beta_{1s} \sin \psi) & = \int_{root}^{tip} r F_{z'1} dr - \int_{root}^{tip} r F_{z'2} dr \\ & + r_p F_{p1} \sin(\theta_1 + \theta_p) - r_p F_{p2} \sin(\theta_2 + \theta_p) \end{aligned}$$

The integration over the rotor disk with $\sin \psi$ gives:

$$\begin{aligned}
& \frac{1}{2\pi} \int_0^{2\pi} K_\beta (\beta_{1c} \cos \psi + \beta_{1s} \sin \psi) \sin \psi d\psi \\
&= \frac{1}{2\pi} \int_0^{2\pi} \int_{root}^{tip} r F_{z'1} dr \sin \psi d\psi - \frac{1}{2\pi} \int_0^{2\pi} \int_{root}^{tip} r F_{z'2} dr \sin \psi d\psi \\
&+ \frac{1}{2\pi} \int_0^{2\pi} r_p F_{p1} \sin (\theta_1 + \theta_p) \sin \psi d\psi - \frac{1}{2\pi} \int_0^{2\pi} r_p F_{p2} \sin (\theta_2 + \theta_p) \sin \psi d\psi
\end{aligned}$$

Considering that: $F_{z'2}(\psi) = F_{z'1}(\psi + \pi)$, it becomes:

$$\begin{aligned}
& \frac{1}{2\pi} \int_0^{2\pi} K_\beta (\beta_{1c} \cos \psi + \beta_{1s} \sin \psi) \sin \psi d\psi = 2 \frac{1}{2\pi} \int_0^{2\pi} \int_{root}^{tip} r F_{z'} dr \sin \psi d\psi \\
&+ \frac{1}{2\pi} \int_0^{2\pi} r_p F_{p1} \sin (\theta_1 + \theta_p) \sin \psi d\psi - \frac{1}{2\pi} \int_0^{2\pi} r_p F_{p2} \sin (\theta_2 + \theta_p) \sin \psi d\psi \\
&\Rightarrow \frac{K_\beta}{4} \beta_{1s} = \frac{1}{2\pi} \int_{root}^{tip} r \int_0^{2\pi} F_{z'} \sin \psi d\psi dr \\
&+ \frac{1}{2} \left(\frac{1}{2\pi} \int_0^{2\pi} r_p F_{p1} \sin (\theta_1 + \theta_p) \sin \psi d\psi - \frac{1}{2\pi} \int_0^{2\pi} r_p F_{p2} \sin (\theta_2 + \theta_p) \sin \psi d\psi \right)
\end{aligned}$$

In the same way, it leads to:

$$\begin{aligned}
& \frac{K_\beta}{4} \beta_{1c} = \frac{1}{2\pi} \int_{root}^{tip} r \int_0^{2\pi} F_{z'} \cos \psi d\psi dr \\
&+ \frac{1}{2} \left(\frac{1}{2\pi} \int_0^{2\pi} r_p F_{p1} \sin (\theta_1 + \theta_p) \cos \psi d\psi - \frac{1}{2\pi} \int_0^{2\pi} r_p F_{p2} \sin (\theta_2 + \theta_p) \cos \psi d\psi \right)
\end{aligned}$$

B.5.1 LIFT PART

Noting that $F'_z = \frac{F_z}{\cos \beta}$, it becomes

Sinus component

$$\int_0^{2\pi} F_{z'} \sin \psi d\psi$$

$$= \frac{1}{2} \rho c \left(\begin{array}{l} \int_0^{2\pi} U_p U_T (a(k_1(\theta - k_5 - \alpha_0) - k_3) - c_d k_2) \sin \psi d\psi \\ + \int_0^{2\pi} U_T^2 a(k_2(\theta - k_5 - \alpha_0) + k_4) \sin \psi d\psi \\ - c_d k_1 \int_0^{2\pi} U_p^2 \sin \psi d\psi \end{array} \right)$$

With β small, it becomes:

$$U_P = \cos \beta V_\lambda + \sin \beta V_\mu \cos \psi + r \dot{\beta} \approx V_\lambda + \beta V_\mu \cos \psi + r \dot{\beta}$$

$$\approx V_\lambda + (\beta_0 V_\mu + r \beta_{1s} \Omega) \cos \psi + \beta_{1c} V_\mu \cos^2 \psi + \beta_{1s} V_\mu \cos \psi \sin \psi - r \beta_{1c} \Omega \sin \psi$$

It leads to:

$$\int_0^{2\pi} F_{z'} \sin \psi d\psi = \frac{1}{2} \rho c \left(\begin{array}{l} (a(k_1(\theta_0 - k_5 - \alpha_0) - k_3) - c_d k_2) (\pi V_\lambda V_\mu + \frac{\pi}{4} \beta_{1c} V_\mu^2 - \pi \beta_{1c} r^2 \Omega^2) \\ + \frac{\pi}{4} (\beta_0 V_\mu + 2\beta_{1s} r \Omega) V_\mu a k_1 \theta_{1c} + (\pi V_\lambda - \frac{\pi}{2} \beta_{1c} V_\mu) r \Omega a k_1 \theta_{1s} \\ + 2\pi a r \Omega V_\mu (k_2(\theta_0 - k_5 - \alpha_0) + k_4) + a k_2 \theta_{1s} (\frac{3\pi}{4} V_\mu^2 + \pi r^2 \Omega^2) \\ + 2c_d k_1 \pi r \beta_{1c} \Omega V_\lambda - \frac{\pi}{2} c_d k_1 \beta_{1s} V_\mu (\beta_0 V_\mu + r \beta_{1s} \Omega) + \frac{\pi}{2} c_d k_1 r \beta_{1c} \Omega \beta_{1c} V_\mu \end{array} \right)$$

Cosinus component In the same way as the sinus component:

$$\begin{aligned}
& \int_0^{2\pi} F_{z'} \cos \psi d\psi \\
&= \frac{1}{2} \rho c \left(\begin{array}{l} \int_0^{2\pi} U_p U_T (a(k_1(\theta - k_5 - \alpha_0) - k_3) - c_d k_2) \cos \psi d\psi \\ + \int_0^{2\pi} U_T^2 a(k_2(\theta - k_5 - \alpha_0) + k_3) \cos \psi d\psi \\ - c_d k_1 \int_0^{2\pi} U_p^2 \cos \psi d\psi \end{array} \right) \\
&= \frac{1}{2} \rho c \left(\begin{array}{l} (a(k_1(\theta_0 - k_5 - \alpha_0) - k_3) - c_d k_2) \left(\frac{\pi}{4} \beta_{1s} V_\mu^2 + \pi(\beta_0 V_\mu + r \beta_{1s} \Omega) r \Omega \right) \\ + a k_1 \theta_{1c} (\pi V_\lambda r \Omega + \frac{\pi}{2} \beta_{1c} V_\mu r \Omega) + \frac{\pi}{4} a k_1 \theta_{1s} (\beta_0 V_\mu + 2r \Omega \beta_{1s}) V_\mu \\ + a k_2 \theta_{1c} \left(\frac{\pi}{4} V_\mu^2 + \pi r^2 \Omega^2 \right) \\ - 2\pi c_d k_1 (\beta_0 V_\mu + r \beta_{1s} \Omega) V_\lambda - c_d k_1 \beta_{1c} V_\mu \left(\frac{3\pi}{2} \beta_0 V_\mu + \pi \beta_{1s} r \Omega \right) \end{array} \right)
\end{aligned}$$

B.5.2 PROPULSION PART

The propulsion part becomes:

$$\begin{aligned}
r_p F_p \sin(\theta + \theta_p) &= r_p F_p \sin(\theta_p + \theta_0 + \theta_{1c} \cos \psi + \theta_{1s} \sin \psi) \\
&= r_p F_p \sin(\theta_p + \theta_0) \cos(\theta_{1c} \cos \psi + \theta_{1s} \sin \psi) + r_p F_p \cos(\theta_p + \theta_0) \sin(\theta_{1c} \cos \psi + \theta_{1s} \sin \psi)
\end{aligned}$$

Then, considering that θ_0 can be high but θ_{1c} and θ_{1s} remains low, the following approximation is made:

$$\begin{aligned}
r_p F_p \sin(\theta + \theta_p) &\approx r_p F_p \sin(\theta_p + \theta_0) + r_p F_p \cos(\theta_p + \theta_0) (\theta_{1c} \cos \psi + \theta_{1s} \sin \psi) \\
&\approx r_p F_p \sin(\theta_p + \theta_0) + r_p F_p \cos(\theta_p + \theta_0) \theta_{1c} \cos \psi + r_p F_p \cos(\theta_p + \theta_0) \theta_{1s} \sin \psi
\end{aligned}$$

The propulsion force is assumed to be of the form: $F_p = F_{p0} + F_{pc} \cos \psi + F_{ps} \sin \psi$, since both powerplants are offset by an angle of π , it leads to:

$$F_{p1} = F_{p0} + F_{pc} \cos \psi + F_{ps} \sin \psi$$

$$F_{p2} = F_{p0} + F_{pc} \cos(\psi + \pi) + F_{ps} \sin(\psi + \pi) = F_{p0} - F_{pc} \cos \psi - F_{ps} \sin \psi$$

Doing the integration over the rotor disk, it leads to:

$$\begin{aligned}
& \frac{1}{2\pi} \int_0^{2\pi} r_p F_{p1} \sin(\theta_1 + \theta_p) \sin \psi d\psi - \frac{1}{2\pi} \int_0^{2\pi} r_p F_{p2} \sin(\theta_2 + \theta_p) \sin \psi d\psi \\
& \approx \frac{1}{2\pi} \int_0^{2\pi} [r_p F_{p1} \sin(\theta_p + \theta_0) + r_p F_{p1} \cos(\theta_p + \theta_0) \theta_{1c} \cos \psi + r_p F_{p1} \cos(\theta_p + \theta_0) \theta_{1s} \sin \psi] \sin \psi d\psi \\
& - \frac{1}{2\pi} \int_0^{2\pi} \left[\begin{array}{l} r_p F_{p2} \sin(\theta_p + \theta_0) + r_p F_{p2} \cos(\theta_p + \theta_0) \theta_{1c} \cos(\psi + \pi) \\ + r_p F_{p2} \cos(\theta_p + \theta_0) \theta_{1s} \sin(\psi + \pi) \end{array} \right] \sin \psi d\psi \\
& \approx r_p F_{ps} \sin(\theta_p + \theta_0) + r_p F_{p0} \cos(\theta_p + \theta_0) \theta_{1s}
\end{aligned}$$

In the same way $\cos(\psi)$ equation becomes:

$$\begin{aligned}
& \frac{1}{2\pi} \int_0^{2\pi} r_p F_{p1} \sin(\theta_1 + \theta_p) \cos \psi d\psi - \frac{1}{2\pi} \int_0^{2\pi} r_p F_{p2} \sin(\theta_2 + \theta_p) \cos \psi d\psi \\
& \approx \frac{1}{2\pi} \int_0^{2\pi} [r_p F_{p1} \sin(\theta_p + \theta_0) + r_p F_{p1} \cos(\theta_p + \theta_0) \theta_{1c} \cos \psi + r_p F_{p1} \cos(\theta_p + \theta_0) \theta_{1s} \sin \psi] \cos \psi d\psi \\
& - \frac{1}{2\pi} \int_0^{2\pi} \left[\begin{array}{l} r_p F_{p2} \sin(\theta_p + \theta_0) + r_p F_{p2} \cos(\theta_p + \theta_0) \theta_{1c} \cos(\psi + \pi) \\ + r_p F_{p2} \cos(\theta_p + \theta_0) \theta_{1s} \sin(\psi + \pi) \end{array} \right] \cos \psi d\psi \\
& \approx r_p F_{pc} \sin(\theta_p + \theta_0) + r_p F_{p0} \cos(\theta_p + \theta_0) \theta_{1c}
\end{aligned}$$

B.5.3 FINAL FLAP RESULTS

The global result is eventually found summing the lift and propulsion components:

$$\begin{aligned}
\frac{K_\beta}{2}\beta_{1s} &= \frac{1}{1} \int_{root}^{tip} r \int_0^2 F_{z'} \sin \psi d\psi dr \\
&+ \left(\frac{1}{2} \int_0^2 r_p F_{p1} \sin(\theta_1 + \theta_p) \sin \psi d\psi - \frac{1}{2} \int_0^2 r_p F_{p2} \sin(\theta_2 + \theta_p) \sin \psi d\psi \right) \\
\Leftrightarrow \frac{K_\beta}{2}\beta_{1s} &= \int_{root}^{tip} \frac{r\rho c}{2} \left(\begin{aligned} &(a(k_1(\theta_0 - k_5 - \alpha_0) - k_3) - c_d k_2)(V_\lambda V_\mu + \frac{1}{4}\beta_{1c} V_\mu^2 - \beta_{1c} r^2 \Omega^2) \\ &+ \frac{1}{4}(\beta_0 V_\mu + 2\beta_{1s} r \Omega) V_\mu a k_1 \theta_{1c} + (V_\lambda - \frac{1}{2}\beta_{1c} V_\mu) r \Omega a k_1 \theta_{1s} \\ &+ 2ar \Omega V_\mu (k_2(\theta_0 - k_5 - \alpha_0) + k_4) + a k_2 \theta_{1s} (\frac{3}{4} V_\mu^2 + r^2 \Omega^2) \\ &+ 2c_d k_1 r \beta_{1c} \Omega V_\lambda - \frac{1}{2} c_d k_1 \beta_{1s} V_\mu (\beta_0 V_\mu + r \beta_{1s} \Omega) + \frac{1}{2} c_d k_1 r \beta_{1c} \Omega \beta_{1c} V_\mu \end{aligned} \right) dr \\
&+ r_p F_{ps} \sin(\theta_p + \theta_0) + r_p F_{p0} \cos(\theta_p + \theta_0) \theta_{1s}
\end{aligned} \tag{B.6}$$

and:

$$\begin{aligned}
\frac{K_\beta}{2}\beta_{1c} &= \frac{1}{1} \int_{root}^{tip} r \int_0^2 F_{z'} \cos \psi d\psi dr \\
&+ \left(\frac{1}{2} \int_0^2 r_p F_{p1} \sin(\theta_1 + \theta_p) \cos \psi d\psi - \frac{1}{2} \int_0^2 r_p F_{p2} \sin(\theta_2 + \theta_p) \cos \psi d\psi \right) \\
\Leftrightarrow \frac{K_\beta}{2}\beta_{1c} &= \int_{root}^{tip} \frac{r\rho c}{2} \left(\begin{aligned} &(a(k_1(\theta_0 - k_5 - \alpha_0) - k_3) - c_d k_2) \\ &(\frac{1}{4}\beta_{1s} V_\mu^2 + (\beta_0 V_\mu + r \beta_{1s} \Omega) r \Omega) + a k_1 \theta_{1c} (V_\lambda r \Omega + \frac{1}{2}\beta_{1c} V_\mu r \Omega) \\ &+ \frac{1}{4} a k_1 \theta_{1s} (\beta_0 V_\mu + 2r \Omega \beta_{1s}) V_\mu \\ &+ a k_2 \theta_{1c} (\frac{1}{4} V_\mu^2 + r^2 \Omega^2) \\ &- 2c_d k_1 (\beta_0 V_\mu + r \beta_{1s} \Omega) V_\lambda - c_d k_1 \beta_{1c} V_\mu (\frac{3}{2}\beta_0 V_\mu + \beta_{1s} r \Omega) \end{aligned} \right) dr \\
&+ r_p F_{pc} \sin(\theta_p + \theta_0) + r_p F_{p0} \cos(\theta_p + \theta_0) \theta_{1c}
\end{aligned} \tag{B.7}$$

C

APPENDIX: DYNAMICS MODEL DERIVATIVE

This appendix provides the derivatives expressions of the dynamics model constructed in chapter 2, page 53.

C.1 DYNAMICS RELATIONS DERIVATIVE

C.1.1 QUATERNION MODEL

Applying the “small disturbance” theory [?] to equation (2.23), page 67, with $v_0 = p_0 = q_0 = r_0 = \phi_0 = 0$ and a constant wind $\Delta W_x = \Delta W_y = \Delta W_z = 0$, it leads to:

$$\begin{aligned}
X_0 + \Delta X + 2mg(q_{20}q_{40} + q_{20}\Delta q_4 + \Delta q_2q_{40} - q_{10}q_{30} - q_{10}\Delta q_3 - \Delta q_1q_{30}) &= m(\dot{u}^E + qw_0^E - rv_0^E) \\
Y_0 + \Delta Y + 2mg(q_{10}q_{20} + q_{10}\Delta q_2 + \Delta q_1q_{20} + q_{30}q_{40} + q_{30}\Delta q_4 + \Delta q_3q_{40}) &= m(\dot{v}^E + ru_0^E - pw_0^E) \\
Z_0 + \Delta Z + mg(1 - 2(q_{20}^2 + q_{30}^2)) - 2mg(2q_{20}\Delta q_2 + 2q_{30}\Delta q_3) &= m(\dot{w}^E - qu_0^E) \\
L_0 + \Delta L &= I_x\dot{p} - I_{zx}\dot{r} \\
M_0 + \Delta M &= I_y\dot{q} \\
N_0 + \Delta N &= I_z\dot{r} - I_{zx}\dot{p} \\
\dot{q}_1 &= -\frac{1}{2}(pq_{20} + qq_{30} + rq_{40}) \\
\dot{q}_2 &= \frac{1}{2}(pq_{10} + rq_{30} - qq_{40}) \\
\dot{q}_3 &= \frac{1}{2}(qq_{10} - rq_{20} + pq_{40}) \\
\dot{q}_4 &= \frac{1}{2}(rq_{10} + qq_{20} - pq_{30}) \\
\dot{x}^E + \Delta\dot{x}^E &= (u_0^E + \Delta u^E)(1 - 2(q_{30}^2 + q_{40}^2)) - 2u_0^E(2q_{30}\Delta q_3 + 2q_{40}\Delta q_4) \\
&+ 2(v_0^E + \Delta v^E)(q_{20}q_{30} - q_{10}q_{40}) + 2v_0^E(q_{20}\Delta q_3 + \Delta q_2q_{30} - q_{10}\Delta q_4 - \Delta q_1q_{40}) \\
&+ 2(w_0^E + \Delta w^E)(q_{10}q_{30} + q_{20}q_{40}) + 2w_0^E(q_{10}\Delta q_3 + \Delta q_1q_{30} + q_{20}\Delta q_4 + \Delta q_2q_{40}) \\
\dot{y}^E + \Delta\dot{y}^E &= 2(u_0^E + \Delta u^E)(q_{20}q_{30} + q_{10}q_{40}) + 2u_0^E(q_{20}\Delta q_3 + \Delta q_2q_{30} + q_{10}\Delta q_4 + \Delta q_1q_{40}) \\
&+ (v_0^E + \Delta v^E)(1 - 2(q_{20}^2 + q_{40}^2)) - 2v_0^E(2q_{20}\Delta q_2 + 2q_{40}\Delta q_4) \\
&+ 2(w_0^E + \Delta w^E)(q_{30}q_{40} - q_{10}q_{20}) + 2w_0^E(q_{30}\Delta q_4 + \Delta q_3q_{40} - q_{10}\Delta q_2 - \Delta q_1q_{20}) \\
\dot{z}^E + \Delta\dot{z}^E &= 2(u_0^E + \Delta u^E)(q_{20}q_{40} - q_{10}q_{30}) + 2u_0^E(q_{20}\Delta q_4 + \Delta q_2q_{40} - q_{10}\Delta q_3 - \Delta q_1q_{30}) \\
&+ 2(v_0^E + \Delta v^E)(q_{10}q_{20} + q_{30}q_{40}) + 2v_0^E(q_{10}\Delta q_2 + \Delta q_1q_{20} + q_{30}\Delta q_4 + \Delta q_3q_{40}) \\
&+ (w_0^E + \Delta w^E)(1 - 2(q_{20}^2 + q_{30}^2)) - 2w_0^E(2q_{20}\Delta q_2 + 2q_{30}\Delta q_3) \\
u_0^E + \Delta u^E &= u_0 + \Delta u + W_x \\
v_0^E + \Delta v^E &= \Delta v + W_y \\
w_0^E + \Delta w^E &= w_0 + \Delta w + W_z \\
J_{rotor}\dot{\Omega} &= -Q_{r0} - \Delta Q_r
\end{aligned} \tag{C.1}$$

The steady state is obtained setting all the “small disturbances” to zero:

$$\begin{aligned}
X_0 + 2mg(q_{20}q_{40} - q_{10}q_{30}) &= 0 \\
Y_0 + 2mg(q_{10}q_{20} + q_{30}q_{40}) &= 0 \\
Z_0 + mg(1 - 2(q_{20}^2 + q_{30}^2)) &= 0 \\
L_0 &= 0 \\
M_0 &= 0 \\
N_0 &= 0 \\
\dot{x}^E &= u_0^E(1 - 2(q_{30}^2 + q_{40}^2)) + 2v_0^E(q_{20}q_{30} - q_{10}q_{40}) + 2w_0^E(q_{10}q_{30} + q_{20}q_{40}) \\
\dot{y}^E &= 2u_0^E(q_{20}q_{30} + q_{10}q_{40}) + v_0^E(1 - 2(q_{20}^2 + q_{40}^2)) + 2w_0^E(q_{30}q_{40} - q_{10}q_{20}) \\
\dot{z}^E &= 2u_0^E(q_{20}q_{40} - q_{10}q_{30}) + 2v_0^E(q_{10}q_{20} + q_{30}q_{40}) + w_0^E(1 - 2(q_{20}^2 + q_{30}^2)) \\
u_0^E &= u_0 + W_x \\
v_0^E &= W_y \\
w_0^E &= w_0 + W_z \\
Q_{r0} &= 0
\end{aligned} \tag{C.2}$$

Substituting equation (C.2) in (C.1) It becomes:

$$\begin{aligned}
\Delta X + 2mg(q_{20}\Delta q_4 + \Delta q_2 q_{40} - q_{10}\Delta q_3 - \Delta q_1 q_{30}) &= m(\dot{u}^E + qw_0^E - rv_0^E) \\
\Delta Y + 2mg(q_{10}\Delta q_2 + \Delta q_1 q_{20} + q_{30}\Delta q_4 + \Delta q_3 q_{40}) &= m(\dot{v}^E + ru_0^E - pw_0^E) \\
\Delta Z - 2mg(2q_{20}\Delta q_2 + 2q_{30}\Delta q_3) &= m(\dot{w}^E - qu_0^E) \\
\Delta L &= I_x \dot{p} - I_{zx} \dot{r} \\
\Delta M &= I_y \dot{q} \\
\Delta N &= I_z \dot{r} - I_{zx} \dot{p} \\
\dot{q}_1 &= -\frac{1}{2}(pq_{20} + qq_{30} + rq_{40}) \\
\dot{q}_2 &= \frac{1}{2}(pq_{10} + rq_{30} - qq_{40}) \\
\dot{q}_3 &= \frac{1}{2}(qq_{10} - rq_{20} + pq_{40}) \\
\dot{q}_4 &= \frac{1}{2}(rq_{10} + qq_{20} - pq_{30}) \\
\Delta \dot{x}^E &= \Delta u^E (1 - 2(q_{30}^2 + q_{40}^2)) - 2u_0^E (2q_{30}\Delta q_3 + 2q_{40}\Delta q_4) \\
&+ 2\Delta v^E (q_{20}q_{30} - q_{10}q_{40}) + 2v_0^E (q_{20}\Delta q_3 + \Delta q_2 q_{30} - q_{10}\Delta q_4 - \Delta q_1 q_{40}) \\
&+ 2\Delta w^E (q_{10}q_{30} + q_{20}q_{40}) + 2w_0^E (q_{10}\Delta q_3 + \Delta q_1 q_{30} + q_{20}\Delta q_4 + \Delta q_2 q_{40}) \\
\Delta \dot{y}^E &= 2\Delta u^E (q_{20}q_{30} + q_{10}q_{40}) + 2u_0^E (q_{20}\Delta q_3 + \Delta q_2 q_{30} + q_{10}\Delta q_4 + \Delta q_1 q_{40}) \\
&+ \Delta v^E (1 - 2(q_{20}^2 + q_{40}^2)) - 2v_0^E (2q_{20}\Delta q_2 + 2q_{40}\Delta q_4) \\
&+ 2\Delta w^E (q_{30}q_{40} - q_{10}q_{20}) + 2w_0^E (q_{30}\Delta q_4 + \Delta q_3 q_{40} - q_{10}\Delta q_2 - \Delta q_1 q_{20}) \\
\Delta \dot{z}^E &= 2\Delta u^E (q_{20}q_{40} - q_{10}q_{30}) + 2u_0^E (q_{20}\Delta q_4 + \Delta q_2 q_{40} - q_{10}\Delta q_3 - \Delta q_1 q_{30}) \\
&+ 2\Delta v^E (q_{10}q_{20} + q_{30}q_{40}) + 2v_0^E (q_{10}\Delta q_2 + \Delta q_1 q_{20} + q_{30}\Delta q_4 + \Delta q_3 q_{40}) \\
&+ \Delta w^E (1 - 2(q_{20}^2 + q_{30}^2)) - 2w_0^E (2q_{20}\Delta q_2 + 2q_{30}\Delta q_3) \\
\Delta u^E &= \Delta u \\
\Delta v^E &= \Delta v \\
\Delta w^E &= \Delta w \\
J_{rotor} \dot{\Omega} &= -\Delta Q_r
\end{aligned}$$

It can be seen that there is no more need to do the distinction between earth and air velocities.

The equations thus become:

$$\begin{aligned}
\Delta X + 2mg(q_{20}\Delta q_4 + \Delta q_2 q_{40} - q_{10}\Delta q_3 - \Delta q_1 q_{30}) &= m(\dot{u}^E + qw_0^E - rv_0^E) \\
\Delta Y + 2mg(q_{10}\Delta q_2 + \Delta q_1 q_{20} + q_{30}\Delta q_4 + \Delta q_3 q_{40}) &= m(\dot{v}^E + ru_0^E - pw_0^E) \\
\Delta Z - 2mg(2q_{20}\Delta q_2 + 2q_{30}\Delta q_3) &= m(\dot{w}^E - qu_0^E) \\
\Delta L &= I_x \dot{p} - I_{zx} \dot{r} \\
\Delta M &= I_y \dot{q} \\
\Delta N &= I_z \dot{r} - I_{zx} \dot{p} \\
\dot{q}_1 &= -\frac{1}{2}(pq_{20} + qq_{30} + rq_{40}) \\
\dot{q}_2 &= \frac{1}{2}(pq_{10} + rq_{30} - qq_{40}) \\
\dot{q}_3 &= \frac{1}{2}(qq_{10} - rq_{20} + pq_{40}) \\
\dot{q}_4 &= \frac{1}{2}(rq_{10} + qq_{20} - pq_{30}) \\
\Delta \dot{x}^E &= \Delta u(1 - 2(q_{30}^2 + q_{40}^2)) - 2u_0^E(2q_{30}\Delta q_3 + 2q_{40}\Delta q_4) \\
&+ 2\Delta v(q_{20}q_{30} - q_{10}q_{40}) + 2v_0^E(q_{20}\Delta q_3 + \Delta q_2 q_{30} - q_{10}\Delta q_4 - \Delta q_1 q_{40}) \\
&+ 2\Delta w(q_{10}q_{30} + q_{20}q_{40}) + 2w_0^E(q_{10}\Delta q_3 + \Delta q_1 q_{30} + q_{20}\Delta q_4 + \Delta q_2 q_{40}) \\
\Delta \dot{y}^E &= 2\Delta u(q_{20}q_{30} + q_{10}q_{40}) + 2u_0^E(q_{20}\Delta q_3 + \Delta q_2 q_{30} + q_{10}\Delta q_4 + \Delta q_1 q_{40}) \\
&+ \Delta v(1 - 2(q_{20}^2 + q_{40}^2)) - 2v_0^E(2q_{20}\Delta q_2 + 2q_{40}\Delta q_4) \\
&+ 2\Delta w(q_{30}q_{40} - q_{10}q_{20}) + 2w_0^E(q_{30}\Delta q_4 + \Delta q_3 q_{40} - q_{10}\Delta q_2 - \Delta q_1 q_{20}) \\
\Delta \dot{z}^E &= 2\Delta u(q_{20}q_{40} - q_{10}q_{30}) + 2u_0^E(q_{20}\Delta q_4 + \Delta q_2 q_{40} - q_{10}\Delta q_3 - \Delta q_1 q_{30}) \\
&+ 2\Delta v(q_{10}q_{20} + q_{30}q_{40}) + 2v_0^E(q_{10}\Delta q_2 + \Delta q_1 q_{20} + q_{30}\Delta q_4 + \Delta q_3 q_{40}) \\
&+ \Delta w(1 - 2(q_{20}^2 + q_{30}^2)) - 2w_0^E(2q_{20}\Delta q_2 + 2q_{30}\Delta q_3) \\
J_{rotor} \dot{\Omega} &= -\Delta Q_r
\end{aligned} \tag{C.3}$$

C.1.2 EULER ANGLES BASED MODEL

The linear model derived from Euler equation (2.22) is:

$$\begin{aligned}
\dot{u} &= \frac{\Delta X}{m} - g\Delta\theta \cos\theta_0 - qw_0 \\
\dot{v} &= \frac{\Delta Y}{m} + g\phi \cos\theta_0 - ru_0 + pw_0 \\
\dot{w} &= \frac{\Delta Z}{m} - g\Delta\theta \sin\theta_0 + qu_0 \\
\dot{p} &= \frac{I_z\Delta L + I_{xz}\Delta N}{I_x I_z - I_{xz}^2} \\
\dot{q} &= \frac{\Delta M}{I_y} \\
\dot{r} &= \frac{I_{xz}\Delta L + I_x\Delta N}{I_x I_z - I_{xz}^2} \\
\dot{\phi} &= p + r \tan\theta_0 \\
\dot{\theta} &= q \\
\dot{\psi} &= r \sec\theta_0 \\
\Delta\dot{x}_E &= \Delta u^E \cos\theta_0 - u_0^E \Delta\theta \sin\theta_0 + \Delta w^E \sin\theta_0 + w_0^E \Delta\theta \cos\theta_0 \\
\Delta\dot{y}_E &= u_0^E \psi \cos\theta_0 + v^E + w_0^E \sin\theta_0 \psi - w_0^E \phi \\
\Delta\dot{z}_E &= -\Delta u^E \sin\theta_0 - u_0^E \Delta\theta \cos\theta_0 + \Delta w^E \cos\theta_0 - w_0^E \Delta\theta \sin\theta_0 \\
J_{rotor}\dot{\Omega} &= -\Delta Q_r
\end{aligned} \tag{C.4}$$

C.2 STABILITY DERIVATIVES

The forces and moments derivatives have to be evaluated to complete the dynamics model. According to C.3, the dynamics equations are constituted of 6 degrees of freedom. In addition to those degrees of freedom, the control inputs may be added: there is four flaperons, two rudders, three rotor controls and three motor controls. The aerodynamic derivatives are of the form:

$$\begin{aligned}
\Delta\chi &= \frac{\partial\chi}{\partial u}\Delta u + \frac{\partial\chi}{\partial v}\Delta v + \frac{\partial\chi}{\partial w}\Delta w \\
&+ \frac{\partial\chi}{\partial p}\Delta p + \frac{\partial\chi}{\partial q}\Delta q + \frac{\partial\chi}{\partial r}\Delta r \\
&+ \frac{\partial\chi}{\partial U_{a1}}\Delta U_{a1} + \frac{\partial\chi}{\partial U_{a2}}\Delta U_{a2} + \frac{\partial\chi}{\partial U_{f1}}\Delta U_{f1} + \frac{\partial\chi}{\partial U_{f2}}\Delta U_{f2} + \frac{\partial\chi}{\partial U_r}\Delta U_r + \frac{\partial\chi}{\partial U_{ab}}\Delta U_{ab} \\
&+ \frac{\partial\chi}{\partial U_{\theta_{1c}}}\Delta U_{\theta_{1c}} + \frac{\partial\chi}{\partial U_{\theta_{1s}}}\Delta U_{\theta_{1s}} + \frac{\partial\chi}{\partial U_{\theta_0}}\Delta U_{\theta_0} + \frac{\partial\chi}{\partial U_{F_{pc}}}\Delta U_{F_{pc}} + \frac{\partial\chi}{\partial U_{F_{ps}}}\Delta U_{F_{ps}} + \frac{\partial\chi}{\partial U_{F_{p0}}}\Delta U_{F_{p0}}
\end{aligned}$$

where χ represents any force X , Y and Z or moment L , M or N of the equations exposed in section 2.2.3, page 67. All equations are linear; the derivations are therefore obvious. However the derivation of the rotor resultant forces expressions may be detailed:

$$R_z = T_z \sin \beta_{1c} - F_x \cos \beta_{1c}$$

It leads to:

$$\frac{\partial R_z}{\partial T_z} = \sin \beta_{1c}$$

$$\frac{\partial R_z}{\partial F_x} = -\cos \beta_{1c}$$

$$\frac{\partial R_z}{\partial \beta_{1c}} = \frac{\partial T_z}{\partial \beta_{1c}} \sin \beta_{1c} + T_z \cos \beta_{1c} - \frac{\partial F_x}{\partial \beta_{1c}} \cos \beta_{1c} + F_x \sin \beta_{1c}$$

In the same way R_x can be expressed as:

$$R_x = T_z \cos \beta_{1c} + F_x \sin \beta_{1c}$$

It leads to:

$$\frac{\partial R_x}{\partial T_z} = \cos \beta_{1c}$$

$$\frac{\partial R_x}{\partial F_x} = \sin \beta_{1c}$$

$$\frac{\partial R_x}{\partial \beta_{1c}} = \frac{\partial T_z}{\partial \beta_{1c}} \cos \beta_{1c} - T_z \sin \beta_{1c} + \frac{\partial F_x}{\partial \beta_{1c}} F_x \sin \beta_{1c} + F_x \cos \beta_{1c}$$

Lastly, R_y can be expressed as:

$$R_y = -T_z \cos \beta_{1c} \sin \beta_{1s} - F_x \sin \beta_{1c} \sin \beta_{1s} + F_y \cos \beta_{1s}$$

It leads to:

$$\frac{\partial R_y}{\partial T_z} = -\cos \beta_{1c} \sin \beta_{1s}$$

$$\frac{\partial R_y}{\partial F_x} = -\sin \beta_{1c} \sin \beta_{1s}$$

$$\frac{\partial R_y}{\partial F_y} = \cos \beta_{1s}$$

$$\begin{aligned}\frac{\partial R_y}{\partial \beta_{1c}} &= -\frac{\partial T_z}{\partial \beta_{1c}} \cos \beta_{1c} \sin \beta_{1s} + T_z \sin \beta_{1c} \sin \beta_{1s} \\ &\quad -\frac{\partial F_x}{\partial \beta_{1c}} \sin \beta_{1c} \sin \beta_{1s} - F_x \cos \beta_{1c} \sin \beta_{1s} + \frac{\partial F_y}{\partial \beta_{1c}} \cos \beta_{1s} \\ \frac{\partial R_y}{\partial \beta_{1s}} &= -\frac{\partial T_z}{\partial \beta_{1s}} \cos \beta_{1c} \sin \beta_{1s} - T_z \cos \beta_{1c} \cos \beta_{1s} - \frac{\partial F_x}{\partial \beta_{1s}} \sin \beta_{1c} \sin \beta_{1s} \\ &\quad -F_x \sin \beta_{1c} \cos \beta_{1s} + \frac{\partial F_y}{\partial \beta_{1s}} \cos \beta_{1s} - F_y \sin \beta_{1s}\end{aligned}$$

C.2.1 Rotor derivatives

C.2.1.1 Speeds and angles

Equation 2.33, page 70 leads to:

$$\frac{\partial V}{\partial u} = \frac{1}{2\sqrt{u^2 + w^2}} 2u = \frac{u}{V}$$

In the same way:

$$\frac{\partial V}{\partial w} = \frac{w}{V}$$

Equation 2.35, page 71 leads to:

$$\frac{\partial \alpha}{\partial u} = -\frac{1}{1 + \left(\frac{w}{u}\right)^2} \frac{w}{u^2} = -\frac{u^2}{u^2 + w^2} \frac{w}{u^2} = -\frac{w}{V}$$

and:

$$\frac{\partial \alpha}{\partial w} = \frac{1}{1 + \left(\frac{w}{u}\right)^2} \frac{1}{u} = \frac{u^2}{u^2 + w^2} \frac{1}{u} = \frac{u}{V}$$

C.2.1.2 Derivatives of β

Derivatives of speeds and angle From equation 2.36, page 71, the derivative relations of the angles of attacks become:

$$\frac{\partial \alpha'_r}{\partial \alpha} = -1$$

In the same way, equations 2.37 and 2.38, page 71 lead to:

$$\frac{\partial V'_\lambda}{\partial V} = \sin \alpha'_r$$

$$\frac{\partial V'_\lambda}{\partial \alpha'_r} = V \cos \alpha'_r$$

$$\frac{\partial V'_\mu}{\partial V} = \cos \alpha'_r$$

$$\frac{\partial V'_\mu}{\partial \alpha'_r} = -V \sin \alpha'_r$$

V'_λ derivatives

$$0 = \frac{\partial \Delta \beta_{1c}}{\partial V'_\lambda} \left(\frac{1}{4}(A_\beta + \theta_0 B_\beta) V'_\mu{}^2 - (C_\beta + \theta_0 D_\beta) \Omega^2 - \frac{1}{2} E_\beta \theta_{1s} V'_\mu \Omega + 2J_\beta \Omega V'_\lambda \right) + \frac{\partial \Delta \beta_{1s}}{\partial V'_\lambda} \left(\frac{1}{2} E_\beta \Omega V'_\mu \theta_{1c} \right) + \Delta \beta_{1c} (2J_\beta \Omega) + (A_\beta + \theta_0 B_\beta) V'_\mu + E_\beta \Omega \theta_{1s}$$

$$0 = \frac{\partial \Delta \beta_{1s}}{\partial V'_\lambda} \left(\frac{1}{4}(A_\beta + \theta_0 B_\beta) V'_\mu{}^2 + (C_\beta + \theta_0 D_\beta) \Omega^2 + \frac{1}{2} E_\beta \theta_{1s} V'_\mu \Omega - 2J_\beta \Omega V'_\lambda \right) + \frac{\partial \Delta \beta_{1c}}{\partial V'_\lambda} \left(\frac{1}{2} E_\beta V'_\mu \Omega \theta_{1c} \right) + \Delta \beta_{1s} (-2J_\beta \Omega) + E_\beta \Omega \theta_{1c}$$

V'_μ derivatives

$$0 = \frac{\partial \Delta \beta_{1c}}{\partial V'_\mu} \left(\frac{1}{4}(A_\beta + \theta_0 B_\beta) V'_\mu{}^2 - (C_\beta + \theta_0 D_\beta) \Omega^2 - \frac{1}{2} E_\beta \theta_{1s} V'_\mu \Omega + 2J_\beta \Omega V'_\lambda \right) + \frac{\partial \Delta \beta_{1s}}{\partial V'_\mu} \left(\frac{1}{2} E_\beta \Omega V'_\mu \theta_{1c} \right) + \Delta \beta_{1c} \left(\frac{1}{2} (A_\beta + \theta_0 B_\beta) V'_\mu - \frac{1}{2} E_\beta \theta_{1s} \Omega \right) + \Delta \beta_{1s} \left(\frac{1}{2} E_\beta \Omega \theta_{1c} \right) + (A_\beta + \theta_0 B_\beta) V'_\lambda + (F_\beta + \theta_0 G_\beta) \Omega + H_\beta \frac{3}{2} V'_\mu \theta_{1s}$$

$$0 = \frac{\partial \Delta \beta_{1s}}{\partial V'_\mu} \left(\frac{1}{4}(A_\beta + \theta_0 B_\beta) V'_\mu{}^2 + (C_\beta + \theta_0 D_\beta) \Omega^2 + \frac{1}{2} E_\beta \theta_{1s} V'_\mu \Omega - 2J_\beta \Omega V'_\lambda \right) + \frac{\partial \Delta \beta_{1c}}{\partial V'_\mu} \left(\frac{1}{2} E_\beta V'_\mu \Omega \theta_{1c} \right) + \Delta \beta_{1s} \left(\frac{1}{2} (A_\beta + \theta_0 B_\beta) V'_\mu + \frac{1}{2} E_\beta \theta_{1s} \Omega \right) + \Delta \beta_{1c} \left(\frac{1}{2} E_\beta \Omega \theta_{1c} \right) + H_\beta \frac{1}{2} V'_\mu \theta_{1c}$$

Ω derivatives

$$0 = \frac{\partial \Delta \beta_{1c}}{\partial \Omega} \left(\frac{1}{4}(A_\beta + \theta_0 B_\beta) V'_\mu{}^2 - (C_\beta + \theta_0 D_\beta) \Omega^2 - \frac{1}{2} E_\beta \theta_{1s} V'_\mu \Omega + 2J_\beta \Omega V'_\lambda \right) + \frac{\partial \Delta \beta_{1s}}{\partial \Omega} \left(\frac{1}{2} E_\beta \Omega V'_\mu \theta_{1c} \right) + \Delta \beta_{1c} \left(-2(C_\beta + \theta_0 D_\beta) \Omega - \frac{1}{2} E_\beta \theta_{1s} V'_\mu + 2J_\beta V'_\lambda \right) + \Delta \beta_{1s} \left(\frac{1}{2} E_\beta V'_\mu \theta_{1c} \right) + E_\beta V'_\lambda \theta_{1s} + (F_\beta + \theta_0 G_\beta) V'_\mu + 2I_\beta \Omega \theta_{1s}$$

$$0 = \frac{\partial \Delta \beta_{1s}}{\partial \Omega} \left(\frac{1}{4}(A_\beta + \theta_0 B_\beta) V'_\mu{}^2 + (C_\beta + \theta_0 D_\beta) \Omega^2 + \frac{1}{2} E_\beta \theta_{1s} V'_\mu \Omega - 2J_\beta \Omega V'_\lambda \right) + \frac{\partial \Delta \beta_{1c}}{\partial \Omega} \left(\frac{1}{2} E_\beta V'_\mu \Omega \theta_{1c} \right) + \Delta \beta_{1s} \left(2(C_\beta + \theta_0 D_\beta) \Omega + \frac{1}{2} E_\beta \theta_{1s} V'_\mu - 2J_\beta V'_\lambda \right) + \Delta \beta_{1c} \left(\frac{1}{2} E_\beta V'_\mu \theta_{1c} \right) + E_\beta V'_\lambda \theta_{1c} + 2I_\beta \theta_{1c} \Omega$$

θ_0 derivatives

$$\begin{aligned}
0 &= \frac{\partial \Delta \beta_{1c}}{\partial \theta_0} \left(\frac{1}{4} (A_\beta + \theta_0 B_\beta) V_\mu'^2 - (C_\beta + \theta_0 D_\beta) \Omega^2 - \frac{1}{2} E_\beta \theta_{1s} V_\mu' \Omega + 2 J_\beta \Omega V_\lambda' \right) \\
&+ \Delta \beta_{1c} \left(\frac{1}{4} B_\beta V_\mu'^2 - D_\beta \Omega^2 \right) \\
&+ \frac{\partial \Delta \beta_{1s}}{\partial \theta_0} \left(\frac{1}{2} E_\beta \Omega V_\mu' \theta_{1c} \right) + V_\lambda' V_\mu' B_\beta + G_\beta \Omega V_\mu' + r_p F_{p_s} \cos(\theta_0 + \theta_p) - r_p F_{p_0} \theta_{1s} \sin(\theta_0 + \theta_p) \\
\\
0 &= \frac{\partial \Delta \beta_{1s}}{\partial \theta_0} \left(\frac{1}{4} (A_\beta + \theta_0 B_\beta) V_\mu'^2 + (C_\beta + \theta_0 D_\beta) \Omega^2 + \frac{1}{2} E_\beta \theta_{1s} V_\mu' \Omega - 2 J_\beta \Omega V_\lambda' \right) \\
&+ \Delta \beta_{1s} \left(\frac{1}{4} B_\beta V_\mu'^2 + D_\beta \Omega^2 \right) \\
&+ \frac{\partial \Delta \beta_{1c}}{\partial \theta_0} \left(\frac{1}{2} E_\beta V_\mu' \Omega \theta_{1c} \right) + r_p F_{p_c} \cos(\theta_0 + \theta_p) - r_p F_{p_0} \theta_{1c} \sin(\theta_0 + \theta_p)
\end{aligned}$$

θ_{1s} derivatives

$$\begin{aligned}
0 &= \frac{\partial \Delta \beta_{1c}}{\partial \theta_{1s}} \left(\frac{1}{4} (A_\beta + \theta_0 B_\beta) V_\mu'^2 - (C_\beta + \theta_0 D_\beta) \Omega^2 - \frac{1}{2} E_\beta \theta_{1s} V_\mu' \Omega + 2 J_\beta \Omega V_\lambda' \right) \\
&+ \frac{\partial \Delta \beta_{1s}}{\partial \theta_{1s}} \left(\frac{1}{2} E_\beta \Omega V_\mu' \theta_{1c} \right) - \frac{1}{2} E_\beta V_\mu' \Omega \Delta \beta_{1c} + E_\beta V_\lambda' \Omega + H_\beta \frac{3}{4} V_\mu'^2 + I_\beta \Omega^2 + r_p F_{p_0} \cos \theta_0 \\
\\
0 &= \frac{\partial \Delta \beta_{1s}}{\partial \theta_{1s}} \left(\frac{1}{4} (A_\beta + \theta_0 B_\beta) V_\mu'^2 + (C_\beta + \theta_0 D_\beta) \Omega^2 + \frac{1}{2} E_\beta \theta_{1s} V_\mu' \Omega - 2 J_\beta \Omega V_\lambda' \right) \\
&+ \frac{\partial \Delta \beta_{1c}}{\partial \theta_{1s}} \left(\frac{1}{2} E_\beta V_\mu' \Omega \theta_{1c} \right) + \frac{1}{2} E_\beta V_\mu' \Omega \Delta \beta_{1s}
\end{aligned}$$

θ_{1c} derivatives

$$\begin{aligned}
0 &= \frac{\partial \Delta \beta_{1c}}{\partial \theta_{1c}} \left(\frac{1}{4} (A_\beta + \theta_0 B_\beta) V_\mu'^2 - (C_\beta + \theta_0 D_\beta) \Omega^2 - \frac{1}{2} E_\beta \theta_{1s} V_\mu' \Omega + 2 J_\beta \Omega V_\lambda' \right) \\
&+ \frac{\partial \Delta \beta_{1s}}{\partial \theta_{1c}} \left(\frac{1}{2} E_\beta \Omega V_\mu' \theta_{1c} \right) + \frac{1}{2} E_\beta \Omega V_\mu' \Delta \beta_{1s} \\
\\
0 &= \frac{\partial \Delta \beta_{1s}}{\partial \theta_{1c}} \left(\frac{1}{4} (A_\beta + \theta_0 B_\beta) V_\mu'^2 + (C_\beta + \theta_0 D_\beta) \Omega^2 + \frac{1}{2} E_\beta \theta_{1s} V_\mu' \Omega - 2 J_\beta \Omega V_\lambda' \right) \\
&+ \frac{\partial \Delta \beta_{1c}}{\partial \theta_{1c}} \left(\frac{1}{2} E_\beta V_\mu' \Omega \theta_{1c} \right) + \frac{1}{2} E_\beta V_\mu' \Omega \Delta \beta_{1c} + E_\beta V_\lambda' \Omega + H_\beta \frac{1}{4} V_\mu'^2 + I_\beta \Omega^2 + r_p F_{p_0} \cos(\theta_0 + \theta_p)
\end{aligned}$$

F_{p_s} derivatives

$$\begin{aligned}
0 &= \frac{\partial \Delta \beta_{1c}}{\partial F_{p_s}} \left(\frac{1}{4} (A_\beta + \theta_0 B_\beta) V_\mu'^2 - (C_\beta + \theta_0 D_\beta) \Omega^2 - \frac{1}{2} E_\beta \theta_{1s} V_\mu' \Omega + 2 J_\beta \Omega V_\lambda' \right) \\
&+ \frac{\partial \Delta \beta_{1s}}{\partial F_{p_s}} \left(\frac{1}{2} E_\beta \Omega V_\mu' \theta_{1c} \right) + r_p \sin(\theta_0 + \theta_p) \\
\\
0 &= \frac{\partial \Delta \beta_{1s}}{\partial F_{p_s}} \left(\frac{1}{4} (A_\beta + \theta_0 B_\beta) V_\mu'^2 + (C_\beta + \theta_0 D_\beta) \Omega^2 + \frac{1}{2} E_\beta \theta_{1s} V_\mu' \Omega - 2 J_\beta \Omega V_\lambda' \right) + \frac{\partial \Delta \beta_{1c}}{\partial F_{p_s}} \left(\frac{1}{2} E_\beta V_\mu' \Omega \theta_{1c} \right)
\end{aligned}$$

F_{p_c} derivatives

$$0 = \frac{\partial \Delta \beta_{1c}}{\partial F_{p_c}} \left(\frac{1}{4}(A_\beta + \theta_0 B_\beta) V_\mu'^2 - (C_\beta + \theta_0 D_\beta) \Omega^2 - \frac{1}{2} E_\beta \theta_{1s} V_\mu' \Omega + 2 J_\beta \Omega V_\lambda' \right) + \frac{\partial \Delta \beta_{1s}}{\partial F_{p_c}} \left(\frac{1}{2} E_\beta \Omega V_\mu' \theta_{1c} \right)$$

$$0 = \frac{\partial \Delta \beta_{1s}}{\partial F_{p_c}} \left(\frac{1}{4}(A_\beta + \theta_0 B_\beta) V_\mu'^2 + (C_\beta + \theta_0 D_\beta) \Omega^2 + \frac{1}{2} E_\beta \theta_{1s} V_\mu' \Omega - 2 J_\beta \Omega V_\lambda' \right) + \frac{\partial \Delta \beta_{1c}}{\partial F_{p_c}} \left(\frac{1}{2} E_\beta V_\mu' \Omega \theta_{1c} \right) + r_p \sin(\theta_0 + \theta_p)$$

F_{p_0} derivatives

$$0 = \frac{\partial \Delta \beta_{1c}}{\partial F_{p_0}} \left(\frac{1}{4}(A_\beta + \theta_0 B_\beta) V_\mu'^2 - (C_\beta + \theta_0 D_\beta) \Omega^2 - \frac{1}{2} E_\beta \theta_{1s} V_\mu' \Omega + 2 J_\beta \Omega V_\lambda' \right) + \frac{\partial \Delta \beta_{1s}}{\partial F_{p_0}} \left(\frac{1}{2} E_\beta \Omega V_\mu' \theta_{1c} \right) + r_p \theta_{1s} \sin(\theta_0 + \theta_p)$$

$$0 = \frac{\partial \Delta \beta_{1s}}{\partial F_{p_0}} \left(\frac{1}{4}(A_\beta + \theta_0 B_\beta) V_\mu'^2 + (C_\beta + \theta_0 D_\beta) \Omega^2 + \frac{1}{2} E_\beta \theta_{1s} V_\mu' \Omega - 2 J_\beta \Omega V_\lambda' \right) + \frac{\partial \Delta \beta_{1c}}{\partial F_{p_0}} \left(\frac{1}{2} E_\beta V_\mu' \Omega \theta_{1c} \right) + r_p \theta_{1c} \sin(\theta_0 + \theta_p)$$

All the derivatives are of the form:

$$\begin{cases} A \Delta \beta_{1s} + B \Delta \beta_{1c} + C = 0 \\ A' \Delta \beta_{1s} + B' \Delta \beta_{1c} + C' = 0 \end{cases} \Rightarrow \begin{cases} \Delta \beta_{1c} = \frac{AC' - A'C}{A'B - AB'} \\ \Delta \beta_{1s} = \frac{-B'x - C'}{A'} \end{cases}$$

Equations 2.41 and 2.42, page 73 give:

$$\frac{\partial \beta_{1c}}{\partial \Delta \beta_{1c}} = 1$$

$$\frac{\partial \beta_{1c}}{\partial \Delta \beta_{1s}} = 1$$

C.2.1.3 Angle and speed

From equation 2.43, page 73, the derivative relations of the angles of attacks are:

$$\frac{\partial \alpha_r}{\partial \alpha} = -1$$

$$\frac{\partial \alpha_r}{\partial \beta_{1c}} = 1$$

In the same way, equations 2.44 and 2.45, page 73 lead to:

$$\frac{\partial V_\lambda}{\partial V} = \sin \alpha_r$$

$$\frac{\partial V_\lambda}{\partial \alpha_r} = V \cos \alpha_r$$

$$\frac{\partial V_\mu}{\partial V} = \cos \alpha_r$$

$$\frac{\partial V_\mu}{\partial \alpha_r} = -V \sin \alpha_r$$

C.2.1.4 Derivatives of T_z

V_λ derivatives

$$\frac{\partial T_z}{\partial V_\lambda} = \Omega (A_T + \theta_0 B_T) + \theta_{1s} V_\mu C_T - 2V_\lambda I_T$$

V_μ derivatives

$$\frac{\partial T_z}{\partial V_\mu} = \theta_{1s} V_\lambda C_T + 2V_\mu (D_T + \theta_0 E_T) + \theta_{1s} \Omega H_T$$

Ω derivatives

$$\frac{\partial T_z}{\partial \Omega} = V_\lambda (A_T + \theta_0 B_T) + 2\Omega (F_T + \theta_0 G_T) + \theta_{1s} V_\mu H_T$$

θ_0 derivatives

$$\frac{\partial T_z}{\partial \theta_0} = V_\lambda \Omega B_T + V_\mu^2 E_T + \Omega^2 G_T + 2F_{p0} \cos(\theta_p + \theta_0) - \sin(\theta_p + \theta_0) (\theta_{1c} F_{pc} + \theta_{1s} F_{ps})$$

θ_{1s} derivatives

$$\frac{\partial T_z}{\partial \theta_{1s}} = V_\lambda V_\mu C_T + V_\mu \Omega H_T + F_{ps} \cos(\theta_p + \theta_0)$$

θ_{1c} derivatives

$$\frac{\partial T_z}{\partial \theta_{1c}} = F_{pc} \cos(\theta_p + \theta_0)$$

F_{p0} derivatives

$$\frac{\partial T_z}{\partial F_{p0}} = 2\sin(\theta_p + \theta_0)$$

F_{pc} derivatives

$$\frac{\partial T_z}{\partial F_{pc}} = \theta_{1c} \cos(\theta_p + \theta_0)$$

F_{ps} derivatives

$$\frac{\partial T_z}{\partial F_{ps}} = \theta_{1s} \cos(\theta_p + \theta_0)$$

C.2.1.5 Derivatives of F_y

V_λ derivatives

$$\frac{\partial F_y}{\partial V_\lambda} = -2\theta_{1c}V_\lambda A_y - \theta_{1c}\Omega B_y$$

V_μ derivatives

$$\frac{\partial F_y}{\partial V_\mu} = 0$$

Ω derivatives

$$\frac{\partial F_y}{\partial \Omega} = -\theta_{1c}V_\lambda B_y$$

θ_0 derivatives

$$\frac{\partial F_y}{\partial \theta_0} = -F_{pc} \sin(\theta_p + \theta_0) - F_{p0}\theta_{1c} \cos(\theta_p + \theta_0)$$

θ_{1s} derivatives

$$\frac{\partial F_y}{\partial \theta_{1s}} = 0$$

θ_{1c} derivatives

$$\frac{\partial F_y}{\partial \theta_{1c}} = -V_\lambda^2 A_y - V_\lambda \Omega B_y - F_{p0} \sin(\theta_p + \theta_0)$$

F_{p0} derivatives

$$\frac{\partial F_y}{\partial F_{p0}} = -\theta_{1c} \sin(\theta_p + \theta_0)$$

F_{ps} derivatives

$$\frac{\partial F_y}{\partial F_{ps}} = 0$$

F_{pc} derivatives

$$\frac{\partial F_y}{\partial F_{pc}} = \cos(\theta_p + \theta_0)$$

C.2.1.6 Derivatives of F_x

V_λ derivatives

$$\frac{\partial F_x}{\partial V_\lambda} = 2\theta_{1s}V_\lambda A_x + V_\mu (B_x + \theta_0 C_x) + \theta_{1s}\Omega D_x$$

V_μ derivatives

$$\frac{\partial F_x}{\partial w} = V_\lambda (B_x + \theta_0 C_x) + \Omega E_x$$

Ω derivatives

$$\frac{\partial F_x}{\partial \Omega} = \theta_{1s}V_\lambda D_x + V_\mu E_x$$

θ_0 derivatives

$$\frac{\partial F_x}{\partial \theta_0} = V_\lambda V_\mu C_x + F_{ps} \sin(\theta_p + \theta_0) + F_{p0} \theta_{1s} \cos(\theta_p + \theta_0)$$

θ_{1s} derivatives

$$\frac{\partial F_x}{\partial \theta_{1s}} = V_\lambda^2 A_x + V_\lambda \Omega D_x + F_{p0} \sin(\theta_p + \theta_0)$$

θ_{1c} derivatives

$$\frac{\partial F_x}{\partial \theta_{1c}} = 0$$

F_{p0} derivatives

$$\frac{\partial F_x}{\partial F_{p0}} = \theta_{1s} \sin(\theta_p + \theta_0)$$

F_{ps} derivatives

$$\frac{\partial F_x}{\partial F_{ps}} = -\cos(\theta_p + \theta_0)$$

F_{pc} derivatives

$$\frac{\partial F_x}{\partial F_{pc}} = 0$$

C.2.1.7 Derivatives of Q_r

V_λ derivatives

$$\frac{\partial Q_r}{\partial V_\lambda} = 2V_\lambda (A_Q + \theta_0 B_Q) + \Omega (C_Q + \theta_0 D_Q) + \theta_{1s} V_\mu E_Q$$

V_μ derivatives

$$\frac{\partial Q_r}{\partial V_\mu} = \theta_{1s} V_\lambda E_Q + 2V_\mu F_Q$$

Ω derivatives

$$\frac{\partial Q_r}{\partial \Omega} = V_\lambda (C_Q + \theta_0 D_Q) + 2\Omega G_Q$$

θ_0 derivatives

$$\frac{\partial Q_r}{\partial \theta_0} = V_\lambda^2 B_Q + V_\lambda \Omega D_Q + r_p (2F_{p0} \sin(\theta_p + \theta_0) + \cos(\theta_p + \theta_0) (F_{pc} \theta_{1c} + F_{ps} \theta_{1s}))$$

θ_{1c} derivatives

$$\frac{\partial Q_r}{\partial \theta_{1c}} = F_{pc} r_p \sin(\theta_p + \theta_0)$$

θ_{1s} derivatives

$$\frac{\partial Q_r}{\partial \theta_{1s}} = V_\lambda V_\mu E_Q + F_{ps} r_p \sin(\theta_p + \theta_0)$$

F_{p0} derivatives

$$\frac{\partial Q_r}{\partial F_{p0}} = -2r_p \cos(\theta_p + \theta_0)$$

F_{ps} derivatives

$$\frac{\partial Q_r}{\partial F_{ps}} = r_p \sin(\theta_p + \theta_0) \theta_{1s}$$

F_{pc} derivatives

$$\frac{\partial Q_r}{\partial F_{pc}} = r_p \sin(\theta_p + \theta_0) \theta_{1c}$$

C.2.2 STEADY AIRFRAME

The downwash velocity is supposed to evolve slowly. However, a change in the flap angle is likely to modify the downwash angle of attack. Therefore, equation 2.50, page 78 leads to:

$$\frac{\partial \alpha_v}{\partial \beta_{1c}} = 1$$

From equation 2.51, page 78, it derives:

$$\frac{\partial u_{downwash}}{\partial v} = \cos(\alpha_v)$$

and:

$$\frac{\partial u_{downwash}}{\partial \alpha_v} = -v \sin(\alpha_v)$$

Equation 2.52, page 78, leads to:

$$\frac{\partial w_{downwash}}{\partial v} = \sin(\alpha_v)$$

and:

$$\frac{\partial w_{downwash}}{\partial \alpha_v} = v \cos(\alpha_v)$$

From equation 2.53, 79, the derivatives of V_i becomes:

$$\frac{\partial V_i}{\partial u} = \frac{2}{2\sqrt{(u + u_{downwash})^2 + (w_i + w_{downwash})^2}} (u + u_{downwash}) = \frac{(u + u_{downwash})}{V_i}$$

in the same way, it leads to:

$$\begin{aligned}\frac{\partial V_i}{\partial u_{downwash}} &= \frac{(u + u_{downwash})}{V_i} \\ \frac{\partial V_i}{\partial w_i} &= \frac{(w_i + w_{downwash})}{V_i} \\ \frac{\partial V_i}{\partial w_{downwash}} &= \frac{(w_i + w_{downwash})}{V_i}\end{aligned}$$

From equation 2.54, page 79, the derivatives of w_i are computed as:

$$\frac{\partial w_i}{\partial w} = 1$$

$$\frac{\partial w_i}{\partial p} = Y_i$$

$$\frac{\partial w_i}{\partial q} = X_i - X_{CG}$$

For equation 2.55, page 79, the derivatives of the angle of attack α_i are:

$$\frac{\partial \alpha_i}{\partial w_i} = \frac{1}{1 + \left(\frac{w_i + w_{download}}{u_i + u_{download}}\right)^2} \frac{1}{u_i + u_{download}} = \frac{u_i + u_{download}}{(u_i + u_{download})^2 + (w_i + w_{download})^2} = \frac{u_i + u_{download}}{V_i}$$

and:

$$\frac{\partial \alpha_i}{\partial w_{download}} = \frac{u_i + u_{download}}{V_i}$$

$$\frac{\partial \alpha_i}{\partial u_i} = -\frac{w_i + w_{download}}{V_i}$$

$$\frac{\partial \alpha_i}{\partial u_{download}} = -\frac{w_i + w_{download}}{V_i}$$

Derivatives of $v_{downwash}$ comes from equation 2.56, page 79:

$$\frac{\partial v_{download}}{\partial u_{download}} = -\sin \beta_{1s}$$

$$\frac{\partial v_{download}}{\partial \beta_{1s}} = -u_{download} \cos \beta_{1s}$$

Equation 2.57, page 79 leads to:

$$\frac{\partial v_i}{\partial v} = 1$$

$$\frac{\partial v_i}{\partial r} = -(X_i - X_{CG})$$

Lastly, equation 2.58, page 79 gives:

$$\frac{\partial \beta_i}{\partial u} = -\frac{v_i + v_{download}}{(u + u_{download})^2}$$

$$\frac{\partial \beta_i}{\partial u_{download}} = -\frac{v_i + v_{download}}{(u + u_{download})^2}$$

$$\frac{\partial \beta_i}{\partial v_i} = \frac{1}{u + u_{download}}$$

$$\frac{\partial \beta_i}{\partial v_{download}} = \frac{1}{u + u_{download}}$$

C.2.2.1 FUSELAGE

Equation 2.59, page 82 gives:

$$\frac{\partial Fz_{fus}}{\partial V} = \rho V \sin^2 \alpha S_{lateralsection} C_c$$

$$\frac{\partial Fz_{fus}}{\partial \alpha} = \rho V^2 \sin \alpha \cos \alpha S_{lateralsection} C_c$$

In the same way equations 2.17, page 83 and D.3.2, page 219 give:

$$\frac{\partial M_{fus}}{\partial V} = \rho V \sin^2 \alpha C_c \int_{nose}^{tail} x \frac{dS_{lateralsection}}{dx} \cdot dx$$

$$\frac{\partial M_{fus}}{\partial \alpha} = \rho V^2 \sin \alpha \cos \alpha C_c \int_{nose}^{tail} x \frac{dS_{lateralsection}}{dx} \cdot dx$$

and:

$$\frac{\partial Fx_{fus}}{\partial V} = \rho V \cos^2 \alpha \frac{Fx_{fus}}{q}$$

$$\frac{\partial Fx_{fus}}{\partial \alpha} = -\rho V^2 \sin \alpha \cos \alpha \frac{Fx_{fus}}{q}$$

C.2.2.2 WING

STALLED WING Equation 2.62, page 84 leads to:

$$\frac{\partial Fz}{\partial V} = \rho V \sin \alpha S_{wing_i} \quad (1.8 \text{ to } 2.0)$$

$$\frac{\partial Fz}{\partial \alpha} = \frac{1}{2} \rho V^2 \cos \alpha S_{wing_i} \quad (1.8 \text{ to } 2.0)$$

In the same way equation 2.63, page 84 leads to:

$$\frac{\partial}{\partial V} = \rho V \sin(\alpha + \delta e_i) S_{surface_i} \quad (1.8 \text{ to } 2.0)$$

$$\frac{\partial}{\partial \alpha} = \frac{1}{2} \rho V^2 \cos(\alpha + \delta e_i) S_{surface_i} \quad (1.8 \text{ to } 2.0)$$

$$\frac{\partial}{\partial \delta e_i} = \frac{1}{2} \rho V^2 \cos(\alpha + \delta e_i) S_{surface_i} \quad (1.8 \text{ to } 2.0)$$

ATTACHED AIRFLOW WING Equation 2.64, page 84 gives:

$$\frac{\partial Cl}{\partial \alpha} = 0.1106$$

And equation 2.65, page 85 gives:

$$\frac{\partial \Delta Cl}{\partial \delta e} = 0.0393$$

Equation 2.66, page 85 leads to:

$$\frac{\partial Cm}{\partial \alpha} = 0.0057$$

And equation 2.67, page 85 leads to:

$$\frac{\partial \Delta Cm}{\partial \delta e} = -0.0051$$

Equation 2.68, page 86 gives:

$$\frac{\partial Cd}{\partial \alpha} = 0.0006\alpha - 0.001$$

Those derivatives are used to compute the following ones: From equation 2.69, page 86, it comes:

$$\frac{\partial F^{z_{w1}}}{\partial V} = \rho V S_{wing_i} (Cl \cos \alpha + Cd \sin \alpha)$$

$$\frac{\partial F^{z_{w1}}}{\partial \alpha} = \frac{1}{2} \rho V^2 S_{wing_i} (-Cl \sin \alpha + Cd \cos \alpha)$$

$$\frac{\partial F^{z_{w1}}}{\partial Cl} = \frac{1}{2} \rho V^2 \cos \alpha S_{wing_i}$$

$$\frac{\partial F^{z_{w1}}}{\partial Cd} = \frac{1}{2} \rho V^2 \sin \alpha S_{wing_i}$$

Equation 2.70, page 86 gives:

$$\begin{aligned}\frac{\partial Fx_{w1}}{\partial V} &= \rho V S_{wing} (-\sin \alpha Cl + \cos \alpha Cd) \\ \frac{\partial Fx_{w1}}{\partial \alpha} &= -\frac{1}{2}\rho V^2 S_{wing} (\cos \alpha Cl + \sin \alpha Cd) \\ \frac{\partial Fx_{w1}}{\partial Cl} &= -\frac{1}{2}\rho V^2 \sin \alpha S_{wing} \\ \frac{\partial Fx_{w1}}{\partial Cd} &= \frac{1}{2}\rho V^2 \cos \alpha S_{wing}\end{aligned}$$

Equation 2.71, page 86 gives:

$$\begin{aligned}\frac{\partial M_{w1}}{\partial V} &= \rho V C_m S_{wing_i} \\ \frac{\partial M_{w1}}{\partial C_m} &= \frac{1}{2}\rho V^2 S_{wing_i}\end{aligned}$$

From equation 2.72, page 86 follows:

$$\begin{aligned}\frac{\partial \Delta Fz_{flapi}}{\partial V} &= \rho V \Delta Cl_i \cos \alpha S_{wing_i} \\ \frac{\partial \Delta Fz_{flapi}}{\partial \alpha} &= -\frac{1}{2}\rho V^2 \Delta Cl_i \sin \alpha S_{wing_i} \\ \frac{\partial \Delta Fz_{flapi}}{\partial \Delta Cl_i} &= \frac{1}{2}\rho V^2 \cos \alpha S_{wing_i}\end{aligned}$$

Lastly equation 2.73, page 86 provides:

$$\begin{aligned}\frac{\partial \Delta M_{flapi}}{\partial V} &= \rho V \Delta C m_i S_{wing_i} \\ \frac{\partial \Delta M_{flapi}}{\partial \Delta C m_i} &= \frac{1}{2}\rho V^2 S_{wing_i}\end{aligned}$$

C.2.2.3 FIN

Equation 2.74, page 87 gives:

$$\frac{\partial Cl}{\partial \beta} = 0.1174$$

and equation 2.75, page 87 gives:

$$\frac{\partial \Delta Cl}{\partial \delta e} = 0.033$$

Equation 2.76, page 89 leads to:

$$\frac{\partial Cd}{\partial \alpha} = 0$$

and equation 2.77, page 89 leads to:

$$\frac{\partial \Delta Cd}{\partial \delta e} = 1.8 \cdot 10^{-4} \delta e$$

Those derivatives are used to compute the following ones: Equation 2.78, page 89, leads to:

$$\frac{\partial F y_{VTPi}}{\partial V} = \rho V Cl S_{VTP}$$

$$\frac{\partial F z_{w1}}{\partial Cl} = \frac{1}{2} \rho V^2 S_{VTP}$$

Equation 2.70, page 86 gives:

$$\frac{\partial F x_{VTPi}}{\partial V} = \rho V Cd S_{VTP}$$

$$\frac{\partial F x_{VTPi}}{\partial Cd} = \frac{1}{2} \rho V^2 S_{VTP}$$

From equation 2.80, page 90 follows:

$$\frac{\partial \Delta F y_{VTPi}}{\partial V} = \rho V \Delta Cl_i S_{section}$$

$$\frac{\partial \Delta F y_{VTPi}}{\partial \Delta Cl_i} = \frac{1}{2} \rho V^2 S_{section}$$

Lastly equation 2.81, page 90 provides:

$$\frac{\partial \Delta F x_{VTPi}}{\partial V} = \rho V \Delta Cd_i S_{section}$$

$$\frac{\partial \Delta F x_{VTPi}}{\partial \Delta Cd_i} = \frac{1}{2} \rho V^2 S_{section}$$

C.2.3 Modified dynamics

The additional derivatives relatives to the angle vector $\vec{\theta}$ are:

$$\vec{q} = e^{\frac{\vec{\theta}}{2}}$$

where the exponential is defined as:

$$e^{\vec{\theta}} = \begin{cases} \begin{pmatrix} \cos\left(\frac{\|\vec{\theta}\|}{2}\right) \\ \frac{\vec{\theta}}{\|\vec{\theta}\|} \sin\left(\frac{\|\vec{\theta}\|}{2}\right) \end{pmatrix}, & \text{if } \|\vec{\theta}\| \neq 0 \\ \begin{pmatrix} 1 \\ \vec{0} \end{pmatrix}, & \text{if } \|\vec{\theta}\| = 0 \end{cases}$$

where:

$$\|\vec{\theta}\| = \sqrt{\theta_1^2 + \theta_2^2 + \theta_3^2}$$

It leads to:

$$d\vec{q} = \begin{cases} \begin{pmatrix} -\frac{1}{2} \sin\left(\frac{\|\vec{\theta}\|}{2}\right) d\|\vec{\theta}\| \\ \frac{1}{\|\vec{\theta}\|} \sin\left(\frac{\|\vec{\theta}\|}{2}\right) d\vec{\theta} - \frac{\vec{\theta}}{\|\vec{\theta}\|^2} \sin\left(\frac{\|\vec{\theta}\|}{2}\right) d\|\vec{\theta}\| + \frac{1}{2} \frac{\vec{\theta}}{\|\vec{\theta}\|} \cos\left(\frac{\|\vec{\theta}\|}{2}\right) d\|\vec{\theta}\| \end{pmatrix}, & \text{if } \|\vec{\theta}\| \neq 0 \\ \begin{pmatrix} 0 \\ \frac{d\vec{\theta}}{2} \end{pmatrix}, & \text{if } \|\vec{\theta}\| = 0 \end{cases}$$

where, when $\|\vec{\theta}\| \neq 0$, it becomes:

$$d\|\vec{\theta}\| = \frac{1}{2\sqrt{\theta_1^2 + \theta_2^2 + \theta_3^2}} (2d\theta_1 + 2d\theta_2 + 2d\theta_3) = \frac{(d\theta_1 + d\theta_2 + d\theta_3)}{\|\vec{\theta}\|}$$

D

APPENDIX: CONCEPTUAL DESIGN

D.1 AMBIENT CONDITION

In this section are defined the ambient conditions used to performed the study.

D.1.1 METEOROLOGY

The meteorology definition is based on the International Standard Atmosphere or ISA, the standard of the ICAO (International Civil Aviation):

- The sea level meteorological conditions are shown in Table [D.1](#): The atmospheric con-

Atmospheric parameter	<i>Symbol</i>	<i>Value</i>	<i>Unity</i>
Density	ρ_0	1.225	$Kg.m^{-3}$
Pressure	P_0	101325	Pa
temperature	T_0	288.25	K
Sound speed	a_0	340.35	$m.s^{-1}$
Dynamique viscosity	μ_0	0.000018	$Pa.s$

Table D.1: Sea level meteorologic conditions

stant will also be required. They are shown in Table [D.2](#): Then, the different atmospheric parameters can be estimated at the different altitudes Z (in m):

Adiabatic index	γ	1.4	
Massic gas constant	R	287.058	$J.Kg^{-1}.K^{-1}$
Specific heat capacity	c_p	1004	$J.Kg^{-1}.K^{-1}$

Table D.2: Meteorologic constants

- Temperature T (in K):

$$T = T_0 - \frac{6,5 \cdot Z}{1000}$$

- Pressure P (in Pa):

$$P = P_0 \left(\frac{288 - 0.0065 \cdot Z}{288} \right)^{5.255}$$

- Air density ρ (in $kg.m^{-3}$):

$$\rho = \frac{P}{RT}$$

- Speed of sound a (in $m.s^{-1}$):

$$a = \sqrt{\gamma \cdot R \cdot T}$$

- Dynamic viscosity μ (in $Pa.s$):

$$\mu = \frac{0.0000014586 \cdot T^{3/2}}{T + 110.4}$$

D.1.2 GEOLOGY

The gravity of Earth, denoted g , is assumed to be constant:

$$g = 9.81m.s^{-2}$$

The average elevation of earth's land surface $h_{average}$ is:

$$h_{average} = 840m$$

D.2 WEIGHT AND BALANCE

Because of its unusual configuration halfway between an aeroplane and a helicopter, the estimation of the different constituting systems masses is carried out thanks to the semi-empirical methods initially developed for the latter two. The helicopter components weight estimations are based on the most accurate estimation method referenced in the NASA Contractor Report 3580 [?]. The aeroplane components weight estimations are based on the general aviation aeroplanes estimation method referenced by Raymer ([?]; ch. 15.3) or Roskam ([?];PART V Chapter 4 - 7). For the components common to the two kinds of aircraft, the two estimations are done, and the heaviest is retained.

D.2.1 FORE PLANE

The fore plane is used both as a canard wing and as rotor blades:

- Aeroplane wing: The fore plane weight estimation is estimated using the Raymer formula to support the horizontal aeroplane load ([?]; eq. 15.46):

$$W_{wing} = 0.036 \times S_w^{0.758} \times W_{fw}^{0.0035} \left(\frac{A}{\cos^2 \Lambda} \right)^{0.6} q^{0.006} \times \lambda^{0.04} \left(\frac{100t/c}{\cos \Lambda} \right)^{-0.3} (N_z W_{dg})^{0.49} \quad (\text{D.1})$$

where W_{wing} is the mass of the wing (in lb), S_w is the trapezoidal wing area (in ft^2), W_{fw} is the weight of fuel in wing (in lb), A is the aspect ratio, Λ is the wing sweep at 25% of the MAC, q is the dynamic pressure at cruise (in lb/ft^2), λ is the taper ratio, t/c is the wing airfoil thickness ratio, N_z is the ultimate load factor ($= 1.5 \times \text{limitloadfactor}$), W_{dg} is the design cross weight (in lb). W_{dg} is here only the portion of the lift supported in flight (tandem wing configuration)

- Helicopter rotor blade: It seems that the best blade estimation is given by the RTL (Research and Technology Labs) formula ([?]; eq. 2.3):

$$n_{bl} \times W_{bl} = 0.02638 \times n_{bl}^{0.6826} \times c^{0.9952} \times R^{1.3607} \times V_t^{0.6663} \times v_1^{2.5231}$$

where n_{bl} is the number of blades, W_{bl} is the mass of a blade (in lb), c is the blade

mean chord (in ft), R is the rotor radius (in ft), V_t the tip speed (in fps) and v_1 the first natural blade flapping frequency (assumed equal to 1.03).

The fore plane mass is eventually equal to:

$$W_{W2} = F f_{wing} \times MAX(n_{bl} \times W_{bl}; W_{wing})$$

where $F f_{wing}$ is the weight factor for composite use ([?]: $F f_{wing} = 0.85$).

The weight of the fore plane is assumed to apply to half of the chord for the calculation of the aircraft centre of gravity position.

D.2.2 MAIN-ROTOR HUBS AND HINGES

It seems that the best Main-Rotor and Hinges weight estimation is given by the RTL (Research and Technology Labs) formula ([?] ; eq. 2.7):

$$W_h = 0.002116 \times n_{bl}^{0.2965} \times R^{1.5717} \times V_t^{0.5217} \times v_1^{1.9550} (n_{bl} \times W_{bl})^{0.5292}$$

where W_h is the mass of the Main-Rotor and Hinges (in lb), n_{bl} is the number of blade, R is the rotor radius (in ft), V_t the tip speed (in fps) and v_1 the first natural blade flapping frequency (assumed equal to 1.03) and W_{bl} is the mass of a blade (in lb). The main rotor hub centre of gravity is supposed to be at the base of the blades.

D.2.3 MAIN WING WEIGHT

The main wing weight is estimated using the Raymer formula just as for the fore plane in horizontal flight D.1. As for the fore plane, a factor is applied to account the composite weight saving, and the weight of the main wing is assumed to apply to half of its chord.

D.2.4 VERTICAL TAIL WEIGHT

The vertical tail weight is estimated using the Raymer formula ([?] ; eq. 15.48):

$$W_{verticaltail} = 0.073 \left(1 + 0.2 \frac{H_t}{H_v} \right) (N_z W_{dg})^{0.376} q^{0.122} S_{vt}^{0.873} \left(\frac{100t/c}{\cos \Lambda_{vt}} \right)^{-0.49} \left(\frac{A}{\cos^2 \Lambda_{vt}} \right)^{0.357} \lambda_{vt}^{0.039}$$

where $W_{verticaltail}$ is the mass of the vertical tail (in lb), $\frac{H_t}{H_v}$ is 0 for conventional tail, N_z is the ultimate load factor ($= 1.5 \times limitloadfactor$), W_{dg} is the design gross weight (in lb), q is the dynamic pressure at cruise (in lb/ft^2), S_{vt} is the vertical tail area (in ft^2), t/c is the wing aerofoil thickness ratio, Λ_{vt} is the vertical tail sweep at 25% of the MAC, λ_{vt} is tail plane taper ratio and A is the aspect ratio. As for the fore plane, a factor, Ff_{tail} , is applied due to the composite use ([?]: $Ff_{tail} = 0.85$):

$$W_{Vertical\ tail} = Ff_{tail} \times W_{verticaltail}$$

And the weight is assumed to apply at half of its chord.

D.2.5 FUSELAGE

- Aeroplane fuselage: The fuselage weight estimation for aeroplane is done using the USAF formula exposed by Roskam (since it is the only one which does not consider the number of passengers or the pressurisation) ([?]; eq. 5.25):

$$W_f = \left[200 \left(\frac{W_{TO} n_{ult}}{10^5} \right)^{0.286} \left(\frac{l_f}{10} \right)^{0.857} \left(\frac{w_f + h_f}{10} \right) \left(\frac{V_c}{100} \right)^{0.338} \right]^{1.1}$$

where W_{TO} is the MTOW (in kts), n_{ult} is the ultimate load factor in aeroplane mode, l_f is the fuselage length (in ft), w_f is the maximum fuselage width (in ft), h_f is the maximum fuselage height (in ft), V_c is the design cruise speed (in $KEAS$),

- Helicopter fuselage: The fuselage weight estimation for helicopter is done using the RTL (Research and Technology Labs) formula ([?]; eq. 2.19):

$$W_{bg} = 10.13 \left(10^{-3} W_{gr_{max}} \right)^{0.5719} n_{ult}^{0.2238} L_{\infty}^{0.5558} S_f^{0.1534} I_{ramp}^{0.5242}$$

where $W_{gr_{max}}$ is the maximum flying weight (assumed to be the MTOW; in lb), n_{ult} is the ultimate load factor in helicopter mode, L_{∞} is the total length of the fuselage (in the present case, because of the 'Tail-sitter' configuration, the length is actually the fuselage diameter; in ft), S_f is the fuselage wetted area (in f^2), I_{ramp} is a ramp presence indicator ($I_{ramp} = 1.0$ here).

The fuselage mass is eventually equal to:

$$W_{fuselage} = Ff_{fuselage} \times MAX(W_{bg}; W_f)$$

where $Ff_{fuselage}$ is the weight factor for composite use ([?]: $Ff_{fuselage} = 0.9$). The weight of the fuselage is supposed to apply to half of its length.

D.2.6 LANDING GEAR

The landing gear weight estimation is the most in doubt because of its configuration. Indeed the main landing gear is merged with the vertical tail-plane. Therefore the weight of the assembly is likely to be less than the sum of the mass estimations of each component taken separately. Nevertheless, at this stage of the design, it is assumed to be equal to this latter sum to remain conservative.

- Aeroplane landing gear: The aeroplane landing gear weight estimation is done for the main and the nose landing gear separately, using the formula proposed by Raymer ([?]; eq. 15.50, eq. 15.51):

$$W_{main\ landing\ gear} = 0.095 (N_l W_l)^{0.768} \left(\frac{L_m}{12} \right)^{0.409}$$

$$W_{nose\ landing\ gear} = 0.125 (N_l W_l)^{0.566} \left(\frac{L_n}{12} \right)^{0.845}$$

where N_l is the ultimate landing factor ($N_l = 1.5 \times N_{gear}$), W_l is the maximum landing weight (in *lb*), L_m is the length of the main landing gear (in *ft*) and L_n is the length of the nose landing gear (in *ft*).

- Helicopter landing gear: The RTL (Research and Technology Labs) formula is used ([?]; eq. 2.27):

$$W_{lgw} = 36.76 \left(\frac{W_{gr_{max}}}{1000} \right)^{0.719} n_{wl}^{0.4626} I_{rig}^{0.0773}$$

where W_{max} is the maximum flying weight (in *lb*), n_{wl} is the number of wheeled landing gear legs; I_{rig} is the retraction landing-gear coefficient ($I_{rig} = 2$ here).

The landing gear mass is eventually equal to:

$$W_{Landing\ gear} = Ff_{LG} \times MAX(W_{lgw}; W_{main\ landing\ gear} + W_{nose\ landing\ gear})$$

where Ff_{LG} is the weight factor for composite use ([?]: $Ff_{LG} = 0.95$). Because of its configuration exposed in section 4.2.1, page 113, the weight of the landing gear is considered to apply at the CG location.

D.2.7 FUEL SYSTEM

- Aeroplane fuel system: The fuel system weight estimate is done using the Torenbeek method exposed by Roskam ([?]; eq. 6.18):

$$W_{fs} = 2 \left(\frac{W_F}{5.87} \right)^{0.667}$$

where W_{fs} is the fuel system weight (in *lb*), W_F is the mission fuel weight (includes reserves; in *lbs*)

- Helicopter fuel system: The fuel system weight estimation for helicopter is done using the RTL approach. The estimation is done in two steps. On the first hand, the estimation of the system minus the fuel tank is done ([?]; eq. 2.42):

$$W_{fs-t} = C_1 + C_2 (0.01n_{ft} + 0.06n_{eng}) FF_{max}^{0.866}$$

where W_{fs-t} is the fuel system minus tank weight (in *lb*), C_1 is a constant accounting for special items (0 here), C_2 is a crashworthiness and survivability factor for the fuel system (1 here), n_{ft} is the number of fuel tank (3, one in the front, and two in the wing), n_{eng} is the number of engines, FF_{max} is the maximum engine fuel flow (in *lb/hr*). On the other hand, the fuel tank weight estimation is done. In the present case, the only fuel tank considered is the one in the front since the one in the wing is of integral fuel tank kind, and is therefore included in the main wing weight estimation ([?]; eq. 2.41):

$$W_{ft} = 0.4341G_t^{0.7717} n_{ft}^{0.5897} F_{cr}^{0.393} F_{bs}^{1.9491}$$

where W_{ft} is fuel tank weight tank estimation (in *lb*), n_{ft} is the number of fuel tank (only 1 in the front), G_t is the total fuel tank capacity (in *gallon*), F_{cr} is the fuel tank and supporting structure crashworthiness factor (1 here), F_{bs} is the fuel tanks and supporting structure tolerance factor (1 here).

The fuel system mass $W_{fuelsystem}$ is eventually equal to:

$$W_{fuelsystem} = MAX(W_{fs}; W_{fs-t} + W_{ft})$$

D.2.8 FLIGHT CONTROLS SYSTEM

The estimation of the flight controls system is a bit different from the method used up to now in the sense that the weight of the flight controls of each mode of flight (aeroplane or helicopter) are estimated separately, and then added to obtain the overall flight control system's weight estimation.

- Aeroplane Flight Controls System: The aeroplane flight control system weight estimation is done using the method proposed by Raymer ([?]; eq. 15.54):

$$W_{flightcontrolaircraft} = 0.053 \cdot L^{1.536} B_w^{0.371} \left(\frac{N_z W_{dg}}{10000} \right)^{0.8}$$

where $W_{flightcontrolaircraft}$ is the aircraft flight control system weight estimation (in *lb*), L is the fuselage length (in *ft*), B_w is the wing span (in *ft*), N_z is the ultimate load factor ($1.5 \times limitload$), W_{dg} is the design gross weight (in *lb*).

- Helicopter Flight Controls System: The flight control system weight estimation for helicopter is done using the RTL approach. The present aircraft being a UAV, the weight of the cockpit controls are neglected ([?]; eq. 2.53):

$$W_{rfc} = 0.1657 (F_{cb})^{1.3696} c^{0.4481} F_{cp}^{0.4469} W_{gr_{max}}^{0.6865}$$

where W_{rfc} is the helicopter flight control system weight estimation (in *lb*), F_{cb} is a coefficient (one here), c is the blade chord (in *ft*), F_{cp} is the flight control ballistic tolerance coefficient (1 here), $W_{gr_{max}}$ is the design gross weight (in *lb*).

The flight control system mass $W_{flight-control}$ is eventually equal to:

$$W_{flight-control} = W_{flightcontrolaircraft} + W_{rfc}$$

As for the fuel system, the weight of the flight control system is assumed to apply at two different locations:

The weight of the helicopter flight control is expected to apply at the main-rotor hub location, and the weight of the aeroplane flight control is assumed to apply at the main wing location.

D.2.9 PROPULSION SYSTEM :

As speculated in section 0.2.3 page 13, the present aircraft being propelled by a “series” type hybrid propulsion system. Because the aircraft is likely to fly in two distinct modes, the electric powertrain is composed of main generator and boost generator. The boost generator is kept turned off except when the required power is greater than the main generator maximum one (i.e. in helicopter mode). The heaviest electric system components accounted in the propulsion system mass estimation. Their characteristics are assumed to be the one forecast in ten years.

- Electric motors The electrical motor characteristics are prognosticated to be: a specific power of 10 kg/kW and an efficiency of 95%. These characteristics are assumed to be the same for the electrical generators used for the estimation of the thermal generators characteristics. The rotors blades accommodate the electric motors at the very beginning of the aircraft.
- Main generator: The main generator can be of 4 types: Otto, Wankel, diesel or gas turbine, since these types of engine are widely used and available for a broad range of power. The characteristics of each engines are exposed in Table D.3. The engines specific power is assumed to be constant over the range of studied power. Its weight $W_{main\ generator}$ is obtained multiplying the specific power of the selected type by the optimized maximum power. The application location of the main generator weight is optimized to tweak the CG location.

Type	Specific power dry engine (kW/kg)	SFC engine (g/kWhr)	specific power electrical generator (kW/kg)	SFC electrical generator (g/kWhr)
Gas turbine	3	440	2,19	463,15
wankel	2,32	276,36	1,79	290,91
gazoline otto engine	1,27	222,73	1,07	234,45
diesel	0,91	181,82	0,79	191,39

Table D.3: Electrical generator characteristics

- Boost generator: The same method is applied to the boost generator, which provides its weight $W_{boost\ generator}$. The location of its CG is assumed to be the same as the one of the main generator.
- Battery: The battery mass $W_{battery}$ (in kg) is directly proportional to its capacity $E_{battery}$ (in $kwhr$), and follows:

$$W_{battery} = \left(\frac{W}{E}\right)_{battery} E_{battery}$$

where, $\left(\frac{W}{E}\right)_{battery}$ is the battery weight to energy ratio (in $kg/kWhr$), which is conservatively fixed to $5kg/kWhr$, in view of the oncoming technologies. The capacity of the battery capacity $E_{battery}$ is sized to supplement the first engine in a safe evasive manoeuvre when the boost engine is turned off. The wings accommodate the batteries.

D.3 AERODYNAMICS

D.3.1 INDUCED DRAG

The estimation of the induced drag coefficient Cd_i is done thanks to the theory developed by Ludwig Prandtl ([?]; ch. 12.6):

$$Cd_i = \frac{Cz^2}{\pi \cdot A \cdot e}$$

where Cz is the lift coefficient, A is defined as $\frac{(longer\ span)^2}{S_{W1}+S_{W2}}$ with S_{W1} and S_{W2} the wing area of respectively the main wing and the fore plane. Lastly, e is an adjustment coefficient for

no perfectly elliptical lift distribution which is estimated as:

$$e = \frac{\mu^2 (1 + r^2)}{\mu^2 + 2 \cdot \sigma \cdot \mu \cdot r + r^2}$$

where: $\mu = \frac{\text{Shorter span}}{\text{Longer span}}$, $r = \frac{\text{Lift of shorter wing}}{\text{Lift of longer wing}}$ and σ is the interference factor shown in Figure D.1.

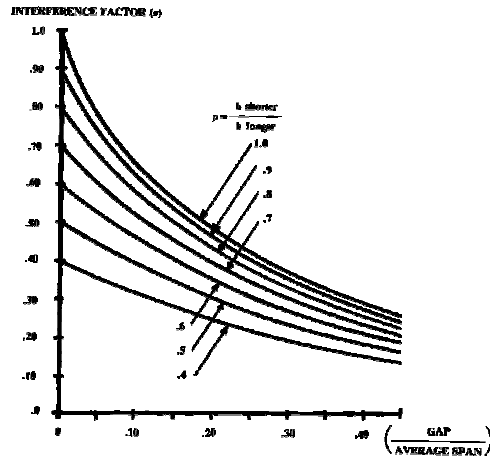


Figure D.1: Prandtl biplane interference factor ([?], Figure 5-10)

D.3.2 FUSELAGE

The drag of the fuselage is estimated following the method proposed by Raymer ([?]; ch. 12). The estimation of the drag is based on the assimilation of the wetted area to a flat plate surface. The drag computed is then multiplied by factors to approximate the actual one ([?]; eq. 12.24):

$$Cd_{0_{fuselage}} = \frac{C_{fc} \cdot FF_c Q_c S_{wet}}{S_{ref}} + Cd_{misc} + Cd_{prot}$$

where $Cd_{0_{fuselage}}$ is the fuselage drag coefficient, C_{fc} is the equivalent flat plate drag coefficient, FF_c is the "form factor" corresponding to the pressure drag, S_{wet} is the fuselage wet area (in m^2), S_{ref} is the reference area (here the main wing area; in m^2), Cd_{misc} is the miscellaneous drag component and Cd_{prot} is the protuberance component. Raymer suggests first to calculate the drag for both laminar and turbulent flow and then to average the two computed values. However, this method does not seem to be representative of the reality. Indeed in the real world, the flow starts being laminar and becomes turbulent at a defined

location. The method is therefore customized using the basic idea of the method proposed by Schmollgruber [?]. The proposed method is illustrated in Figure D.2 proceeds as follow:

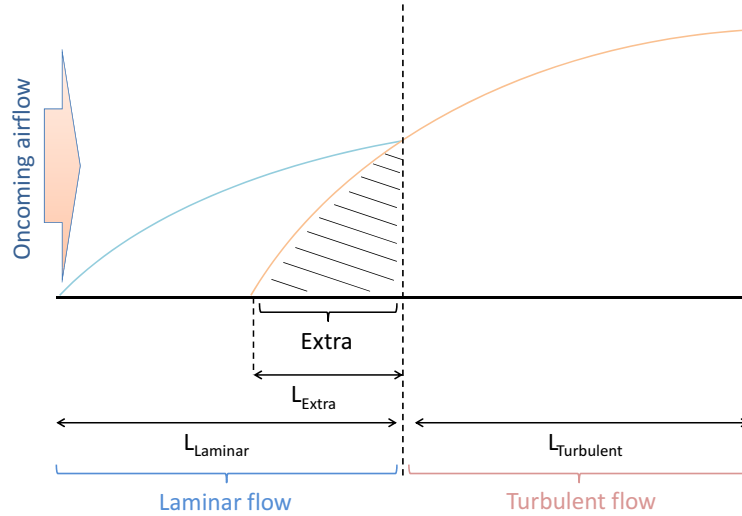


Figure D.2: Friction drag estimation method

- The friction drag coefficient $C_{l_{laminar}}$ is computed for a laminar flow between the leading edge and the transition ([?]; eq. 12.25):

$$C_{l_{laminar}} = \frac{1.328}{\sqrt{Re_{laminar}}}$$

where $Re_{laminar}$ is the laminar Reynolds number computed as ([?]; eq. 12.26):

$$Re_{laminar} = \frac{\rho \cdot V \cdot L_{laminar}}{\mu}$$

where $L_{laminar}$ is the characteristic dimension (here the length of the assumed laminar flow body portion (in m)).

- The thickness of the boundary layer $\delta_{laminar}$ (in m) is computed at the transition location $L_{laminar}$, for a laminar flow [?]:

$$\delta_{laminar} = \frac{5.2 \cdot L_{laminar}}{\sqrt{Re_{laminar}}}$$

-
- The equivalent flat plate length $L_{equivalent}$ (in m) is computed to get the same boundary layer thickness in turbulent flow [?].

$$\delta_{turbulent} = \frac{0.37 \cdot L_{equivalent}}{Re_{turbulent}^{0.2}}$$

where $Re_{turbulent}$ is the turbulent Reynolds number computed as the laminar one but taking into account the length of the turbulent flow body portion $L_{turbulent}$ (in m).

$$L_{equivalent} = \frac{\delta_{turbulent} \cdot Re_{turbulent}^{0.2}}{0.37}$$

At the transition, $\delta_{turbulent} = \delta_{laminar}$ So:

$$L_{equivalent} = \frac{\delta_{laminar} \cdot Re_{turbulent}^{0.2}}{0.37}$$

- The friction drag is computed for a turbulent flow, for a distance $L_{equivalent} = L_{turbulent} + L_{extra}$ ([?]; eq. 12.27):

$$Cl_{turbulent} = \frac{0.455}{((\log_{10}(R_{cutoff}))^{2.58} \cdot (1 + 0.144 \cdot M^2)^{0.65})}$$

where M is the Mach number and R_{cutoff} is the "cut-off Reynolds number" defined as ([?]; eq. 12.28):

$$R_{cutoff} = 38.21 \cdot \left(\frac{L_{equivalent}}{k}\right)^{1.053}$$

where k is the skin roughness value ($k = 1.08 \cdot 10^{-5}$ here assuming that the fuselage will be painted).

- The excess drag corresponding to the turbulent flow before the transition is computed ([?]; eq. 12.27):

$$Cl_{excess} = \frac{0.455}{((\log_{10}(R_{cutoff}))^{2.58} \cdot (1 + 0.144 \cdot M^2)^{0.65})}$$

where R_{cutoff} is computed for L_{extra} .

- Finally, the total friction drag $D/q_{flatplate}$ is computed:

$$D/q_{flatplate} = C_{l_{turbulent}} \cdot (S_{turbulent} + S_{extra}) + C_{l_{laminar}} \cdot S_{laminar} - C_{l_{extra}} \cdot S_{extra}$$

where $S_{turbulent}$, $S_{laminar}$ and S_{extra} are respectively the turbulent, laminar and extra wet surfaces (in m^2).

Then, having the equivalent flat plate friction drag, the component form factor FF is evaluated to add the pressure drag due to viscous separation ([?]; eq. 12.31):

$$FF = \left(1 + \frac{60}{f^3} + \frac{f}{400} \right)$$

with ([?]; eq. 12.33)

$$f = \frac{L}{D} = \frac{L}{\sqrt{\left(\frac{4}{\pi}\right) \cdot A_{max}}}$$

where L is the body length (in m), A_{max} is the maximum surface area (in m^2) and D is the body diameter (in m). Then the component interference factor is estimated. This element accounts the drag due to the interaction between the different bodies. The wing on the fuselage can be considered as mid-wing mounted, therefore $Q = 1$. Cd_{misc} is now evaluated. It takes into account the drag due to specific characteristics such as the upsweep of the rear for the fuselage. For the present aircraft, the fuselage tail is particularly aerodynamic. Therefore this component is neglected. The last drag component Cd_{prot} . This component includes all the devices that disturb the flow such as antennas. Propellers driven aircraft are likely to present a protuberance drag between 5% and 10% of the total drag. Therefore it is assumed that the present aircraft have a protrusion drag of 7%. Therefore the following coefficient is introduced:

$$\partial Cd_{prot} = 0.07$$

Eventually the fuselage total drag is:

$$D/q_{fuselage} = D/q_{flatplate} \cdot FF \cdot (1 + \partial Cd_{prot})$$

D.3.3 ELECTRIC MOTOR NACELLES

As described in section 4.2.4, page 119, the electric motor nacelle are designed to aerodynamically shape the motors. The estimation of their aerodynamics starts thus with an estimation of the motors size.

Motor size: The diameter and the length versus vs the maximum power of the Siemens motor powering the DA36 E-Star 2 ($80kW$), the Yuneec motor family (from $10kW$ to $60kW$), and Turnigy RotoMax motor family (from $1.924kW$ to $9.8kW$) are shown in Figure D.3.

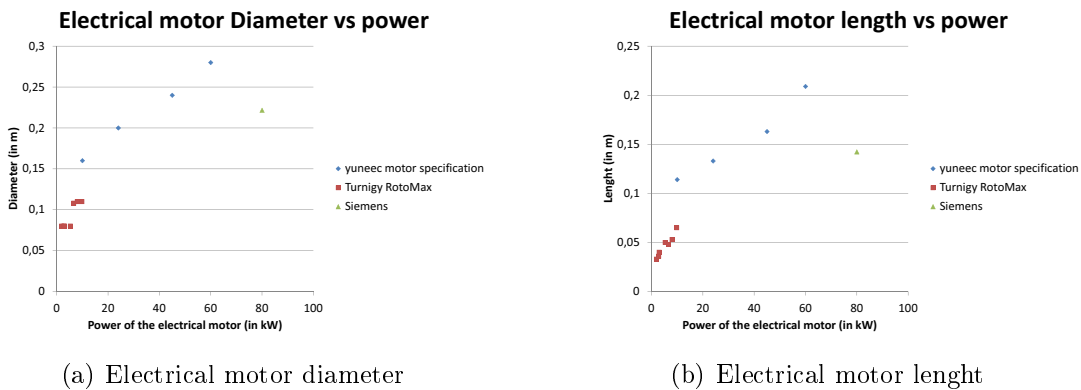


Figure D.3: Electrical motor characteristics

It can be seen that there is a linear relation between the length, the diameter and the maximum power of the rotor, except for the Siemens one which is of different technology (reduced one). The size of the electric motor is therefore directly estimated from its required maximum power.

Internal aerodynamic: The internal aerodynamic is analysed to provide enough cooling to the electric motors while minimising as much as possible the drag of the nacelle. The variables required for the study are shown in Figure D.4.

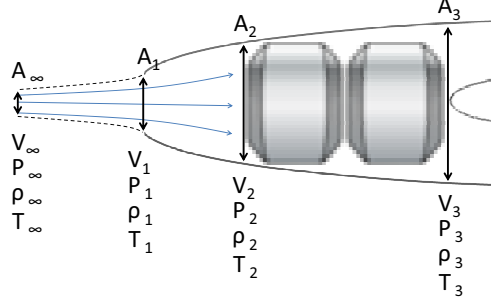


Figure D.4: Nacelle intake zoom

where A is the area of the flow tube section (in m), V is the air velocity (in $m.s^{-1}$), ρ is the air density (in $kg.m^{-3}$) and T is the temperature (in K) at each studied locations denoted by the subscripts ∞ for the upstream air, 1 for the intake, 2 for the engine beginning and 3 for the engine end. **A_2 is not the frontal area of the motor but the area of the outer part of the motor starting with the electromagnet.**

First the transformation between A_∞ and A_2 is studied. According to Bernoulli's Theorem:

$$\frac{1}{2}\rho_\infty \cdot V_\infty^2 + P_\infty = \frac{1}{2}\rho_2 \cdot V_2^2 + P_2$$

Assuming that the air is a perfect gas, It comes:

$$\frac{1}{2}\rho_\infty \cdot V_\infty^2 + \rho_\infty \cdot R \cdot T_\infty = \frac{1}{2}\rho_2 \cdot V_2^2 + \rho_2 \cdot R \cdot T_2$$

The mass conservation gives:

$$\dot{m} = \rho_\infty \cdot V_\infty \cdot A_\infty = \rho_2 \cdot V_2 \cdot A_2$$

where \dot{m} is the time derivative of the mass (in $kg.s^{-1}$). Assuming that the flow is incompressible, and combined with the Bernoulli's Theorem, it gives:

$$\frac{1}{2}V_\infty^2 + R \cdot T_\infty = \frac{1}{2} \left(V_\infty \frac{A_\infty}{A_2} \right)^2 + R \cdot T_2 \quad (D.2)$$

Then the transformation between A_2 and A_3 is studied. It is supposed to be a heating

at constant pressure $P_2 = P_3$. According to the thermodynamic second law:

$$\begin{aligned} dQ &= cp \cdot dT \\ \Leftrightarrow dQ &= m \cdot cp_m \cdot dT \end{aligned}$$

where Q is the heat transfer (in J), cp is the heat capacity (in $J.K^{-1}$), cp is the specific heat capacity (in $J.K^{-1}.kg^{-1}$), m is the air mass (in kg) and T is the air temperature. Deriving the equation with respect to the time:

$$P_{heat} = \dot{m} \cdot cp_m (T_3 - T_2)$$

which combined with the mass conservation result gives:

$$\begin{aligned} P_{heat} &= \rho_\infty \cdot V_\infty \cdot A_\infty \cdot cp_m (T_3 - T_2) \\ \Leftrightarrow T_2 &= T_3 - \frac{P_{heat}}{\rho_\infty \cdot V_\infty \cdot A_\infty \cdot cp_m} \end{aligned} \quad (D.3)$$

It becomes eventually:

$$\begin{aligned} \frac{1}{2}V_\infty^2 + R \cdot T_\infty &= \frac{1}{2} \left(V_\infty \frac{A_\infty}{A_2} \right)^2 + R \left(T_3 - \frac{P_{heat}}{\rho_\infty \cdot V_\infty \cdot A_\infty \cdot cp_m} \right) \\ \Leftrightarrow A_\infty^3 + \left(\frac{2 \cdot A_2^2 \cdot R (T_3 - T_\infty)}{V_\infty^2} - A_2^2 \right) A_\infty - \frac{2 A_2^2 R \cdot P_{heat}}{\rho_\infty \cdot V_\infty^3 \cdot cp_m} &= 0 \end{aligned}$$

which is solved using the method of Cardan. Then the air intake area can be assumed. According to Becker [?], to obtain the minimum drag possible, the following relation should be respected:

$$\frac{V_1}{V_\infty} = 0.4$$

which combined with the mass conservation condition applied between A_∞ and A_1 , assuming an incompressible flow, leads to:

$$A_1 = \frac{A_\infty}{0.4}$$

The downstream part of the motor is then studied. It is done taking inspiration from the method proposed by George W. Stickle [?]. The variables required for the study

are shown in Figure D.5.

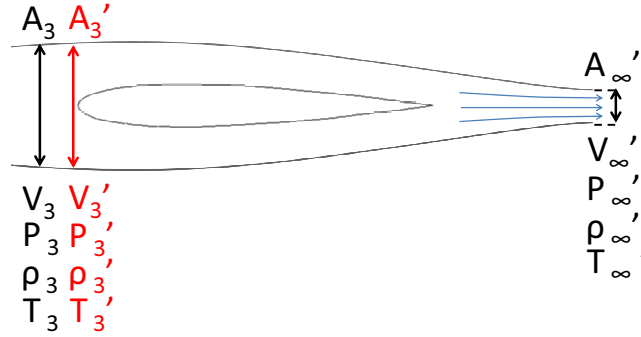


Figure D.5: Nacelle exhaust zoom

where A is the area of the flow tube section (in m), V is the air velocity (in $m.s^{-1}$), ρ is the air density (in $kg.m^{-3}$) and T is the temperature (in K) at each studied locations denoted by the subscripts ∞' for the downstream air, 3 for the engine end and 3' which correspond to the end of the engine baffles as defined by Stickle [?]. This is done to take into account the pressure drop that happens at the rear of the engine depending on the baffle device design. The exhaust of the nacelle typically acts as an air pump that blows the air within the motor and cools it, ensuring that no under pressure is encountered at the exhaust location A_∞' at any phase of the flight. The study starts with an evaluation of the pressure at A_3 . In the same manner than before, applying the Bernoulli's Theorem between A_∞ and A_2 :

$$P_3 - P_\infty = \frac{1}{2} \cdot \rho \cdot (V_\infty^2 - V_2^2) \quad (D.4)$$

where V_2 is evaluated applying the conservation of mass:

$$V_2 = V_\infty \frac{A_\infty}{A_2} \quad (D.5)$$

The pressure drop due to the baffles is evaluated as follows. Stickle [?] makes an analogy between the pressure and voltage of an electric circuit. The nacelle is represented by

resistances mounted in series, each resistance representing a part of the nacelle. The pressure drop in the entire downstream part of the nacelle follows the relation:

$$\frac{\Delta P}{q} = \left(\frac{Q}{F \cdot V} \right)^2 \left(\frac{1}{K^2} + \frac{1}{K_2^2} \right)$$

where ΔP is the overall downstream nacelle part pressure drop (in Pa), q is the dynamic pressure of the airstream (in Pa), Q is the quantity of the air flowing through the cowling (in $m^3 \cdot s^{-1}$), f is the engine cooled frontal area (in m^2), V is the velocity of the air stream (in $m \cdot s^{-1}$), K is the "conductivity" between A_3 and A'_3 , K_2 is the "conductivity" between A'_3 and A_∞

Applied between A_3 and A'_3 , it gives:

$$\Leftrightarrow P'_3 - P_3 = -\frac{1}{2} \rho \cdot V_\infty^2 \left(\frac{A_\infty}{A_2 \cdot K} \right)^2 \quad (D.6)$$

According to Stickle [?], the "conductivity" factor of poorly designed baffles engine is around 0.65. Because of the usual very poor design of electric motor baffles (mostly inexistent), a margin is taken, and the factor K is fixed at 0.5. Then the exhaust area A'_∞ evaluation is carried out. The condition is:

$$P_\infty = P'_\infty$$

Therefore, it leads to:

$$P'_\infty - P'_3 = P'_\infty - (P'_3 - P_3 + P_3) = -(P_3 - P'_\infty) - (P'_3 - P_3) = -(P_3 - P_\infty) - (P'_3 - P_3)$$

where $P_3 - P_\infty$ and $P'_3 - P_3$ are computed with equations (D.4) and (D.6). Applying the Bernoulli's Theorem and the mass conservation principle between A'_3 and A'_∞ (assuming that the air is incompressible), it leads to:

$$A'_\infty = \frac{V'_3 \cdot A'_3}{V'_\infty}$$

with:

$$V_{\infty}'^2 = V_3'^2 - \frac{2(P_{\infty}' - P_3')}{\rho_3'}$$

V_3' and ρ_3' must be evaluated to complete the calculation: Applying the relation of the perfect gas at A_2 A_3 , it gives:

$$\begin{aligned} P_2 &= P_3 = \rho_2 \cdot R \cdot T_2 = \rho_3 \cdot R \cdot T_3 \\ \Leftrightarrow \rho_3' &= \frac{\rho_{\infty} \cdot T_2}{T_3} \end{aligned}$$

where T_3 comes from equation (D.3) and T_2 comes from equation (D.2). The speed V_3' can then be evaluated using the mass conservation principle:

$$\begin{aligned} \rho_3' \cdot V_3' \cdot A_3' &= \rho_2 \cdot V_2 \cdot A_2 \\ \Leftrightarrow V_3' &= \frac{\rho_{\infty} \cdot V_2 \cdot A_2}{\rho_3' \cdot A_3'} \end{aligned}$$

where V_2 comes from equation (D.5): Therefore, the exhaust area A_{∞}' can be fixed and the conditions at its location can be estimated for every flight conditions using the above equations. Then the cooling drag $D_{cooling}$ can be estimated:

$$\begin{aligned} D_{cooling} &= \dot{m} (V_{\infty}' - V_1) + P_{\infty}' \cdot A_{\infty}' - P_1 \cdot A_1 \\ \Leftrightarrow D_{cooling} &= \rho_{\infty} \cdot A_1 \cdot V_1 (V_{\infty}' - V_1) + P_{\infty}' \cdot A_{\infty}' - P_1 \cdot A_1 \end{aligned}$$

where P_1 is computed thanks to the Bernoulli's Theorem:

$$P_1 = \frac{1}{2} \rho_{\infty} \cdot (V_{\infty}'^2 - V_1^2) + P_{\infty}$$

External aerodynamic As exposed in section 4.2.4, page 119, the nacelle design is based on the aerofoil NACA 65. The thickness of the aerofoil is defined to fit the motor engines. This aerofoil is cut off along the chord, and a distance equal to the diameter of the exhaust area separates the two resulting parts. Then the nose section is defined following the NACA E-type shape as presented by Becker [?]. The resulting aerodynamic shape is shown in Figure D.6

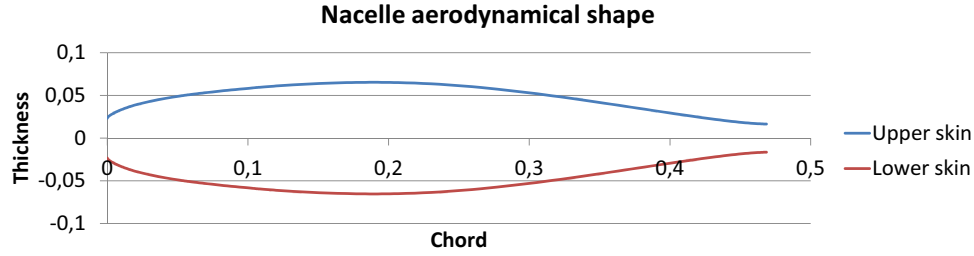


Figure D.6: Nacelle shape

The method developed for the fuselage in section D.3.2, page 219 guides the nacelle friction and form drags estimation. However, the laminar flow is disturbed by the wake of the propellers. Therefore, a first computation is done assuming that the laminar flow spreads up to 50% of the nacelle chord (where the minimum pressure area takes place as indicated by the second digit of the aerofoil denomination). Then a second one is done assuming that the airflow is no longer laminar passing the propellers location. Finally, the two previous values average gives the nacelle frictional drag. The total external drag of the nacelles encountered is denoted: $D/q_{nacelleouterdrag}$ (in m^2)

The total drag of the nacelle can eventually be estimated as:

$$D/q_{nacelle} = \frac{D_{cooling}}{q} + D/q_{nacelleouterdrag}$$

where q is the dynamic pressure of the airstream (in Pa).

D.3.4 SENSOR TURRET

As discussed in section 4.1.2, page 108, the sensor turret is treated as a ball of $0.4m$ in diameter. The evaluation of the drag it generates is done using the method proposed by Raymer ([?]; ch. 12.5). The drag of the spherical ball $D/q_{Sensorturret}$ (in m^2) is assumed to be:

$$D/q_{Sensorturret} = A_{optro} \cdot Cd_{optro}$$

where A_{optro} is the frontal area of the sensor turret and Cd_{optro} is the classical drag coefficient of spherical ball (0.47).

D.3.5 LANDING GEAR

The drag of the landing wear is estimated following the method proposed by Raymer ([?]; ch. 12.5). For the expected weight of the present aircraft, 3.00 – 4” tyres would be suitable. That is to say, a diameter of: $D_{tyre} = 0.25m$ and a width of $T_{tyre} = 0.09m$. Raymer gives the drag coefficient of a regular wheel and tire depending on the frontal area ([?]; Table 12.5) $D/q/A_{frontalarea_{wheel}} = 0.25$. Then the Drag to dynamic pressure ratio of the wheels is D/q_{wheels} :

$$D/q_{wheels} = N_{wheel} \cdot D/q/A_{frontalarea_{wheel}} \cdot D_{tyre} \cdot T_{tyre}$$

where N_{wheel} is the number of wheels (two in the present case since the front wheel is accommodated in the fuselage). The support of the main landing gear is likely to be merged into the vertical tails, therefore:

$$D/q_{strut} = 0$$

Eventually, the total drag of the landing gear is:

$$D/q_{Landinggear} = +D/q_{wheels}$$

D.3.6 ENGINE INSTALLATION DRAG

The drag generated by the thermal engine’s installation is estimated using the method developed by Torenbeek [?]. This drag is composed of two components:

- The drag generated by the air flow bypass to cool the engine down is called cooling drag. This drag is estimated thanks to the following equation ([?]; eq. 13.18):

$$(D/q)_{cooling} = 4.9 \cdot 10^{-7} \frac{bhp \cdot T^2}{\sigma \cdot V}$$

where $(D/q)_{cooling}$ is the equivalent flat plate area of the cooling drag(in ft^2), bhp is the engine power (in hp) T is the air temperature (in R), σ is the relative air density

$(\frac{\rho}{\rho_0})$ and V is the aircraft velocity (in $m.s^{-1}$).

- The engine installation generates additional drag as the drag of the oil cooler, the air intake, the exhaust pipes. Those drags are gathered in the miscellaneous drag that can be estimated thanks to the following equation ([?]; eq. 13.19):

$$(D/q)_{misc} = 2 \cdot 10^{-4} \cdot bhp$$

where $(D/q)_{misc}$ is the equivalent flat plate area of the miscellaneous (in ft^2) and bhp is the engine power (in hp). However, according to Raymer ([?]; ch. 13.6), this drag is usually 2 to 3 times greater than computed one on small aircraft. In the present case it is estimated that:

$$(D/q)_{misc\ effective} = 2 \cdot (D/q)_{misc\ computed}$$

D.4 STABILITY

D.4.1 LONGITUDINAL STABILITY

The longitudinal stability is now studied in order to fix the centre of gravity position. The study is based on the analysis proposed by Raymer [?]. The condition of the equilibrium is:

$$M_{total} = 0$$

The condition of the stability is:

$$\frac{dM_{total}}{d\alpha} \leq 0$$

The different external forces and moments applied to the aircraft are shown in Figure [D.7](#).

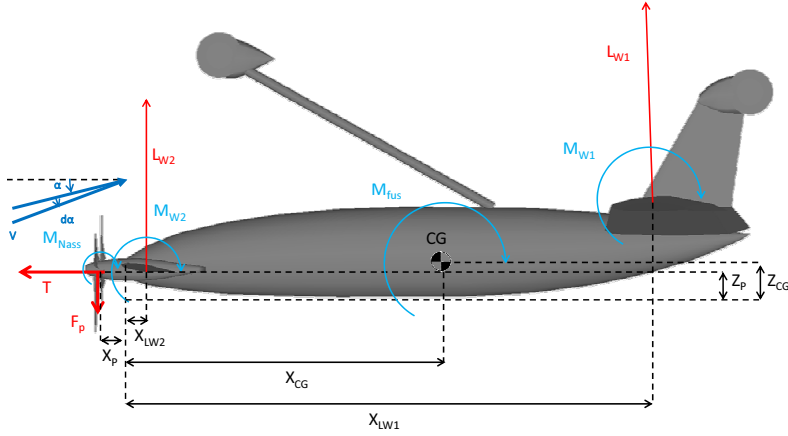


Figure D.7: Stability dynamic

The longitudinal moment M_{total} can be expressed as:

$$M_{total} = - (X_{LW1} - X_{CG}) L_{W1} + (X_{CG} - X_{LW2}) L_{W2} + M_{W1} + M_{W2} + M_{fus} + M_{Nass} - (Z_P - Z_{CG}) T + (X_{CG} - X_P) F_p \quad (D.7)$$

which gives in coefficient terms:

$$M_{total} = \frac{1}{2} \rho \cdot V^2 \left[- (X_{LW1} - X_{CG}) S_{W1} \cdot Cl_{W1} + (X_{CG} - X_{LW2}) S_{W2} \cdot Cl_{W2} + S_{W1} \cdot c_{W1} \cdot Cm_{W1} + S_{W2} \cdot c_{W2} \cdot Cm_{W2} + \frac{M_{fus}}{\frac{1}{2} \rho \cdot V^2} + \frac{M_{Nass}}{\frac{1}{2} \rho \cdot V^2} - (Z_P - Z_{CG}) \frac{T}{\frac{1}{2} \rho \cdot V^2} + (X_{CG} - X_P) \frac{F_p}{\frac{1}{2} \rho \cdot V^2} \right]$$

For the stability analysis, this expression is first derived in function of the aircraft angle of attack α :

$$\frac{dM_{total}}{d\alpha} = \frac{1}{2} \rho \cdot V^2 \left[- (X_{LW1} - X_{CG}) S_{W1} \cdot \frac{dCl_{W1}}{d\alpha_1} \cdot \frac{d\alpha_1}{d\alpha} + (X_{CG} - X_{LW2}) S_{W2} \cdot \frac{dCl_{W2}}{d\alpha_2} \cdot \frac{d\alpha_2}{d\alpha} + \frac{1}{q} \frac{dM_{fus}}{d\alpha} + \frac{1}{q} \frac{dM_{Nass}}{d\alpha} + (X_{CG} - X_P) \frac{1}{q} \frac{dF_p}{d\alpha_p} \frac{d\alpha_p}{d\alpha} \right]$$

where α_1 , α_2 and α_p are the angles of attack encountered respectively by the main wing, the fore plane and the propellers (in rad).

The components $\frac{d\alpha_1}{d\alpha}$ and $\frac{d\alpha_2}{d\alpha}$ represent respectively the effect on the fore plane on the main wing and the effect of this latter on the first one as shown in Figure D.8.

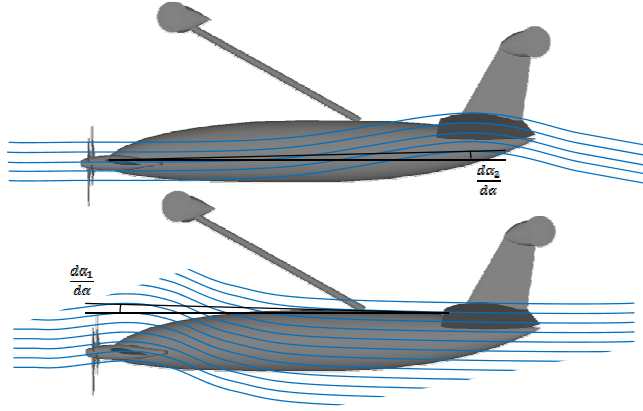


Figure D.8: Angle of attack deflection

These components are expressed as:

$$\alpha_i = \alpha - \varepsilon_j$$

whose derivate gives:

$$\frac{d\alpha_i}{d\alpha} = 1 - \frac{d\varepsilon_j}{d\alpha}$$

where ε_j is the downwash generated by the element i at j location. Finally, rewriting $\frac{dM_{total}}{d\alpha}$ by Cm_α , and noting that:

$$\frac{dCl_{Wi}}{d\alpha_i} = a_{Wi}$$

where a_{W1} and a_{W2} are the lift curve slope of the element i (i.e. the main wing or the fore plane). The expression becomes:

$$\begin{aligned} Cm_\alpha \cdot S_{W1} \cdot c_{W1} = & -(X_{LW1} - X_{CG}) S_{W1} \cdot a_{W1} \left(1 - \frac{d\varepsilon_2}{d\alpha}\right) + (X_{CG} - X_{LW2}) S_{W2} \cdot a_{W2} \left(1 + \frac{d\varepsilon_1}{d\alpha}\right) \\ & + \frac{1}{q} \frac{dM_{fus}}{d\alpha} + \frac{1}{q} \frac{dM_{Nass}}{d\alpha} + (X_{CG} - X_P) \frac{1}{q} \frac{dF_p}{d\alpha_p} \left(1 + \frac{d\varepsilon_p}{d\alpha}\right) \end{aligned} \quad (D.8)$$

According to Raymer ([?]; fig. 16.4), this derivative is included in the range $-0.2 \text{ rad}^{-1} \leq Cm_\alpha \leq -0.05 \text{ rad}^{-1}$ for middle-aged fighter-stable aircraft (i.e. the static margin). The

present aircraft being a drone, its embedded control enables to override this limitation (i.e. fly-by-wire). However, to avoid carrying a Emergency Power Unit ("EPU") to counteract a potential failure, this restriction is kept [?].

The centre of gravity position is thus determined. The different components of the expression can be estimated as follows:

- a_{W1} and a_{W2} : the lift curve slope of the lifting surfaces can be estimated from the 2D aerofoil lift curve slope coupled with the semi-empirical expression proposed by Courtland D. Perkins and Robert E. Hage ([?]; eq. (5-20)).

$$a_W = \frac{a_0}{1 + \frac{57.3 \cdot r \cdot a_0}{\pi \cdot A}}$$

where a_W is the 3D wing curve slope, a_0 is the lift curve slope of its 2D aerofoil (in deg^{-1}), r is the winglet/end plate correction factor (here $r = 1$) and A is its wing aspect ratio, which gives is gradient applied to the present case:

- $\frac{d\varepsilon_2}{d\alpha}$: the derivative by the aircraft angle of attack, of the downwash generated by the fore plane at the main wing location is estimated following the method proposed by Perkins and Hage ([?], ch. 5-3). The method takes into account the aspect ratio and the taper ratio of the fore plane and two geometric dimensioning characteristics, M and R , as shown in Figure D.9.

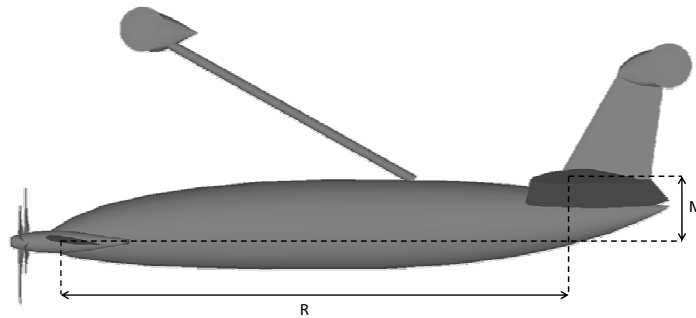


Figure D.9: Inter-wing distance

$$m = \frac{M}{\frac{1}{2}b_{foreplane}} ; r = \frac{R}{\frac{1}{2}b_{foreplane}}$$

The data provided for a wing of a taper ratio of 1 and an aspect ratio of 12 is selected as shown in Figure D.10.

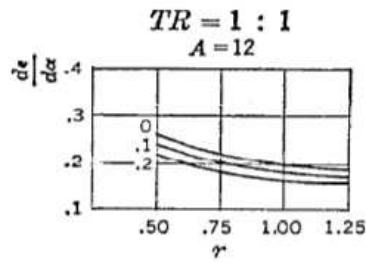


Figure D.10: Downwash charts ([?], Figure 5-10)

As is the case of section 2.2.4.2, page 2.2.4.2, the main wing is not affected by the fore plane downwash all over its span. But the fore plane tip vortexes generate an up wash outboard of it that affects the outer parts of the wing and produce a stabilising effect, as shown D.11.

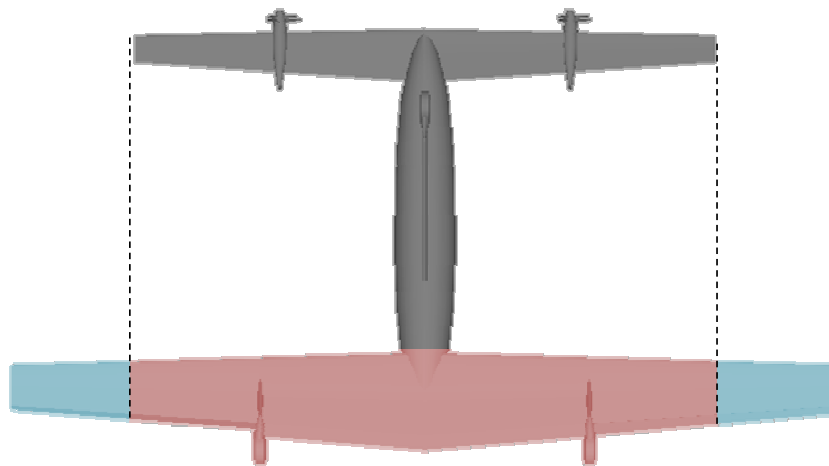


Figure D.11: Main wing airflow

To be conservative, and because this up wash intensity is fairly difficult to evaluate, it is decided to neglect it. Nevertheless, to get the closest CG location estimation, only the inner parts of the wing, which are at a distance of the plane of symmetry, lower than the fore plane span, is assumed to endure the fore plane downwash. The rest of the wing is considered to face the free stream angle of attack.

- $\frac{d\varepsilon_1}{d\alpha}$: the derivative by the aircraft angle of attack, of the downwash generated by the main wing on the fore plane, is estimated following the method proposed by Daniel P. Raymer ([?]; ch. 16.3). The method takes into account the aspect ratio of the main wing and the following geometric dimensioning characteristic.

$$r = \frac{\text{horizontal distance between the aerodynamic centers of tow lifting devices}}{C_{\text{root main wing}}}$$

where $C_{\text{root main wing}}$ is the root chord of the main wing (in m). The downwash evolution is shown in Figure D.12.

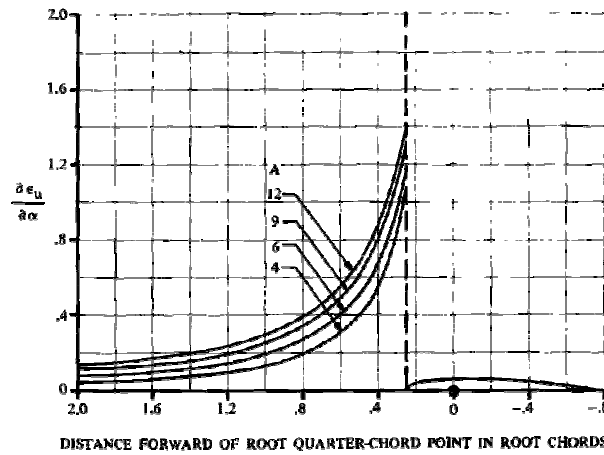


Figure D.12: Upwash charts ([?], Fig. 16.11)

- $\frac{d\varepsilon_p}{d\alpha}$: The derivative by the aircraft angle of attack, of the downwash generated by the fore plane over the propellers is estimated following the same method.
- $\frac{dM_{fus}}{d\alpha}$: The derivative by the aircraft angle of attack, of the moment of the fuselage is estimated following the method proposed by Courtland D. Perkins and Robert E. Hage ([?], ch. 5-4). The part aft of the wing is likely to be stabilising while the front part is known as destabilising compared to the fuselage alone. The method consist in dividing the fuselage in n section normal to the aircraft axis. The derivative is estimated by summing each contribution of the n section of the fuselage ([?], eq. 5-28):

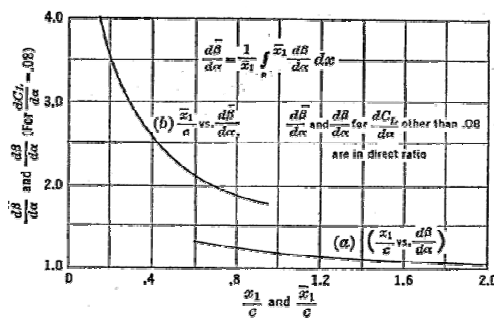
$$\frac{dM}{d\alpha} = \frac{q}{36.5} \sum_1^n w_f^2 \frac{d\beta}{d\alpha} \Delta x$$

where $\frac{dM}{d\alpha}$ is the fuselage moment to angle of attack derivative (in $N.m.deg^{-1}$), q is the dynamic pressure (in Pa), w_f is the width of the fuselage at the position X (in m), Δx is the length of the portion (in m) and $\frac{d\beta}{d\alpha}$ is the effect of the wing on the fuselage. Because of the particular tandem wing of the present aircraft, this latter parameter is computed for each lifting surfaces. Their results are added, subtracting the result calculated for the fuselage taken alone not to double count it (not counting the sections of the fuselage at the lifting surfaces locations, where the results are already forced to zero). This latter contribution can be estimated using the method proposed by Perkins and Hage ([?]; equation (5-27)):

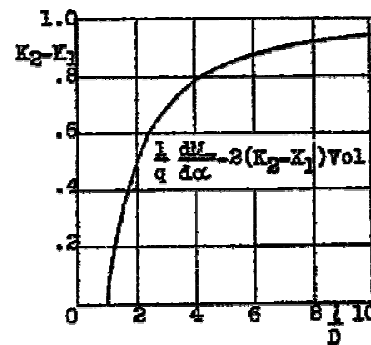
$$\frac{dM}{d\alpha} \approx \frac{q(K_2 - K_1)}{36.5} \sum_0^n w_f^2 \cdot \Delta x$$

where $(K_2 - K_1)$ is an axially asymmetric factor, and w_f is the width of the fuselage at the position X (set to zero for the sections at the lifting surfaces locations; in m).

The experimental values of the parameter $\frac{d\beta}{d\alpha}$, in front of the wing, and the experimental values of the parameter $(K_2 - K_1)$, for the fuselage alone, are plotted in Figure D.13



(a) Fuselage wing effect ([?]; Figure 8.)



(b) $(K_2 - K_1)$ parameter ([?]; Figure 2.)

Figure D.13: Fuselage wing effect and munk-correction

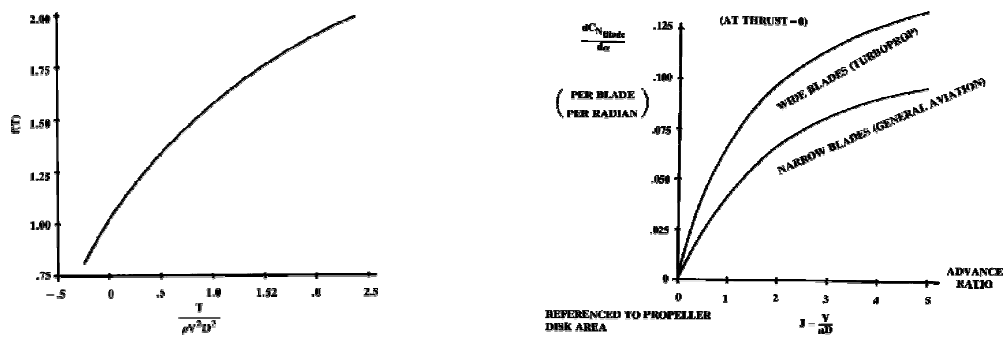
- $\frac{dM_{Nass}}{d\alpha}$: the derivative of the moment of the nacelles with respect to the aircraft angle of attack is estimated in the same way as the main wing contribution of the one of the fuselage.
- $\frac{dF_p}{d\alpha_p}$: the derivative of the lateral propeller force with respect to the aircraft angle of

attack is estimated following the method proposed by Daniel P. Raymer ([?]; ch. 16.3). The method takes into account the disk area A_p (in m^2), the number of blade of the propeller N_B and operation parameters:

$$\frac{dF_p}{d\alpha_p} = q \cdot N_B \cdot A_p \frac{dC_{N \text{ blade}}}{d\alpha} f(T)$$

The propellers are assumed to be composed of two three blade propeller, that is to say $N_B = 2 \cdot 3 = 6$ for efficiency reasons [?] [?] [?].

$\frac{dC_{N \text{ blade}}}{d\alpha}$ is the normal force generated by a single blade at zero thrust and $f(T)$ is adjust for non-zero thrust. Experimental values of both parameters are plotted in Figure D.14.



(a) $f(T)$ parameter ([?]; Figure 16.16)

(b) $\frac{dC_{N \text{ blade}}}{d\alpha}$ parameter ([?]; Figure 16.15)

Figure D.14: Propeller operation parameters

Without more information over the propeller design, it is estimated that it operates at a classical advance ratio of $J = 1.4$.

D.4.2 LATERAL-DIRECTIONAL EQUILIBRIUM AND STABILITY

The directional stability is carried out to size the fins and rudders areas. The lateral stability is the starting point of the dihedral angle computation and the ailerons area sizing. However, only the fins area affect the overall aircraft sizing, influencing both its weight and drag. The main wing dihedral angle and the control surfaces effects are indeed neglected both in the weight estimation semi empirical formulas (cf. section D.2, page 211) and drag coefficients (cf. section 4.2.2.2, page 117). Thus, if they have been thoroughly studied during the

design process to ensure the geometric consistency of the aircraft, their computation won't be detailed in the following of the report in the interests of readability. Nonetheless, the forces equilibria are detailed.

The study is based on the analysis proposed by Raymer [?]. As for the longitudinal equilibrium in section [D.4.1](#), page [231](#), the conditions of the lateral directional equilibria are:

$$N_{total} = 0 ; O_{total} = 0$$

where N_{total} and O_{total} are respectively the yaw and the roll moment (in $N.m$).

The condition of the Lateral stability can be summarized as follows: when the aircraft encounter a small yaw angle perturbation $\partial\beta$, the aerodynamic of the aircraft must produce a moment in the opposed direction dN_{total} to push the aircraft back in its first position. Taking into account the sign convention, the following relation must be verified:

$$\frac{dN_{total}}{d\beta} \geq 0$$

The condition of the directional stability consists in that when the aircraft encounter a small yaw angle perturbation $\partial\beta$, the aerodynamic of the aircraft must produce a moment dO_{total} to tilt the aircraft and therefore initiate a turn that will push it back in its first position. Taking into account the sign convention, the following relation must be verified:

$$\frac{dO_{total}}{d\beta} \leq 0$$

The different external forces and moments applied to the aircraft are shown in Figures [D.15](#) and [D.16](#).

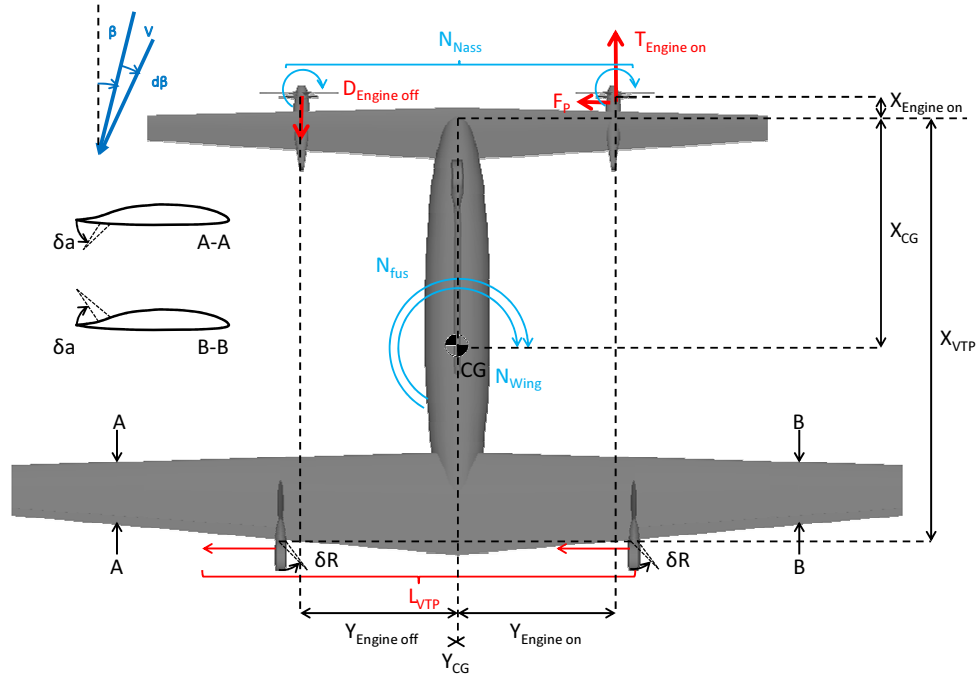


Figure D.15: Stability dynamic (top)

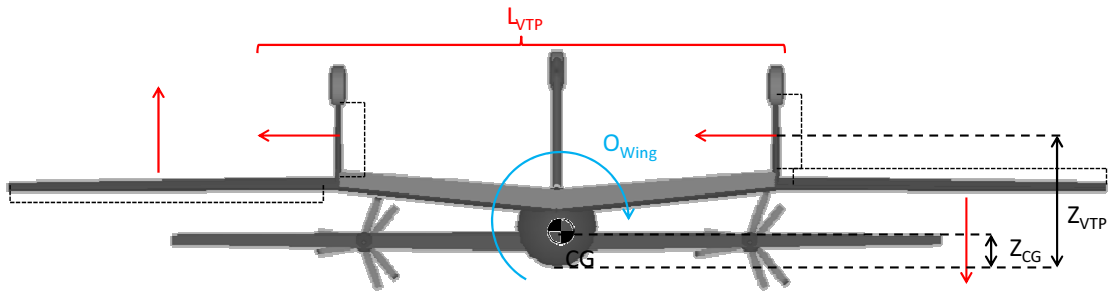


Figure D.16: Stability dynamic (back)

Then the moment around the axis Z can be expressed as:

$$\begin{aligned}
 N_{total} = & N_{Wing} + N_{W\delta a} \cdot \delta a + N_{fus} + N_{NASS} + (X_{VTP} - X_{CG}) L_{VTP} - (Y_{Engine\ on} - Y_{CG}) T_{Engine\ on} \\
 & + (Y_{Engine\ off} - Y_{CG}) D_{Engine\ off} - (X_{CG} - X_{Engine\ on}) F_p
 \end{aligned}
 \tag{D.9}$$

And the moment around the axis X is defined as:

$$O_{total} = O_{Wing} + O_{W\delta a} \cdot \delta a - (Z_{VTP} - Z_{CG}) L_{VTP} \quad (D.10)$$

which gives in coefficient:

$$N_{total} = \frac{1}{2} \rho \cdot V^2 \left[\begin{aligned} & S_{Wing} \cdot b_{Wing} \cdot C_{n_{Wing}} + S_{Wing} \cdot b_{Wing} \cdot C_{n_{W\delta a}} \cdot \delta a + \frac{N_{fus}}{\frac{1}{2} \rho \cdot V^2} + \frac{N_{NASS}}{\frac{1}{2} \rho \cdot V^2} \\ & + (X_{VTP} - X_{CG}) S_{VTP} \cdot Cl_{VTP} - (Y_{Engine\ on} - Y_{CG}) \frac{T_{Engine\ on}}{\frac{1}{2} \rho \cdot V^2} \\ & + (Y_{Engine\ off} - Y_{CG}) \frac{D_{Engine\ off}}{\frac{1}{2} \rho \cdot V^2} - (X_{CG} - X_{Engine\ on}) \frac{F_p}{\frac{1}{2} \rho \cdot V^2} \end{aligned} \right] \quad (D.11)$$

$$O_{total} = \frac{1}{2} \rho \cdot V^2 [S_{Wing} \cdot b_{Wing} \cdot C_{o_{Wing}} + S_{Wing} \cdot b_{Wing} \cdot C_{o_{W\delta a}} \cdot \delta a - (Z_{VTP} - Z_{CG}) S_{VTP} \cdot Cl_{VTP}] \quad (D.12)$$

For the stability analysis, these expressions are first derived in function of the aircraft lateral angle of attack β (in *rad*):

$$\frac{dN_{total}}{d\beta} = \frac{1}{2} \rho \cdot V^2 \left[\begin{aligned} & S_{Wing} \cdot b_{Wing} \cdot \frac{dC_{n_{Wing}}}{d\beta} + \frac{1}{q} \frac{dN_{fus}}{d\beta} + \frac{1}{q} \frac{dN_{NASS}}{d\beta} + (X_{VTP} - X_{CG}) S_{VTP} \cdot \frac{dCl_{VTP}}{d\beta_v} \frac{d\beta_v}{d\beta} \eta_v \\ & - (X_{CG} - X_{Engine\ on}) \frac{1}{q} \frac{dF_p}{d\beta_p} \frac{d\beta_p}{d\beta} \end{aligned} \right]$$

$$\frac{dO_{total}}{d\beta} = \frac{1}{2} \rho \cdot V^2 \left[S_{Wing} \cdot b_{Wing} \cdot \frac{dC_{o_{Wing}}}{d\beta} - (Z_{VTP} - Z_{CG}) S_{VTP} \cdot \frac{dCl_{VTP}}{d\beta_v} \frac{d\beta_v}{d\beta} \eta_v \right]$$

where β_v is the angle of attack of the vertical tail plane (in *rad*) and η_v is the ratio between the dynamic pressure at the tail and the free stream one. Defining the vertical tail plane lift curve slope $a_{VTP} = \frac{dCl_{VTP}}{d\beta_v}$, The expressions become:

$$C_{n_\beta} \cdot S_{W_1} \cdot b_{W_1} = S_{Wing} \cdot b_{Wing} \cdot \frac{dC_{n_{Wing}}}{d\beta} + \frac{1}{q} \frac{dN_{fus}}{d\beta} + \frac{1}{q} \frac{dN_{NASS}}{d\beta} + (X_{VTP} - X_{CG}) S_{VTP} \cdot a_{VTP} \frac{d\beta_v}{d\beta} \eta_v - (X_{CG} - X_{Engine\ on}) \frac{1}{q} \frac{dF_p}{d\beta_p} \frac{d\beta_p}{d\beta} \quad (D.13)$$

$$C_{o_\beta} \cdot S_{W_1} \cdot b_{W_1} = S_{Wing} \cdot b_{Wing} \cdot \frac{dC_{o_{Wing}}}{d\beta} - (Z_{VTP} - Z_{CG}) S_{VTP} \cdot a_{VTP} \frac{d\beta_v}{d\beta} \eta_v \quad (D.14)$$

where C_{n_β} and C_{o_β} are respectively the directional y lateral moment coefficients and S_{W_1} and b_{W_1} are respectively the area and the span of the main wing.

According to Raymer ([?], ch. 16.4), these derivatives depend on the maximum Mach number of the aircraft as shown in Figure D.17 for the directional moment derivative.

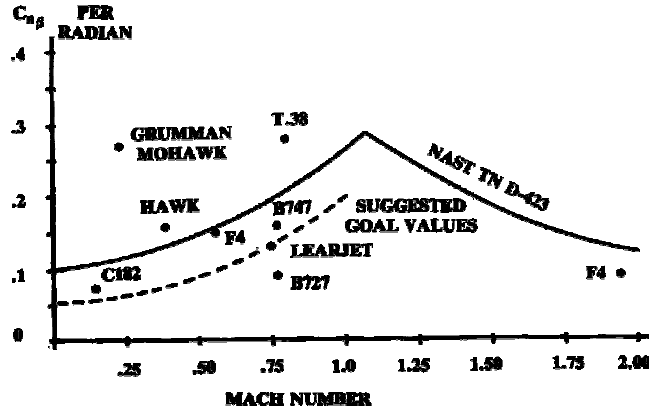


Figure D.17: Yaw moment derivative ([?], fig. 16.20)

The yaw moment derivative of the present aircraft is fixed to match the “Suggested Goal Values” curve. According to Raymer ([?], ch. 16.4), the lateral moment derivative is inversely equal to the directional moment derivative. Therefore the roll moment derivative is defined as:

$$C_{o\beta} = -C_{n\beta}$$

Knowing $C_{n\beta}$, the required surface of vertical tail plane S_{VTP} is extracted from equation (D.13). Reminding that the aircraft is of twin tail configuration and the fins span is defined by the main landing gear length (cf. section 4.2.1, page 113), the fin mean aerodynamic chord is easily found.

The different components of the expression are estimated as:

- $S_{Wing} \cdot b_{Wing} \cdot \frac{dC_{n_{Wing}}}{d\beta}$ ([?], Eq. 16.41):

$$S_{Wing} \cdot b_{Wing} \cdot \frac{dC_{n_{Wing}}}{d\beta} = S_{W1} \cdot b_{W1} \cdot \frac{dC_{n_{W1}}}{d\beta} + S_{W2} \cdot b_{W2} \cdot \frac{dC_{n_{W2}}}{d\beta}$$

where, $i = 1$ for the main wing and $i = 2$ for the fore plane, S_{W_i} is the lifting surface (in m^2), b_{W_i} is the span (in m) and $\frac{dC_{n_{W_i}}}{d\beta}$ is defined as:

$$\frac{dC_{n_i}}{d\beta} = Cl_i^2 \left[\frac{1}{4 \cdot \pi \cdot A_i} - \left(\frac{\tan \Lambda_i}{\pi \cdot A_i (A_i + 4 \cdot \cos \Lambda_i)} \right) \left(\cos \Lambda_i - \frac{A_i}{2} - \frac{A_i^2}{8 \cdot \cos \Lambda_i} + \frac{6(\bar{X}_{LW_i} - \bar{X}_{CG}) \sin \Lambda_i}{A_i} \right) \right]$$

where Cl_i is the lifting surface lift coefficient, Λ_i is the lifting surface sweep at 25% of the MAC (in *rad*), A_i is the lifting surface aspect ratio, \bar{X}_{LW_i} is the lifting surface longitudinal lift position made dimensionless by the wing span and \bar{X}_{CG} is the longitudinal position of the CG made dimensionless by the wing span.

- $\frac{1}{q} \frac{dN_{fus}}{d\beta}$ ([?], Eq. 16.47):

$$\begin{aligned} \frac{1}{q} \frac{dN_{fus}}{d\beta} &= \frac{1}{q} \frac{d(q \cdot S_W \cdot b \cdot Cn_{fus})}{d\beta} = S_W \cdot b \cdot Cn_{\beta fus} \\ &= -S_W \cdot b \cdot 1.3 \frac{V_{fus}}{S_W \cdot b} \left(\frac{D_{fus}}{W_{fus}} \right) = -1.3 \cdot V_{fus} \left(\frac{D_{fus}}{W_{fus}} \right) \end{aligned}$$

where V_{fus} is the fuselage internal volume (in m^3), D_{fus} and W_{fus} are respectively the fuselage depth and width (in m).

- $\frac{1}{q} \frac{dN_{NASS}}{d\beta}$: This parameter is computed in the same manner as the fuselage.

- $\frac{1}{q} \frac{dF_p}{d\beta_p}$:

$$\frac{dF_p}{d\beta_p} = \frac{dF_p}{d\alpha_p}$$

where $\frac{dF_p}{d\alpha_p}$ is the derivative of the lateral propeller force with respect to the aircraft angle of attack computed in section D.4.1, page 237.

- $\frac{d\beta_p}{d\beta}$: Because of the very forward position of the propellers, combine with their distance from the closest vertical lifting surface, it is assumed that the angle encountered by the propeller is the same as the one suffered by the entire aircraft. Therefore:

$$\frac{d\beta_p}{d\beta} = 1$$

The lift curve slope of the fore plane is estimated in the same manner as shown in section D.4.1, page 234 ([?]; eq. (5-20)), with the winglet/end plate correction factor fixed to $r = 1$ and the effective vertical tail plane aspect ratio set as $A = 1.55 \cdot A_{VTP}$ (A_{VTP} is the geometric vertical tail plane aspect ratio), to take into account that the main wing acts here as a endplate ([?], ch: 16.4).

- $\frac{d\beta_v}{d\beta}\eta_v$ ([?], eq: 16.48):

$$\frac{d\beta_v}{d\beta}\eta_v = 0.724 + \frac{3.06 \frac{S_{vs}}{S_{W1}}}{1 + \cos \Lambda} - 0.4 \cdot \frac{Z_{wf}}{D_{fus}} + 0.009 \cdot A_{W1}$$

where Λ is the lifting surface sweep at 25% of the MAC (in *rad*), A_{W1} is the main wing aspect ratio, S_{W1} is the main wing area (in m^2), D_{fus} is the fuselage diameter (in m), Z_{wf} is the vertical height of the wing above the fuselage centreline (in m) and S_{vs} is the area of vertical tail (in m^2)

D.5 PERFORMANCES

D.5.1 HOVER

Has discussed in section 4.1.4, page 111, the aircraft must be able to hover in OGE condition at an altitude of 2500m. A complete design of the rotor shape during the optimisation process would require well to much processing power. The required power in these conditions is therefore assessed thanks to the theory exposed by W. Z. Stepniewski ([?]; ch. III 2.8). The power required by the rotor P_{rotor} (in W) is of the forme ([?]; eq. 3.55a):

$$P_{rotor} = P_{id} \cdot k_{ind} + P_{pr}$$

where P_{id} is the theoretical induced power (in W) and k_{ind} is a efficiency factor defined as $k_{ind} = \frac{P_{ind}}{P_{id}}$ and P_{pr} is the profile power contribution (in W).

The rotor efficiency, also called rotor figure of merit FM , is defined as ([?]; eq. 3.56):

$$FM = \frac{P_{id}}{P_{rotor}} = \frac{P_{id}}{P_{id} \cdot k_{ind} + P_{pr}} = \frac{1}{k_{ind} + \frac{P_{pr}}{P_{id}}}$$

The contribution of the aerofoil characteristics is given by equation ([?]; eq. 6.92):

$$FM = \frac{1}{k_{ind} + \frac{2.6}{\sqrt{\sigma} \left(\frac{\bar{C}_l^{3/2}}{\bar{C}_d} \right)}}$$

where \bar{C}_l is the average rotor lift coefficient, \bar{C}_d is the average drag coefficient, and σ is the

rotor blade solidity calculated as:

$$\sigma = \frac{Area_{blades}}{Area_{rotor\ disk}} = \frac{N \cdot c \cdot R}{\pi \cdot R^2}$$

where N is the number of blade, c is the mean aerodynamic chord (in m) and R is the rotor radius (in m).

The values of $\frac{\bar{C}_l^{3/2}}{\bar{C}_d}$ for the NACA 0012 can be assumed to be 75 [?]; figure 6.55). The theoretical induced velocity can be now calculated based on the theory detailed in section A, page 147. Equation (A.1), page 149 gives the induced velocity (computed to generate of force: $T = MTOW \cdot g$), which is used in equation (A.2), page 149 to compute the required power P_{id} . The total electrical power required in hover P_{hover} can be eventually estimated:

$$\begin{aligned} P_{hover} &= \frac{P_{rotor}}{\eta_{electric\ motor} \cdot \eta_{propeller}} + P_{nacelle-drag} + P_{electrical} \\ &= \frac{P_{id}}{FM \cdot \eta_{electric\ motor} \cdot \eta_{propeller}} + P_{nacelle-drag} + P_{electrical} \end{aligned}$$

where $\eta_{electric\ motor}$ and $\eta_{propeller}$ are respectively the electrical motor and the propeller efficiencies, and $P_{electrical}$ is the electricity power required by the embarked systems and $P_{nacelle-drag}$ is the power due to the nacelle overall drag. This latter is estimated as:

$$P_{nacelle-drag} = N_{nacelle} \cdot V \cdot D_{nacelle} = N_{nacelle} \cdot V \cdot D/q_{nacelle} \cdot \frac{1}{2} \cdot N_{nacelle} \cdot \rho \cdot V^2 = \frac{1}{2} \cdot N_{nacelle} \cdot \rho \cdot V^3 \cdot D/q_{nacelle}$$

where $N_{nacelle}$ is the number of nacelles (here $N = 2$), V is the rotation speed (assumed equal to the max cruise speed as seen in section 4.8, page 120; in $m.s^{-1}$), $D_{nacelle}$ is the nacelle overall drag (in N), $D/q_{nacelle}$ the drag over dynamic pressure (in m^2) and ρ is air density (in $kg.m^{-3}$).

D.5.2 CLIMB PERFORMANCES

The total electrical power that have to produce the electrical generators in climb P_{climb} estimation is done following the same method as the hover one. P_{id} is here computed thanks to equation (A.6), page 150, where the downwash speed v is extracted from equation (A.5), page 150.

D.5.3 OGI ALTITUDE

The OGI altitude can be now computed knowing the power required to have in OGE conditions. The computation of the OGI altitude is done using the theory proposed by Cheeseman and Bennett ([?]; eq. 2):

$$\frac{T}{T_\infty} = \frac{1}{1 - \left(\frac{R}{4z}\right)^2} \quad (\text{D.15})$$

where T , T_∞ are respectively the lift produced by the rotor in OGI and OGE conditions for a same amount of power (in N), R is the rotor radius (in m) and z is the flight height (in m).

The flying height considered is a half of the aircraft length as seen in section 4.1.4, page111. Therefore, the rotor will be at the height of $z = \frac{3}{2}L_{Fuselage}$ of the ground. Equation (A.1), page 149 leads to:

$$T_\infty = 2 \cdot \rho \cdot A \cdot v^2$$

And equations (A.1) and (A.1), page 149 gives:

$$v = \sqrt[3]{\frac{P_{OGE}}{2 \cdot \rho \cdot A}}$$

Injecting those two latter equations in equation (D.15), it leads to:

$$\frac{M \cdot g}{2 \cdot \rho \cdot A \cdot \left(\frac{P_{OGE}}{2 \cdot \rho \cdot A}\right)^{2/3}} = \frac{1}{1 - \left(\frac{R}{4z}\right)^2}$$

In other words:

$$\rho = \frac{\left(M \cdot g \cdot \left(1 - \left(\frac{R}{4z}\right)^2\right)\right)^3}{2 \cdot A \cdot P_{OGE}^2}$$

The altitude is lastly derived from this result using the relations exposed in section D.1.1, page209:

D.5.4 STALL SPEED

As discussed in section A.4, page150, the stall speed must be evaluated since it fix the lower limit of the transition speed. This stall speed is computed at the altitude of the OGI

hovering ceiling which is likely to be the highest one where may happen the transition. The stall speed is directly related to the aerofoil angle of attack which is itself highly dependent on the Reynolds number. This latter is a function of the former airspeed. A recursive solver is therefore integrated into the optimisation tool to extract this speed. To alleviate the optimisation process, the longitudinal moment applied to the CG is simplified as shown in Figure D.18.

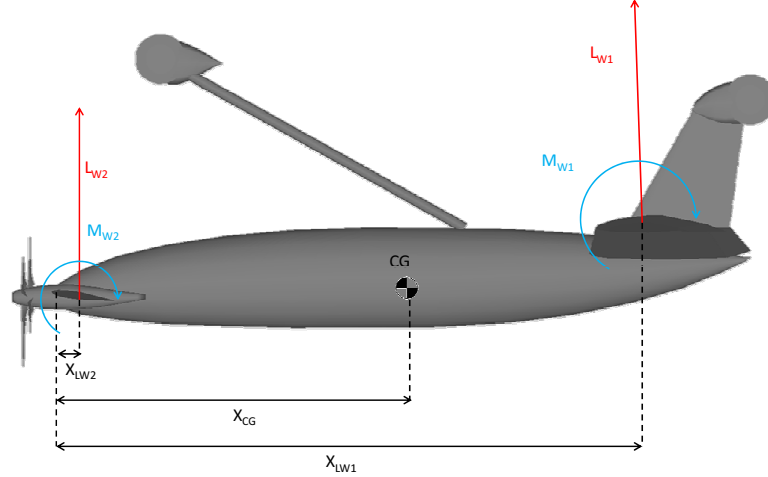


Figure D.18: Stall condition

$$M = -(X_{LW1} - X_{CG}) L_{W1} + (X_{CG} - X_{LW2}) L_{W2} + M_{W1} + M_{W2}$$

The equilibrium condition is achieved when $M = 0$. Therefore, in coefficients:

$$0 = \frac{1}{2} \rho V^2 [- (X_{LW1} - X_{CG}) S_{W1} \cdot Cl_{W1} + (X_{CG} - X_{LW2}) S_{W2} \cdot Cl_{W2} + S_{W1} \cdot c_{W1} \cdot Cm_{W1} + S_{W2} \cdot c_{W2} \cdot Cm_{W2}]$$

For security reasons, the fore plane is designed to stall first, therefore:

$$Cl_{W2} = Cl_{NACA0012_{\max}}$$

where $Cl_{NACA0012_{\max}}$ is the fore plane aerofoil max lift coefficient. Therefore, the main wing lift coefficient becomes:

$$Cl_{W1} = \frac{(X_{CG} - X_{LW2}) S_{W2} \cdot Cl_{W2} + S_{W1} \cdot c_{W1} \cdot Cm_{W1} + S_{W2} \cdot c_{W2} \cdot Cm_{W2}}{(X_{LW1} - X_{CG}) S_{W1}}$$

In steady flight, the lift compensates the aircraft weight:

$$M \cdot g = \frac{1}{2} \rho \cdot V_{stall}^2 [S_{W1} \cdot Cl_{W1} + S_{W2} \cdot Cl_{W2}]$$

Then the stall speed is estimated:

$$V_{stall} = \sqrt{\frac{2 \cdot M \cdot g}{\rho \cdot [S_{W1} \cdot Cl_{W1} + S_{W2} \cdot Cl_{W2}]}}$$

At the end of the process, the condition that the fore plane is the first to stall is checked verifying that Cl_{W1} is lower indeed than the maximum achievable one.

D.5.5 TRANSITION

As discussed in section [A.4](#), page 150, the aircraft must be able to do the transition in OGI hover ceiling conditions at an airspeed of 1.3 the stall speed.

The estimation of the power required during the transition is based on the model detailed in section [2.2.3](#), page 67. However, as explained in section [D.5.1](#), page 244, the precise rotor geometry remains unknown. Therefore the rotor power is once again estimated thanks to the theory of W. Z. Stepniewski.

According to the theory the only difference with power estimation exposed in section [D.5.1](#) is the induced P_{ind} power assessment ([?]; eq. 3.106):

$$P_{ind} = \frac{W \cdot w \cdot k_{ind}}{2 \cdot \rho \cdot V}$$

where W is the rotor lifting force w is the nominal disk loading (in $N.m^{-2}$) with $w = \frac{W}{A}$ where A is the rotor disk area (in m^2), k_{ind} is the efficiency factor (evaluated as in section [D.5.1](#), page 244).

The equilibrium equation exposed in section [2.2.3](#), page 67, is modified again to account the following drags:

- The cooling computed in section [D.3.6](#), page 230
- The sensor turret estimated in section [D.3.4](#), page 229

D.5.6 LOITER

During this phase, the goal is to decrease the fuel consumption of the aircraft and therefore its required power. The analysis is done modifying the method proposed by Raymer ([?], ch. 17.2) to adapt it to tandem wing configuration. The required power in loiter P (in W) can be expressed as:

$$P = D \cdot V = \frac{1}{2} \cdot \rho \cdot V^2 \cdot S_{ref} [Cd_{W1} + Cd_{W2} + Cd_{rest} + Cd_i] V$$

where D is the aircraft drag (in N), ρ is the air density (in $kg.m^{-3}$), V is the aircraft speed (in $m.s^{-1}$), S_{ref} is the reference area (in aeroplane mode, $S_{ref} = S_{W1} + S_{W2}$ where S_{W1} and S_{W2} are respectively the main wing and the fore plane area, in m^2)

The latter equation can be developed as:

$$P = \frac{1}{2} \cdot \rho \cdot V^3 \cdot S_{ref} \left[Cd_{0AH-93-131} \frac{S_{W1}}{S_{ref}} + Cd_{0NACA0012} \frac{S_{W2}}{S_{ref}} + \frac{D/q_{rest}}{S_{ref}} + K_{CDAH-93-131} \cdot \alpha_1^2 \frac{S_{W1}}{S_{ref}} \right. \\ \left. + K_{CDNACA0012} \cdot \alpha_2^2 \frac{S_{W2}}{S_{ref}} + \frac{Cl^2}{\pi \cdot A_{ref} \cdot e} \right]$$

where $Cd_{0AH-93-131}$ and $Cd_{0NACA0012}$ are the zero angle drag coefficient of the aerofoils, $\frac{D/q_{rest}}{S_{ref}}$ is the drag coefficient of the aircraft except the wings, $K_{CDAH-93-131}$ and $K_{CDNACA0012}$ are the components of the drag coefficients of the aerofoils that depend on the angle of attack, Cl is the reference lift coefficient, A_{ref} is the reference aspect ratio and e is the aircraft Oswald efficiency number.

The angle of attack of each lifting surface is fixed by the required lifting force:

$$\alpha_i = \frac{Cl_{Wi} - Cl_{0i}}{a_{Wi}}$$

where $Cl_{Wi} = \frac{L_{Wi}}{\frac{1}{2} \cdot \rho \cdot S_{Wi} \cdot V^2}$, S_{Wi} is the lifting surface (in m^2), Cl_{0i} is the zero angle lift coefficient of the aerofoil and a_{Wi} is the main wing lift curve slope (computed as in section D.4.1, page 234; in rad^{-1}).

Replacing the expressions of the lift coefficient of each lifting surface by the following developments:

$$\frac{Cl_{Wi}}{Cl} = \frac{\frac{L_{Wi}}{q \cdot S_{Wi}}}{\frac{M \cdot g}{q \cdot S_{ref}}} = \frac{L_{Wi}}{M \cdot g} \frac{S_{ref}}{S_{Wi}}$$

And the reference lift coefficient by the following expression:

$$Cl = \frac{M \cdot g}{\frac{1}{2} \cdot \rho \cdot V^2 \cdot S_{ref}}$$

It leads to:

$$\begin{aligned}
P = \frac{1}{2} \rho \left(\begin{aligned} & Cd_{0AH-93-131} \cdot S_{W1} + Cd_{0NACA0012} \cdot S_{W2} + D/q_{rest} \\ & + K_{CDAH-93-131} \left(\frac{Cl_{0AH-93-131}}{a_{W1}} \right)^2 S_{W1} + K_{CDNACA0012} \left(\frac{Cl_{0NACA0012}}{a_{W2}} \right)^2 S_{W1} \end{aligned} \right) V^3 \\
- 2 \left(K_{CDAH-93-131} \cdot L_{W1} \frac{Cl_{0AH-93-131}}{a_{W1}^2} + K_{CDNACA0012} \cdot L_{W2} \frac{Cl_{0NACA0012}}{a_{W2}^2} \right) V \\
+ \left(\frac{K_{CDAH-93-131}}{a_{W1}^2} L_{W1}^2 \frac{1}{S_{W1}} + \frac{K_{CDNACA0012}}{a_{W2}^2} L_{W2}^2 \frac{1}{S_{W2}} + \frac{(M \cdot g)^2}{\pi \cdot A_{ref} \cdot e \cdot S_{ref}} \right) \frac{1}{\frac{1}{2} \rho \cdot V}
\end{aligned} \tag{D.16}$$

The minimum power level flight is achieved when the speed derivation of the power is zero:

$$\frac{dP}{DV} = 0$$

Eventually, the required power in loiter is estimated thanks to equation (D.16).

The different components required for the calculation are:

- L_{W2} : In level flight, the force equilibrium gives:

$$L_{W2} = M \cdot g - L_{W1} \tag{D.17}$$

where M is the aircraft mass (in kg) and g is the gravitational constant (in $m.s^{-2}$).

- L_{W1} :

Equation (D.7), page 232 is simplified by eliminating insignificant members, and applied to equilibrium condition:

$$0 = -(X_{LW1} - X_{CG}) L_{W1} + (X_{CG} - X_{LW2}) L_{W2} + M_{W1} + M_{W2}$$

Combined with equation (D.17), it leads to:

$$L_{W1} = \frac{(X_{CG} - X_{LW2}) m \cdot g + M_{W1} + M_{W2}}{X_{LW1} - X_{LW2}} \quad (\text{D.18})$$

- D_{rest} This parameter include the drag of following components:
 - The fuselage: section D.2.5, page 213
 - The fins: section 4.2.2.3, page 118
 - The cooling: section D.3.6, page 230
 - The sensor turret: section D.3.4, page 229
 - The landing gear: section D.3.5, page 230
- The main wing induced drag components A_{ref} and e : section D.3.1, page 218

D.5.7 MAX SPEED

The analysis is based on the same physic as the one developed for loiter in section D.5.6, page249. Equation (D.16) page250 can be rewritten in the form:

$$a \cdot V^4 + b \cdot V^2 - P \cdot V + c = 0 \quad (\text{D.19})$$

which is a fourth degree polynomial. The maximum speed V is eventually found solving equation (D.19) thanks to the method of Ferrari, ensuring that the result is positive.

E

APPENDIX: MOTOR CONTROL

E.1 BDSM modelisation

E.1.1 Electrical modelisation

The study of the brushless motor starts with the following electrical model [?]. This electrical model is based on the electrical diagram, shown in Figure E.1 ¹.

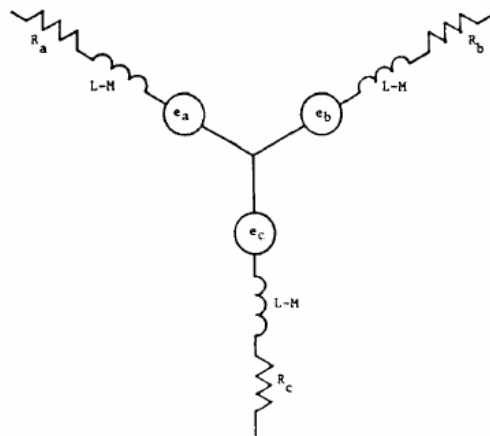


Figure E.1: Equivalent circuit from electric equation, (courtesy of Pillay [?])

¹As explained in [?], Figure E.1 can be simplified by substituting $L-M$ by L and assuming $R_a = R_b = R_c$.

$$\begin{aligned}
\begin{pmatrix} u_a \\ u_b \\ u_c \end{pmatrix} &= \begin{pmatrix} R & 0 & 0 \\ 0 & R & 0 \\ 0 & 0 & R \end{pmatrix} \begin{pmatrix} i_a \\ i_b \\ i_c \end{pmatrix} \\
+ \begin{pmatrix} L & 0 & 0 \\ 0 & L & 0 \\ 0 & 0 & L \end{pmatrix} \frac{d}{dt} \begin{pmatrix} i_a \\ i_b \\ i_c \end{pmatrix} & \\
-p \cdot \Omega \cdot \phi_r \begin{pmatrix} \sin(p \cdot \theta) \\ \sin(p \cdot \theta - \frac{2\pi}{3}) \\ \sin(p \cdot \theta + \frac{2\pi}{3}) \end{pmatrix} &
\end{aligned} \tag{E.1}$$

where a , b and c are the three motor phases, u , i , R and L are respectively the phase voltage, current, resistor and inductance (respectively in V , A , Ω and H), p is the number of poles, Ω is the rotation velocity (in $rad \cdot s^{-1}$), ϕ_r is the rotor magnetic flux (in *Weber*) and θ is the rotor position (in *rad*).

E.1.2 $\alpha \beta \gamma$ transformation

The $\alpha \beta \gamma$ (or Clarke) transformation enables the control computing time reduction. This transformation, used for most three-phase circuits, enables the control of only two equivalent phases instead of three. It consists of passing from the initial a , b c referential to the $\alpha \beta$ reference frame applying the following transformation matrices: $P_{\alpha\beta}^{abc} = \frac{2}{3} \begin{bmatrix} 1 & -\frac{1}{2} & -\frac{1}{2} \\ 0 & \frac{\sqrt{3}}{2} & -\frac{\sqrt{3}}{2} \end{bmatrix}$,

$$P_{abc}^{\alpha\beta} = P_{\alpha\beta}^{abc^{-1}} = \begin{bmatrix} 1 & 0 \\ -\frac{1}{2} & \frac{\sqrt{3}}{2} \\ -\frac{1}{2} & -\frac{\sqrt{3}}{2} \end{bmatrix}$$

This point is critical since FOC has to work at very high frequency and the computation relative to the adaptation is quite heavy compared to a primary control.

Equation (E.1) becomes:

$$\begin{aligned} \begin{pmatrix} u_\alpha \\ u_\beta \end{pmatrix} &= \begin{pmatrix} R & 0 \\ 0 & R \end{pmatrix} \begin{pmatrix} i_\alpha \\ i_\beta \end{pmatrix} + \begin{pmatrix} L & 0 \\ 0 & L \end{pmatrix} \frac{d}{dt} \begin{pmatrix} i_\alpha \\ i_\beta \end{pmatrix} \\ &+ p \cdot \Omega \cdot \phi_r \begin{pmatrix} -\sin(p \cdot \theta) \\ \cos(p \cdot \theta) \end{pmatrix} \end{aligned} \quad (\text{E.2})$$

$$\text{where } \begin{pmatrix} u_\alpha \\ u_\beta \end{pmatrix} = P_{\alpha\beta}^{abc} \begin{pmatrix} u_a \\ u_b \\ u_c \end{pmatrix} \text{ and } \begin{pmatrix} i_\alpha \\ i_\beta \end{pmatrix} = P_{\alpha\beta}^{abc} \begin{pmatrix} i_a \\ i_b \\ i_c \end{pmatrix}$$

E.2 Control construction

The present work aims at designing an adaptive control law that is charged with several tasks. On the one hand, it estimates the two almost constant parameters R and L , to adapt itself perfectly to the motor it manages. On the other hand, it estimates the third term of the addition of equation (E.2) to extract the rotor position θ required by any brushless control as stated in section 5.2. Designing the control in the present reference frame seems to be the best choice. It is indeed the most reduced one, voltages and currents being likely to be sinusoidal at high frequency, which would approach the persistent excited condition. Moreover, on a parameter exploitation point of view, the inverse Clark transformation would help estimate the different phase real parameters and thus detects more precisely any degradation.

The motor is working optimally when the current dynamic synchronises with the rotor magnetic field's one. The second member of equation (E.2) can be therefore written as:

$$p \cdot \Omega \cdot \phi_r \begin{pmatrix} -\sin(p \cdot \theta) \\ \cos(p \cdot \theta) \end{pmatrix} = \begin{pmatrix} k_1 & k_2 \\ k_3 & k_4 \end{pmatrix} \begin{pmatrix} i_\alpha \\ i_\beta \end{pmatrix}$$

where k_1 , k_2 , k_3 and k_4 are constants.

Thus, the electrical equation (E.2) can be rewritten as:

$$\begin{aligned} \begin{pmatrix} u_\alpha \\ u_\beta \end{pmatrix} &= \begin{pmatrix} k_1 + R & k_2 \\ k_3 & k_4 + R \end{pmatrix} \begin{pmatrix} i_\alpha \\ i_\beta \end{pmatrix} \\ &+ \begin{pmatrix} L & 0 \\ 0 & L \end{pmatrix} \frac{d}{dt} \begin{pmatrix} i_\alpha \\ i_\beta \end{pmatrix} \end{aligned} \quad (\text{E.3})$$

As shown in equation (E.3), the considered reference frame is not suitable for an adaptive control implementation. The adaptive part of this control aims indeed at reducing the error of the control varying the different parameters. Therefore, it will tend to overestimate the value of the resistor matrix which is constant, to set to zero the magnetic flux term that is sinusoidal and thus increases the error. It is prohibitive not only because of the loss of the motor parameters estimation but also because the stator magnetic field term is required to estimate the rotor position. One can notice that the problem would be the same in the initial a, b, c referential.

The referential frame must be thereby substituted, one more time, by a new one without any correlation between the different components. To this end, a variant of the $d q 0$ transformation is used.

E.2.1 Modified $d q 0$ transformation

A variant of the $d q 0$ transformation (or Park) is applied considering the estimated motor rotor position $\hat{\theta}$. This transformation removes the sinusoidal nature of the current, voltage and magnetic field terms [?]. The transformation matrix between the two last referential are [?] [?] [?].

$$P_{dq}^{\alpha\beta} = \begin{pmatrix} \cos(p \cdot \hat{\theta}) & \sin(p \cdot \hat{\theta}) \\ -\sin(p \cdot \hat{\theta}) & \cos(p \cdot \hat{\theta}) \end{pmatrix} \text{ and } P_{\alpha\beta}^{dq} = P_{dq}^{\alpha\beta-1} = \begin{pmatrix} \cos(p \cdot \hat{\theta}) & -\sin(p \cdot \hat{\theta}) \\ \sin(p \cdot \hat{\theta}) & \cos(p \cdot \hat{\theta}) \end{pmatrix}$$

Defining $\tilde{\theta}$ as the error of the rotor position estimation, it comes: $\tilde{\theta} = \hat{\theta} - \theta$

Following the same method as exposed in [?], the electric model (E.2) becomes:

$$\begin{aligned} \begin{pmatrix} u_d \\ u_q \end{pmatrix} &= \begin{pmatrix} L_d & 0 \\ 0 & L_q \end{pmatrix} \begin{pmatrix} \dot{i}_d \\ \dot{i}_q \end{pmatrix} \\ &+ \begin{pmatrix} R_d & -L_q \cdot p \cdot \hat{\Omega} \\ L_d \cdot p \cdot \hat{\Omega} & R_q \end{pmatrix} \begin{pmatrix} i_d \\ i_q \end{pmatrix} \\ &+ p \cdot \Omega \cdot \phi_r \cdot \begin{pmatrix} \sin(p \cdot \tilde{\theta}) \\ \cos(p \cdot \tilde{\theta}) \end{pmatrix} \end{aligned}$$

It should be noted that L_d and L_q are now segregated for generalisation reasons since they may vary a bit depending on the saliency of the motor. Nevertheless, classical aero models brushless motors still verify the property: $L = L_d = L_q$.

This latter equation can be written as:

$$U = A\dot{I} + BI + E \quad (\text{E.4})$$

Where: $U = \begin{pmatrix} u_d \\ u_q \end{pmatrix}$, $I = \begin{pmatrix} i_d \\ i_q \end{pmatrix}$, $A = \begin{pmatrix} L_d & 0 \\ 0 & L_q \end{pmatrix}$, $B = \begin{pmatrix} R_d & -L_q \cdot p \cdot \hat{\Omega} \\ L_d \cdot p \cdot \hat{\Omega} & R_q \end{pmatrix}$
and

$$E = \begin{pmatrix} E_d \\ E_q \end{pmatrix} = p \cdot \Omega \cdot \phi_r \cdot \begin{pmatrix} \sin(p \cdot \tilde{\theta}) \\ \cos(p \cdot \tilde{\theta}) \end{pmatrix} \quad (\text{E.5})$$

The rest of the article takes advantage is this final electric model

E.2.2 Adaptive control design

An adaptive control law based on the direct adaptive control method [?] is now proposed.

Control idea: The primary purpose of the present control is to consider that the mechanical dynamics of the motor is much slower than the electrical one. Therefore on an electrical time scale, E , which depends on the motor rotational speed Ω and the rotor drift $\tilde{\theta}$ can be considered as constant and be estimated as an unknown parameter for the adaptative control.

The design starts with the definition of the control law in section E.2.2.1. Then the error

of the control is estimated in section E.2.2.2. A Lyapunov law is proposed in section E.2.2.3 and the adaptive law is extracted to determine the matrices A , B and E of equation (E.4). The rotor position is lastly estimated from parameter E in section E.2.2.4.

E.2.2.1 Control law definition

The aim is to follow a desired current trajectory T . The error of the control Δ is defined as follows:

$$\Delta = T - I \quad (\text{E.6})$$

It is possible to superimpose a white noise to the trajectory T to help the convergence of the parameters.

The aim of the control is to reduce the magnitude of Δ . In order to do so, the following relation is proposed to be satisfied by the error control:

$$\dot{\Delta} = -K\Delta \quad (\text{E.7})$$

where K is the control gain defined positively.

From equations (E.6) and (E.7), it comes:

$$\begin{aligned} \dot{T} - \dot{I} &= -K\Delta \\ \Rightarrow AI &= A(K\Delta + \dot{T}) \end{aligned} \quad (\text{E.8})$$

Then substituting equation (E.8) in equation (E.4), it comes:

$$U = A(K\Delta + \dot{T}) + BI + E \quad (\text{E.9})$$

As the actual control depends on the estimated parameters, noted \hat{A} , \hat{B} and \hat{E} , rather than the real values, equation (E.9) becomes :

$$U = \hat{A}(K\Delta + \dot{T}) + \hat{B}I + \hat{E} \quad (\text{E.10})$$

E.2.2.2 Control error estimation

Now including the estimation errors of the different parameters: $\tilde{A} = \hat{A} - A$, $\tilde{B} = \hat{B} - B$, $\tilde{E} = \hat{E} - E$, equation (E.10) becomes:

$$U = \tilde{A} (K\Delta + \dot{T}) + \tilde{B}I + \tilde{E} + A (K\Delta + \dot{T}) + BI + E \quad (\text{E.11})$$

Then inserting the equation (E.4), in the derivative of the estimation error expression (E.6) $\dot{\Delta} = \dot{T} - \dot{I}$, it comes:

$$A\dot{\Delta} = A\dot{T} + BI + E - U \quad (\text{E.12})$$

Then substituting equation (E.11) in equation (E.12) ²:

$$\begin{aligned} A\dot{\Delta} &= A\dot{T} + BI + E - \tilde{A} (K\Delta + \dot{T}) \\ &\quad - \tilde{B}I - \tilde{E} - AK\Delta - A\dot{T} - BI - E \\ \Leftrightarrow \dot{\Delta} &= -K\Delta - A^{-1} \left(\tilde{A} (K\Delta + \dot{T}) + \tilde{B}I + \tilde{E} \right) \end{aligned} \quad (\text{E.13})$$

Defining: $\tilde{\lambda}^T = \begin{pmatrix} \tilde{A} & \tilde{B} & \tilde{E} \end{pmatrix}$, and: $\eta = \begin{pmatrix} K\Delta + \dot{T} \\ I \\ 1 \end{pmatrix}$, equation (E.13) becomes:

$$\dot{\Delta} = -K\Delta - A^{-1}\tilde{\lambda}^T\eta$$

E.2.2.3 Adaptive law based on Lyapunov function

The following Lyapunov function candidate is proposed to define the stability condition of the control [?]:

$$V = \frac{1}{2}\Delta^T A\Delta + \frac{1}{2}tr \left(\tilde{\lambda}^T \Gamma^{-1} \tilde{\lambda} \right) \quad (\text{E.14})$$

where Γ is a real positive definite diagonal matrix.

²Matrix A being diagonal and strictly positive, it is inversible.

Deriving equation (E.14), it comes:

$$\begin{aligned}
\dot{V} &= \Delta^T A \dot{\Delta} + tr \left(\tilde{\lambda}^T \Gamma^{-1} \dot{\tilde{\lambda}} \right) \\
&= -\Delta^T AK\Delta - \Delta^T AA^{-1} \tilde{\lambda}^T \eta + tr \left(\tilde{\lambda}^T \Gamma^{-1} \dot{\tilde{\lambda}} \right) \\
&= -\Delta^T AK\Delta - tr \left(\tilde{\lambda}^T \eta \Delta^T \right) + tr \left(\tilde{\lambda}^T \Gamma^{-1} \dot{\tilde{\lambda}} \right) \\
&= -\Delta^T AK\Delta - tr \left(\tilde{\lambda}^T \left(\eta \Delta^T - \Gamma^{-1} \dot{\tilde{\lambda}} \right) \right)
\end{aligned}$$

In order to have: $\dot{V} < 0$, the following relation can be imposed:

$$\begin{aligned}
\eta \Delta^T - \Gamma^{-1} \dot{\tilde{\lambda}} &= 0 \\
\Leftrightarrow \dot{\tilde{\lambda}} &= \Gamma \eta \Delta^T
\end{aligned} \tag{E.15}$$

which represents the adaptive part of the control.

E.2.2.4 Rotor position estimation

The estimation of the rotor position is determined from equation (E.5):

- if $\hat{E}_d \geq \hat{E}_q$:

$$\begin{aligned}
\frac{\hat{E}_q}{\hat{E}_d} &= \frac{\Omega \cdot \phi_r \cdot \cos(p \cdot \tilde{\theta})}{\Omega \cdot \phi_r \cdot \sin(p \cdot \tilde{\theta})} \\
\Leftrightarrow p \cdot \tilde{\theta} &= \cot^{-1} \left(\frac{\hat{E}_d}{\hat{E}_q} \right)
\end{aligned}$$

- if $\hat{E}_d < \hat{E}_q$

$$\begin{aligned}
\frac{\hat{E}_d}{\hat{E}_q} &= \frac{\Omega \cdot \phi_r \cdot \sin(p \cdot \tilde{\theta})}{\Omega \cdot \phi_r \cdot \cos(p \cdot \tilde{\theta})} \\
\Leftrightarrow p \cdot \tilde{\theta} &= \tan^{-1} \left(\frac{\hat{E}_d}{\hat{E}_q} \right)
\end{aligned}$$

Following the method proposed in [?], a control like PI is applied to estimate the rotation speed evolution:

$$p \cdot \hat{\Omega} = -K_p \cdot p \cdot \tilde{\theta} - K_i \cdot \int_{t_0}^t p \cdot \tilde{\theta} \quad (\text{E.16})$$

Lastly, the stator position $\hat{\theta}$ is obtained integrating $\hat{\Omega}$:

$$p \cdot \hat{\theta} = \int_{t_0}^t p \cdot \hat{\Omega} \quad (\text{E.17})$$

It is thus possible, using the set of equations (E.10), (E.15), (E.16) and (E.17) to estimate the required position and speed of the rotor. The only condition is to have a sufficient rotating speed to be able to measure E . A standard open loop sensorless control can be used to reach this minimum rotation speed from stop[?]. However, this is beyond the scope of this article.

E.3 Simulation results

The motor with the following characteristics is simulated using Scicos³ software: $P = 5$, $R_d = 110 \cdot 10^{-3}\Omega$, $R_q = 90 \cdot 10^{-3}\Omega$, $L_d = 55 \cdot 10^{-6}H$, $L_q = 60 \cdot 10^{-6}H$ and $\phi_r = 0.00012Wb$

These values are typical for a small-size RC-model brushless motor.

This motor is controlled to obtain the desired path T , as shown in Figure E.2:

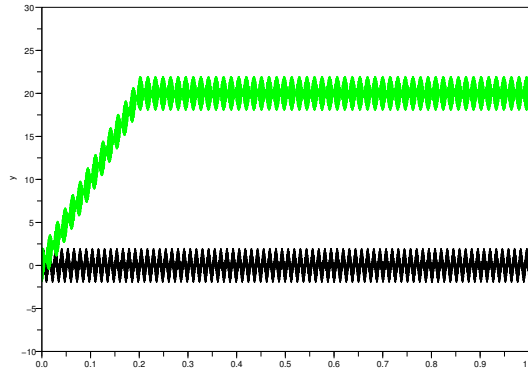


Figure E.2: Desired path T_d in black and T_q in green, A vs s

One can notice that noise has been superimposed all over the initial intended path, which has two reasons. On the first hand, it accelerates the convergence of the different parameters. This noise has been set at a fifth of the expected path on the simulation, but the amplitude

³<http://www.scicos.org/>

must be tweaked depending on the required convergence velocity: the higher is the noise, the faster is the convergence. On the other hand, it simulates the fast path variations that the motors are likely to be subjected as discussed in section 5.2, page 136.

It has to be kept in mind that this noise is only necessary when the motor is started and can be deleted when the parameters have converged. For instance, a white noise could be imposed alone at the very beginning, before starting the real task, but the engine operation strategy is beyond the scope of the present article.

The obtained path and the error are presented in Figure E.3.

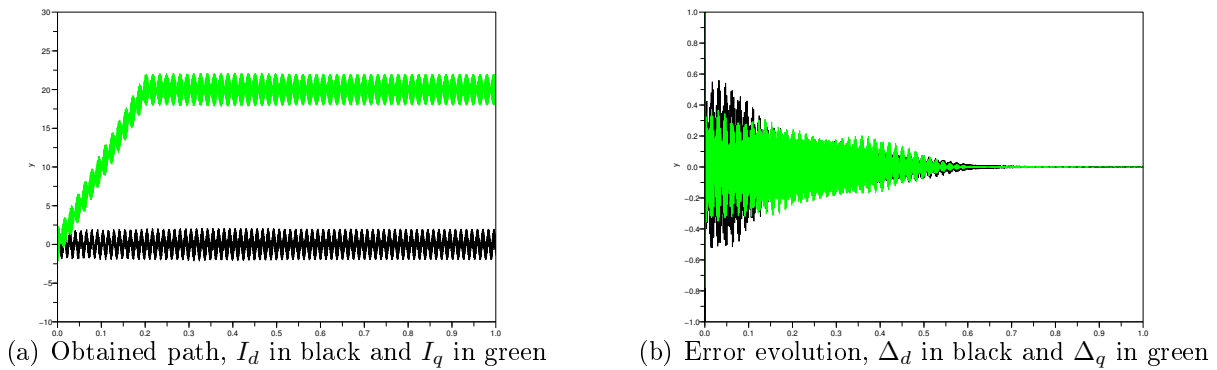


Figure E.3: Obtained path and error evolution, A vs s

One can notice that the convergence is faster than a second. The gain K of the path following control part has been set to: $K = 10^4 \cdot \begin{pmatrix} 1 & 0 \\ 0 & 1 \end{pmatrix}$

The evolution of the parameter estimation is shown in Figure E.4. To obtain such an evolution, the gain Γ_A of the adaptive control part has been set to: $\Gamma_A = 10^{-5}$. This value is much smaller than the following one. It is done so because of the tiny size of a parameter compared to the two others.

In the same manner, the evolution of the parameter B estimation is shown in Figure E.5. The gain Γ_B is here set to : $\Gamma_B = 10$.

Lastly, the evolution of the estimation of the most important parameter, E, is shown in Figure E.6. Zoom on the converged part is visible in Figure E.7. The gain Γ_E is here set to : $\Gamma_E = 10^4$. It is set much higher than the two others to compensate the fact that E is not any more constant.

It can be noticed in Figure E.7 that drift has been superimposed to the time linear position

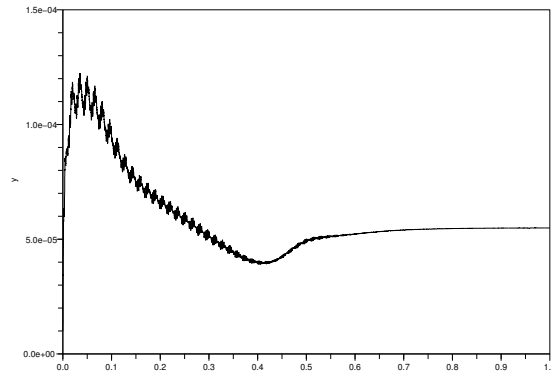


Figure E.4: Parameter L_d estimation, H vs s

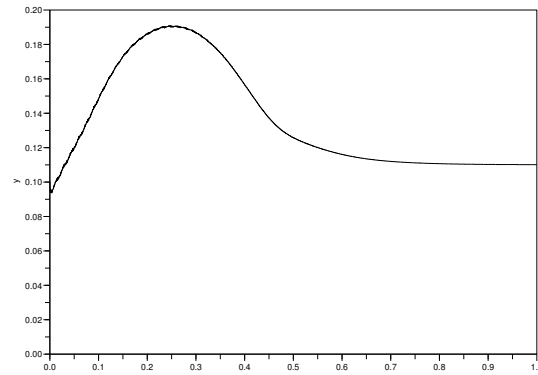


Figure E.5: Parameter R_d estimation, ω vs s

of the motor to simulate the brutal fluctuation of the torque applied to it, mentioned in section 5.2, page 136. However, the convergence of the motor position estimation is both fast and precise, which makes it suitable for performing the necessary rotor position estimation required by the field oriented control.

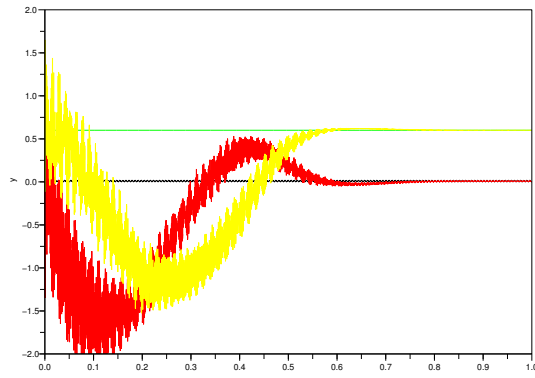


Figure E.6: Parameter E estimation, E_d real and estimated respectively in black and red, E_q real and estimated respectively in green and yellow, ω vs s

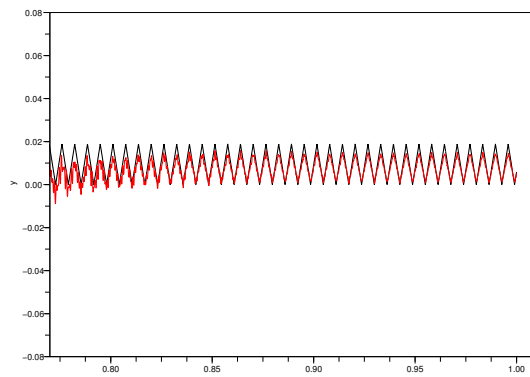


Figure E.7: Parameter E estimation

F

APPENDIX: “FLYING-ROTOR” CONTROL

F.1 Model

F.1.1 Rotor forces

F.1.1.1 Rotor disk referential frame analysis

Rotor analysis is based on the model of the blade element theory exposed in section 2.1.1, page 54. Since the rotor is supposed to generate a homogeneous downwash, this theory can be used both for hover and translation flights. Since the rotor is assumed to be perfectly horizontal, the speeds withstood by the rotor are simplified as presented in Figure F.1. where

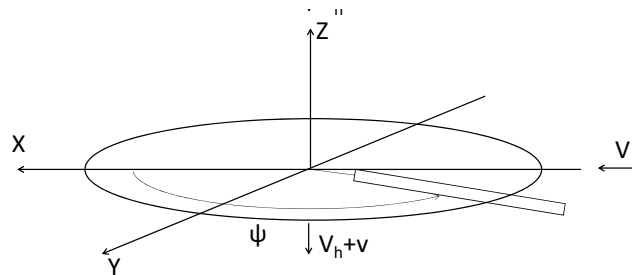


Figure F.1: Rotor references and speeds

V , V_h and v are respectively the horizontal, vertical and downwash speeds and ψ is the angle

between the airspeed direction and the blade. According to [?], this latter speed v , can be assessed as follows:

$$v^4 + v^3 2V \sin \alpha + v^2 V^2 = \left(\frac{T}{2\rho A'} \right)^2 \quad (\text{F.1})$$

where A' is the effective rotor area and follows the expression:

$$A' = B^2 A$$

A being the rotor disk area and B a factor less than unity, α is the airspeed slope: $\alpha = \tan^{-1} \frac{V_h}{V}$, ρ is the air density and T is the rotor lift. However because the vertical velocity V_h is supposed to be very low compared to the downwash velocity v , equation (F.1) becomes:

$$v^4 + v^2 V^2 - \left(\frac{T}{2\rho A} \right)^2 = 0 \quad (\text{F.2})$$

Since v varies slowly with V and T , and these latter vary themselves slowly thanks to the inertia, the former can be considered as constant in the control and computed separately. The resultant aerodynamics forces applied to the portion of the rotor disk of radius r are shown in Figure F.2, in the rotor reference frame, where t , h and y are respectively the vertical, longitudinal, lateral forces q is the torque generated by the rotor. Ω is the rotating velocity of the rotor. Taking advantage of the fact that the blade pitch angle is almost constant $\theta \approx \theta_0$

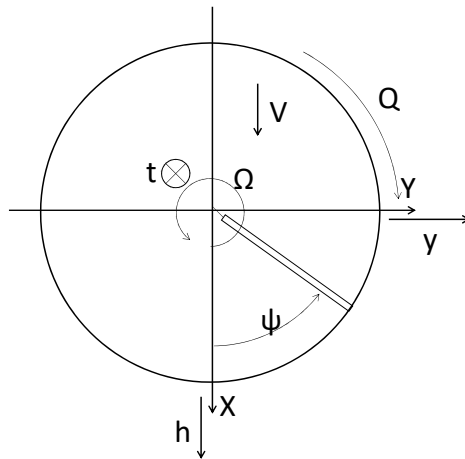


Figure F.2: Rotor forces

and the blade flap angle is almost zero $\beta \approx 0$, the aerodynamics forces become:

$$t = \frac{\rho c a}{4} [(\theta_0 - \alpha_0)V^2 + 2(\theta_0 - \alpha_0)r^2\Omega^2 - 2(V_h + v)r\Omega] \quad (\text{F.3})$$

$$h = \frac{\rho c}{4} [a(\theta_0 - \alpha_0)(V_h + v)V + 2c_d V r \Omega] \quad (\text{F.4})$$

$$y = 0 \quad (\text{F.5})$$

$$q = \frac{r \rho c}{4} [2a(\theta_0 - \alpha_0)(V_h + v)r\Omega - 2a(V_h + v)^2 + c_d V^2 + 2c_d r^2 \Omega^2] \quad (\text{F.6})$$

where c , a , α_0 and c_d are respectively the blade chord, the aerofoil lift curve slope, the aerofoil zero lift angle and the drag coefficient. Then the forces acting on the overall rotor disk are computed. From (F.4), the lift force T_z is:

$$F_z = p \int_{r_0}^r t dr$$

where: $r = B \times R$, R is the rotor geometrical radius, p is the number of blades and r_0 is the radius of the rotor hub. Defining $K_1 = \frac{\rho p}{4} \int_{r_0}^r ca(\theta_0 - \alpha_0) dr$ $K_2 = \frac{\rho p}{2} \int_{r_0}^r ca(\theta_0 - \alpha_0)r^2 dr$ $K_3 = \frac{\rho p}{2} \int_{r_0}^r cardr$ It becomes:

$$F_z = K_1 V^2 + K_2 \Omega^2 - K_3 (V_h + v) \Omega \quad (\text{F.7})$$

From (F.5) the lateral force F_y is:

$$F_y = p \int_{r_0}^R y dr = 0 \quad (\text{F.8})$$

From (F.4) the overall drag F_x is:

$$F_x = p \int_{r_0}^R h dr$$

Defining $K_4 = \frac{pp}{4} \int_{r_0}^R ca(\theta_0 - \alpha_0)dr$ and $K_5 = \frac{pp}{2} \int_{r_0}^R cc_d r]dr$ It becomes:

$$F_x = K_4(V_h + v)V + K_5V\Omega \quad (\text{F.9})$$

And from (F.6), the rotor resistive torque Q is:

$$Q = p \int_{r_0}^R qdr$$

Defining $K_6 = \frac{pp}{2} \int_{r_0}^R r^2 ac(\theta_0 - \alpha_0)dr$, $K_7 = \frac{pp}{2} \int_{r_0}^R cradr$, $K_8 = \frac{pp}{4} \int_{r_0}^R rcc_d dr$ and $K_9 = \frac{pp}{2} \int_{r_0}^R r^3 cc_d dr$
It becomes:

$$Q = K_6(V_h + v)\Omega - K_7(V_h + v)^2 + K_8V^2 + K_9\Omega^2 \quad (\text{F.10})$$

F.1.1.2 Earth base referential frame analysis

One of the advantages of present concept is its symmetry of revolution around the z axis. That is why the control can be advantageously simplified choosing the earth frame as the reference. The three axis are noted X , Y and Z . Equation (F.7), leads to:

$$F_Z = K_1 \left(\dot{X}^2 + \dot{Y}^2 \right) + K_2\Omega^2 - K_3(\dot{Z} + v)\Omega \quad (\text{F.11})$$

Equation (F.9) leads to:

$$F_X = -K_4(\dot{Z} + v)\dot{X} - K_5\dot{X}\Omega \quad (\text{F.12})$$

$$F_Y = -K_4(\dot{Z} + v)\dot{Y} - K_5\dot{Y}\Omega \quad (\text{F.13})$$

Equation (F.10) becomes:

$$Q = -K_6(\dot{Z} + v)\Omega + K_7(\dot{Z} + v)^2 - K_8 \left(\dot{X}^2 + \dot{Y}^2 \right) - K_9\Omega^2 \quad (\text{F.14})$$

ψ is now defined as the positive angle between $-Y$ axis and first blade.

F.1.2 Propellers forces

Propellers generated force is assessed using theoretical propeller power proposed in section 1.1.1.2, page 28. Useful propeller generated power P_{useful} can be estimated, as follows:

$$P_{useful} = \frac{a}{D^2} V^2 \omega + \frac{b}{D} V \omega^2$$

where a , b , D , ω and V are respectively two approximation factors, the propeller diameter, the propeller rotation speed and the propeller axial speed. This can be simplified as:

$$P_{useful} = AV^2\omega + BV\omega^2$$

Noting that $P_{useful} = FV$ with F the generated power, the propeller force becomes:

$$F = AV\omega + B\omega^2 \quad (\text{F.15})$$

In Earth referential frame the axial propeller V is:

$$V_i = r_{prop}\Omega + \dot{X}\cos\psi_i + \dot{Y}\sin\psi_i$$

where ψ is the azimuth of the blade in Earth referential frame and i is the subscript of the propeller from 1 to 3. Defining $\psi_2 = \psi_1 + \frac{2\pi}{3}$ and $\psi_3 = \psi_1 + \frac{4\pi}{3}$ Then the projection of (F.15) gives:

$$F_{X_{propi}} = F_i \sin \psi_i$$

$$F_{Y_{propi}} = F_i \cos \psi_i$$

$$Q_{propi} = rF_i$$

F.1.3 “flying rotor” UAV dynamics

First the state variables are defined. There are three orthogonal speeds \dot{X} , \dot{Y} , \dot{Z} and the rotor rotation speed: $\dot{\Omega}$. Dynamics laws give:

$$M\ddot{X} = F_X + F_{X_{prop1}} + F_{X_{prop2}} + F_{X_{prop3}}$$

$$M\ddot{Y} = F_Y + F_{Y_{prop1}} + F_{Y_{prop2}} + F_{Y_{prop3}}$$

$$M\ddot{Z} = F_Z + -Mg$$

$$J_{zz}\dot{\Omega} = Q + Q_{prop1} + Q_{prop2} + Q_{prop3}$$

where M is “flying rotor” UAV mass and J_{zz} is its moment of inertia around the Z axis.

$$\begin{pmatrix} \ddot{X} \\ \ddot{Y} \\ \ddot{Z} \\ \dot{\Omega} \end{pmatrix} = \begin{pmatrix} \frac{1}{M}F_X \\ \frac{1}{M}F_Y \\ \frac{1}{M}F_Z - g \\ \frac{1}{J_{zz}}Q \end{pmatrix} + \begin{pmatrix} \frac{1}{M}(F_{X_{prop1}} + F_{X_{prop2}} + F_{X_{prop3}}) \\ \frac{1}{M}(F_{Y_{prop1}} + F_{Y_{prop2}} + F_{Y_{prop3}}) \\ 0 \\ \frac{1}{J_{zz}}(Q_{prop1} + Q_{prop2} + Q_{prop3}) \end{pmatrix}$$

Substituting equations (F.12), (F.13), (F.11), (F.14) and projection of (F.15), and defining $K'_i = \frac{K_i}{M}$ for i from 1 to 5 and $K'_i = \frac{K_i}{J_{zz}}$ for i from 6 to 9, it becomes:

$$\begin{pmatrix} \ddot{X} \\ \ddot{Y} \\ \ddot{Z} \\ \dot{\Omega} \end{pmatrix} = \begin{pmatrix} -K'_4(\dot{Z} + v)\dot{X} - K'_5\dot{X}\Omega \\ -K'_4(\dot{Z} + v)\dot{Y} - K'_5\dot{Y}\Omega \\ K'_1(\dot{X}^2 + \dot{Y}^2) + K'_2\Omega^2 - K'_3(\dot{Z} + v)\Omega - g \\ -K'_6(\dot{Z} + v)\Omega + K'_7(\dot{Z} + v)^2 - K'_8(\dot{X}^2 + \dot{Y}^2) - K'_9\Omega^2 \end{pmatrix} + \begin{pmatrix} \frac{1}{M} \left(F_1 \sin \psi + F_2 \sin \left(\psi + \frac{2\pi}{3} \right) + F_3 \sin \left(\psi - \frac{2\pi}{3} \right) \right) \\ \frac{1}{M} \left(F_1 \cos \psi + F_2 \cos \left(\psi + \frac{2\pi}{3} \right) + F_3 \cos \left(\psi - \frac{2\pi}{3} \right) \right) \\ 0 \\ \frac{r}{J_{zz}} (F_1 + F_2 + F_3) \end{pmatrix}$$

For every term of the control part, it is possible to find a F_1 , F_2 and F_3 , and therefore the ω_i that matches. Control part of the dynamics is thus substituted by $\begin{pmatrix} U_1 & U_2 & 0 & U_3 \end{pmatrix}^T$. In addition, the control is based on 3 DoF IMU giving \dot{X} , \dot{Y} and \dot{Z} . The dynamics is hence simplified and becomes:

$$\begin{pmatrix} \ddot{X} \\ \ddot{Y} \\ \ddot{Z} \\ \dot{\Omega} \end{pmatrix} = \begin{pmatrix} -a_X \dot{X} \\ -a_Y \dot{Y} \\ a_Z \Omega^2 + b_Z \Omega + c_Z \\ a_\Omega \end{pmatrix} + \begin{pmatrix} U_1 \\ U_2 \\ 0 \\ U_3 \end{pmatrix}$$

where: $a_X = a_Y = \left[K'_4(\dot{Z} + v) + K'_5\Omega \right]$ (One's can notice that a_X and a_Y are strictly positive), $a_Z = K'_2$, $b_z = -K'_3(\dot{Z} + v)$ and $c_Z = K'_1(\dot{X}^2 + \dot{Y}^2) - g$ and lastly $a_\Omega = -K'_6(\dot{Z} + v)\Omega + K'_7(\dot{Z} + v)^2 - K'_8(\dot{X}^2 + \dot{Y}^2) - K'_9\Omega^2$

F.2 Control

Control study is performed separating the dynamics in three parts. The X and Y controls are built first before the Z and Ω ones.

F.2.1 \dot{X} control

The \dot{X} control U_1 is defined as:

$$U_1 = -K_X e_x$$

where K_X is strictly positive and e_x is the control error defined as: $e_x = \dot{X} - \dot{X}_d$. The X dynamics becomes:

$$\ddot{X} = -a_x \dot{X} - K_X e_x$$

control error becomes:

$$\dot{e}_x = -a_x e_x - K_X e_x = -(a_x + K_X) e_x$$

Defining Lyapunov candidate function:

$$V = \frac{1}{2} e_x^2$$

It becomes:

$$\dot{V} = e_x \dot{e}_x = -(a_x + K_X) e_x^2$$

$\dot{V} < 0$ for \mathfrak{R}^* then \dot{X} is asymptotically stable.

F.2.2 \dot{Y} Control

The \dot{Y} dynamics is very close to the \dot{X} one. Therefore, defining $U_2 = -K_Y e_y$, where K_Y is strictly positive and $e_y = \dot{Y} - \dot{Y}_d$. \dot{Y} is asymptotically stable.

F.2.3 \dot{Z} and Ω controls

\dot{Z} and Ω controls are studied together following the idea of the backstepping method [?]. First \dot{Z} is studied considering Ω as the control input.

$$\ddot{Z} = a_Z \Omega^2 + b_Z \Omega + c_Z$$

If $\ddot{Z} = -K_Z e_z$ where K_Z is defined strictly positive, the control error $e_z = \dot{Z} - \dot{Z}_d$ becomes:

$$\dot{e}_z = -K_Z e_z$$

Defining the Lyapunov candidate function $V = \frac{1}{2} e_z^2$, it leads to:

$$\dot{V} = e_z \dot{e}_z = -K_Z e_z^2$$

$\dot{V} < 0$ for \mathfrak{R}^* then \dot{Z} is asymptotically stable. This imposes that Ω verifies:

$$a_Z \Omega_d^2 + b_Z \Omega_d + c_Z = -K_Z e_z$$

where Ω_d is the expected control. That is to say, defining $\Delta = b_Z^2 - 4a_Z(c_Z + K_Z e_z)$:

$$\Omega_d = \frac{-b_Z + \sqrt{\Delta}}{2a_Z}$$

Then the Ω control is studied in order to cancel the error $e_\Omega = \Omega - \Omega_d$. The \dot{Z} dynamics becomes:

$$\begin{aligned} \ddot{Z} &= a_Z (\Omega_d + e_\Omega)^2 + b_Z (\Omega_d + e_\Omega) + c_Z \\ &= -K_Z e_z + a_Z e_\Omega^2 + 2a_Z \Omega_d e_\Omega + b_Z e_\Omega \end{aligned}$$

Therefore:

$$\dot{e}_z = -K_Z e_z + a_Z e_\Omega^2 + 2a_Z \Omega_d e_\Omega + b_Z e_\Omega$$

The Ω dynamics being $\dot{\Omega} = a_\Omega + U_3$, the control error becomes:

$$\dot{e}_\Omega = \dot{\Omega} - \dot{\Omega}_d = a_\Omega + U_3 - \dot{\Omega}_d$$

Defining the Lyapunov candidate function $V = \frac{1}{2}e_z^2 + \frac{1}{2}e_\Omega^2$ It leads to:

$$\begin{aligned}
\dot{V} &= e_z \dot{e}_z + e_\Omega \dot{e}_\Omega \\
&= (-K_Z e_z^2 + a_Z e_z e_\Omega^2 + 2a_Z \Omega_d e_\Omega e_z + b_Z e_\Omega e_z) \\
&+ e_\Omega (a_\Omega + U_3 - \dot{\Omega}_d) = -K_Z e_z^2 \\
&+ e_\Omega (a_Z e_z e_\Omega + 2a_Z \Omega_d e_z + b_Z e_z + a_\Omega + U_3 - \dot{\Omega}_d)
\end{aligned}$$

Defining $U_3 = \dot{\Omega}_d - K_\Omega e_\Omega - a_Z e_z e_\Omega - 2a_Z \Omega_d e_z - b_Z e_z - a_\Omega$, with K_Ω defined strictly positive. It becomes:

$$\dot{V} = -K_Z e_z^2 - K_\Omega e_\Omega^2$$

$\dot{V} < 0$ for \mathfrak{R}^* then \dot{Z} and Ω are asymptotically stable. Only $\dot{\Omega}_d$ remains to be computed. Recalling that: $a_z = K_{2'}$, $b_Z = -K_3' (\dot{Z} + v)$ and $c_Z = K_1' (\dot{X}^2 + \dot{Y}^2)$ it leads to:

$$\dot{a}_z = 0$$

$$\dot{b}_Z = -K_3' \ddot{Z}$$

$$\dot{c}_Z = 2K_1' (\dot{X} \ddot{X} + \dot{Y} \ddot{Y})$$

Then:

$$\begin{aligned}
\dot{\Omega}_d &= \frac{-\dot{b}_Z}{2a_Z} + \frac{1}{4a_Z \sqrt{\Delta}} \dot{\Delta} \\
&= \frac{-\dot{b}_Z}{2a_Z} + \frac{(2b_Z \dot{b}_Z - 4a_Z (\dot{c}_Z + K_Z \dot{e}_Z))}{4a_Z \sqrt{b_Z^2 - 4a_Z (c_Z + K_Z e_Z)}}
\end{aligned}$$

One can notice that $\dot{\Omega}_d$ is not function of $\dot{\Omega}$ so there is no algebraic loop issue.

F.3 Simulation

In order to assess the control proposed, a simulation has been carried out with the parameters of the prototype currently in construction.

- $K_1 = 0.065769047 \text{ kg.s}^2/m$
- $K_2 = 0.019248329 \text{ kg.s}^{-2}.m$

-
- $K_3 = 0.203888974 \text{ kg.s}^{-1}$
 - $K_4 = 0.065982097 \text{ kg.s}^2/m$
 - $K_5 = 0.000380772 \text{ kg.s}^{-1}$
 - $K_6 = 0.019508803 \text{ kg.s}^{-1}$
 - $K_7 = 0.208316851 \text{ kg.s}^2/m$
 - $K_8 = 0.000190386 \text{ kg.s}^2/m$
 - $K_9 = 9.0024310(-05) \text{ kg.s}^{-2}.m$
 - $M = 4 \text{ kg}$
 - $J_{zz} = 0.133759085 \text{ kg.m}^2$

And the parameters for the propellers are (APC 7x6):

- $r = 0.553883464 \text{ m}$
- $A = -0.000278116 \text{ kg.s}^{-1}$
- $B = 9.12959 * 10(-6) \text{ kg.s}^{-2}.m$

Lastly the velocity control gains are fixed as follows:

$$K_X = K_Y = K_Z = K_\Omega = 5$$

In order to visualise better the behaviour of the control, a straightforward path following control is added by means of a proportional control of gain $K = 1$. The expected path consists in climbing up to 3 followed by a circle of 10 m in radius at constant altitude. It ends descending until touching the ground. The actual behaviour of the drone is superimposed to the expected one in Figure F.3. One can notice that “flying rotor” UAV follows very well the expected trajectory. Then from the generated control, motors velocities are computed and presented in Figure F.4. A zoom of the latter figure is presented in Figure F.5. It can be seen that the motors gyration speeds are sinusoidal with a frequency equal to the rotation speed of the rotor.

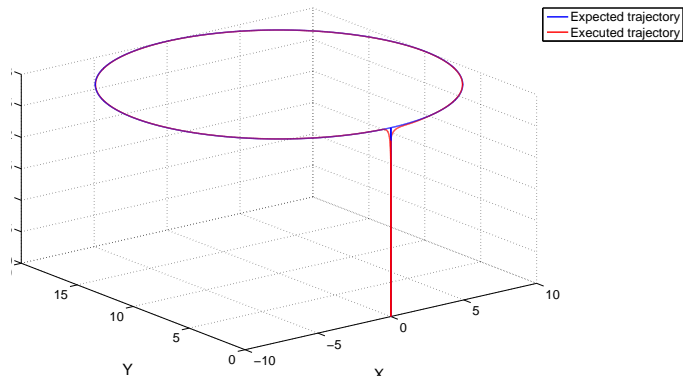


Figure F.3: Trajectory K=1

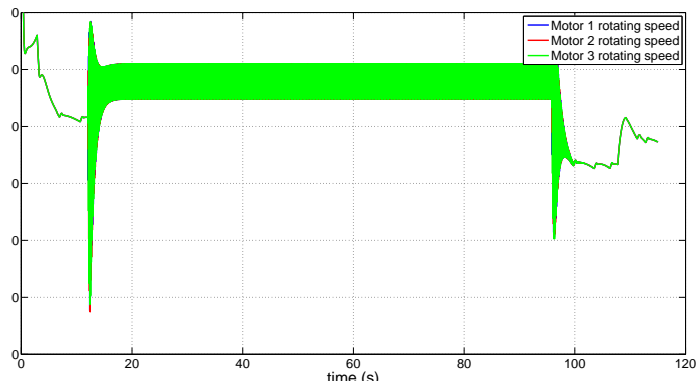


Figure F.4: Control K=1

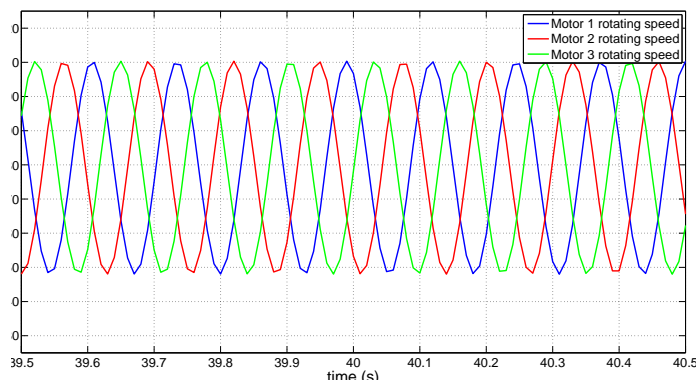


Figure F.5: Control K=1

F.4 Motors acceleration issues:

The aim of this article was to design the general control of “flying rotor” only. The required motor rotation speed has been extracted but its dynamics has been studied. If it seems feasible to obtain the required rotation speeds for small lateral accelerations, those latter will probably be limited by the maximum acceleration of the motors. Therefore it may be interesting to decrease the path following gain to reduce those accelerations. For instance, with $K = 0.25$ one can notice that the variation amplitudes are highly reduced as shown in Figure F.6. However, in this situation, “flying rotor” UAV follows slightly less closely the

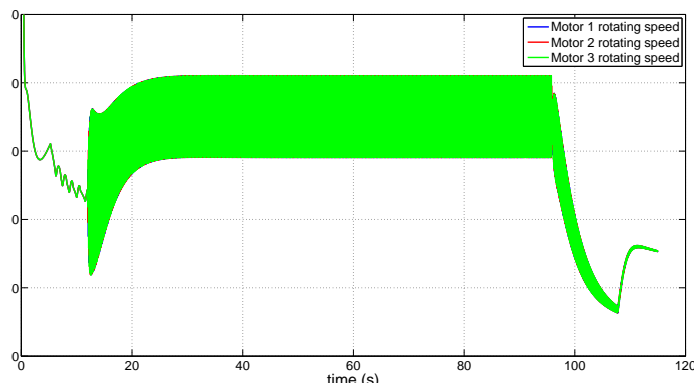


Figure F.6: Control $K=0.25$

expected path as it can be noticed in Figure F.7. An advanced control of the electric motors

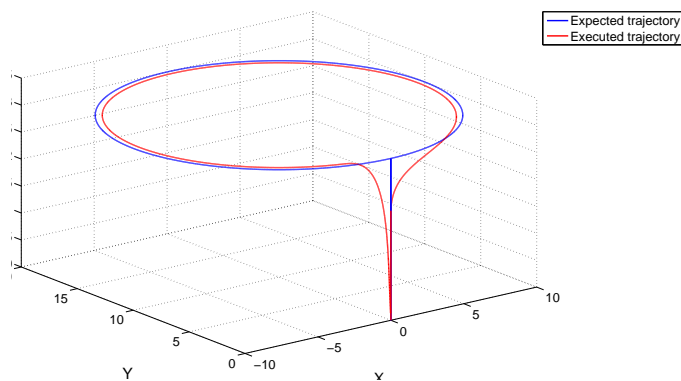


Figure F.7: Trajectory $K=0.25$

such as a FOC (Field Oriented Control) would be of great interest in order to maximise the lateral acceleration limit. [?].